THE UNIVERSITY *of* EDINBURGH

Hydrodynamics and drive-train dynamics of a direct-drive floating wind turbine

Latha Sethuraman

Doctor of Philosophy

THE UNIVERSITY OF EDINBURGH

2014

Abstract

Floating wind turbines (FWTs) are considered a new lease of opportunity for sustaining growth from offshore wind energy. In recent years, several new concepts have emerged, with only a few making it to demonstration or pre-commercialisation stages. Amongst these, the spar-buoy based FWT has been extensively researched concept with efforts to optimise the dynamic response and reduce the costs at acceptable levels of performance. Yet, there exist notable lapses in understanding of these systems due to lack of established design standards, operational experience, inaccurate modelling and inconsistent reporting that hamper the design process. Previous studies on spar-buoy FWTs have shown inconsistencies in reporting hydrodynamic response and adopted simplified mooring line models that have failed to capture the coupled hydrodynamic behaviour accurately. At the same time, published information on drive-trains for FWTs is scarce and limited to geared systems that suffer from reliability issues. This research was aimed at filling the knowledge gaps with regard to hydrodynamic modelling and drive-train research for the spar-buoy FWT.

The research proceeds in three parts, beginning with numerical modelling and experimental testing of a stepped spar-buoy FWT. A 1:100 scale model was constructed and tested in the University of Edinburgh's curved wave tank for various regular and irregular sea states. The motion responses were recorded at its centre of mass and nacelle locations. The same motions were also simulated numerically using finite element method based software, OrcaFlex for identical wave conditions. The hydrodynamic responses were evaluated as Response Amplitude Operator (RAO) and compared with numerical simulations. The results showed very good agreement and the numerical model was found to better capture the non-linearities from mooring lines. A new design parameter, *Nacelle Magnification Factor*, was introduced to quantify coupled behaviour of the system. This could potentially encourage a new design approach to optimising floating wind turbine systems for a given hub height.

The second part of the research was initiated by identification of special design considerations for drive-trains to be successfully integrated into FWTs. A comparative assessment of current state of the art showed good potential for direct-drive permanent magnet synchronous generators (PMSG). A radial flux topology of the direct-drive PMSG was further examined to verify its suitability to FWT. The generator design was qualified based on its structural integrity and ability to ensure minimal overall impact. The results showed that limiting the generator weight without compromising air-gap tolerances or tower-foundation upgrades was the biggest challenge. Further research was required to verify the dynamic response and component loading to be at an acceptable level.

The concluding part of research investigated the dynamic behaviour of the direct-drive generator and the various processes that controlled its performance in a FWT. For this purpose, a fully coupled aero-hydro-servo-elastic model of direct-drive FWT was developed. This exercise yet again highlighted the weight challenge imposed by the direct-drive system entailing extra investment on structure. The drive-train dynamics were analysed using a linear combination of multi-body simulation tools namely HAWC2 and SIMPACK. Shaft misalignment, its effect on unbalanced magnetic pull and the main bearing loads were examined. The responses were found to be within acceptable limits and the FWT system does not appreciably alter the dynamics of a direct-drive generator. Any extra investment on the structure is expected to be outweighed by the superior performance and reliability with the direct-drive generator.

In summary, this research proposes new solutions to increase the general understanding of hydrodynamics of FWTs and encourages the implementation of direct-drive generators for FWTs. It is believed that the solutions proposed through this research can potentially help address the design challenges of FWTs.

Lay Summary

Offshore wind power is expected to play a crucial role in expansion of energy mix from renewable technologies for countries such as the UK. Atleast 18GW of power is expected from Offshore wind installations by the year 2020. Accelerating this growth will require massive cost reductions and introduction of new technologies that can tap high quality wind resources in deeper waters. Floating wind turbine (FWT) is one such technology that can help achieve this. This involves installing turbines on platforms that can float in deep waters and extract much higher energy.

Several concepts of FWTs have emerged in recent years based on the platform topology such as spar, tension-leg and semi-submersible configurations. Yet, large-scale commercialisation of these concepts is impeded by several challenges. So far, research on spar-buoy FWTs has been inadequate in reporting hydrodynamic behaviour with inaccuracies in mooring line representation. Concurrently, there is also very limited information on the dynamics of power transfer with drive-trains for FWTs. This research, was aimed at filling these gaps and improve the understanding with regard to two elements namely hydrodynamics (wave-structure interaction) and drive-train dynamics (mechanical power transfer) of FWTs.

As a first step, a scaled down version of a spar buoy FWT was built and tested in the University's wave tank laboratory in various wave conditions that resembled real ocean conditions. The experimental data was used to validate a numerical model of the hydrodynamic system using finite-element based software, OrcaFlex. The results demonstrated a good accuracy of the numerical model in predicting non-linearities from mooring lines. A new design parameter, Nacelle Magnification Factor (NMF), was introduced to increase the understanding of the hydrodynamics and encourage a new design approach for optimising FWTs for a given hub height.

In the second part of research, focus was shifted to drive-trains where the mechanical power conversion takes place. Among the current state-of-art drive trains, geared systems were identified to be least effective for FWTs as they suffer from low reliability. Direct-drive generators that couple directly to the wind turbine showed

good potential. Studies on generator structural design showed that the biggest challenge with direct-drive system was limiting the generator weight. The next step in the design process was to verify if the dynamic behaviour of the direct-drive system was within acceptable levels.

The final part of research looked at the dynamics of the direct-drive system. To facilitate this study, multi-body model simulations were carried out considering the various interactions within the system. The results showed that the component loading and response of the direct-drive generator was within acceptable levels thus favouring the implementation of direct-drive generator to FWT.

In summary, this research proposed new design models and solutions to address the design challenges related to hydrodynamics and drive-train dynamics of the spar-buoy FWT.

Declaration

I hereby declare that this thesis has been composed by myself and that except where stated, the work contained is my own. I also declare that the work contained in this thesis has not been submitted for any other degree or professional qualification except as specified.

Latha Sethuraman

May 2014

Acknowledgments

Firstly, I thank Almighty for enabling me to undertake this research work. It has been a great privilege for me to spend the last three years at the Institute for Energy systems in the University of Edinburgh at the behest of my journey leading to a PhD degree. It has been quite an experience filled with some memorable moments. I consider myself as fortunate and am thankful to the following people that have contributed directly or indirectly towards this thesis.

I am grateful to my supervisor, Dr. Vengatesan Venugopal who gave me the opportunity and necessary advice to proceed through my doctoral program, the freedom to pursue independent work and complete my dissertation. I am deeply indebted to Prof. Markus Mueller for his valuable guidance with my research direction in making a meaningful transition across research disciplines. I am thankful for the opportunities provided by both of them for training in different fields and also establishing a resourceful network of colleagues.

Thanks are due to Neil Wood and Kevin Anderson for their assistance with model fabrication and set-up, to Gregory Payne for tutoring me on wave tank operation and providing the repair whenever necessary, to Remy Pascal and Russell Bannerman for their help with wave probe calibration. Acknowledgments are due to Aristides Zavvos(Power lab) for his contributions towards ANSYS modelling; to Yihan Xing, Professor Zhen Gao, Professor Torgeir Moan and Zhiyu Jiang from NTNU for their significant contributions to aero-elastic modelling and assistance with multi-body simulation; to Guillaume Tollé and Holger Strieder from TIMKEN for providing me with the necessary inputs on bearing stiffness calculation. Special thanks go to David Forehand, Laura Finlay and Aby Iyer for their invaluable friendly assistance. Members of Power Lab deserve loud thanks - especially Ozan, Nisaar, Richard, Eddie, JP, Joe, Siraj and Kaswar for their generosity in sharing knowledge, jokes and some great food.

Finally, I would like to dedicate this work to my family-my father, Mr. S. Sethuraman, my mother, Mrs. V Banumathi and my brother, S. Balasubramaniyan for their constant love and support that provided my inspiration and driving force. I owe them everything and wish I could show them just how much I love and appreciate them. I hope this work makes them proud.

Table of Contents

Abstract i
Lay Summary iii
Declaration v
Acknowledgments vii
Abbreviations xxv
Nomenclature xxv
Chapter 1 Introduction 1
1.0 Background 1
1.1 Offshore Wind Energy 2
1.2 Current trends in Offshore Wind Market 3
1.3 Deep water wind and its implications 4
1.4 Floating platforms for wind turbines 5
1.5 Research on Floating wind turbines 6
1.6 SPAR buoy type wind turbine 8
1.7 Motivation for Research 9
Problem Statement 1: Hydrodynamic modeling and Response Prediction 10
Problem Statement 2: Drive-train Configuration 11
1.8 Scope of this research 14
1.9 Objectives 16
1.11.1 Part - I 16
1.11.2 Part - I Tasks 17
1.11.3 Part - II 17
1.11.4 Part – II Tasks 18
1.11.5 Part – III 18
1.11.6 Part – III Tasks 19
1.10 Outline of the thesis 21
1.11 Publications 21
Chapter 2 Literature Review 23
2.0 General 23
2.1 Literature review for Part-I: Hydrodynamics of FWTs 23
2.1.1 Hydrodynamic response and Mooring line models 24
2.1.1.1 Modelling the dynamics of mooring lines 26
2.1.1.2 Reporting Hydrodynamic Response 28

2.1.2 Response Amplitude Operator 29
2.1.3 Significant motion amplitude 30
2.1.4 RAO Vs Significant motion response 31
2.1.5 Observation 32
2.2 Literature review for Part-II & III: Drive-trains for FWTs 32
2.2.1 Current trends in drive-train technology for Floating wind turbines 34
2.2.2 Towards cost effective drive-trains 37
2.2.2.1 Structural design aspects of Floating Wind Turbines 37
2.2.2.2 Assessment of key design parameters for drive-train selection 39
2.2.3 An overview of technology options 41
2.2.3.1 Geared drive-trains 41
2.2.3.2 1-stage/2-stage geared drives 42
2.2.3.3 Gearless drive-trains 43
2.2.3.4 Comparison 45
2.2.3.5 Direct-drive generators for floating wind turbines 46
2.2.3.6 Assessing the suitability of permanent magnet generators for FWTs 48
2.2.3.7 Observation 49
2.2.3.8 Summary 49
Chapter 3 Experimental and Numerical Modelling Techniques 51
3.0 General 51
3.1 Experimental Spar buoy model of a floating wind turbine 51
3.2 Testing Environment and measurement 54
3.2.1 The Curved Tank Facility 54
3.2.2 Motion measurement and recording 57
3.2.3 Wave height measurement 59
3.2.4 Wave probe calibration 60
3.3 Experimental Testing 62
3.3.1 Free vibration tests and model calibration 62
3.3.2 The mooring configuration and the basis for selection 64
3.4 Testing in regular waves 68
3.5 Testing in random waves 69
3.6 Modelling in OrcaFlex 72
3.6.1 Modelling the spar-buoy 72
3.6.2 Modelling the mooring lines 78
3.7 Simulating the sea states and motion response 80

3.8 Summary 82
Chapter 4 Part I – Results and Discussions 83
4.0. General 83
4.1. Results 83
4.1.1. Wave elevation profile and motion response for regular waves 84
4.1.2. Pitch-coupled surge component- Nacelle Magnification Factor 92
4.1.3. Wave elevation profiles and motion response for irregular waves 95
4.2. Summary – Part I 121
Chapter 5 Part – II Structural Integrity of a Direct-drive generator 123
5.0 General 123
5.1 Introduction 123
5.2 Generator structural integrity 124
5.3 Methodology 127
5.4 The Floating wind turbine -full scale model 128
5.5 Nacelle motions 129
5.6 Generator Model 130
5.7 Evaluation of Structural integrity of the generator 132
5.8 Analytical model 134
5.9 Modelling in FEMM 138
5.10 Structural dynamic analysis in ANSYS 139
5.10.1 Magnetic Field only 141
5.10.2 Nacelle Motions Only 142
5.10.3 Load combination 144
5.11 Contributions to air-gap eccentricity from bearing compliance 145
5.11.1 Bearing stiffness Versus Magnetic stiffness-theory 145
5.11.2 Sensitivities of air-gap eccentricity to bearing compliance 149
5.12 Magneto-elastic stability of the generator - Secondary deflection 154
5.13 Comparison of results with FEMM 158
5.14 Possible Solutions for prevention of air-gap from closing 160
5.14.1 Design Option I -Increasing Structural Stiffness 161
5.14.2 Design Option II -Increasing the design air-gap 165
5.15 Discussions 170
5.16 Summary – Part II 171
Chapter 6 Aero-hydro-servo-elastic model of a FWT with a direct-drive generator 173
6.0 General 173

6.1 Introduction 173
6.2 A fully-coupled mechanical model 175
6.3 Direct-drive generator topology 176
6.3.1 Modelling the direct-drive generator 177
6.3.2 Development of drive-train mechanical properties 178
6.4 Hub and Nacelle Properties 183
6.5 The floating spar system 185
6.5.1 Tower and platform properties 186
6.6 Wind turbine Controller properties 193
6.6.1 Generator-Torque Control 194
6.6.2 Blade-Pitch Controller 197
6.7 Modelling the FWTDD system in HAWC2 199
6.7.1 Environmental loads 199
6.7.2 Controller stability 202
6.7.3 Global motion response 208
6.7.4 Internal drive-train behaviour 210
6.8 Summary 211
Chapter 7 Drive-train dynamics of a 5MW FWTDD system 213
7.0 General 213
7.1 Introduction 213
7.1.1 Drive-train dynamics 214
7.1.2 Dynamics of direct-drive generator 214
7.2 Theory and methodology 217
7.2.1 Internal drive-train response and feedback effects 217
7.2 Modelling generator response 224
7.3 Analysis of FWTDD drive-train system using the 2-step de-coupled approach 233
7.3.1 FWTDD HAWC2 model 233
7.3.2 Design load Case 233
7.3.3 Stand-Alone SIMPACK Model for the FWTDD system 234
7.4 Analysis and comparison of global drive-train responses 236
7.4.1 Comparison of main shaft loads 236
7.5 Internal drive-train response 241
7.5.1 Shaft Displacements 250
7.5.2 Net radial Forces due to unbalanced magnetic pull (UMP) 253
7.5.3 Bearing Loads 255

7.6 Bearing life 257
7.7 Summary – Part III 264
Chapter 8 Conclusions and Recommendations for further work 267
8.0 General 267
8.1 Part - I 267
8.2 Part - II 269
8.3 Part - III 270
8.4 Recommendations for further work 272
8.5 Summary 274
Bibliography 275
APPENDIX-A 289
APPENDIX-B 293

List of Figures

Fig.No ***Page***

Fig. 1.1 Offshore wind farm locations in the World 3
Fig. 1.2 UK Offshore Wind Energy Map 4
Fig. 1.3 Offshore wind development plans 5
Fig. 1.4 Offshore wind turbine foundation market share as of 2013 8
Fig. 1.5 Floating wind turbine concepts 9
Fig. 1.6 The various branches of design in a Floating wind turbine 15
Fig. 1.7 Research Flow-chart 20
Fig. 2.1 Typical wind turbine drive-train 33
Fig. 2.2 Wind turbine drive-trains 34
Fig. 2.3 De-stabilising moment in a floating wind turbine 38
Fig. 2.4 GE 4.0MW Turbine 40
Fig. 2.5 Mechanical layout of a typical high-speed geared drive-train 42
Fig. 2.6 Mechanical layout of a medium–speed geared drive-train 43
Fig. 2.7 Mechanical layout of a typical gearless drive-train 44
Fig. 3.1 Available depth in the curved wave tank for different scale factors 52
Fig. 3.2 The spar-model built for the study 53
Fig. 3.3 (a) Plan view of floating wind turbine in the wave basin 56
Fig. 3.3 (b) Sectional view of floating wind turbine in the wave basin 56
Fig. 3.4 Model Spar in the wave basin 57
Fig. 3.5 The marker system and mooring lines 58
Fig. 3.6 Calibration rig used for wave gauge calibration 60
Fig. 3.7 Wave probe calibration – Voltage Versus depth 61
Fig. 3.8 Experimental set-up and data measurement 61
Fig. 3.9 Sample time response measured during the free-decay tests 64
Fig. 3.10 Mooring configurations. 65
Fig. 3.11 Surge RAO for the 2-point and 4-point mooring configurations 66
Fig. 3.12 Heave RAO for the 2-point and 4-point mooring configurations 67
Fig. 3.13 Pitch RAO for the 2-point and 4-point mooring configurations 67
Fig. 3.14 Yaw RAO for the 2-point and 4-point mooring configurations 68
Fig. 3.15 Mass and Geometry properties of the spar as entered into Orcaflex 73
Fig. 3.16 OrcaFlex models of the stepped-spar floating wind turbine 74
Fig. 3.17 Drag coefficient data of the spar as entered into Orcaflex 77
Fig. 3.18 Added Mass and Damping data 77

Fig. 3.19 Mooring line modelling in OrcaFlex..... 78
Fig. 3.20 Screenshots of the model in OrcaFlex 81
Fig. 4.1 (a) Wave elevation time history for 1 minute duration (regular wave, H=30mm, f=0.5Hz), (b) Surge response time history, (c) Heave response time history(d) Pitch response time history for 1 minute duration 85
Fig. 4.2 (a) Wave elevation time history for 1 minute duration (regular wave, H=30mm, f=1.44Hz), (b) Surge response time history, (c) Heave response time history and (d) Pitch response time history. 86
Fig. 4.3 Wave Elevation time history for 1 minute duration (regular wave, H=30mm, f=1 Hz), (b) Surge Response History, (c) Heave response time history and (d) Pitch response time history. 87
Fig. 4.4 Surge Response amplitude operator for regular waves of height H=30mm, 60mm and 90mm. 89
Fig. 4.5 Heave Response amplitude operator for regular waves of height H=30mm, 60mm and 90mm. 90
Fig. 4.6 Pitch Response amplitude operator for regular waves of height H=30mm, 60mm and 90mm. 91
Fig. 4.7 Dynamic scaling effect of pitch coupled surge response. 92
Fig. 4.8 Surge response with and without damping of pitch induced surge motion..... 94
Fig. 4.9 Wave elevation time history for a duration of 128sec(irregular wave, H_{m0}= 30mm and f_p=0.8Hz). 97
Fig. 4.10 Wave spectrum computed from experimental measurements and OrcaFlex simulations(irregular wave, H_{m0}= 30mm and f_p=0.8Hz) 97
Fig. 4.11 (a) Surge response time history (b) Heave response time history (c) Pitch response time history. All response time histories were recorded at the C.O.M for duration =128sec (irregular wave based on JONSWAP spectrum, H_{m0}=30mm and f_p=0.8Hz). . 98
Fig. 4.12 Surge Response Amplitude Operator computed at the C.O.M for irregular waves defined by JONSWAP spectrum, H_{m0}=30mm. 99
Fig. 4.13 Heave Response Amplitude Operator computed at the C.O.M for irregular waves defined by JONSWAP spectrum, H_{m0}=30mm. 100
Fig. 4.14 Pitch Response Amplitude Operator computed at the C.O.M for irregular waves defined by JONSWAP spectrum, H_{m0}=30mm. 101
Fig. 4.15 Surge Response Amplitude Operator computed at the nacelle for irregular waves defined by JONSWAP spectrum, H_{m0}=30mm. 102

Fig. 4.16 Heave Response Amplitude Operator computed at the nacelle for irregular waves defined by JONSWAP spectrum, H_{m0}=30mm. 103
Fig. 4.17 Pitch Response Amplitude Operator computed at the nacelle for irregular waves defined by JONSWAP spectrum, H_{m0}=30mm. 104
Fig. 4.18 Surge Response Amplitude Operator computed at the C.O.M for irregular waves defined by JONSWAP spectrum, H_{m0}=60mm. 105
Fig. 4.19 Heave Response Amplitude Operator computed at the C.O.M for irregular waves defined by JONSWAP spectrum, H_{m0}=60mm. 106
Fig. 4.20 Pitch Response Amplitude Operator computed at the C.O.M for irregular waves defined by JONSWAP spectrum, H_{m0}=60mm. 107
Fig. 4.21 Surge Response Amplitude Operator computed at the nacelle for irregular waves defined by JONSWAP spectrum, H_{m0}=60mm. 108
Fig. 4.22 Heave Response Amplitude Operator computed at the nacelle for irregular waves defined by JONSWAP spectrum, H_{m0}=60mm. 109
Fig. 4.23 Pitch Response Amplitude Operator computed at the nacelle for irregular waves defined by JONSWAP spectrum, H_{m0}=60mm. 110
Fig. 4.24 Surge Response Amplitude Operator computed at the C.O.M for irregular waves defined by JONSWAP spectrum, H_{m0}=90mm. 111
Fig. 4.25 Heave Response Amplitude Operator computed at the C.O.M for irregular waves defined by JONSWAP spectrum, H_{m0}=90mm. 112
Fig. 4.26 Pitch Response Amplitude Operator computed at the C.O.M for irregular waves defined by JONSWAP spectrum, H_{m0}=90mm. 113
Fig. 4.27 Surge Response Amplitude Operator computed at the nacelle for irregular waves defined by JONSWAP spectrum, H_{m0}=90mm. 114
Fig. 4.28 Heave Response Amplitude Operator computed at the nacelle for irregular waves defined by JONSWAP spectrum, H_{m0}=90mm. 115
Fig. 4.29 Pitch Response Amplitude Operator computed at the nacelle for irregular waves defined by JONSWAP spectrum, H_{m0}=90mm. 116
Fig. 4.30 Surge response spectrum computed at the C.O.M and nacelle based on Welch's averaged periodogram method for JONSWAP wave spectrum, H_{m0}=30mm, f_p=0.8Hz. 118
Fig. 4.31 Heave response spectrum computed at the C.O.M and nacelle based on Welch's averaged periodogram method for JONSWAP wave spectrum, H_{m0}=30mm, f_p=0.8Hz. 119

Fig. 4.32 Pitch response spectrum computed at the C.O.M and nacelle based on Welch's averaged periodogram method for JONSWAP wave spectrum, H_{m0}=30mm, f_p=0.8Hz. 120
Fig. 5.1 Eccentricity due to structural deformation 126
Fig. 5.2 Eccentricity due to bearing Tolerance 126
Fig. 5.3 Assessment Methodology 127
Fig. 5.4 Nacelle acceleration and pitch velocity components for regular wave of height of 9 m and wave period 6.9 s 130
Fig. 5.5 Generator support structures 130
Fig. 5.6 Air gap computation from deformed rotor and stator profiles 137
Fig. 5.7(a) Flux density contour plots from FEMM; (b) Radial air gap flux density variation per pole-pair 139
Fig. 5.8 Stator and rotor deformation profiles along the periphery 140
Fig. 5.9 Nacelle alignment 141
Fig. 5.10 Air-gapvariation due to magnetic field only 141
Fig. 5.11 Air-gap variation due to Nacelle motions only 142
Fig. 5.12 Nacelle acceleration and pitch velocity components for regular wave of height, H=3m and wave period 6.9s (From OrcaFlex). 143
Fig. 5.13 Axial and radial variation of air-gap 143
Fig. 5.14 Air-gap variation due to Load combination (Magnetic field+ wave loads) 144
Fig. 5.15 Shaft-bearing arrangement 146
Fig. 5.16 Shaft radial displacements (g_{ash}) measured for different bearing stiffness 150
Fig. 5.17 UMP and bearing forces for Stiffness Case 1 151
Fig. 5.18 UMP and bearing forces for Stiffness Case 2 152
Fig. 5.19 UMP and bearing forces for Stiffness Case 3 152
Fig. 5.20 UMP and bearing forces for Stiffness Case 4 153
Fig. 5.21 Shaft Induced Eccentricity at different wind speeds for FWT system 154
Fig. 5.22 Iterative procedure for air-gap deflection for radial flux PMSG 156
Fig. 5.23 Percentage air-gap reduction after each iteration 157
Fig. 5.24 Air-gap variation as a function of position and iteration 157
Fig. 5.25 Stress variation as a function of position and iteration 158
Fig. 5.26 Flux contour and variation of normalised stress between 0º-100º along the periphery 159
Fig. 5.27 Percentage reduction in air-gap after each iteration 163
Fig. 5.28 Flux line plots for (a) Base case (b) 8mm and (c) 12mm air-gap designs 167

Fig. 5.29 Percentage reduction in air-gap after each iteration 168
Fig. 5.30 Stress variation as a function of air gap length 169
Fig. 5.31 Comparison of Stiffer structures (Design Option I)with structures of larger air-gap (Design Option II) 169
Fig. 6.1 Drive-train analysis methodology 174
Fig. 6.2 Rotor Nacelle Assembly of a direct-drive generator 176
Fig. 6.3 (a) Simple mechanical model of a direct-drive generator (b) Direct-drive generator Topology 178
Fig. 6.4 (a) Typical Nacelle layout for a direct-drive generator 183
Fig. 6.5 Main dimensions at the nacelle 184
Fig. 6.6 C.O.M location for the adjusted system 188
Fig. 6.7 Mooring layout of the FWTDD system 193
Fig. 6.8 A comparison of FWTDD system with existing designs 193
Fig. 6.9 Generator Speed-Torque Characteristics 196
Fig. 6.10 Tower response and controller response for the FWTDD system for a deterministic wind speed 203
Fig. 6.11 Step response. 205
Fig. 6.12 Step response - longer duration. 206
Fig. 6.13 Step response-adjusted 207
Fig. 6.14 Nacelle motion response statistics from HAWC2 simulations 208
Fig. 6.15 Nacelle motion response spectra for FWTDD system 209
Fig. 6.16 Drive-train analysis methodology 210
Fig. 7.1 Shaft Displacement 219
Fig. 7.2 (a) Concentric Shaft (b) Eccentric Shaft 219
Fig.7.3 Eccentricity versus Forces due to UMP 221
Fig. 7.4 Shaft–Bearing assembly 221
Fig. 7.5 Shaft Response (a) Radial displacement (b) Orbital motion 222
Fig. 7.6 A multi-body model of the direct-drive generator wind turbine in SIMPACK 226
Fig. 7.7 Time history of Vibration induced torque measured by SIMPACK 228
Fig. 7.8 Mean pitch response and torque at different wind speeds 229
Fig. 7.9 Vibratory torque as a percentage of operating torque 229
Fig. 7.10 Torque spectral density as obtained from SIMPACK and HAWC2 simulations under constant wind 230
Fig. 7.11 Torque spectral density as obtained from SIMPACK and HAWC2 simulations under turbulent wind 231

Fig. 7.12 Shaft node deflection profiles at different wind speeds 232
Fig. 7.13 Shaft loads, moments and nacelle motions applied to the stand-alone SIMPACK model 235
Fig. 7.14 SIMPACK topology diagram for FWTDD analysis 235
Fig. 7.15 % Difference in Main Shaft loads –WTDD Vs FWTDD (a) Mean Values (b) Standard deviation (c) Maximum Values 238
Fig. 7.16 Frequency spectra of main shaft Shear Forces 239
Fig. 7.17 Frequency spectra of main shaft Axial forces 240
Fig. 7.18 Frequency spectra of main shaft bending moments 240
Fig. 7.19 Frequency spectra of main shaft torque 241
Fig. 7.20 Internal drive-train responses - % Difference in Mean Values: FWTDD Vs WTDD 243
Fig. 7.21 Internal drive-train response -% Difference in Standard Deviation: FWTDD Vs WTDD 244
Fig. 7.22 Internal drive-train response - % Difference in Maximum Values: FWTDD Vs WTDD 245
Fig. 7.23 Frequency spectra of Radial Shaft Displacements 246
Fig. 7.24 Frequency spectra of Axial Shaft Displacements 246
Fig. 7.25 Frequency spectra of UMP forces 247
Fig. 7.26 Frequency spectra of BR2 Axial forces 247
Fig. 7.27 Frequency spectra of BR2 Radial forces 248
Fig. 7.28 Frequency spectra of BR2 Bending moments 248
Fig. 7.29 Frequency spectra of BR1 Axial Forces 249
Fig. 7.30 Frequency spectra of BR1 Radial Forces 249
Fig. 7.31 Frequency spectra of BR1 Bending Moments 250
Fig. 7.32 Eccentricity (%) for different wind speeds for WTDD and FWTDD system 251
Fig. 7.33 Main Shaft Tilt displacement history for a wind speed of 25m/s. 253
Fig. 7.34 Shaft Tilt displacement spectra for WTDD and FWTDD systems 253
Fig. 7.35 Net forces due to UMP at different wind speeds for WTDD and FWTDD systems 254
Fig. 7.36 Time histories of bearing radial load (BR2) and forces due to UMP 256
Fig. 7.37 Bearing life estimation methodology 258
Fig. 7.38 Wind speed PDF for IEC turbine classes I, II and III 259
Fig. 7.39 Time history of bearing radial loads 259
Fig. 7.40 Time history of bearing axial loads 260

Fig. 7.41 Dynamic equivalent radial load 260
Fig. 7.42 Load range histogram for Bearing BR2..... 261
Fig. 7.43 Load range histogram for bearing BR1 262
Fig. 7.44 Basic Rating life for bearings for different wind speeds: FWTDD Vs WTDD... 263

List of Tables

Table No ***Page***

Table 1.1 Spar Concepts……..... 12
Table 2.1 Drive train trends in floating wind turbines……..36
Table 2.2 Rank Matrix for drive-trains for floating wind turbines 45
Table 2.3 Comparison of Radial, axial and transverse flux PM generators..... 47
Table 3.1 Hydrostatic properties of the stepped-spar floating wind turbine..... 54
Table 3.2 Natural frequencies of the stepped-spar floating wind turbine 63
Table 3.3 Model sea state parameters for irregular waves..... 71
Table 3.4 Line structural properties 79
Table 5.1 Properties of a stepped-spar floating wind turbine scaled for prototype model... 128
Table 5.2 Tower top mass estimate used for stability calculations. 129
Table 5.3 Electro-magnetic and structural design data for generator 131
Table 5.4 Generator Mass data 132
Table 5.5 Comparison of normalised stresses computed using the analytical model and FEMM simulations..... 160
Table 5.6 Generator mass and air-gap deflection for design Cases 1-8..... 162
Table 5.7 Effect of Generator (Nacelle) Mass on Hydrostatic and resonance properties of the floating wind turbine..... 164
Table 5.8 Generator mass and air-gap deflection for structures with larger air-gap..... 167
Table 6.1 Generator Properties 177
Table 6.2 Drive-train mass and dimensions..... 180
Table 6.3 Drive-train properties and mass of major equipment..... 182
Table 6.4 Hub and Nacelle properties..... 185
Table 6.5 Resonance properties for different configurations..... 187
Table 6.6 Spar properties 188
Table 6.7 Undistributed Tower Properties..... 189
Table 6.8 Distributed Tower Properties..... 190
Table 6.9 Platform Structural properties..... 191
Table 6.10 Mooring system properties 192
Table 6.11 Controller properties 198
Table 6.12 Load Cases used for this study..... 202
Table 7.1 Bearing load factor and ratings 263

Abbreviations

BEM	Blade Element Momentum
BR	Bearing
COM	Centre of Mass
CRB	Cylindrical Roller Bearing
DFIG	Double-Fed Induction Generator
DLL	Dynamic Link Library
DOF	Degree of freedom
FEM	Finite Element Method
FWT	Floating Wind Turbine
FWTDD	Floating Wind Turbine with Direct-drive generator
PMSG	Permanent Magnet Synchronous Generator
RAO	Response Amplitude Operator
SCIG	Squirrel Cage Induction Generator
SWL	Sea Water Level
SWOT	Strengths, Weaknesses, Opportunities, and Threats
TDI	Double row tapered roller bearing –inner race
UMP	Unbalanced Magnetic Pull
WTDD	Wind Turbine with Direct-drive generator(Land based)

Nomenclature

Symbol	***Unit***	***Description***
a	m	Peak wave amplitude
a_r	m/s^2	Fluid acceleration relative to body
a_w	m/s^2	Fluid linear acceleration
$\hat{B}_g$	Wb/m^2	Magnetic peak flux density
C_a	-	Added mass co-efficient
C_d	-	Drag co-efficient
C_p	-	Power co-efficient
D_g	m	Air-gap Diameter
e	m	Eccentricity
f	Hz	wave frequency(regular wave)
f_n	Hz	Natural frequency of torsional vibration
f_p	Hz	Peak wave frequency(irregular wave)

Symbol	*Unit*	*Description*
F_{mag}	N/m	Magnetic stiffness
$F_{structure}$	N/m	Generator structural stiffness
g	m/s^2	acceleration due to gravity
g_a	m	Measured air-gap
g_{ash}	m	air-gap change due to shaft displacement
g_{nom}	m	Nominal air-gap length
h_m	m	Magnet height
H_{m0}	m	Significant Wave height
I	kg-m^2	Combined Inertia of generator and turbine
I_p	m^4	Shaft polar moment of Inertia
ka	-	Scattering parameter
K_I	-	Integral gain
K_{ls}	Nm/rad	Equivalent drive-train torsional stiffness
K_p	-	Proportional gain
k_T	-	Torque constant
P_{rated}	W	Generator rated power
R	m	Turbine Radius
S_{JS}	m^2/rad/s	JONSWAP wave spectrum
S_{PM}	m^2/rad/s	Pierson-Moskowitz spectrum
S_η	m^2/rad/s	Wave Spectrum
S_ζ	m^2/rad/s	Response Spectrum
T_{rated}	N-m	Generator rated torque
V_r	m/s	Fluid velocity relative to body
η	m	Amplitude of wave
λ	-	Model Scale factor
λ_*	-	Tip-speed ratio
Ω_0	rpm	Turbine rated speed
θ	deg	Angular position along generator rotor
ρ	kg/m^3	Sea water density
σ	-	Bandwidth parameter
$\sigma(\theta,t)$	N/m^2	Instantaneous magnetic stress
ω	rad/s	Wave frequency
ζ	m	Amplitude of response

Chapter 1

Introduction

1.0 Background

Energy in all of its forms is an indispensable element in the modern world. As the global population continues to grow, the demand for electricity has been increasing exponentially for continued urbanisation and economic growth. Of late, climate change issues, increasing insecurity from fossil fuels and rising energy prices have threatened the sustainability of existing power supplies that are carbon-intensive.
Under the extended Kyoto protocol[1] major countries have already committed to internally binding emission reduction targets. De-carbonizing the electricity supply and bridging the supply-demand gaps within the climate change framework would mean an aggressive growth trajectory from renewable energy industry, encouraging more research and investments in newer, cleaner forms of energy.

Thanks to the evolution of technology enabling policies, there has been a rise in the penetration of energy from land-based and Ocean-based technologies into the energy mix(wind, solar, nuclear, biomass, geothermal, wave and tidal). According to BP [1] energy from renewables is expected to grow at an average rate of 6.4% a year to 2035. There are high expectations for greater diffusion of renewable energy sources as more than half of world's largest cities are planning to increase their uptake of renewable energy [2]. However, new capacity additions from onshore technologies are proving to be a major challenge. A host of practical constraints are beginning to curtail their development; Seasonal variations for solar power, farmland and feedstock constraints for biomass and increasing global competition for nuclear resource.

[1] The Kyoto second commitment period applies to about 15% of annual global emissions of greenhouse gases

With an annual growth rate of 25-30%, wind power has been the biggest contributor to the electricity fuel mix in the last decade. Their growth is but limited by non-availability of inexpensive land and visual impact caused by large wind turbines. Further, the challenge of transmitting the electricity to large coastal load centres is a major disincentive for grid penetration of onshore renewables. Besides, the pressure to replace ageing energy infrastructure and reduce the risk of energy prices has forced countries like the UK to gravitate into offshore renewables.

1.1 Offshore Wind Energy

The offshore renewable sector encompassing offshore wind, wave and tidal energy has now been recognised as a quantum leap into delivering the ambitious renewable energy targets set by governments around the world. Currently, offshore wind power is one of the commercially well-established ocean-based renewable energy industries. Ever since the world's first commercial offshore wind farm opened in 1991 in Denmark[2] , Offshore wind development has witnessed a steady growth in the last two decades. Europe leads the developments with the majority of offshore wind farms set up in North Sea, Baltic and Irish Seas, and the English Channel. According to the European Wind Energy association [3], the cumulative installed offshore wind capacity stood at 6.56 GW by the end of 2013. Wind resource assessment studies have shown enormous offshore wind potential in countries like the US, UK and most of Europe [4-6]. The analyses also indicate that if renewables have to form a substantial portion in the energy mix by 2020, rapid deployment of offshore wind will be necessary.

Building wind farms offshore has a number of interesting prospects to offer. Offshore wind is stronger and more consistent than on land, resulting in higher productivity. Offshore wind turbines have less acoustic and aesthetic requirements and therefore face less public resistance. Turbines can be made larger due to the availability of transportation facilities by ship vessels. They can be located closer to densely populated coastal load centres by avoiding the need for long transmission lines.

[2] Vindeby Windfarm is located in the Baltic Sea off the coast of Vindeby, Denmark

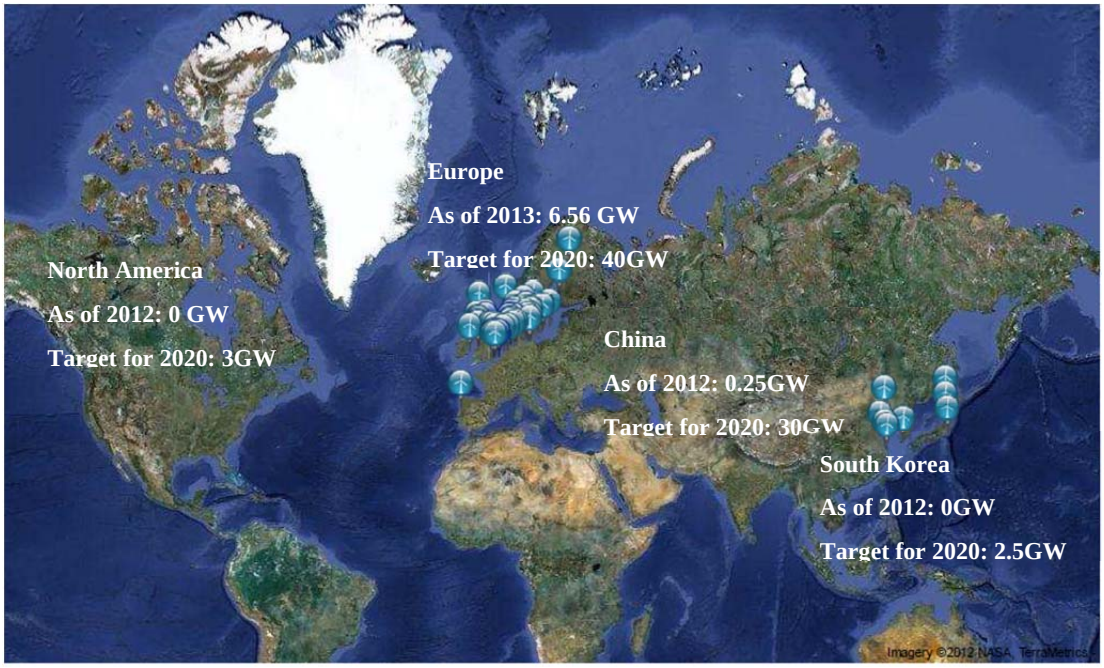

Fig. 1.1 Offshore wind farm locations in the World[7, 8]

1.2 Current trends in Offshore Wind Market

A good number of offshore wind farms have already been set up in areas combining high windiness, near shore and shallow waters off the coasts of Europe (Fig. 1.1 shows the location of wind farms, the worldwide installed offshore wind capacity and targets for 2020). The ocean is a big opportunity, but there are also a lot of issues and existing uses that need to be addressed. Variations in bathymetry, fluctuations in wind speeds close to shoreline, stringent environmental restrictions along coastal waters and a host of other technological and economic factors have restricted offshore developments to shallow waters (depth < 30m). In Europe, for instance, approvals of new offshore wind farms are becoming increasingly difficult with multiple parameters to satisfy. At the same time, major wind turbine manufacturers have ventured into development of larger turbines rated up to 10MW exclusively for offshore installations. Installing these wind turbines would need much higher and steadier wind speeds. With already a crowded coastline and the suitability of remaining shallow water sites being doubtful, efforts have been extended to building wind farms located at greater distance from the shore in deeper waters.

1.3 Deep water wind and its implications

Deep water wind development is an emerging sector in offshore wind market. As water has less surface roughness, wind speeds are considerably higher and less variable with lower turbulence implying much higher energy yields. For the United Kingdom, for example, wind resource potential is greater in deeper waters at greater distance from the shore. Exploiting this vast wealth of resource requires careful consideration of a number of factors. Deep water wind is not a lone resource; deep seas are also sources of long period wave swells. The wave heights in such locations are relatively large (4-8.5m). The offshore wind-wave climate and bathymetry maps (based on [9, 10]) in Fig.1.2 highlight the wind resource potential and implications of deep water wind development for United Kingdom.

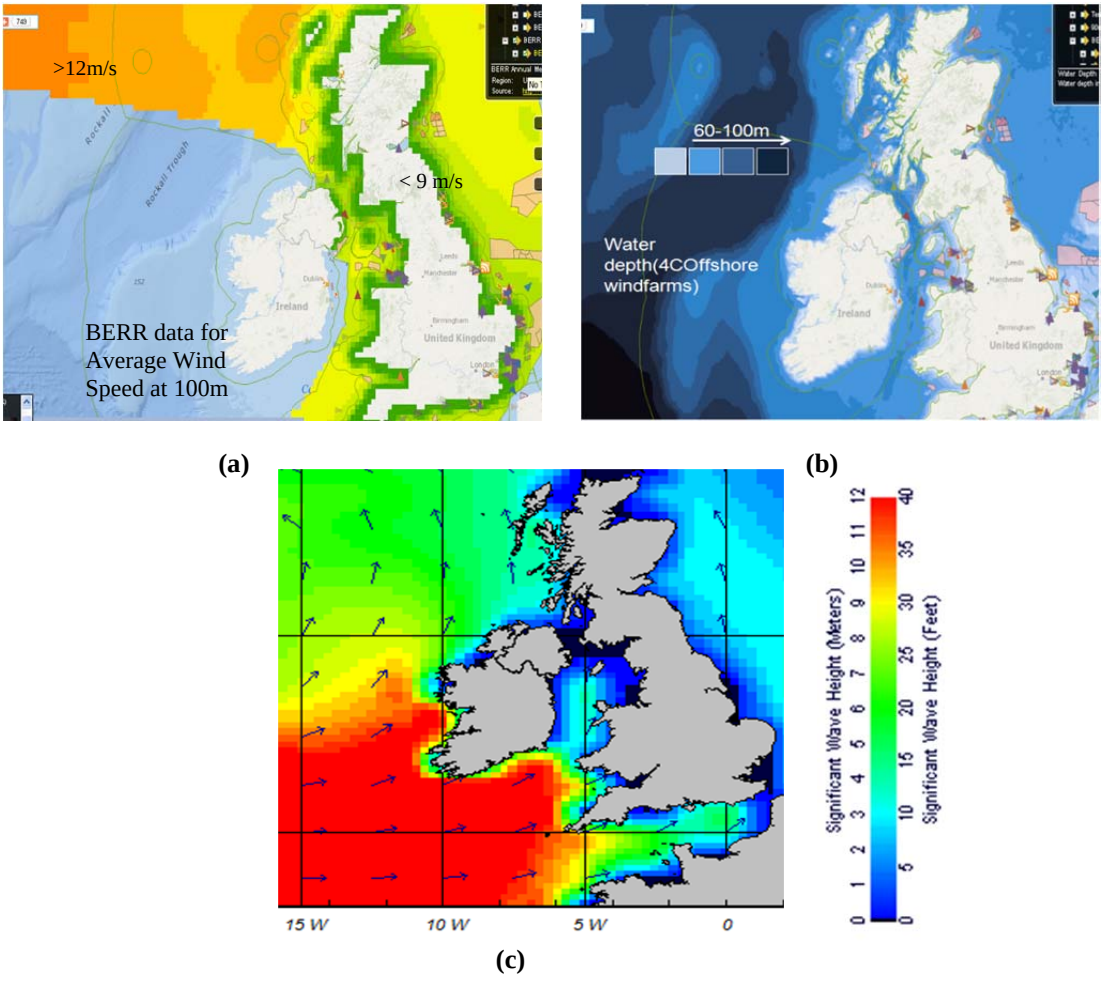

Fig. 1.2 UK Offshore Wind Energy Map (a) The BERR[3] data for average wind speed, (b) water depth and (c) Significant Wave height

[3] Department for Business, Enterprise and Regulatory Reform

The existing offshore wind technology needs a number of modifications to contend with such harsh met-ocean profiles in deep seas. Turbine platforms must be adequately stiff to external loading from wind and wave spectrums. Traditionally, offshore wind turbines have been built using bottom mounted technology (gravity based, monopiles, jackets, tripods or suction bucket). This technology limits the potential area for offshore wind energy generation to sea depths less than 60 m. For depths beyond 60m, bottom mounted constructions are prohibitively expensive. In such cases, the possibility of transferring loads to water is more attractive than bottom mounted foundations because of two principal reasons: water being much closer, the load path is shorter and peak bending moments are commensurately less. Because water is a compliant media, there is flexibility and the peak forces may be lower. Consequently, the designs likely to be practical for deeper water shall be floating type tethered to the sea bottom. The European national action plans for the next decade indicate major developments in water depths exceeding 60m (Fig. 1.3), where floating foundations are likely to be more relevant [11].

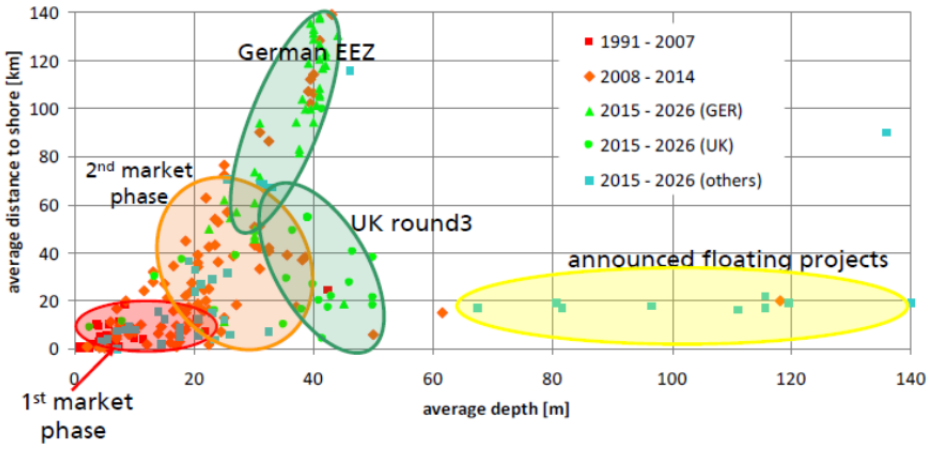

Fig. 1.3 Offshore wind development plans[11]

1.4 Floating platforms for wind turbines

Floating structures are not a new idea - the technology is a well-established one with very large structures being engineered for the Oil and Gas Industry since the 1950s. Offshore platforms that are used extensively for oil/gas exploration namely Tension leg platforms, SPAR, barges and semi-submersible structures are now being

considered for potentially accommodating wind turbines. As wind turbine application will have substantially reduced requirements for above water deck areas and will not be placed in depths commonly achieved by the oil and gas industry, significant cost reductions can be expected. Statoil's spar concept, Hywind[12],the TLP concept by Blue H [13] and Principlepower's windfloat [14] are currently into prototype development. The floating platform technology, per se, when used for wind turbines, requires major adjustments with different design requirements to satisfy.

Wind turbine is an inherently complicated system in which the tower structural dynamics are carefully tuned to avoid interactions with the spinning turbine, and advanced control systems are implemented to maximize power output [15]. When such a system is placed on a floating foundation, interactions between platform motions and turbine performance are significant. An optimal floater configuration must be robust enough to ensure minimal dynamic response without adverse implications on power production during normal and extreme wind/wave climates. The optimisation approach has important requisites to consider:

1. Unlike the oil and gas industry where platforms are engineered to minimize vertical motion(less attention paid to angular motions), for wind turbines minimizing rotational motions namely (pitch and roll) is critical [16].
2. Foundations must support a taller tower (because of the additional height due to water depth), and withstand forces from waves, currents and wind [17].
3. The floater must support a large payload; i.e. the wind turbine, nacelle and the tower with large aerodynamic loads high above the water surface.
4. The floater must remain relatively stable and stationary despite the movement of the sea surface.

Above all, the design must be economically feasible under the constraints imposed by the purpose of the structure.

1.5 Research on Floating wind turbines

A floating wind turbine (henceforth termed as FWT) is a sophisticated multi-body system that exhibits a complex aero-hydro-servo-elastic structural behaviour. The kinematics of such a system is governed by the excitation and damping forces caused

by wind, wave, control system, mooring system and turbine response that are highly non-linear. There exists a dynamic coupling between the platform, tower, the wind turbine and the control system behaviour that needs to be well understood. The floating wind technology is still in the early stages of development; being a nascent industry, global knowledge is minimal as several challenges remain to be addressed.

Designing a floating wind turbine is a multi-disciplinary research problem. Huge challenges remain when trying to combine the existing wind technology know-how for deep water application. A number of permutations and combinations of platform and wind turbine configurations are currently being researched. While platforms are designed to accommodate single or multiple turbines, wind turbines are redesigned with two or three blades suitable for upwind, downwind, vertical or horizontal mounting. Design of appropriate control system, power transmission systems and appropriate material choice for greater durability are also being actively pursued. Significant R&D effort has been spent in recent years with different research directions that can be broadly categorised into the following:

1) Foundation design: optimising & conceiving floater designs that ensure minimal dynamic response.
2) New wind turbine designs, for example, [18].
3) Design optimisation of mooring systems, for example, [19].
4) Demonstration or reduced scale testing for feasibility studies.
5) Development of computational tools to accurately predict the dynamics of coupling wind turbines to floating structures for e.g. [20].
6) Global performance analysis for understanding the dynamic interactions between the various elements of the system due to the coupled aero-hydro-servo-elastic loads for e.g.[21, 22].
7) Establishment of design rules and standards for certification and classification [23, 24].
8) Hydrodynamics in extreme waves for e.g. [25, 26]

Besides, minimising the costs of operation, manufacture, transportation, assembly, and installation are other major areas to look at. With so many research challenges, it is not surprising that the move towards commercialization of the technology has been protracted. As of 2013, according to the European Offshore wind statistics [3], only

three installations have been successful with two being grid connected, giving floating structures a tiny stake (Fig. 1.4) in the offshore foundations market.

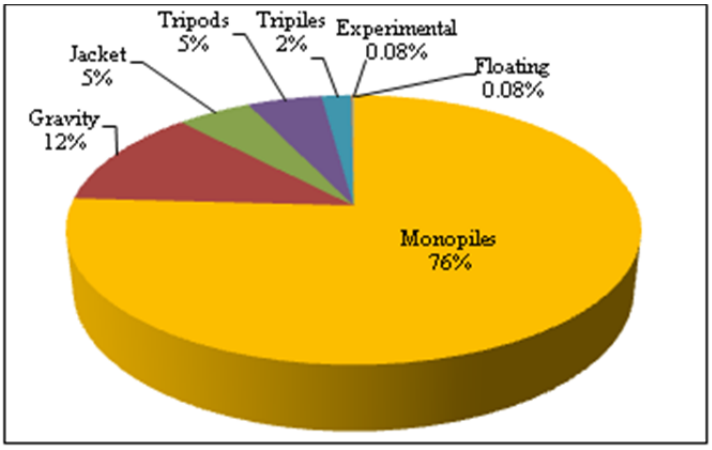

Fig. 1.4 Offshore wind turbine foundation market share as of 2013

1.6 SPAR buoy type wind turbine

In recent years, several new concepts for floating wind turbines have been proposed and prototypes are being built for experimental purposes. These systems are categorised based on the mechanism by which they achieve their stability as SPAR[4], TLP (Tension Leg Platform), barge and hybrid system, each applicable for different bands of deep waters. The TLP stabilises by tension in the mooring system and excess buoyancy. The SPAR buoy utilises a deep draft combined with ballast while the barge uses a large water-plane area and shallow draft. Hybrid systems such as a semi-submersible rely on all three methods namely large water-plane, deep draft and ballasting to maintain stability.

Among these concepts the spar-buoy type wind turbine has been the most extensively researched and tested concept. Hywind[5], the world's first floating wind demonstrator project is based on the spar-buoy concept. A spar platform consists of a single vertical cylinder with a central buoyancy tank held at the required draft by using ballast weights. Unlike the larger diameter structures used for offshore oil industry, spar platforms for wind turbines are slender with narrower section at water-

[4] Acronym for Single-point anchored reservoir system.
[5] Hywind Demonstrator project was commissioned in the year 2009.

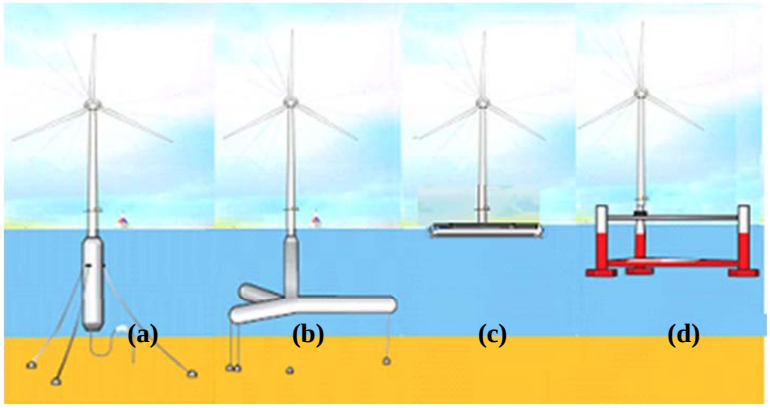

Fig. 1.5 Floating wind turbine concepts (a) SPAR (b) TLP (c) Barge (d) Semi-submersible

plane. Ballast at the base of spar not only provides stability, but also the required righting moment and high inertial resistance to pitch/roll motions. Moorings are generally of catenary arrangement and meant for station keeping only. Simple construction, lower dynamic response per displacement and relatively lesser offshore effort (e.g.: sea-bed preparation, mooring) renders the spar concept as a promising option. The simple geometry of the spar is a design advantage, although variations are possible. The bottom structure of the spar can be a shell structure (Classic Spar), or a truss structure (Truss Spar) with a soft tank at the keel and added mass/damping plates in between. Spars are generally not subjected to large dynamic mooring line forces, but weakly damped in surge and pitch motions. The high static heel angles require special considerations for the mechanical design and strength of components at the nacelle. Because the buoy dimension has to be greater than 50m for stability reasons, the concept may not work in shallow waters. This results in a massive structure to support wind turbines in deep waters.

1.7 Motivation for Research

Operating a wind turbine at greater distance from the shore in deeper waters, drives the capital costs significantly thereby challenging the economics of the energy generated. Statoil's 2.3MW Hywind demonstrator turbine is estimated to cost $29million/MW [27]. According to an estimate by Bloomberg New Energy Finance, this is approximately five times higher than the current fixed offshore wind farms ($5.5 million/MW). Despite the success of the Hywind demonstrator project, efforts

are underway to further optimise the spar system: reduce the structural mass, size and therefore the costs at acceptable levels of performance. Ever since the first concept was studied in the late 90s, the spar platform has evolved a long way. Every effort has been made to identify the best control methods to mitigate the effects of negative damping [27, 28]. Measures to reduce the material cost for the buoyancy tank and the ballast needed have been investigated. Design trade-offs include truncating the spar length or reducing the hull diameter [29, 30], inclusion of appendages such as drag fin and drag plates [31-34], altering the mooring configurations [29, 35] and using non-uniform cross-section [36]. These have led to the conceptualisation of OC3-Hywind, UMaine-Hywind [37] and the hybrid-SPAR floating wind turbines [38]. More sophisticated concepts such as the SWAY design [39],the advanced spar concept by [40] and hybrid systems (combining wind and wave energy, for eg. [41]) are under development. Table 1.1 shows some spar concepts that have evolved since 1998. While some of these concepts are in the early conceptual stages of development, only a few have entered the experimental phase. As with any new technology, large scale development requires extensive model testing and demonstration to establish credibility on a concept. A significant amount of work on the qualification of optimal configurations is still needed with a greater understanding of the dynamics of the various elements of the system. The following gaps were observed in the research activities that have been carried out so far for the spar-buoy based wind turbine.

Problem Statement 1: Hydrodynamic modeling and Response Prediction

Optimal floater for a wind turbine must resist the wave induced forces and must satisfy some motion requirements for optimal performance. The current design of the spar relies on carefully tuned control system and hydrodynamic damping for reducing the system motions. Previous studies on the spar buoy wind turbine, for example, reference [42] claims that the spar platform suffers from weak damping characteristics in surge, pitch and heave motions. For example, the natural frequency of the Hywind spar is very low and far from the wave frequency, therefore aerodynamic damping is not effective on wave-induced oscillations [43]. While other methods of damping have been investigated (for e.g.: heave plates [32],

fins [25, 33]), damping from mooring lines is a less researched topic and can be significant for catenary moored systems such as the spar buoy wind turbine. A number of computational techniques employing different hydrodynamic codes are available to perform an integrated analysis coupling the dynamics from wave, structure and wind [20]. However to start with, it is important to confirm the accuracy of predictions of the motions of a floating support before coupling the dynamics from wind. So far, only a few studies have confirmed the numerical accuracy or capability of the models to qualitatively reproduce experimental observations. Although, these studies demonstrated good predictive ability of the tools, they follow simplistic approach in modelling the dynamics of mooring systems, raising questions on the predicted coupled hydrodynamic behaviour. Most methods employ quasi-static mooring models that do not capture non-linear behaviour of mooring lines accurately, for e.g.: [21],[44]. Since, accurate computer modelling is critical to achieving cost effective designs, loss of accuracy results in a conservative or under-estimated designs. Also, there is every possibility that such numerical approximations can ignore peculiar physical effects observed during experimental testing. This highlights the need for improved mooring line models and the importance of validation by experiments. There is a need to quantify the damping from mooring lines by the use of better models which can help significantly drive down the motion response and help alleviate the control system effort.

Problem Statement 2: Drive-train Configuration

The drive-train of a wind turbine constitutes those components that are involved in mechanical-electrical energy conversion including the turbine, shaft, gearbox and generator. The current drive-train architecture used for the Hywind concept consists of a 3-bladed turbine coupled to a 3-stage planetary gear box with a squirrel cage induction generator. Previous studies on the spar buoy wind turbine have assumed geared driven power trains as the standard configuration [45-47]. Having such an arrangement in the nacelle of a floating wind turbine system which is prone to an already highly dynamic motion environment would have to suffer from low efficiency, high maintenance requirements and entail complex control system. Few

	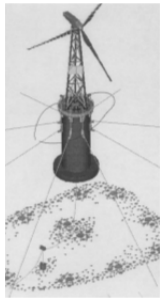	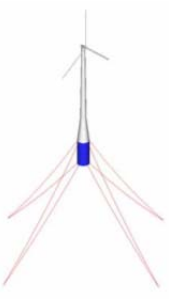	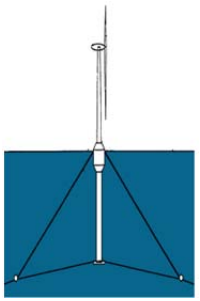	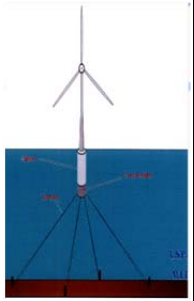		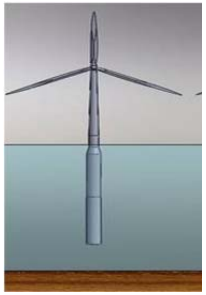
Year	1998[31]	2005[48]	2005 [49]	2008[42]	2009	2009
Type	Catenary	Taut	Taut	Taut	Catenary	Catenary
Developing Institution/Company	Technomare	MIT	Ocean Technology LLC	MIT	Statoil, Norway	NREL, USA
Turbine rating	1.4 MW	1.5 MW	2-3.6 MW	5 MW	2.3 MW	5 MW
Draft	~27 m	20 m	NA*	60 m	120-700 m	120 m
Mass of floater	3570 ton	NA*	NA*	8043 ton	NA*	7,466 ton
Diameter	12 m	12 m	NA*	14 m	8.3 m	9.4 m
Mooring	8 point mooring	Double layered, taut	3-6 cables at the base, with auxiliary for interconnection	4 point mooring separated by 90°	Three point catenary	Three point catenary
Status	Infeasible	Research	Patented concept	Research	Demonstration	Research

* Not Available

Table 1.1 Spar Concepts

		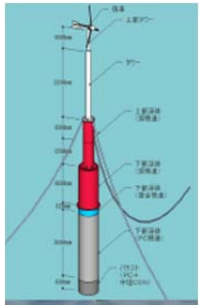		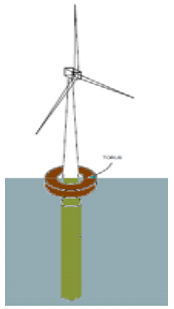	
Year	2009[29]	2010 [38]	2012[50]	2012[41]	2014[40]
Type	Taut Leg Spar	Hybrid Spar	Tension leg	Spar-Torus Configuration	Advanced Spar[6]
Developing Institution/Country	UMB, Norway	Kyoto University, Industrial Partners, Japan	Sway, Norway	Norway	The University of Tokyo, Industrial Partners
Turbine rating	5 MW	2 MW	5 MW	5 MW	7 MW
Draft	NA*	60-70 m	100 m	120 m	NA*
Mass of floater	NA*	NA*	1240[7] ton	8016 ton	NA*
Diameter	NA*	2 sections,(lower-9.2m, upper-5m)	NA*	9.4 m	NA*
Mooring	Multiple point	3 anchor chains	Single-point (tension leg)	Three catenary lines	Catenary lines
Status	Ongoing	Ongoing	Demonstration	Feasibility studies	Demonstration

* Not Available

Table 1.1 Spar Concepts (Continued)

[6] Demonstration planned between 2014-2015
[7] Foundation integrated and included in tower weight

studies that examined the component behaviour based on this configuration have identified greater loading and internal drive-train responses [51, 52]. In the case of a floating wind turbine, a strong dynamic coupling exists between the rotating wind turbine and buoy motion resulting in a substantial increase in loads on the nacelle and tower that are dominated by inertia. The loads subject the wind turbine, the nacelle components and tower to cyclic multi-axial stress conditions. The impact of these loads on nacelle design, turbine design, drive-train components and their structural adequacy has been less studied. There is limited public information on the performance of drive-trains for spar-buoy floating wind turbines that are currently under development. Furthermore, the lack of adequate design standards indicates the need for identification of any special requirements for the mechanical design and strength requirements of components at the nacelle. Reducing the energy costs to make floating wind more competitive would mean that these systems need to work more efficiently. Current trends in offshore drive-train designs are towards direct-drive generators which can be made smaller for higher rotational speeds. However, direct-drive generators suffer from large size and weight and the need to maintain a small air-gap between the generator stator and rotor structures. Implementing such a configuration for a floating wind turbine can bring new design challenges that need to be addressed. There is a need to identify a cost-effective drive-train system that ensures both minimal dynamic response and high availability without adverse implications on power production. In this context, direct-drive generators for floating wind turbines can be a prospective research direction to potentially ensure higher reliability and efficiency.

1.8 Scope of this research

Energy from floating wind is a challenging engineering field that requires significant research to make it reliable and cost effective. In brief, identification of the optimal floating wind turbine design still remains a subject of research. Several fields of engineering are involved; these include but are not limited to aerodynamics, hydrodynamics, structural dynamics, control system dynamics, dynamics of power conversion and transmission. Fig. 1.6 provides an illustration. Based on the research

problems identified in previous section, hydrodynamics & drive-train dynamics were two themes that were identified as potential areas for further research on a spar-buoy wind turbine. These parts are highlighted in yellow in the figure.

Firstly, with regard to hydrodynamics, this research aims to provide a greater understanding of coupled hydrodynamic behaviour using more accurate representation of mooring models. It is intended to establish the validity of such models by experimental data. Secondly, this research also aims to investigate the prospects of a direct-drive generator as a cost-effective drive-train for floating wind turbines. It is intended to increase the understanding of the dynamics of direct-drive generator as applied to FWTs.

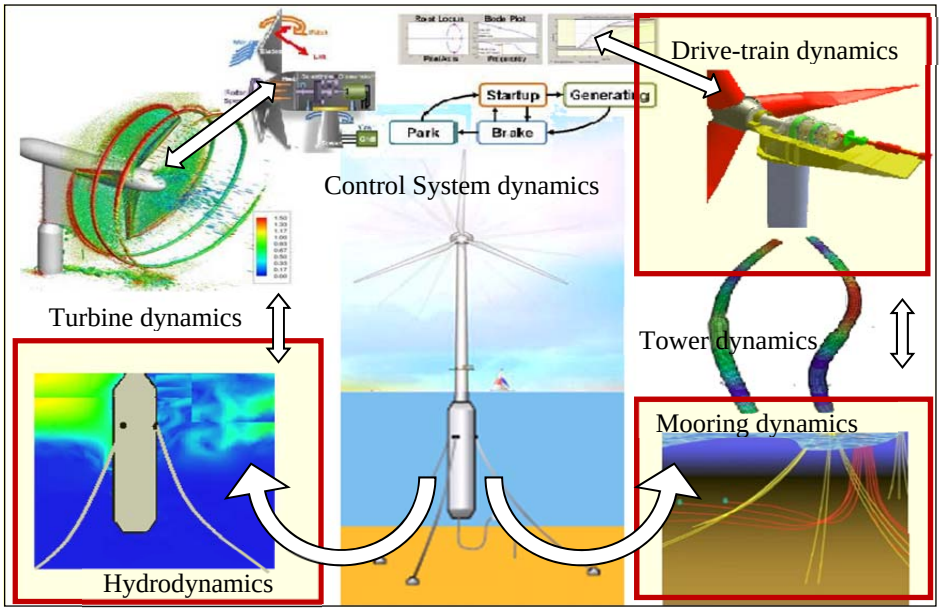

Fig. 1.6 The various branches of design in a Floating wind turbine

Given the significance of the research problems that were identified, this research work required a three-part investigation. Part-I of the research deals with the investigation of coupled hydrodynamic behaviour of the platform and mooring lines by ***Improved Hydrodynamic Modelling (Numerical & Experimental methods)*.**

Part-II & III examine the *p**rospects of implementing a direct-drive permanent magnet generator for floating wind turbine*.**

There exists a strong coupling between the two research elements (hydrodynamics & drive-train dynamics) as well as with the dynamics of the rest of the system. Yet for the purpose of the research, a de-coupled approach was used to treat the two elements separately considering the limitations on modelling resources that were available earlier on during the research. Results from Part-I served as research inputs to Part-II. The ensuing interactions between these two research elements, the implications they have on each other in part forms the first hypothesis of this research, though the dynamics of the rest of the system (i.e. from wind and control system action) cannot be ignored. Part-III forms the concluding part of the research when further modelling resources were made available. As the drive-train forms one of the most critical components of a floating wind turbine, the opportunity was utilised to extend the investigation on the drive-train considering the dynamics from the rest of the system.

1.9 Objectives

In the following, the major objectives for each part of the research and the tasks required to achieve the objectives are identified.

1.11.1 Part - I

The first part of the research is focussed on the hydrodynamic response characteristics of a spar-buoy type wind turbine by accurate modelling of dynamics from mooring line. This involves numerical modelling and validation by experimental testing. This part of investigation is aimed at:

(a) Providing a better understanding of coupled hydrodynamic behaviour of platform and mooring lines.

(b) Performance verification of a spar buoy concept by laboratory scale testing and validation.

(c) Developing a new approach to response evaluation.

(d) Establishing an improvement/decline in performance of the system.

1.11.2 Part - I Tasks

To accomplish the above objectives, it was intended to examine a scale model of a floating wind turbine. The following tasks formed the part of the investigation

1. Review of previous research and identification of geometrical properties of model spar buoy wind turbine, research methodology.
2. To build a physical model of a spar buoy wind turbine.
3. To determine the inertia and resonance properties by carrying out a still water vibration tests.
4. To test the model in uni-directional regular and random seas at the University's curved wave tank facility.
5. To identify optimal mooring-line configuration.
6. To measure and quantify the hydrodynamic response.
7. To establish a numerical model to simulate the coupled hydrodynamic behaviour of the system.
8. To validate the numerical model with results from experiments.
9. Comparison of results with previous research.
10. Inferences from the research.

1.11.3 Part - II

The second part of research examines the challenges of designing a direct-drive generator that is robust enough to cope with the nacelle accelerations in a floating wind turbine. The structural and mechanical integrity of the generator design is the main focus of the investigation. Results from Part-I serve as research inputs to Part-II that was mainly aimed at:

(a) Investigating the mechanical design considerations for implementing drive-trains for floating wind turbines.
(b) Examining the effect of external loads (for e.g.: wave induced motions) on the structural/mechanical integrity of a direct-drive generator.
(c) Exploring methodologies to address the design problems if any.
(d) Examining the implications of implementing the direct-drive generator on the

rest of the system.

1.11.4 Part – II Tasks

A set of seven tasks were identified to accomplish the afore-mentioned objectives. These include:

1. A review of drive-train architecture for floating wind turbines.
2. Identification of a direct-drive topology suitable for the spar buoy wind turbine.
3. Analysis of the structural-mechanical stability of the chosen generator topology in response to the largest nacelle accelerations identified from Part-I.
4. Identification of various factors that influence the design.
5. Identification of methods for dealing with stability problem if any.
6. Assessment of impact of generator design on the rest of the floating wind turbine system.
7. Inferences from the research.

1.11.5 Part – III

The final part of research extends the investigation on the direct-drive system by examining its internal dynamics in response to wave, wind and control system action. The main focus of research was to examine if the drive-train component loading and responses are within acceptable levels so as to qualify their implementation for a FWT system. This part of the work was carried out in partnership with the faculty of Norwegian technical National University, Trondheim as part of the FP7 MARINA project. The main objectives of the work were to:

a) Provide a greater understanding of the internal drive-train behaviour of a direct-drive generator and identifying the various processes that control its performance in a FWT system.

b) Verify the adequacy of drive-train components to be at an acceptable level.

c) Identify further opportunities and challenges of implementing direct-drive generators for FWT.

1.11.6 Part – III Tasks

To accomplish these objectives, the following tasks were identified

1. Establish the research methodology for examining the internal drive-train dynamics.
2. Develop a fully-coupled aero-hydro-servo-elastic model of the FWT system supporting a direct-drive generator- this includes development of specifications for the platform, tower, control system and the drive-train.
3. To carry out fully-coupled multi-body simulations for the operating conditions of the FWT system and examine the drive-train response.
4. Estimate the main loads on the drive-train; identify the important internal drive-train response variables and quantify the responses.
5. Estimate the component lives and reliability.
6. Inferences from the research.

The three parts of the investigation, together with the main elements that form the part of research are illustrated in the flow-chart in Fig.1.7.

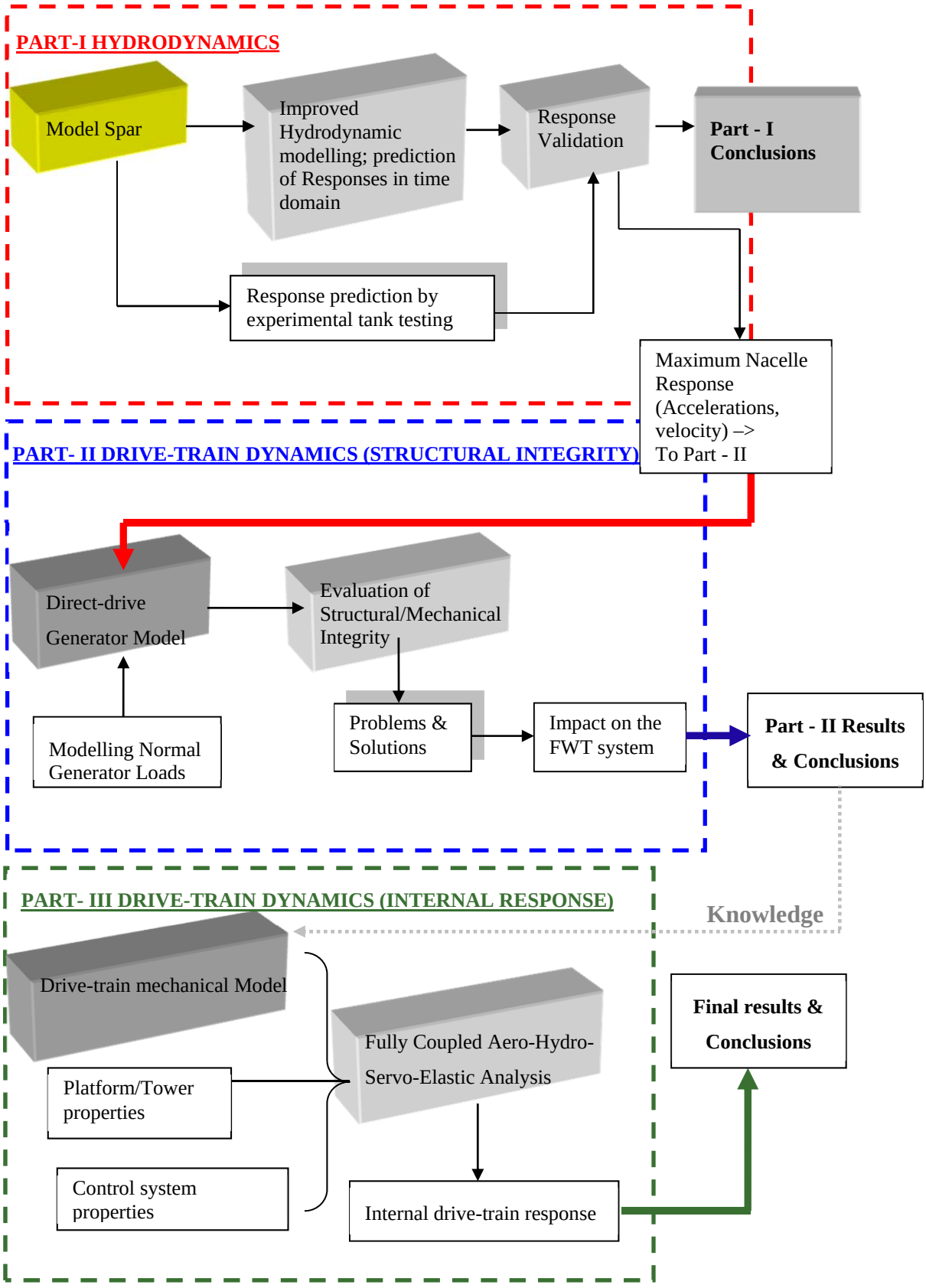

Fig. 1.7 Research Flow-chart

1.10 Outline of the thesis

This thesis is presented in three parts. Chapter 2 provides a review of available literature with regard to the two research elements namely hydrodynamics and drive-train dynamics of FWT. Part-I of the investigation begins with Chapter 3 that describes the experimental and numerical techniques for modelling the hydrodynamic response of a spar buoy FWT. Chapter 4 introduces a new approach to response prediction. The results and discussion on the comparison between experimental and numerical model are presented together with major conclusions from Part-I. Chapter 5 initiates Part-II investigations on the drive-train that forms the main subject of interest for the remaining part of the research. A detailed assessment of the structural dynamics of a direct-drive generator is carried out in response to nacelle motions in a FWT system. Some early observations and challenges of implementing the structural design are presented. Chapters 6 & 7 form the concluding part of the research that extends the investigations on the direct-drive generator by examining the internal drive-train response. Chapter 6 describes the development of a fully coupled aero-hydro-servo-elastic model of a FWT system supporting a direct-drive generator. Chapter 7 presents a detailed investigation on the dynamics of the drive-train for assessing the performance and component reliability when applied to FWT. Further challenges and opportunities in implementing the system are identified. Chapter 8 provides a summary of the three research parts with conclusions and recommendations for future research.

1.11 Publications

Significant parts of the work outlined in this thesis have been published the following academic papers:

1. L.Sethuraman and V. Venugopal. *Hydrodynamic response of a stepped spar floating wind turbine: Numerical modelling and tank testing*. In: Renewable Energy, Vol. 52, April 2013, p. 160-174.

2. L. Sethuraman, V.Venugopal, M.A.Mueller. *Drive-train configurations for Floating Wind turbines: On the assessment of key design parameters and Technology Options*. Eighth International Conference & exhibition on Ecological Vehicles and Renewable Energy 2013.26-30 March, Monaco.

3. L.Sethuraman, V. Venugopal, A.Zavvos, M.A.Mueller, *Structural integrity of a direct-drive generator for a floating wind turbine*. In: Renewable Energy, Vol. 52, April 2013, p. 160-174.

4. L. Sethuraman, Y. Xing, Z. Gao, V. Venugopal, M.A.Mueller, T. Moan, *A 5MW direct-drive generator for floating spar-buoy wind turbine: Development of a fully-coupled Mechanical model*. Proceedings of IMechE, Part A: Journal of Power and Energy, Article in press.

5. L. Sethuraman, Y. Xing, Z. Gao, V. Venugopal, M.A.Mueller, T. Moan, *A multi-body model of a direct-drive generator for a wind turbine*. Proceedings of the European wind energy conference, Barcelona, 10-14 March 2014.

6. L. Sethuraman, Y. Xing, Z. Gao, V. Venugopal, M.A.Mueller, T. Moan, *A 5MW direct-drive generator for floating spar-buoy wind turbine: Drive-train dynamics*. Under Preparation.

Chapter 2

Literature Review

2.0 General

A floating wind turbine system creates unique operating conditions with dynamic effects from a combination of aerodynamic, hydrodynamic, drive-train, mooring-system and control system action. Inaccurate modelling and insufficient knowledge of important dynamic behaviour limits the validity of results obtained from analyses studies thereby precluding opportunities to check or improve reliability of the system. The previous chapter identified key research problems with regard to hydrodynamic modelling and drive-train research for FWTs.

As the first step in the research process, this chapter presents separate reviews of available literature to elaborate the research problems handled by Part-I, Part-II & Part-III of this research. Section 2.1 provides an assessment of research problems with regard to hydrodynamics of FWTs. Section 2.2 focuses on research gaps in drive-train research for FWTs (Part-II & III) providing a comparative assessment of the current state-of art.

2.1 Literature review for Part-I: Hydrodynamics of FWTs

Dynamic motion response prediction is one of the most critical aspects for estimating the efficiency of floating offshore structures in achieving the purpose they are designed for. With no design guidelines yet for FWTs, this aspect is more challenging where the combined effects of aerodynamics, hydrodynamics and mooring-system create new operating conditions and unpredictable behaviour. In the past, several numerical and experimental studies have been carried out to verify the dynamic behaviour of FWTs. Studies employing different methods and models have been used to simulate their dynamic behaviour, with a few considering the dynamic interactions, few others ignoring them and making simplifications.

In the following, some major observations are presented on previous studies that have employed experimental and numerical techniques in the evaluation of floating wind turbine response. In particular, those works that have dealt with numerical modelling and experimental validation from the point of view of hydrodynamic response measurement and mooring line modelling have been reviewed.

2.1.1 Hydrodynamic response and Mooring line models

For the spar-buoy wind turbine, the slack catenary asymmetric mooring system with lines uniformly distributed at 120º has been considered the most cost-effective arrangement. Such an arrangement introduces non-linearities into the equations of motion for a floating platform from the geometrically non-linear restoring forces and quadratic drag on the mooring lines. The dynamics due to drag damping also has a significant impact on the platform motions [53]. In the prediction of the coupled dynamic behaviour of FWTs, most studies employing time-domain simulations or experiments have assumed a quasi-static representation for mooring restoring forces due to ease of modelling. However this modelling assumption cannot sufficiently describe the dynamics of the system and introduce errors in measurement, thereby questioning the validity of hydrodynamic prediction.

Validation of the results using simplified numerical models for mooring lines by experimental measurements have invariably resulted in discrepancies and extraneous judgment. For example, the numerical and experimental study by [54] identified that linear spring model for catenary mooring system leads to an overestimation of surge response at resonance state for the catenary mooring system. So far only a few studies have confirmed the numerical accuracy or capability of the numerical models to qualitatively reproduce experimental observations. Skaare *et al.,*[55] compared the experimental response of scale model of the Hywind spar buoy with numerical model in SIMO/RIFLEX tool. Myhr *et al*.,[29] compared the experimental values of motions and line tensions for scale model of OC3 Hywind spar buoy with motions computed using 3Dfloat and ANSYS. They found that uncertainties in calibration resulted in amplitude differences between experiments and computations. Kim *et al*.,[56, 57] tested and validated a more comprehensively scaled version of the OC3-

Hywind system in regular and irregular seas including wind loads and rotating rotor. The trends in RAOs and resonance bandwidth obtained from the experiments were found to agree with those obtained from the FAST coupled simulations[58] using WAMIT and AQWA. Measurement errors introduced irregularities in yaw response; differences were observed when motion response was statistically quantified as significant motion amplitudes.

Gueydon *et al*.,[59] carried out experiments on a scale model of the spar that was geometrically identical to OC3-Hywind system, but modelled for a depth of 200 m with modifications to the mooring system and tower modes. The numerical models for mooring and hydrodynamics created using a multi-body time domain simulation tool, aNySIM[60] were calibrated by matching the response during decay tests. The first order wave response was found to agree with the experimental results. However, the numerical model failed to capture horizontal drift motions that were present in the tests, resulting in notable differences in motion response statistics.

In reference[44], aero-elastic simulations of a 5MW floating wind turbine adapted from OC3 Hywind model using FAST were compared to results obtained by scaling the results of tank tests on a 1:50 Froude-scale model built by UMaine. The numerical model was validated by comparing the results from free-decay tests, periodic-wave tests with no wind, and irregular-wave tests with wind. Mooring lines were modelled as quasi-static catenary lines with effects of stretching, mass density, buoyancy, geometric non-linearity and seabed interactions included. However, the dynamic mooring line effects and mooring line drag were not included. The results showed good agreement between experiment and the simulation for the wave-spectra frequencies. However, significant discrepancies were noted in damping behaviour between the experiment and the FAST simulation. Inconsistencies in surge, sway motions were observed with greater tower-top response and heave motion at the natural frequencies since the damping from non-linear drag effects of mooring lines were ignored by FAST simulations.

A group of researchers from Japan [38] built and tested several scaled versions of a stepped-spar FWT to validate their simulation code that was based on the modified Morison's equation (relative velocity formulation). The spar cylinder was divided

into two segments with a small cross-section closer to the water surface and larger cross-section for a greater depth. Static catenary-line theory was used to model the mooring lines and equations of motion were solved in time domain. They have noticed differences in predictions of significant motion response, owing to discrepancies in drag force calculations and absence of damping from mooring lines.

Although all of these studies demonstrated reasonably good predictive ability of the tools, they follow simplistic approach to model the dynamics of mooring systems, raising questions on the predicted coupled hydrodynamic behaviour. For instance, the results of the stepped-spar FWT[38] show a need for further refinement in mooring line modelling to verify its feasibility. Further, it is important to ascertain the efficiency of such a design by examining the appropriate hydrodynamic characteristics that accurately describe the behaviour of the system. In this regard accurate response reporting is equally important. In the following the different modelling options for mooring lines and hydrodynamic response reporting are discussed.

2.1.1.1 Modelling the dynamics of mooring lines

Accurate modelling of the mooring system for FWT is an important design step as it has huge influences on the stability and the dynamic behaviour, for example, it can significantly alter the response characteristics and can cause the system to fail if the resonance properties of the platform and mooring lines are not carefully considered. The key issue with regard to mooring-line modelling is whether it is acceptable to ignore the dynamic effects of mooring lines.

Most modern tools that are now available for fully coupled time domain simulations employ some kind of linearization to the mooring line model. The impact of these assumptions are well known for offshore oil platforms, but for a FWT, the wind-to-wave load ratio is higher, and the experiences from the offshore industry cannot be applied directly [53]. A study by [61]concluded that dynamic effects are important for mooring systems such as the catenary systems that experience very low or moderate mooring line tension. The effects from mooring lines can be sources of increased structural loading on the turbine, for e.g.: snap loads during extreme events

or ringing from high line tensions. For shallow water mooring systems, the total mass of the lines is negligible and the motion is small. Therefore, even though the drag force of the lines through the fluid might be significant, it is generally accepted that dynamics can be neglected. For deeper-water configurations, however, mooring-line dynamics become increasingly important.

Real mooring behaviour requires a step-wise treatment for solution. A number of different numerical tools are available to model the mooring lines. These vary from simple quasi-static models and look-up tables to more sophisticated tools based on finite-element methods or multi-body simulation (MBS) methods. Their impact on global system response tends to be different because of the fundamental differences in the modelling approach.

The quasi-static mooring models are based on the continuous-line theory. They employ nonlinear springs that have the same stiffness characteristic as the mooring system. Line forces at every time step are computed by assuming that the cable is in static equilibrium, considering its weight only. The resulting forces are used to solve the dynamic equations of motion for the rest of the system. Alternatively, the relationship between restoring force and platform displacement may be defined using a look-up table at the mooring-line interface point [20]. The spring is modelled at the fairlead position using dynamic line analysis codes that derive the force-displacement relationships or by analytical solutions for slack lines in static equilibrium. This method however ignores the dynamic properties such as inertia and drag through the fluid, seabed friction, vortex shedding and damping from mooring lines. This approach is computationally efficient in coupled aero-hydro-elastic simulations, particularly when waves are small and platform-line displacements are small. However, such a conservative approach can significantly underestimate the damping or stabilising effect from the mooring lines when the amplitude of motions is large [21]. For deeper water configurations such as spar, this can have significant effect on the motions response. Ignoring the dynamics can cause increased structural loading leading to overdesigned system that compromises the economics of the system. Recent studies have shown improved modelling fidelity when dynamic line

models are included. These include the finite element methods and the MBS approach. The finite element approach modifies the physical system of the mooring line by incorporating the nonlinear material properties and dynamic properties before mathematical formulation. The mooring line is discretised into finite elements with mass distributed as elements or lumped at nodes connected by inextensible mass-less spring elements. The equations of motion for each element/node are then solved at every time step. Because the mooring line responds to varying excitation loads and displacements that cannot be predicted by the quasi-static model, the finite element approach can give a deeper insight into non-linear mooring behaviour. Tools such as OrcaFlex, RIFLEX employ this technique. Kallesoe *et al*., [62] showed a reduction in fatigue loads for the OC3 Hywind system with FEM-based mooring model. The FEM based mooring line model used by Hall *et al*.,[63] showed greater platform damping than the quasi-static model. The FAST coupled simulations using FEM based mooring models have shown higher modelling fidelity[63, 64] .The FEM approach was numerically stable and could also capture the high frequency vibration components in mooring tension due to resonance matching.

The MBS approach results in a more sophisticated model that has the capacity to model line contact with seabed. The mooring line is divided into rigid or flexible multi-body elements connected by visco-elastic spring-damper elements [65]. The line interaction with the sea-bed is implemented using a simple coulombic friction element with spring and hysteresis characteristics as a function of the translational forces. This approach was investigated by Matha *et al*.,[66] using a multi-body simulation code (SIMPACK). They identified considerable differences in the predictions of platform displacements due to the hydrodynamic nonlinearities from mooring lines.

2.1.1.2 Reporting Hydrodynamic Response

Accurate prediction of motions of a FWT is a fundamental problem in examining the efficacy of the design. For a FWT, motions in six degrees of freedom are possible; these include three for translation motion: surge, sway, and heave; and three for rotational motion about three axes: roll, pitch and yaw. According to a study by[42], for floating wind turbines it is desirable to limit the nacelle accelerations to less than

0.3*g* (where *g* is the acceleration due to gravity)and dynamic pitch angle to 10º to avoid significant loss of turbine performance. In the literature two different methods have been considered for reporting the hydrodynamic behaviour of a FWT platform design, namely Response Amplitude Operator (RAO) and Significant Response Amplitude. The following is a description of the two methods and the relative merits of these methods.

2.1.2 Response Amplitude Operator

In the evaluation of platform design, the most useful and widely used engineering statistic is the Response amplitude Operator (RAO). Defined as a non-dimensional transfer function, the response amplitude operator relates the wave elevation to the motion response component under consideration and is given by:

$$RAO_i(\omega) = \frac{\zeta_i(\omega)}{\eta_i(\omega)} \tag{2.1}$$

Where, ζ_i refers to the amplitude of response for the i^{th} degree of freedom and η_i refers to the incident (regular) wave amplitude. The response amplitude operator is usually determined in the frequency domain with frequency-dependent excitation forces. This relationship represents a linear approximation of the frequency response of motion in regular waves allowing the principle of superposition to be applied to determine the response. Since random waves are described by regular wave components, a connection to the stochastic model for random waves can also be established from the knowledge of the spectrums. If the energy distribution of irregular wave, $S_{\eta_i}(\omega)$ over different frequencies is known, then the motion response components for the i^{th} degree of freedom, $S_{\zeta_i}(\omega)$ can be determined by transforming the corresponding regular wave components by a transfer function[67];

$$\underbrace{S_{\zeta_i}(\omega)\cdot d\omega}_{\text{Regular response components}} = \underbrace{\left|\frac{\zeta_i(\omega)}{\eta_i(\omega)}\right|^2}_{\text{Transfer function}} \times \underbrace{S_{\eta_i}(\omega)\cdot d\omega}_{\text{regular wave components}} \tag{2.2}$$

Using equations (2.1) and (2.2) we have the transfer function for irregular waves described as:

$$RAO_i(\omega) = \sqrt{\frac{S_{\zeta_i}(\omega)}{S_{\eta_i}(\omega)}} \tag{2.3}$$

The Response Amplitude Operator depends on the platform geometry, the wave loads and their direction. Because RAOs interpret results in frequency domain, it is possible to examine various physical effects distinctly according to their periods of occurrence. Yet, only a few studies in the past have used this approach with success for the spar-buoy FWTs [35, 56, 59].

2.1.3 Significant motion amplitude

A second parameter that can implicitly indicate the performance of a system is the significant response amplitude. This parameter heavily relies on the statistical distribution of motion response for every sea state. The hydrodynamic response of the floating wind turbine in irregular waves varies with the sea state (wave height and wave period). The performance can be therefore evaluated by analysing the response statistics for each sea state. Significant response value for i^{th} degree of freedom, denoted by $\zeta_{i1/3}$ is defined as the average of the highest one-third of the peak or peak-to-peak values of the motion response[68], a concept inherited from an equivalent concept of significant wave height[8].

$$\zeta_{i1/3} = 4\sqrt{m_{0i}} \tag{2.4}$$

Where m_{0_i} is the zero-th spectral moment computed as the area under the response spectrum

$$m_{0i} = \int_0^\infty S_{\zeta_i}(\omega)\, d\omega \tag{2.5}$$

[8] The significant wave height $H_{1/3}$ is defined as the average of one third of the highest observations of the wave amplitude

This statistic can be computed as time average or ensemble average thus allowing the frequency domain description to compute the response statistic using numerical models and compare them with the statistics obtained from experimental tank tests.

Notable discrepancies were observed in some numerical and experimental validation studies that compared significant motion responses [34, 36, 38, 57]. Because most numerical models assume an ideal wave generation environment - they disregard the inconsistency in generation of significant wave height after each test run that is typically present in a wave tank. In such cases, one can expect significant differences between response statistics from numerical models and experimental observations.

2.1.4 RAO Vs Significant motion response

Both the above parameterisations are based upon the simplifying assumption that the motion response of platform is linear with respect to the wave amplitude. The RAO approach consists of integrating the forces and moments over the wetted surface taking into account, the load conditions and the geometry of platform. The RAO is a more useful design indicator as it can be generalised for any sea state and generally the first step in the design process. Whereas, significant response statistic is unique to a particular sea state of interest and requires the response spectrum to be established at first. Although significant motions give some idea about the behaviour, they do not convey enough information to qualify or modify a particular design as do the RAOs. In the evaluation of significant response, it is assumed that the most common responses are smaller than $\zeta_{i1/3}$. This suggests that the frequency of occurrence of significant motion is low. However, practically, it is possible to encounter responses that are several times higher than this value and qualifying a design based on significant motions can misrepresent the actual scenario or underestimate design needs. Knowledge of RAOs at the design phase provides a certain assurance about the performance of a particular design and allows designers to investigate opportunities to improve the system performance or make adjustments to the design to cope with extreme sea conditions.

2.1.5 Observation

Review of past literature with regard to Part-I showed limitations with mooring line models and few inconsistencies in reporting hydrodynamic response particularly for the stepped spar-buoy FWT. Dynamic mooring line models (FEM or MBS techniques) have shown to be superior to quasi-static models in better capturing the dynamics from mooring lines, yet only very few investigations have been carried out so far. In this regard the results already established using FEM approach [64] encourages a further study to understand the mechanisms that cause the mooring lines to influence the wind turbine response. Studies have also shown that Response Amplitude Operator is a more accurate approximation of the structural response[69] compared to significant motion response. This research will explore the FEM approach for increasing the understanding of the coupled hydrodynamic behaviour and also re-examine the RAO method. These approaches will be tested on a stepped-spar buoy configuration FWT similar to [38].

2.2 Literature review for Part-II & III: Drive-trains for FWTs

As the wind industry is migrating towards developments at multi-MW scale, the costs of energy of FWTs must be proven to be competitive enough for large scale development. This calls for improvements in design and manufacturing process of substructure and mooring systems, learning effects, supply chain improvements and measures for ensuring high energy yield. Radical improvements in wind turbine generators, use of alternative technology and materials to increase their efficiency and reliability are potential routes to cost reductions [70]. For a successful integration of a wind turbine generator onto a floating platform, the durability and structural adequacy of the components at the nacelle must be verified in response to the various loads endured during their operation. Two intrinsic factors that can greatly influence the costs and the success of a system are:

1) The choice of drive-train technology.

2) Performance of the chosen drive-train considering the dynamics of the floater, turbine and the control system.

Drive-train is the central part of a wind turbine that governs some of the key factors

that determine the competitiveness of energy from wind. The term *mechanical drive-train* encompasses all rotating parts from rotor hub to electrical generator that are involved in mechanical-electrical energy conversion in a wind turbine[71]. A typical drive-train generally includes the turbine rotor, shaft, a gearbox, bearings, couplings and generator(as shown in Fig. 2.1) The system enables conversion of low-speed, high-torque rotation of the turbine's rotor to constant frequency electrical power by accommodating variation in rotational speeds. Selection of a drive-train that is appropriate for a floating wind turbine is extremely challenging given the structural constraints, complex nature of loading and high reliability requirement to lower the costs of energy.

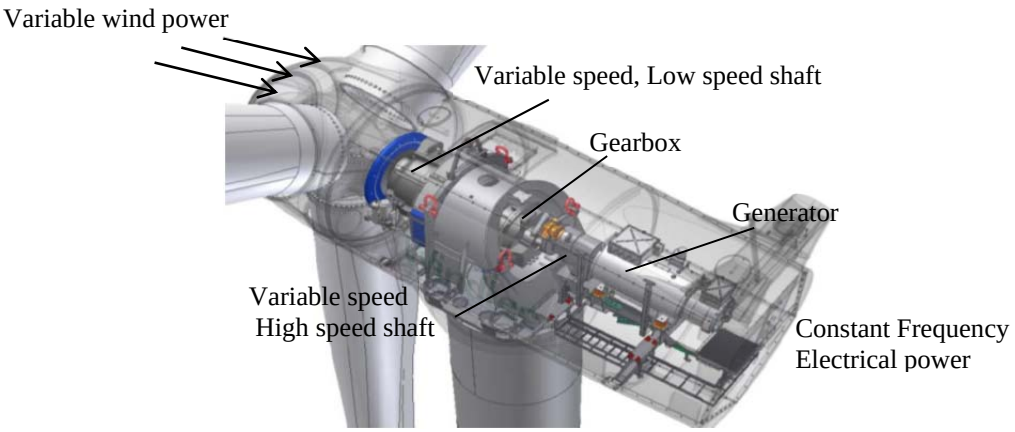

Fig. 2.1 Typical wind turbine drive-train[72]

Drive-trains in wind turbines utilise standard industrial drives. They are broadly categorised as geared and gearless concepts based on the mode of torque transmission from the turbine to the generator. A geared drive-train consists of a turbine rotor connected to a gearbox, coupling and medium/high speed generator (Fig. 2.2(a)). A low-speed shaft couples the turbine to a gearbox main frame. The shaft rotates at roughly 12-30rpm, while the gearbox steps up the speed to match the high rotational speed of a generator rated for a low torque operation. Power electronics (feed the rotor winding of the generator with a power rating of 30% of the turbine rated power) enable variable speed operation and condition the electrical power before integrating to the grid. A gearless drive-train on the other hand, directly couples the low-frequency rotation of shaft to a generator that operates at very high

torque (Fig. 2.2(b)). This arrangement requires a power electronic converter for the full rated power for grid connection.

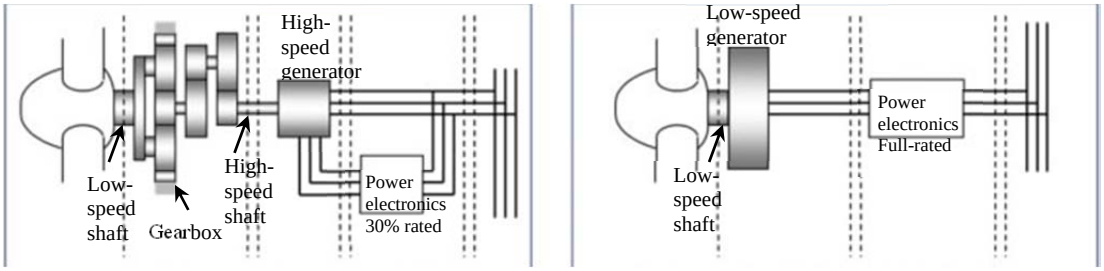

(a) **(b)**

Fig. 2.2 Wind turbine drive-trains[73] (a)Geared system (b)Gearless system

Several other advanced transmission concepts (For e.g.: superconducting drive-trains, hydraulic transmission) appear to be emerging [74]. Since they are in their early stages of development, their technical feasibility and potential advantages over the current state of art have still not been established. Hence their relevance to FWTs can be premature. The following sections present a review of the state-of-art drive-trains and identify the key attributes for an ideal system for a FWT. The prospects of implementing a direct-drive generator for spar buoy type FWT are discussed with emphasis to research needs for its successful integration.

2.2.1 Current trends in drive-train technology for Floating wind turbines

A survey was carried out on six of the prominent FWT prototypes that are under development. Details of the power train employed in these designs are presented in Table 2.1 based on information available in the public domain. The Hywind spar [12] utilizes a Siemens 2.3MW upwind wind turbine driving a high speed drive-train consisting of a 3-stage gearbox coupled to a squirrel cage induction generator (SCIG). The semi-submersible floater design by Principlepower employs a 2MW V80 turbine by Vestas [75]. This turbine drives a high speed Double-fed induction generator (DFIG) through a 3-stage gearbox. Both these technologies benefit from lighter nacelle design owing to the high speed drive systems, but the upwind rotor design imposes several restrictions on the blade flexibility and nacelle angle to prevent the blades from hitting the towers. The Norwegian Sway floater design [39] capable of supporting 2.5-5MW downwind turbine is adapted to drive a medium speed drive system developed by Areva multi-brid [76]. The power train comprises a

1-stage helical planetary gear and a permanent magnet synchronous generator (PMSG) integrated into a single housing. The geometric assembly promises significant space and weight savings at the nacelle. Several other technologies have been explored for reducing the tower top-mass and hence the nacelle loads for floating wind turbines – e.g.: active mass dampers [77] and active ballast systems. Researchers are also considering methods (for example, using two-bladed turbines) that were rejected for land-based systems where acoustic emissions or aesthetics were important. For instance, the TLP floater concept by Blue H [13], supports a two-bladed wind turbine operating at very high tip speeds. The non-integrated drive system comprises a main shaft, a two and a half stage planetary gear box, an intermediate shaft driving an induction generator.

Being the wind industry's standard design, the conventional geared drive system appears to be the most sought after design choice among 4 of the 6 floating designs that were surveyed. With 21.2% share in the offshore wind market [78], direct-drive generators are a promising technology option, but have been less investigated for floating wind turbines. The Japanese hybrid spar is based on a 2MW downwind turbine connected to a direct-drive generator [38], yet the details on the drive-train are not available for review. Boulder wind power [79] developed a direct-drive model suitable for a 6MW floating spar buoy wind turbine. The drive-train employs a modular air-core axial flux permanent magnet generator.

For all of the concepts that were surveyed, very limited information was available on the performance of drive-train systems on floating supports. The nature of the response, support structure requirements, and control philosophy differs from one floater configuration to another; therefore it is difficult to make a comprehensive evaluation of the advantages and disadvantages of implementing a technology for a particular floater configuration. Nevertheless, it is important to isolate the technology that is best suited for a given system.

Name/ Company	Hywind	WindFloat	Sway	Blue-H	Japanese hybrid	Boulder wind power
Type	Catenary moored spar	Semi-submersible	Spar buoy with single taut tether	Tension-leg concept	Catenary moored spar	Catenary moored spar
				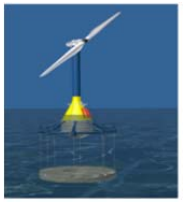		
Drive train	High speed	High speed	Medium speed Multibrid[1]	Medium speed	Direct-drive[2]	Direct-drive
Gearbox	3 planetary stages,1 helical (1:91)	3 planetary stages, 1 helical stage(1:100)	1-stage 1:10	2-stage/2.5 stages planetary 1:34.81[1]	NA*	NA*
Speed(rev)	NA*	NA*	45:148/min	NA*	NA*	11.5/min
Generator	SCIG	DFIG	PMSG	SCIG	PMSG	PMSG
Rating	2.3MW	2MW	5MW	5MW	2MW	6MW
Rotor mass	54 ton	37 ton	132 ton	79 ton	42 ton	106 ton
Nacelle	82 ton	78 ton	NA*	187 ton	34 ton	178 ton
Top mass	138 ton	115 ton	345 ton	266 ton	136 ton	342 ton

* Not available ; [1] Data based on Condor5 turbine[80]; [2] Proposed concept based on data for a direct-drive generator JSWJ82[81].

Table 2.1 Drive train trends in floating wind turbines

2.2.2 Towards cost effective drive-trains

In recent years, several competing drive-train technologies have emerged in an attempt to offer the best balance of efficiency, reliability, weight and costs. Yet, the long-term reliability of the current generation of offshore megawatt-scale drive-trains still remains to be verified, while newer concepts such as hydraulic transmission, superconducting generators [74] are undergoing a difficult development phase.

As new floater concepts are emerging, inconsistency in response between different designs, the lack of adequate design standards and published information on the drive-train performance from floating prototypes or designs under development make drive-train selection for floating wind turbines a difficult task. Decisions on technology-route require a more sensitive treatment and must be carefully considered as they determine the success of the overall system. Component selection will be a crucial design step in designing a cost-effective system that ensures both high availability and minimal dynamic response without adverse implications on power production. The following section presents the important design challenges that need to be dealt with when designing cost-effective drive-trains for FWTs.

2.2.2.1 Structural design aspects of Floating Wind Turbines

In case of floating wind turbines, certain mechanical and structural design requisites significantly constrain the available design space. The following two critical issues need to be addressed in the design process.

i. **Tower Top mass:** The inertia loads on the nacelle of a FWT will make a significant contribution to the tower top loads apart from the wind thrust on the rotor. This is particularly important in larger turbines that have higher tower top masses as it directly manifests upon the stability of the system. As the tower top masses increase, the centre of gravity of the system also increases thereby increasing the support structure requirements (e.g.: ballast). If the same hub height is assumed, then the water-piercing members of the floater will have to increase in diameter to provide sufficient hydrostatic stiffness. This will in turn increase the hydrodynamic loading on the structure and displacements at the nacelle. A de-stabilizing moment is created by the pitching (angular) motion of

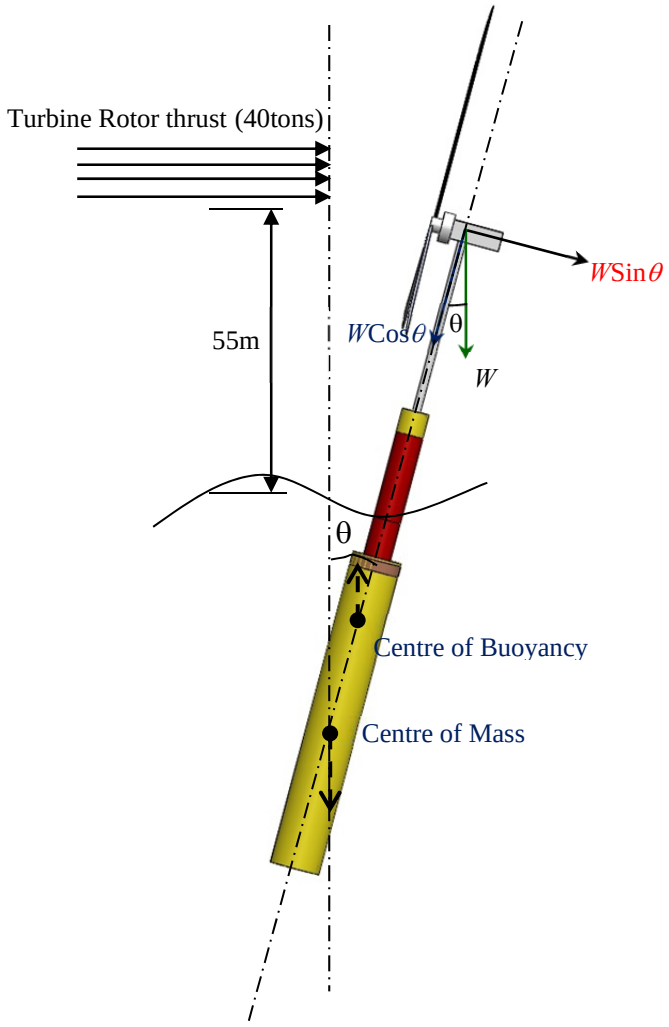

Fig. 2.3 De-stabilising moment in a floating wind turbine

the tower as it generates additional weight components. This effect is particularly significant when the hub height is large and the tower top mass is already high. Figure 2.3 illustrates this effect. For a hub height of 55m and nacelle weight of 200 tons, a moment of (200 *Sinθ* x 55) acts at the nacelle to de-stabilize the structure. If the hub height is a constant and fixed, then reducing the nacelle mass can greatly minimise this de-stabilizing moment. A lower top head mass is also important to avoid overlap with critical eigen frequencies of the tower and the other sources of excitation [82]. As the tower top mass increases, the lower limit on the eigen frequency demands larger towers and a stiffer foundation system [75].

ii. **Vibrations:** Another important aspect of wind turbine design is vibration in the overall turbine structure, and this aspect is more pronounced in FWTs. O&M experience from Hywind's demonstrator project suggests a very high downtime caused by vibrations [83]. Vibrations are the root cause for drive-train mechanical failures that arise from mechanical looseness, gear damage, resonance problems, high wear, rotor-stator eccentricities caused by shaft misalignment, for example. Weak and inadequately designed components can further accentuate these problems. A FWT system experiences a substantial increase in loads on the nacelle and tower [37]. The loads are cyclic and highly transient in nature capable of causing structural excitations that can have a significant impact on the design life of the turbine and drive-train components. Therefore, stiffer drive-train components and newer controller algorithms will be required to cope with the high heel angles and increased nacelle displacements.

Both the above problems impose special measures to reduce the loads at the nacelle, improve stability and incorporate better control strategies. FWTs have been shown to experience much higher fatigue and ultimate loading than onshore or fixed bottom offshore turbines, and could therefore benefit greatly from load or weight reduction. In this regard, lightweight nacelles and drive-train technology can play a vital role. At the same time, there is a need for a better understanding on the influence of nacelle motions on the dynamics of the drive-train. This will be helpful in deciding the strength requirements of drive-train systems that are better suited for offshore wind turbines with floating supports.

2.2.2.2 Assessment of key design parameters for drive-train selection

As explained in the previous section, the structural requirements for a wind turbine system are very demanding especially with floating foundation. The technology must be simple to implement, easy to manufacture, assemble and install, require low maintenance, minimal control requirements and exhibit good structural and mechanical performance. The dynamics of floater motion and turbine operation depend on the type of floater configuration and the control mechanism. Therefore the performance of a given type of drive-train technology may not be consistent when applied to different floater design concepts. Because, design decisions for the drive-

train can have a huge impact on the overall performance of the system, it is necessary to evaluate their suitability based on the following general principles

a) Number of parts or rotating components: Considering the high probability of mechanical failures in a FWT system, the drive-train must have fewer components or rotating wear parts. This reduces the number of interfaces between the components, mechanical stresses, thereof the causes of failure and increases the technical service life of the equipment. Fewer parts also help achieve a more compact design allowing better conservation of space and volume at the nacelle.

b) **Design simplicity:** From the economics point of view, it is desirable to have a simple construction allowing the use of standard parts and methods that can minimise manufacturing costs. Because, it may be difficult to control the system performance with increasing complexity (for e.g.: air-gap control/power requirements) simpler designs are preferable.

c) **Physical size and location:** The density, volume and location of the components at the nacelle decide the distribution of weight at the top. It is important to ensure that the size of the components and location conserve the weight distribution so that the overall stability and floatability is not compromised. For instance, the drive-line arrangement for 4.0MW wind turbine developed by GE[84] allows optimal placement of power electronics and control equipment, while the rotor and generator act as counter-weight.

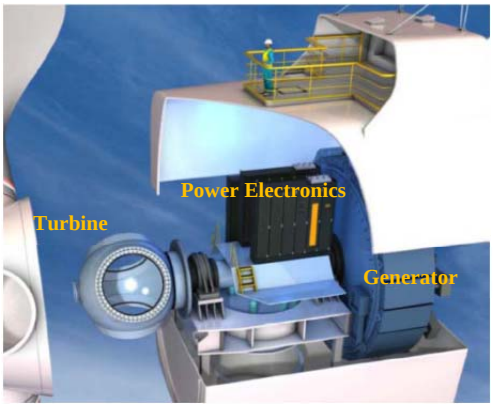

Fig. 2.4 GE 4.0MW Turbine[84]

d) **Lightweight structure**: The weight of the nacelle affects the size and cost of the buoyancy tank required to support the total weight of the system.

Therefore, the drive-train must be designed for low mass to keep the tower top mass as low as practically possible. This is also important to avoid overlap with critical eigen frequencies of the tower and the other sources of excitations.

e) **Strength of components:** Wind turbines on floating supports are subjected to a harsher load environment, therefore the structural integrity of the drive-train must be demonstrated at an acceptable safety level. A lighter drive design must still ensure the necessary design strength to cope with tower top accelerations in a FWT system. The component ratings of shafts, couplings, bearings and gearbox must be adequate to meet the design life and reliability requirements. The structural stiffness must ensure that deflections and nominal maximum stress values are within prescribed limits.

Although the features described above impose less flexibility in the design and construction process, they serve as useful initial indicators for an ideal drive-train candidate to be integrated to a FWT system.

2.2.3 An overview of technology options

In the past, several comparisons of drive-trains have been conducted for offshore wind turbines [85-89]. These comparisons were based on costs, efficiency and weight of the drive-trains. In the following sections, these technologies are assessed with regard to their applicability to FWTs based on the attributes identified in section 2.2.2.2. The results of the assessment are summarized in Table 2.2.

2.2.3.1 Geared drive-trains

Geared drive-trains generally use multi-stage gearboxes with one planetary stage and two high-speed stages to step up the speed. Both Hywind[12] and WindFloat[14] designs employ high speed gears. The high speed operation allows the mechanical elements like the generator to be of lightweight construction to reduce the overall weight of the nacelle. An average drive-train consists of an intricate assembly of components, resulting in a fairly extended nacelle layout (Figure 2.5). The total number of bearings for an assembly can easily exceed twenty[90]. Although lightweight designs are possible, driveline reliability and quality have been

historically affected by poor load sharing in planetary stages, poor temperature control of races, inadequate control of bearing pre-load, hydrogen embrittlement and the effect of tower dynamics[91]. The presence of a gearbox also brings the eigen frequency of torsional vibration very close to rated (i.e. rotational speed). Implementing geared drive-trains for floating wind turbines can further exacerbate these problems. The first studies on the dynamics of a geared drive-train for FWTs reported by Xing *et al.,* [51, 52] identified greater shaft loading and internal drive-train responses(tooth contact forces, gear deflections and bearing loads) as compared to bottom fixed wind turbines due to excitations from wave and platform natural frequencies. Their study also suggested greater fatigue loads and therefore greater cost implications with the geared drive-train when applied for FWTs. Viadero *et al.,*[92] examined the behaviour of a similar drive-train for transient load case. Their study showed occurrence of reversing contacts and deflection in support shaft due to excitation of gear train resonance. These studies clearly highlight the mechanical and structural limitations of the geared power trains when applied to turbines with floating supports. As the nacelle of a FWT is subjected to a diverse spectrum of loads with a large number of load cycles, these mechanical inadequacies can potentially reduce the life and availability of components, thus rendering the geared concept unsuitable for floating wind turbines.

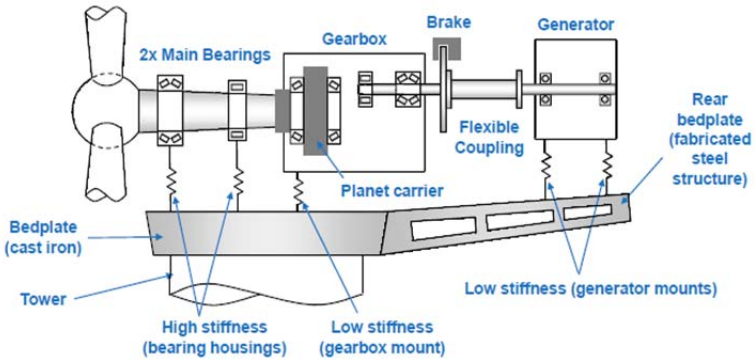

Fig. 2.5 Mechanical layout of a typical high-speed geared drive-train[93]

2.2.3.2 1-stage/2-stage geared drives

One of the ways that has been explored for reducing the tower top mass in FWTs is by using turbines with higher tip speeds. Because high tip speeds allow for smaller blade plan form, they can be made lighter for the same energy output. Higher speeds

also mean lower input torque implemented with lower gear ratios or fewer number of stages requiring smaller shafts and gearboxes. This is possible using a hybrid solution that uses a single or two-stage gear coupled to a medium speed generator (Fig. 2.6). The hybrid technology is basically a trade-off between improved efficiency, gearbox reliability, reduced gearbox cost and increased generator mass (compared to a conventional high speed generator). The power train is expected to be compact, with the generator and gearbox integrated into a common housing requiring

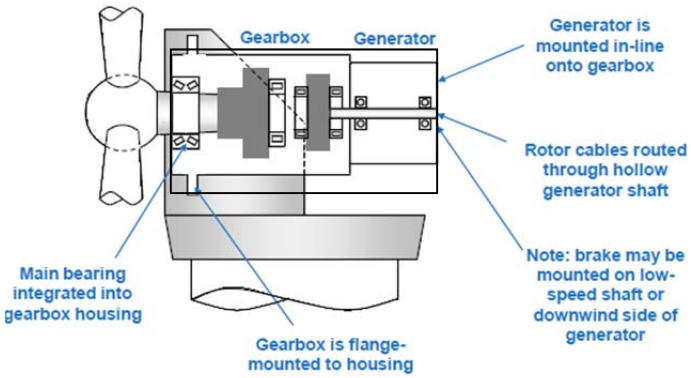

Fig. 2.6 Mechanical layout of a medium–speed geared drive-train[93]

fewer components. The Blue-H design [13] and Sway concept floater design [39] are based on the hybrid drive-train technology, yet it is unclear whether the hybrid design route is a viable alternative given the low reliability of the gear box and high probability of vibrations in floating wind turbines.

2.2.3.3 Gearless drive-trains

In gearless drive-trains the rotor hub is directly coupled to the generator that operates at a low speed. The length of the nacelle, shaft are substantially reduced with less than half the number of components used by the geared drive-trains (Fig. 2.7). The wind loads are transmitted to the tower via the bearings to the axle/spindle/shaft or generator depending on the load path [94]. The elimination of gearbox provides a definite efficiency advantage. The absence of high speed bearings, brakes etc., makes way for a simple configuration with only one rotating part in the drive-train. The risk of resonance from torsional loads can be reduced with gearless drives because of higher eigen frequency of the fundamental vibration [95]. The possibility of vibration

induced mechanical failures therefore is greatly reduced, which is a favourable design attribute for FWTs.

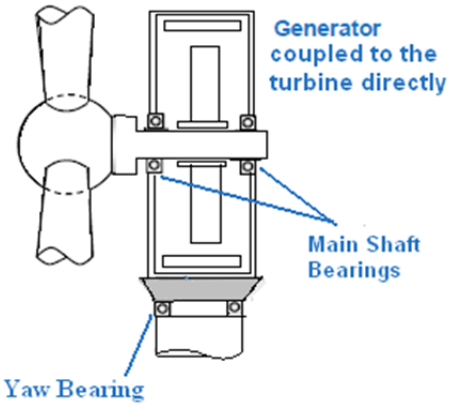

Fig. 2.7 Mechanical layout of a typical gearless drive-train

The low speed of the drive shaft implies a high torque and hence a large tangential force to produce the desired power output. Generator design at low rotary speeds requires a substantially larger rotor diameter to increase the effective rotary motion relative to the stator coils so that high torques can be developed. Also, these generators are designed to operate at a small air gap, requiring more structural material to provide the required stiffness against deflection. The size and the weight of the generator increases disproportionately with the turbine rating ($P \alpha D^2L$, where P is the turbine rating, D and L are the machine diameter and lengths respectively)[96] imposing more mechanical and structural constraints when considered for FWTs. In a FWT where the probability of shaft misalignments is high, the air gap design must be adequate to prevent rotor-stator rubbing under all operating conditions.

Not enough literature is available yet to assess the performance of the direct-drive-train for FWTs. Though some vertical axis floating wind turbine designs [97-102] have incorporated direct-drive technology. Boulder wind power's design of a direct-drive generator [79] for a horizontal axis spar-buoy FWT showed opportunities in nacelle weight reductions and reduction in extreme loads. However the generator was substantially large in size with a diameter of 20m.

2.2.3.4 Comparison

Based on the above discussions and review of previous literature, a ranking system was used to grade the drive-train technologies with regard to their suitability for FWTs. The designs were rated according to their relative conformities to the requirements of simplicity, light-weight and component strength. Besides, torque density, efficiency and costs were also considered for an inclusive assessment. The designs were ranked on a scale of 1-3, with rank 1 and 3 implying the most and the least compliant respectively. The most favourable design was chosen from the linear sum of the scores for the different criteria. Results of ranking system are presented in Table 2.2. Preliminary assessment shows that the geared drive-train concept is likely to suffer from reliability and strength issues, despite having the most favourable weights. Direct-drive generators have a slight margin of superiority over the hybrid system and appear to be the most promising drive-train candidate for FWTs. The simplicity and efficiency of direct-drive generators can offset the cost and weight differences that are manageable with permanent magnet machines. Nevertheless, when comparing the drive-trains, some factors may be more important than others. Yet, a linear sum of the factors gives an initial conjecture. A weighted-sum model (WSM) may be more appropriate in determining the best design [103]. Further work may be required to verify this argument.

Item/Description	**3-Stage Geared drive-train**	**1-Stage/ 2-Stage Geared Drive-train**	**Direct-drive system**
No. of parts/rotating parts	3	2	1
Design simplicity	3	2	1
Size of generator	2	1	3
Weight	1	2	3
Resonance/probability of failures	3	2	1
Component Strength	3	2	1
Torque Density	1	2	2
Efficiency	3	2	1
Costs	1	2	3
Overall rank	20	17	16

Table 2.2 Rank Matrix for drive-trains for floating wind turbines

2.2.3.5 Direct-drive generators for floating wind turbines

Several topologies of direct-drive generators for wind turbines have emerged in recent years; these include electrically excited synchronous generators(EESG), Permanent magnet synchronous generators(PMSG), Switch reluctance machines (SRM) [104] and Induction generators[105]. Amongst these, permanent magnet synchronous generators hold the largest share in the drive-train market[106]. EESGs are much larger in size, requiring extra space and parts to accommodate excitation windings, slip-rings, brushes, rotating rectifier etc., and have known to have high failure rates [107]. These generators are subjected to higher mechanical stresses when compared to machines excited using permanent magnets[108]. SRMs can achieve high torque densities but generally lead to heavier and expensive construction[104]. On the other hand, induction generators require fewer parts and are expected to be more reliable than EESG; however, limitation on pole numbers can result in designs that are considerably heavier.

In this respect, permanent magnet (PM) generators show considerable potential to achieve weight reductions and improved efficiency for the same power output. The structural flexibility of permanent magnet machines allows for different configurations to be designed as iron-cored or core-less construction with flux paths in the radial, axial or transverse directions. Each of these constructions already has different consequence to the size, weight, torque density and efficiency of the design[109, 110]. Details of these topologies available in some scientific literature[104, 111, 112] were reviewed to identify the generator concept that can best adapt to FWTs. Table 2.3 summarises the advantages and disadvantages of the generator concepts.

In reference[102], first attempts were made to design and optimise a transverse flux machine for a vertical axis FWT. The generator had a substantially large air-gap diameter and pole count. This is perfectly acceptable for vertical axis FWT systems because the generators have lesser mechanical restrictions on size, mass and strength as they can be located closer to the centre of gravity of the system where the motion induced loads are substantially reduced. Whereas, implementing such a generator for a Horizontal axis FWTs will be much more challenging as the nacelle design space is

			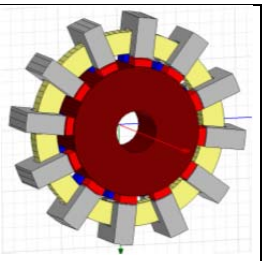
Item/Description	**Radial Flux**	**Axial Flux**	**Transverse flux**
Flux Path	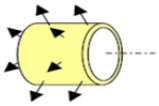	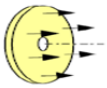	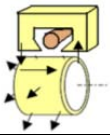
Weight	Heavy, but scope for Optimised construction	Slot-less machines are lighter	Light weight designs possible
No of parts	Few	More rotating parts, bearings, could have single rotor	More
Torque/mass	High	Low	High
Air-gap Stability/Structural Strength	Easier to achieve sufficient stability	Difficult with slotted construction. Strength implies complicated construction	Not suitable for large air gap
Simplicity /Ease of Manufacturing	Simple, flexible, Length/diameter variable	Complex Stator, Difficult	Difficult; need for special methods

Table 2.3 Comparison of Radial, axial and transverse flux PM generators

highly constrained. Although lightweight configurations are possible with axial and transverse flux machines, they require more parts and special methods of manufacturing. Also, the mechanical dynamic balance for air gap stability is difficult to achieve because of complicated construction[113]. Research on ironless direct-drive generators is also gaining momentum in an effort to enable FWT technology rated above 5MW[79, 114]. These designs suggest significant cost and weight advantages, yet are still in their experimental phases of development. Also, with the complexity in design and manufacturing, the robustness of the system entirely relies on the effectiveness of stator-rotor air-gap control which can be difficult especially at higher magnitude nacelle accelerations.

On the other hand, the most common type of PM machines used in wind industry use the iron-core radial flux topology owing to their simple, robust construction and

standard manufacturing techniques. In these machines, air-gap control is relatively simpler to achieve (by suitable adjustment to generator support structure).With the availability of a number of configuration choices for rotor/stator geometry and magnet mounting, they can be made lighter for higher torque ratings. From the view of rotor position, there are outer rotor type and inner rotor type PM machines. Based on the mounting mode of the PM on the rotor, there are surface mounted type and embedded type PM machines. The radial flux inner rotor machine with surface mounted magnets seems to be an interesting choice due to its simple structure, ease of manufacture, shorter load path, higher air gap flux density and better thermal management as compared to outer rotor configuration [94]. Further research is required to examine and ascertain the suitability of this configuration for a FWT.

2.2.3.6 Assessing the suitability of permanent magnet generators for FWTs

In order to be able to verify the compatibility of radial flux permanent magnet generator with a floating wind turbine, there is a need for a good understanding of various processes that control the drive-train behaviour. These include, but are not limited to the electro-mechanical interaction at generator, the torsional and translational responses of its mechanical components, aero-dynamic interaction with the wind and control system and the nacelle accelerations. Since the components of the drive-train perform both structural and mechanical functions at the same time, it is crucial to understand the various physical interactions, simulate the loads properly, evaluate their performance and assess their suitability.

Direct-drive PMSGs are designed with stringent manufacturing tolerances and are particularly sensitive to changes in air-gap (the gap that separates the stator from rotor) and imbalances in magnetic forces. Possible consequences of these effects include vibrations, noise and bearing wear that can have an impact on the design life of the drive-train components. Two important aspects are vital to scrutinise the feasibility of the direct-drive generator for a FWT system: (1) structural integrity and (2) dynamic response. Both these aspects can help evaluate component strength and durability to be at an acceptable level and make any design changes if necessary before implementation to a floating wind turbine.

2.2.3.7 Observation

The nacelle of a floating wind turbine is highly constrained mechanically and structurally. While stability and resonance limits place a practical limit on the weight of the drive-trains that can be implemented, vibrations and high probability of failure stipulate the need for simple mechanisms with fewer and stronger components. Gearless drive-trains show good potential, with a number of methods available for weight optimized construction and greater flexibility in design. Of the many topologies available, a radial flux permanent magnet generator (RFPMG) is a potential design choice for FWTs. For a successful integration onto a FWT system, further research must examine the structural, mechanical integrity of the RFPMG considering the aero-hydro-servo elastic interactions.

2.2.3.8 Summary

This chapter discussed the research problems pertaining to Part-I, II &III in greater detail. Review of literature with reference to hydrodynamics research for FWTs highlighted deficiencies with the existing methods for reporting hydrodynamic response and mooring line models. With regard to response reporting, Response Amplitude Operator (RAO) was identified as the more useful design parameter compared to statistical approach as it provides direct information about the effect of any sea state upon platform design and stability. Concerning mooring models, fewer studies have attempted to establish dynamic effects with little success. Studies employing MBS approach or Finite-Element Methods have showed marked improvements in simulating mooring behaviour thus encouraging the use of such tools for Part-I.

On the other hand, published information on drive-trains for FWTs is scarce in the public domain. The need for light-weight drive-trains with robust mechanisms that ensure high reliability and cost-effectiveness are particularly important for FWTs. Despite being light-weight, greater fatigue loads invalidate the implementation of geared drives for floating wind turbines. Direct-drive generators appear to be a promising alternative with fewer components and greater design flexibility. Of the many topologies available, a radial flux permanent magnet generator is a prospective

design choice. Yet, for a cost-effective implementation, further research must address weight issues to avoid tower/foundation upgrades without compromising on the material strength and air-gap tolerances. Dynamic response and component loading need to be demonstrated at an acceptable level. In summary, the review provided the necessary groundwork for steering the research ahead in Part - I, II & III.

Chapter 3

Part-I: Experimental and Numerical Modelling Techniques

3.0 General

Experimental testing by means of physical scale models in a wave basin has been considered as one of the most reliable means for reproducing realistic behaviour particularly for complex systems such as FWTs where various kinds of static and dynamic coupling effects may occur. At the same time, numerical modelling is considered the most economical way of conceptualising systems and helpful in closely illustrating the physical behaviour. The optimal solution is often a combination of numerical study validated by experimental testing, so that critical design parameters can be verified at an acceptable level of accuracy.

Based on the observations from Chapter 2, it was decided to build and analyse the hydrodynamic behaviour a spar buoy wind turbine both numerically and experimentally. In the process it was intended to:

1) Employ the RAO model (described in Section 2.1.2 of Chapter 2) for reporting the hydrodynamic response in both regular and irregular wave environments.
2) Develop an accurate numerical model to represent the mooring line dynamics using the FEM approach and
3) Validate the numerical model by experimental testing.

3.1 Experimental Spar buoy model of a floating wind turbine

A physical spar model floating wind turbine was built for the purpose of carrying out experiments and predicting the hydrodynamic response. The model is fundamentally comparable to the configuration studied by Utsunomiya *et al.,* [38], with the exception to differences in geometry, inertia properties and mooring arrangement. The model spar shown in Fig. 2.1 (page 53) consists of a two-stage hull

supporting a tower structure and RNA (Rotor Nacelle Assembly) representing a 2MW wind turbine. The hull shape was divided into two segments with a small cross -section closer to the water surface and a larger cross-section for a greater depth. This non-constant hull shape is advantageous in stability aspects and reducing the wave excitation [115]. While the lower cross-section elevates the buoyancy, an upward pointing surface near the water plane offers good wave-counteracting effect by heave force cancellation. The lower and upper parts of the spar structure were fabricated out of acrylic.

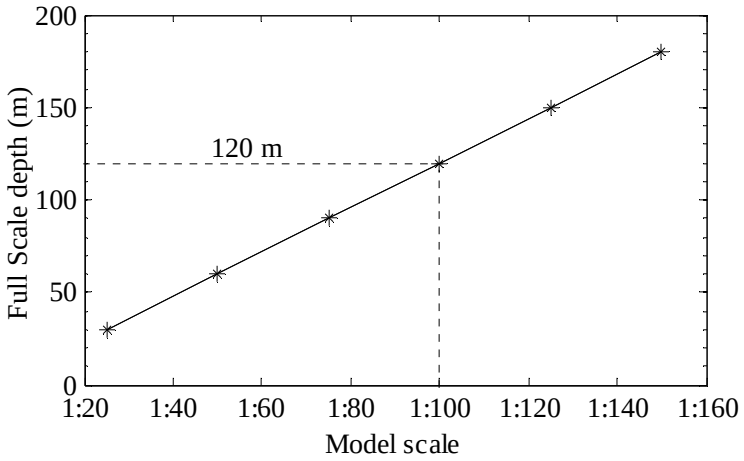

Fig. 3.1 Available depth in the curved wave tank for different scale factors

The physical model was intended to be tested in University's curved wave tank in conditions representing deep-water systems (approximately 120m). Considering the practical size of the tank, use of very small scale ratios was necessary to facilitate deep-water testing. The available full scale depth matched this condition at a scale factor of 1:100 (refer to Fig. 3.1). Therefore, the model scale factor of 1:100 was chosen as it also ensured reasonable accuracy at lower operational sea states while also preserving the Froude ratio. This allowed a good range of sea states to be tested in conditions representing deep water within the limitations of the wave-making facility. A model turbine with a rotor diameter of 800 mm was fabricated of balsa wood and mounted on a tower structure (made of PVC) with a hub height of 550 mm. The inertia of the tower nacelle structure was computed to allow sufficient stability. The aerodynamic shape for the blades was indicative only and not optimised to operate on a wind turbine. Four steel wire ropes each measuring 2mm in

diameter and weighing 16g/m (in air) were attached to the upper end of the lower cylinder to model a slack catenary formation. The mooring lines were spaced 90° apart. The basis for the selection of this mooring arrangement is explained in detail under section 3.2. Dry fine sand was used as a ballast material to adjust the centre of gravity. The hydrostatic properties of the model are presented in Table 3.1.

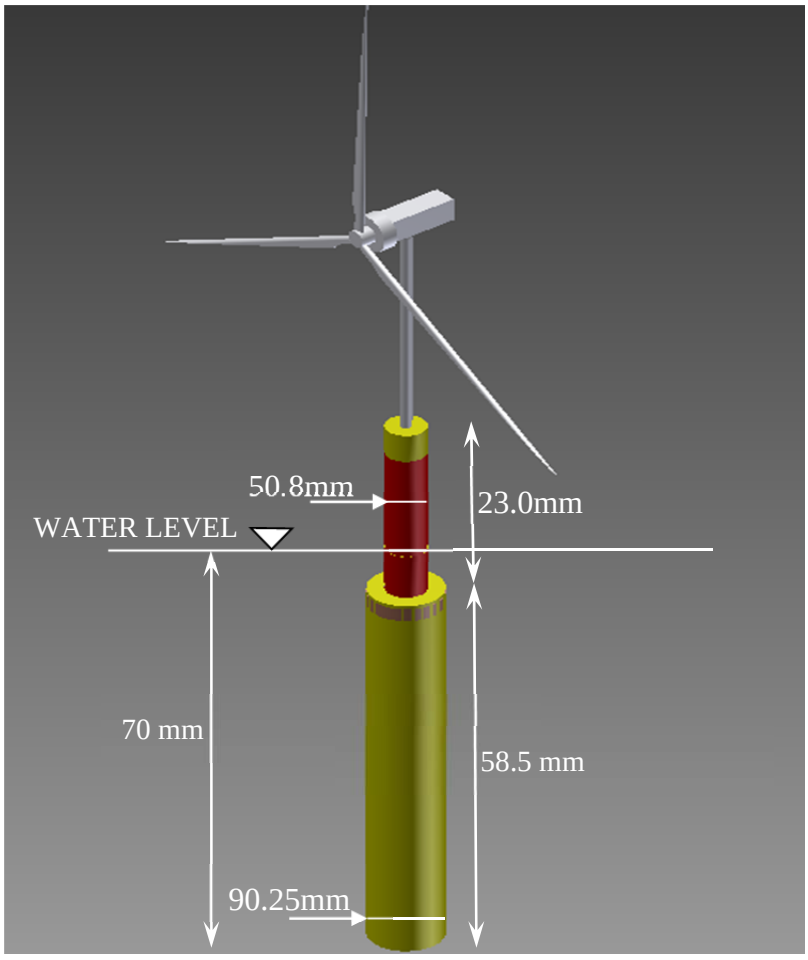

Fig. 3.2 The spar-model built for the study

Item / Description	**Units**	**Value**
Total Mass of the structure	kg	3.87
Weight of Rotor nacelle assembly	kg	0.156
Turbine diameter	mm	800
Hub height	mm	550
Volume Displacement	N	38.9
Centre of gravity above keel	mm	295
Centre of buoyancy	mm	338
Meta centric Height	mm	43
Radius of gyration(Pitch/roll)	mm	264
Draft	mm	700
Depth	mm	1200
Ballast height	mm	298
Height of upper SPAR	mm	230
Height of lower SPAR	mm	585
Diameter of upper part	mm	50.8
Diameter of the lower part	mm	90.25
Weight of mooring line in air	g/m	16
Height of mooring line attachment from keel	mm	570

Table 3.1 Hydrostatic properties of the stepped-spar floating wind turbine

3.2 Testing Environment and measurement

3.2.1 The Curved Tank Facility

The model spar floating wind turbine was tested in the Edinburgh University's curved wave tank. The tank has a unique design with 48 absorbing-type wave maker paddles disposed in an arc of radius 9m. Figures 3.3(a) and (b) show the plan and sectional views of the model in the test facility. Figure 3.4 shows the experimental model spar in the wave basin.

The tank is 1.2m deep and designed to generate small-medium amplitude waves for a frequency range of 0.5-1.6Hz. The quality of the waves at the higher end (~1.6Hz) is not always satisfactory and the deep water waves approximation at the lower end is no longer valid (for frequencies < 0.5Hz). Wedge-shaped wave absorbing beach modules are located on the opposite side of wave-makers to quickly dissipate waves thereby reducing the settling time between the tests.

The optimal operation of the tank is at 1Hz. Ocean, the wave programming language provided by Edinburgh Designs Ltd [116] was used for defining and generating the required sea states for the experiments. Built-in functions of this software, allow generation of regular sine waves, simple long-crested 2D waves as well as fully realistic three-dimensional sea-states with directional spreading or combination sea states(e.g.: swell and wind seas). As a first step the target sea state is defined using wave front components described by amplitude, frequency, starting phase and angle relative to wave-maker. Depending on the target sea state, the software generates a wave elevation command signal for the tank control system. A tank transfer function translates the command signal into physical wave height. The regular wave elevation, z is characterised by its peak wave amplitude (a) and wave frequency (defined by repeat time of the wave paddle motion) and is described by

$$z = a\cos\left(\frac{2\pi F \times 2^{rnum}}{clock\ rate}t + \phi\right) \tag{3.1}$$

where, F is the front number, *rnum* is the run number with a pre-set clock rate (i.e. the sampling frequency of data output from the tank) for a time, t. For the regular wave generation, the clock rate was set at 32 Hz with a run number of 10. This gave a frequency discretization of approximately 0.031Hz for a sample time of 64seconds. Irregular wave generation is by Fourier synthesis of wave-fronts using the deterministic approach. The wave elevation time series of the target spectrum is obtained by IDFT method. The amplitude of the DFT components of the target spectrum is proportional to the square root of the desired spectral density and the phase is randomly generated by a seed number [117]. Tank transfer function converts the time series to a command signal (with a repeat period determined by the length of the series) for physical wave generation.

Reflection from the beaches can induce significant reflected spectrum, which in turn affects the performance of the system. The beach reflection co-efficient(ratio of reflected wave amplitude to incident wave amplitude) for monochromatic seas (for a range of frequencies 0.75-1.375Hz) were estimated using the method proposed by[118] and were found to be below 10% .

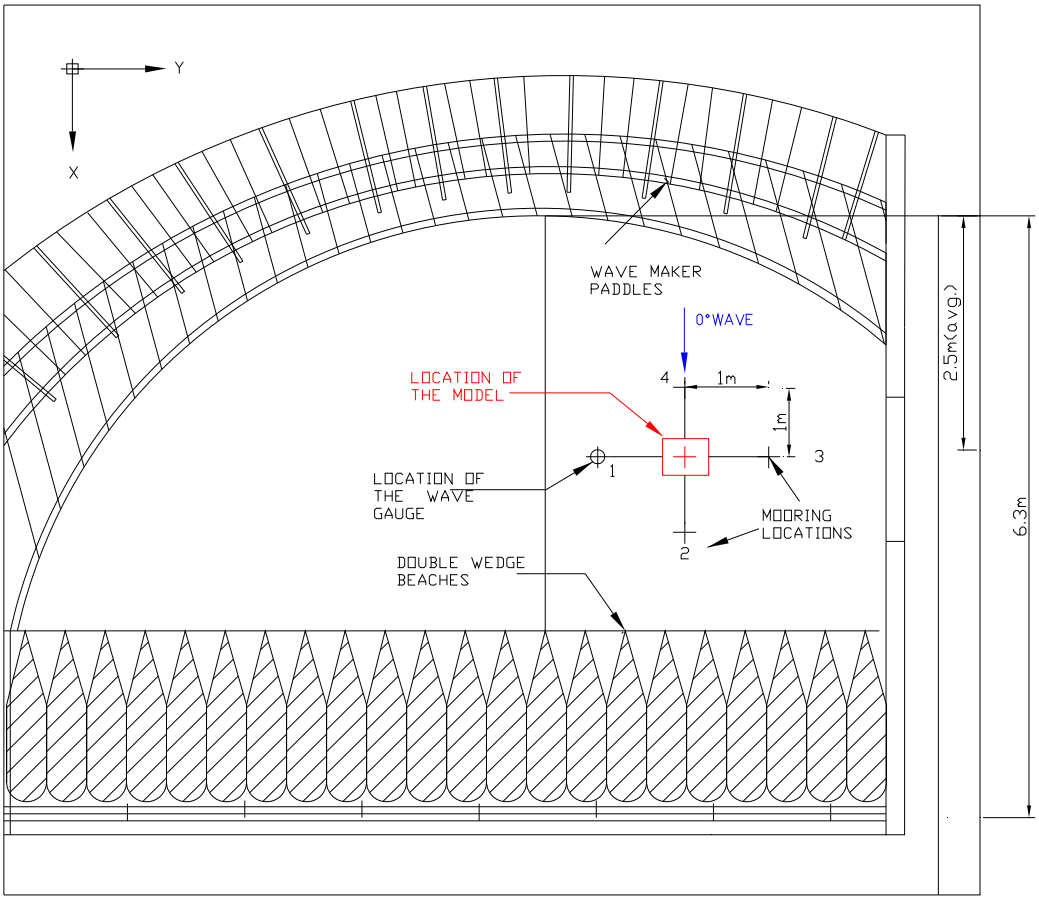

(a)

Fig. 3.3 (a) Plan view of floating wind turbine in the wave basin (Not to scale)

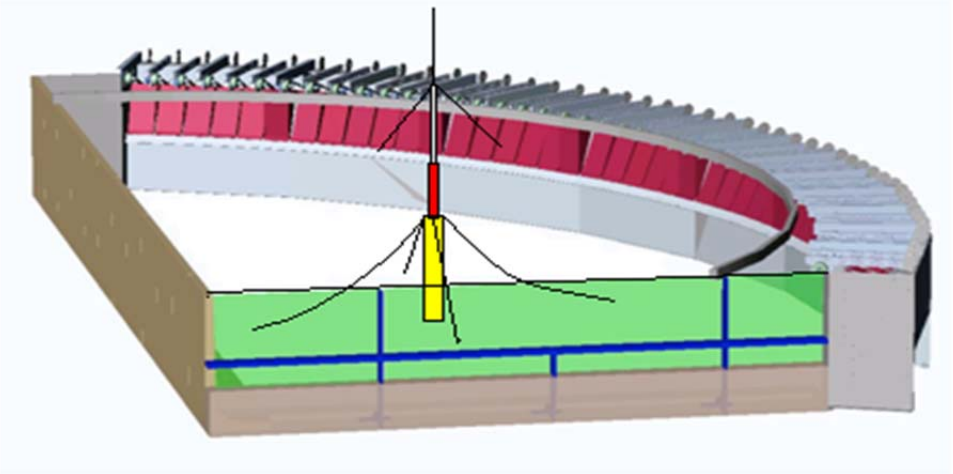

(b)

Fig. 3.3 (b) Sectional view of floating wind turbine in the wave basin (Not to scale)

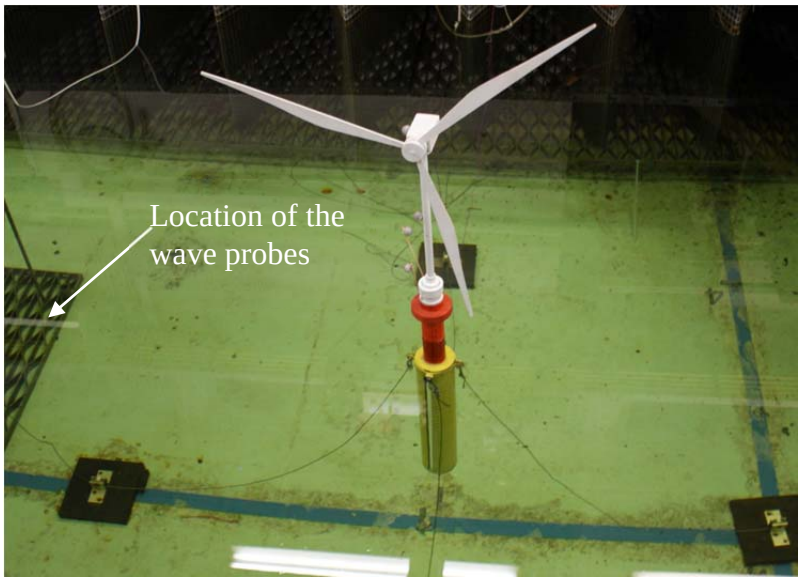

Fig. 3.4 Model Spar in the wave basin

3.2.2 Motion measurement and recording

As waves are generated, the translation and the rotational response of the structure due to wave action must be captured in real time. For this purpose, the Optical tracking system from QTM software, Qualisys [119] was used to record the 6 degrees of freedom motions in real-time(these include surge, sway, heave, roll, pitch and yaw motions). The system works by using two infrared cameras which detect the three-dimensional position of marker balls placed on the model over time by

stereoscopy. This system enables non-intrusive measurements to be taken using the principles of triangulation. The two cameras, each with 250 infrared diodes, were rigidly positioned, calibrated following the manufacturers' suggested procedure to obtain the appropriate focus and aperture. The camera accuracy as setup in the Curved Wave Tank was 0.1 mm at 32 Hz [120]. The markers used were spherically shaped with a diameter of 10mm, painted with a reflective coating. Four reflective markers were positioned closer to the mast and at the nacelle for this purpose (refer to Fig. 3.5).

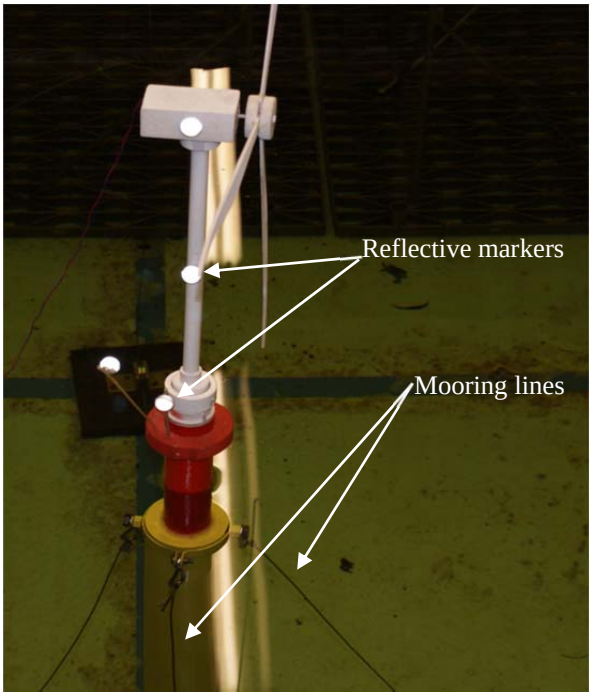

Fig. 3.5 The marker system and mooring lines

The stereoscopic measurements of the spar motion from the cameras are retrieved by the host computer where diagnostics of the data are performed. A sampling frequency of 32Hz was used for the acquisition procedure. A delay of approximately 2 minutes was allowed between initiation of waves and the commencement of data capture to allow sufficient duration for response to stabilise. The position and orientation of the body along the 3 co-ordinate axes are measured typically at successive time instants and decomposed into separate time series for surge, sway, heave, roll, pitch and yaw directions. QTM generates data files (.mat) to be analysed

by MATLAB, containing the 6DOF motion at each time step together with the residual (average error of each measured marker). Fourier analysis of the raw motion data is later done to extract the amplitude of motion response or the response spectrum corresponding to the input wave frequency. These were then used to compute the motion Response Amplitude Operator (RAO) as defined in Chapter 2. Fig. 3.8 shows the experimental set-up and arrangement for data measurement and processing.

3.2.3 Wave height measurement

While the motions were being recorded, the wave elevation profile was concurrently measured using four numbers of twin-rod resistance-type wave probes positioned close to the location where the model was tested (as may be noted from Fig. 3.3 (a) and Fig. 3.4). Each probe consists of two parallel steel rods approximately 300mm long separated by 20-30mm partially immersed in the water with the conductance between them proportional to the depth of immersion and conductivity of the water.

A high frequency ac power supply energised the gauges and a time division multiplex system allowed the use of very closely spaced probes without cross-talk between them. The probes were spaced at 100mm centres along a frame mounted close to the model and connected to a signal conditioning unit developed by Edinburgh designs Ltd [121]. A digital PCI interface for data acquisition, control and serial communication was used to interconnect the wave probes to a computer with a LabVIEW control program [122]. Prior to data acquisition, the wave probes were calibrated to obtain the calibration coefficient that relates gauge output to wave height. Data acquisition was initiated by a trigger pulse from wave maker control output. A delay of at least 2 minutes was allowed between initiation of waves and the commencement of data capture to allow reflections within the wave tank to build up and stabilise. Data was then recorded at a sample frequency of 32Hz. The wave elevation recorded at each wave probe was modified by subtracting the mean water level. Fourier analysis of the raw wave data gave the amplitude/spectrum of the sea state.

3.2.4 Wave probe calibration

The wave probes were calibrated to account for changes in conductivity of water due to temperature changes throughout the day. Before the first calibration, vigorous waves were run to mix water and attain uniform water conductivity. The calibration process provides the relationship between the output voltage signal from the probe electronic conditioning circuit and the depth of immersion. The wave probes were calibrated statically using an in-house built calibration rig (Fig. 3.6). A detailed description of the rig is available in [123].

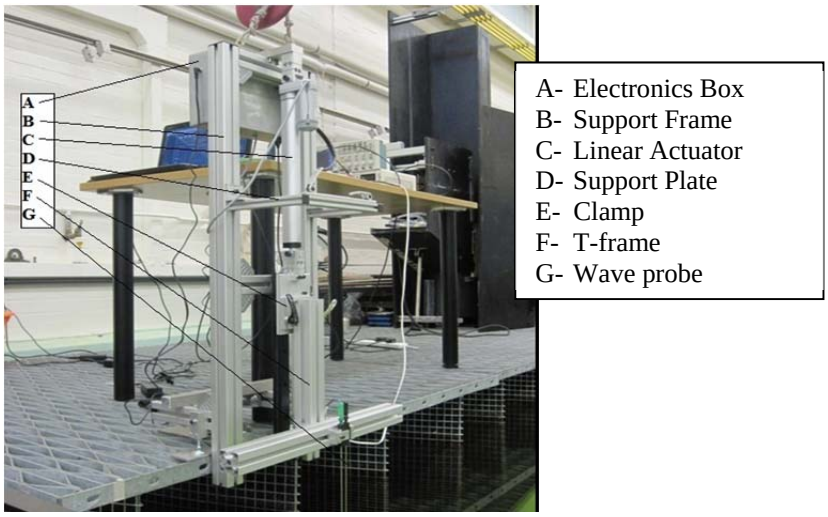

Fig. 3.6 Calibration rig used for wave gauge calibration

The wave probes were mounted to a translating T-frame that was fastened to a moving block of a linear guide. The frame is driven up and down by a linear actuator that is fitted with a digital motion encoder which allows position control (accuracy of the order of 1mm). Calibration is achieved by translating the wave probes vertically above still water over a height corresponding to the range of the probe. The process was done initially by recording the zero position of the wave probe, then incrementally changing its height to pre-set positions under computer control. The voltages were recorded at each position to a maximum of 180mm and minimum of 45mm. These voltages were then plotted against the respective depth on a linear plot to determine the least-squares linear regression which effectively gave a calibration

factor. Fig. 3.7 shows the voltage versus depth plots for one of the wave probes with a slope of 0.019.

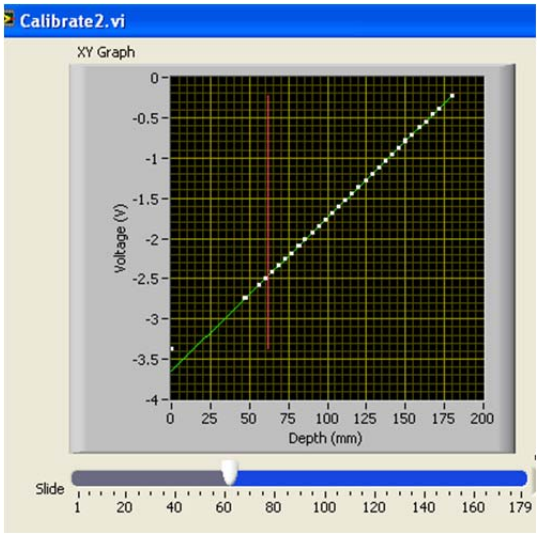

Fig. 3.7 Wave probe calibration – Voltage Versus depth

The wave elevation and motion recording systems were monitored on two separate computers. Data acquisition was manually synchronised since the two measurement systems could not be configured to share the trigger signal from wave maker simultaneously. Fig. 3.8 illustrates this arrangement.

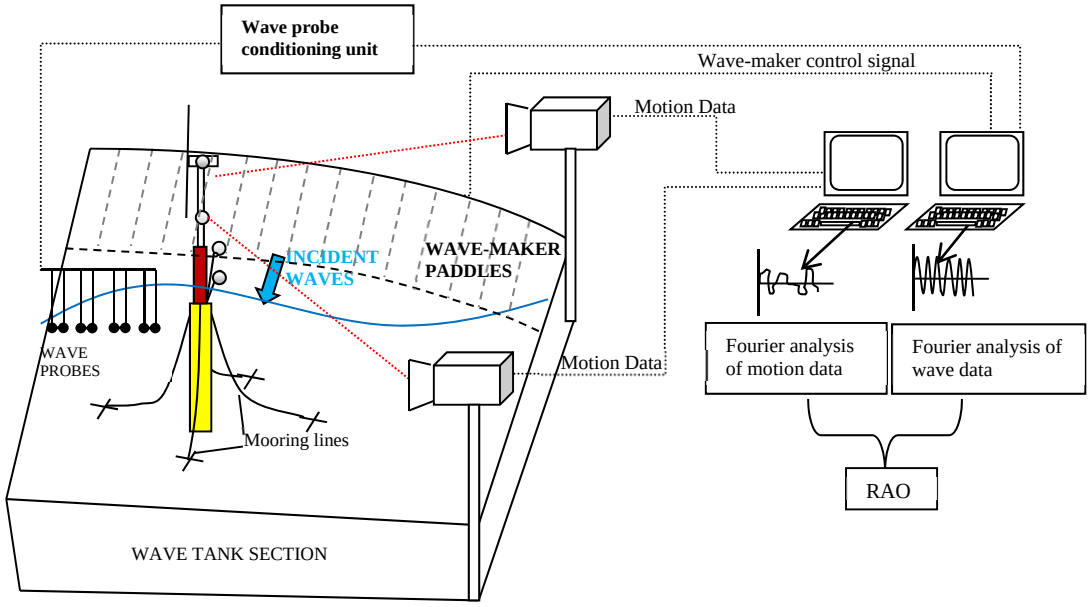

Fig. 3.8 Experimental set-up and data measurement

3.3 Experimental Testing

The experimental testing plan consisted of determining the resonance properties of the system and measurement of response at the centre of gravity and nacelle.

3.3.1 Free vibration tests and model calibration

As a first step, still-water vibration tests were conducted to determine the resonance properties of the system for heave and pitch motions. Results of these tests also served to calibrate a numerical model, to validate the inertia properties and hydrodynamic coefficients applicable for the testing conditions. The model's operating draft was set at 700 mm (same as in [38]). The model was placed in the wave basin and suitably ballasted to achieve this required draft once the mooring lines were attached. The mass of the model was confirmed by the weights computed for each element of the model and the displacement (i.e., 38.9 N) computed for the draft in its free floating condition (i.e., 655mm) before attaching the mooring lines. When in the moored condition, the inertia of the four mooring lines and their attachments (total weight of 91g) contributed to an additional displacement resulting in a final draft of 700 mm. The weight of accessories (i.e., markers) used for measurement system was assumed to be negligible. The model’s centre of gravity remained at 300 mm above the keel. The model was given an initial displacement in the heave and pitch directions, then released. The time response of the motions were measured for a period long enough until the oscillations were dispensed with. The process was repeated atleast five times and natural frequencies were obtained from the average of five records. The sample time histories for heave and pitch responses are shown in Figure 3.9.

The inertia properties of the model were computed in a 3-D CAD modelling tool, SolidEdge [124] and were fed to a numerical model of the spar buoy created using OrcaFlex [125]. A detailed discussion on the spar-buoy model in OrcaFlex is provided under section 3.6. The overall mass and inertia properties were assumed to be constant and lumped at the centre of gravity. This assumption diagonalised the stiffness matrix in the evaluation of natural periods of the system. The computed

equilibrium position of the moored spar model in OrcaFlex matched with the model draft in the experimental model. Heave and rock tests were simulated in OrcaFlex to validate the system natural frequencies. The latter were obtained by plucking the model and observing the time history of certain displacements. The model was given an initial offset from its computed still water equilibrium position and simulations were run with no waves. The buoy motions were monitored to assess the natural period. During the simulations, the normal and axial drag and damping moments were adjusted in the OrcaFlex model by several attempts of trial and error to match the time-series of decay tests obtained from the experiments. The heave and pitch response histories obtained during the free-decay tests were overlaid on the experimental results in Fig.3.9. The time and phase agreement were good for the first few cycles; however phase lag developed as the responses decayed. This difference was used to adjust the hydrodynamic properties of the spar in the OrcaFlex model until good agreement was achieved between measured and calculated values for heave and pitch natural frequencies. This also helped to validate the hydrodynamic properties (viz, drag moments and added moments of inertia) that were discretely characterised and instantaneously generated for each degree of freedom in OrcaFlex. The natural frequencies obtained from the experiments and numerical model are presented in Table 3.2. Further details about the numerical model using OrcaFlex are presented in section 3.6.

	Experiment	OrcaFlex
Surge	0.0625	0.0625
Heave	0.3438	0.3438
Pitch	0.2188	0.2188

Table 3.2 Natural frequencies of the stepped-spar floating wind turbine (in Hz)

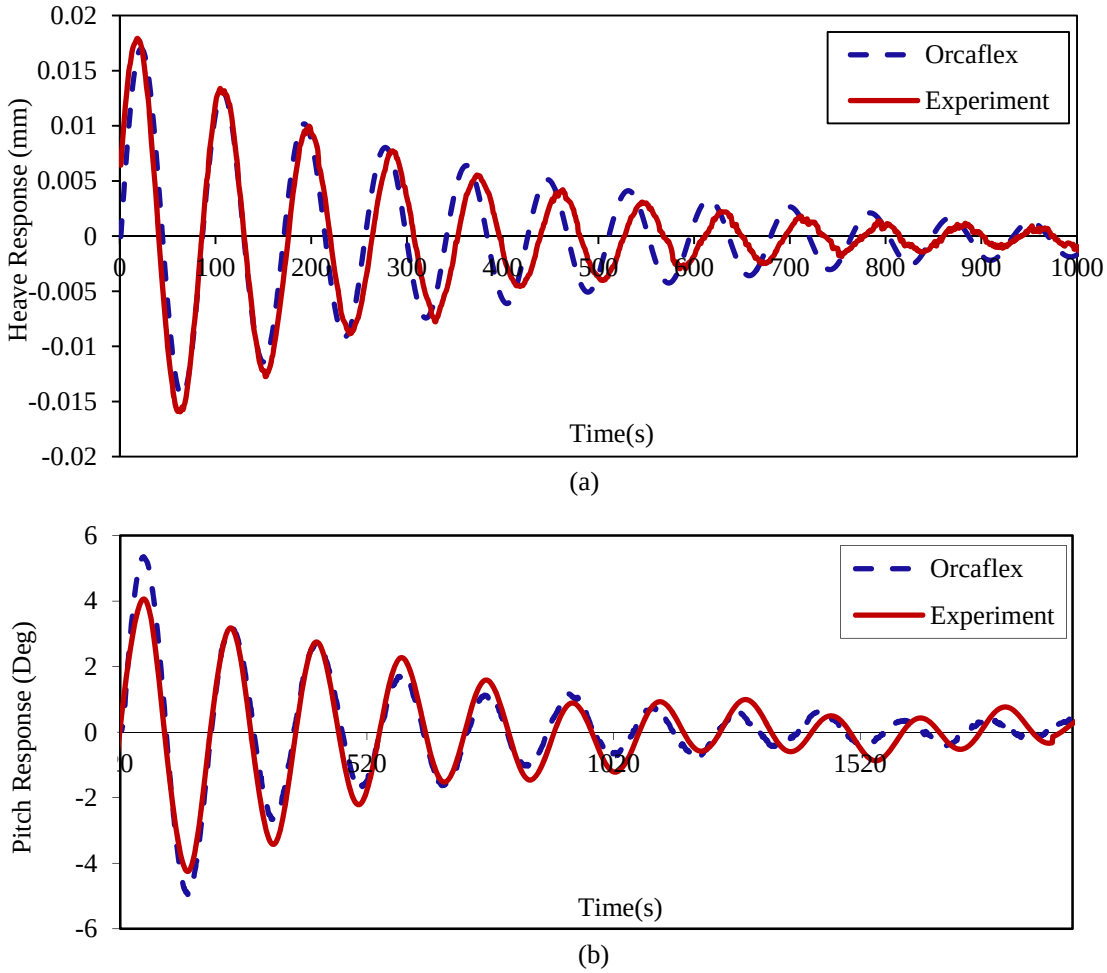

Fig. 3.9 Sample time response measured during the free-decay tests for (a) pitch response and (b) heave response by experiments and OrcaFlex

3.3.2 The mooring configuration and the basis for selection

The three-point asymmetric mooring system with lines uniformly distributed at 120º has been the most preferred approach for the spar system as noted in most of the previous research [126]. Although this arrangement is expected to reduce the foundation costs, because fewer lines are used, these lines have to be made of much larger cross-sections to survive storm conditions. Theoretically, a unidirectional wave does not excite a system in yaw. However in an experimental testing environment such as a wave basin, the waves near the vicinity of the model are not purely two-dimensional; reflected and radiated waves may be present. Hence yaw motion cannot be completely avoided when model scale testing is done in uni-

directional seas. Evidence of yaw response in the absence of rotor rotation was reported by Murai *et al.,*[127]. Also experimental testing with such an arrangement tends to induce considerable influence on surge and pitch response (Myhr *et al.,*[29]). A slender spar structure of the nature considered in this study, in general will require a minimum of two mooring lines to restrain it from drifting and preserve the geometric symmetry about equilibrium. A three-point mooring configuration would necessitate a larger mooring cross-section to contribute to the system inertia and hence the required displacement.

For the present study, it was decided to use small steel wire ropes of 2 mm diameter, weighing 16 g/m in air. To decide on the optimal number of mooring lines that minimised the yaw influence, 4-point symmetric mooring was considered. The response was initially studied for the 2-point configuration before proceeding with the four lead arrangement (refer to Fig. 3.10). Moorings were attached to restrain the model in a direction parallel (Case 1) and perpendicular to wave fields (Case 2). The fairleads were connected to the lower cylinder at 130 mm below the still water level and were spaced at 180º apart. This symmetric arrangement was chosen to explore the possibility of reduction in motion response. Besides, the addition of fourth leg can completely decouple yaw motion from the other modes [128] while providing the required stability and redundancy in the event of a mooring line failure.

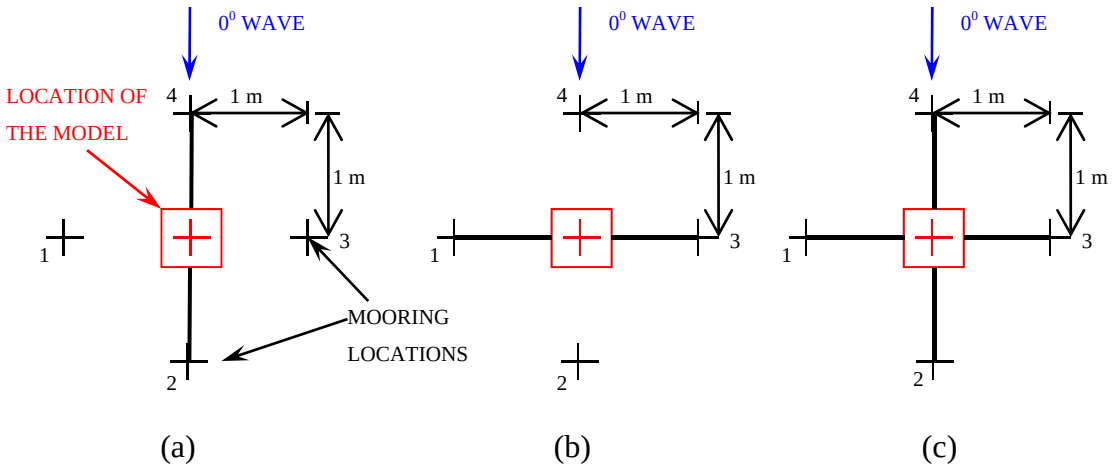

Fig. 3.10 Mooring configurations : (a) Case-1: two-point mooring parallel to waves (b) Case-2 : two-point mooring perpendicular to waves and (c) Case-3 : Four-point mooring.

To assess the behaviour of the mooring design, the model was subjected to a series of regular waves (height 30mm) with frequencies from 0.5-1.59Hz. As illustrated in

Figure 3.8, the motion responses and wave elevations were measured simultaneously and were used to compute the Response Amplitude Operator (equation (2.1)). Figures 3.11 to 3.14 show the plots for the Response Amplitude Operators (RAO) for surge, heave, pitch and yaw motions, expressed as a function of wave scattering parameter, *ka* where, *a* is the radius of the spar, *k* the wave number given by $\frac{2\pi}{L}$ (where *L* is the wavelength). The scattering parameter is a useful to represent the extent of incident wave diffraction from the structure. It can be observed from the plots that the symmetric slack catenary mooring does not significantly affect motion in horizontal directions (surge and pitch). The 4-point configuration, however introduced higher resistance in the vertical direction resulting in a reduced heave motion. The yaw response was found to be lowest for the 2-point mooring configuration with lines perpendicular to the wave direction. For the 4-point mooring, much of yaw response was restricted to below 0.025°/mm of incident wave height at model scale. Considering the overall response, the four point mooring configuration was selected, since the 2-point mooring configuration can only represent an idealistic case that would prove to be inadequate and impracticable considering the directional variability of sea states.

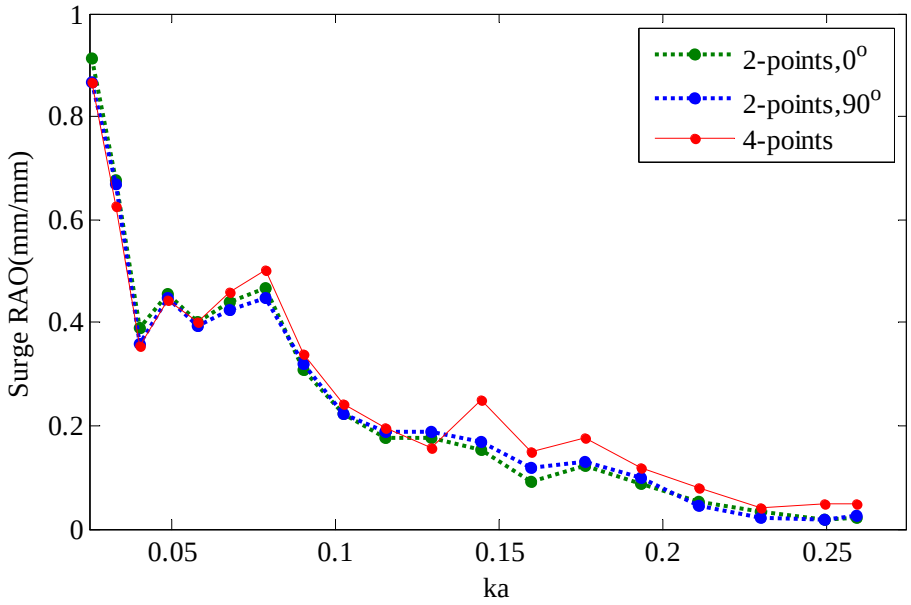

Fig. 3.11 Surge RAO for the 2-point and 4-point mooring configurations shown in Figures 3.10 (a), (b) and (c) respectively.

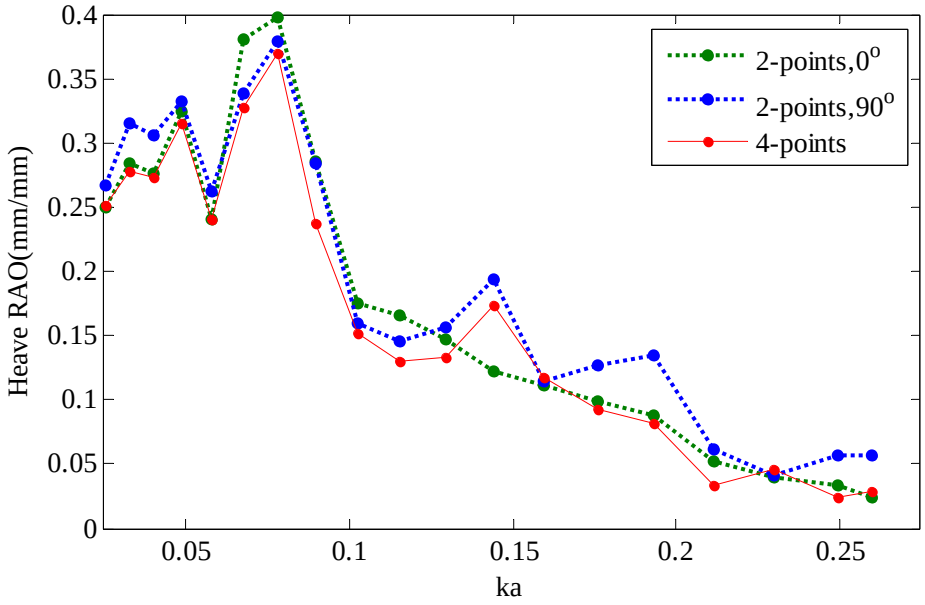

Fig. 3.12 Heave RAO for the 2-point and 4-point mooring configurations shown in Figures 3.10 (a), (b) and (c) respectively.

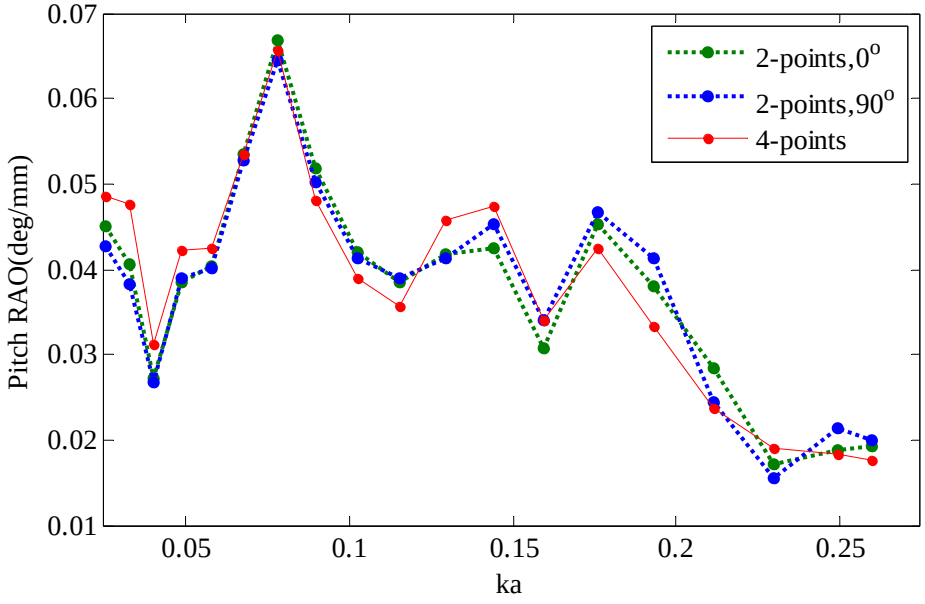

Fig. 3.13 Pitch RAO for the 2-point and 4-point mooring configurations shown in Figures 3.10 (a), (b)and (c) respectively.

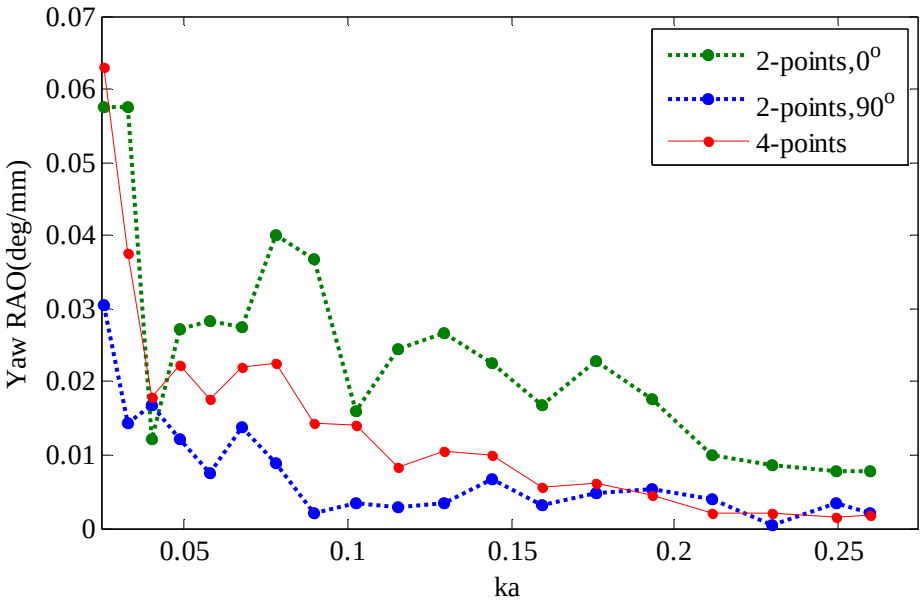

Fig. 3.14 Yaw RAO for the 2-point and 4-point mooring configurations shown in Figures 3.10 (a), (b) and (c) respectively.

3.4 Testing in regular waves

Testing a model in regular waves help to gain an initial understanding of the system behaviour in an environment controlled by few parameters namely wave height and frequency. These tests were performed for 30 mm, 60 mm and 90 mm wave heights at zero degree heading (refer to Fig.3.3). The frequencies being tested ranged from 0.5 Hz to 1.6 Hz as this was also the operating range of the Curved tank. A set of 19 single frequency regular sinusoidal waves were generated at fixed frequencies that were integer multiples of the sampling duration, n/32 Hz, (where n is a positive integer). The wave components for response calculation were selected with frequencies that were also integer multiples of sampling frequency. In this way the frequency leakage effect[9] is avoided during Fourier synthesis for RAO calculations. These waves were run for a duration long enough until a steady state in platform response was reached. Testing in 90 mm waves (corresponding to scaled-up value of 9 m wave height) was limited to a narrow band of frequencies. An upper frequency limit of 1.44 Hz was chosen, beyond which the linear wave theory was no longer

[9] Frequency leakage refers to the smearing out of signal energy over a wide frequency range in the FFT when it has to be a narrow frequency range

applicable (generated waves began to break and were of poor quality). The lower frequency limit was set at 0.75Hz as was permitted by the maximum possible wave maker stroke. The time response of motions to regular waves in six degrees of freedom was recorded for a duration of 64 sec at two locations, namely at the centre of mass(located 30.5 mm below water plane) and at the nacelle (approximately 550 mm above the water plane). Fast Fourier transform (FFT) was applied to the time series to extract the response that corresponded to frequency component of wave field. The Response Amplitude Operator (RAO) for regular waves was then computed using equation (2.1).

3.5 Testing in random waves

Although regular waves give a qualitative and quantitative understanding of the system in a simplistic environment, realistic sea states are rather complex. Testing in more realistic irregular waves is important as they help identify irregularities in response, for e.g., coupled excitation introduced by non-linear forces at periods other than the wave periods. For testing in random seas, the deterministic wave generation method based on random phase approach was used to synthesise the drive signals for the wave-maker. The time series output for the IDFT (Inverse Discrete Fourier Transform) was derived from a target JONSWAP spectrum that was defined using 281 wave components with phases randomly generated by a seed number. The spectral representation used for the generation of random waves is given by (Tucker *et al.,*[129]).

$$S(f) = A \cdot f \exp(-Bf^{-4})\gamma^{\exp\left\{\frac{(f-f_p)^2}{2\sigma^2 f_p^2}\right\}} \tag{3.2}$$

where, the coefficients A and B are derived from peak spectral frequency f_{p} and significant wave height $H_{\mathrm{m0,}}$ respectively.

$$B = \left(\frac{1.034}{f_p}\right)^4 \tag{3.3}$$

$$A = B\left(\frac{H_{m0}^2}{f_p}\right) \tag{3.4}$$

and the bandwidth parameter, σ was given by

$$\sigma = \begin{cases} 0.07 \ \ for \ \ f < f_p \\ 0.09 \ \ for \ \ f > f_p \end{cases} \tag{3.5}$$

Table 3.3 presents the model sea state parameters used to generate the spectra. The design waves were simulated for three significant wave heights of 30 mm, 60 mm and 90 mm with peak frequencies defined between 0.6 Hz - 1.5Hz. These tests were run for 2-minute duration as the wave reflections in the tank are considered to be small for this length of time. The measured wave and response spectrums were used to compute the response amplitude operator for irregular waves in frequency domain using equation (2.3) (in Chapter 2). The response amplitude operators were computed at the centre of mass and nacelle, plotted as a function of the wave scattering parameter, *k*a.

H_{m0}(m)	f_p(Hz)	*A*	*B*
0.03	0.6	2.54E-05	0.113
	0.7	4.71E-05	0.210
	0.8	8.04E-05	0.357
	0.9	1.29E-04	0.573
	1	1.96E-04	0.873
	1.1	2.87E-04	1.278
	1.2	4.07E-04	1.810
	1.3	5.61E-04	2.493
	1.4	7.54E-04	3.353
	1.5	9.94E-04	4.418
0.06	0.7	1.89E-04	0.210
	0.8	3.22E-04	0.357
	0.9	5.15E-04	0.573
	1	7.85E-04	0.873
	1.1	1.15E-03	1.278
	1.2	1.63E-03	1.810
	1.3	2.24E-03	2.493
	1.4	3.02E-03	3.353
	1.5	3.98E-03	4.418
0.09	0.7	4.24E-04	0.210
	0.8	7.24E-04	0.357
	0.9	1.16E-03	0.573
	1	1.77E-03	0.873
	1.1	2.59E-03	1.278
	1.2	3.66E-03	1.810
	1.3	5.05E-03	2.493
	1.4	6.79E-03	3.353
	1.5	8.95E-03	4.418

Table 3.3 Model sea state parameters for irregular waves

3.6 Modelling in OrcaFlex

In an effort to re-create the experimental conditions and validate the system behaviour, OrcaFlex was used as the hydrodynamic modelling tool. OrcaFlex is a time-domain finite element solver that can provide fast and accurate predictions of the coupled response of a surface vessel and its moorings [125]. The software has the capability to capture wave loading and the non-linear loads from the mooring lines, but not equipped to handle the aerodynamic loads for turbine control or power take-off systems. Coupling the hydrodynamics module of OrcaFlex with FAST simulations is an ongoing research [64]. This study focuses on the response validation of the coupled hydrodynamic model of a stepped-spar floating wind turbine considering improved line dynamics using OrcaFlex. Therefore, no attempt was made to model the aerodynamic loads.

3.6.1 Modelling the spar-buoy

The 1:100 scale model of the stepped spar structure was modelled using the 6D buoy theory for surface piercing bodies in OrcaFlex. The spar body is treated as a rigid body with 3 translational and 3 rotational degrees of freedom. OrcaFlex provides the time simulation of motions of the spar for a specified period of time in response to an external load input (i.e. waves). At the start of simulation, the initial positions and orientations of all bodies are known from the static analysis. The steady state position is calculated by iterative solution for position until any out of balance loads on the body becomes zero. For the time simulation of motions, the basic equation of motion is described using Newton's second law with 6-dimensional load vector F, mass matrix M and acceleration vector A as:

$$[F]=[M][A] \tag{3.6}$$

OrcaFlex solves for the local acceleration vector for every free body at the beginning of time step from the knowledge of system damping vector[C], stiffness [K] and external load vector [F] , velocity and position vectors [V] and [P] respectively.

$$[M][A] = [F] - [C]\,[V] - [K]\,[P] \tag{3.7}$$

This equation is then integrated using forward Euler integration to determine the values at the end of each time step. The various load contributions to the *F* matrix come from the weight, structural inertia and fluid loads from buoyancy, hydrodynamic drag, damping and added mass effects, tension and shearing(mooring lines), seabed reaction and friction, contact forces with other objects(if any).

The physical properties of the experimental model were used to define the mass and inertia properties for the spar. The draft of the model in free-floating condition was 655 mm. The weight and the structural inertia were computed using SolidEdge[124] and applied at the buoy's centre of mass(refer to Figure 3.15 showing the snapshot from OrcaFlex). It may be noted that the centre of mass (-360mm) specified refers to the buoy centre of mass in air defined with respect to the water plane. OrcaFlex uses this data to compute the hydrostatic equilibrium position including the weight of the mooring lines during static analysis.

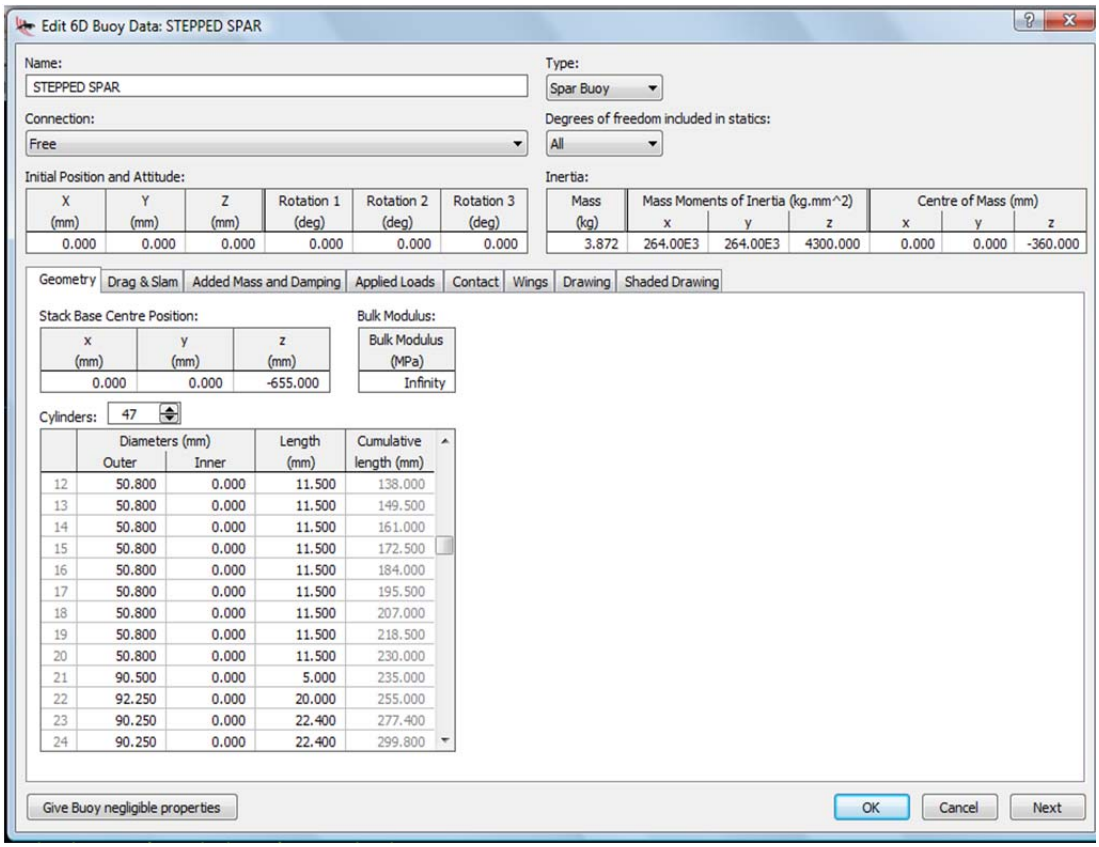

Fig. 3.15 Mass and Geometry properties of the spar as entered into Orcaflex(a snapshot)

To model the spar buoy, the structure was segmented into a stack of 47 numbers of short axi-symmetric co-axial cylinders mounted end-to end along the vertical axis. The upper spar comprised of a wire-frame of 20 segments each measuring 11.5mm in length and 50.8mm in diameter and the lower SPAR comprised of 27 segments (2nos to represent the mooring attachment) and 25 segments each measuring 22.4mm in length and 90.25mm in diameter. The wire-frame model and the graphically rendered version of the spar are shown in the Fig. 3.16.

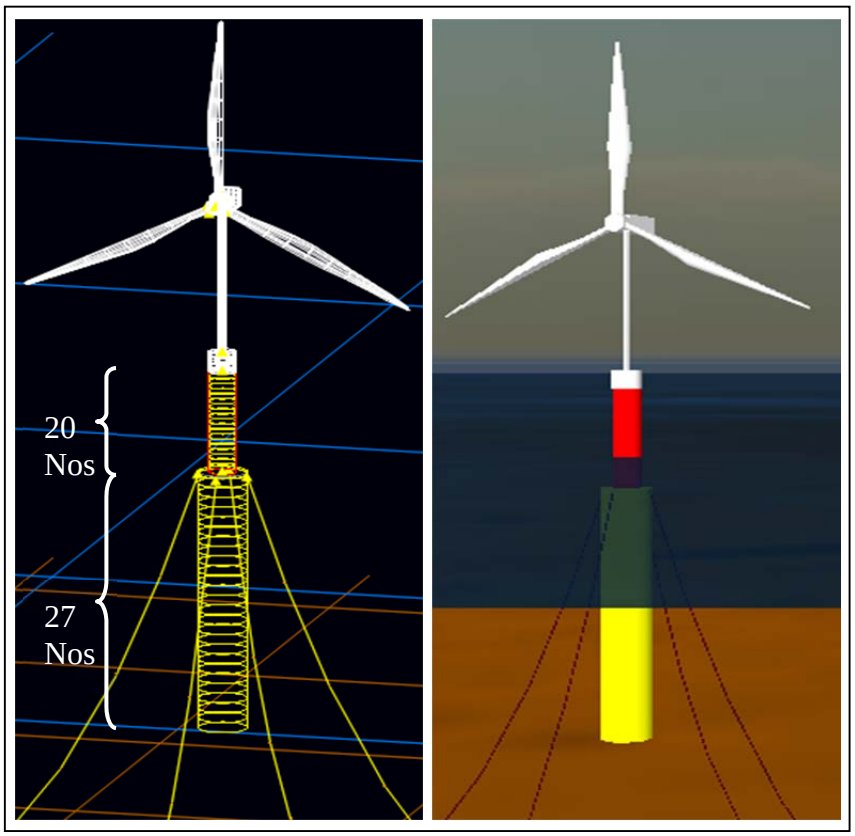

Fig. 3.16 OrcaFlex models of the stepped-spar floating wind turbine

For each wetted segment of the spar buoy, contributions to the total fluid force come from buoyancy forces, added mass, drag effects plus any additional damping if specified. OrcaFlex computes the hydrodynamic loads on each of these segments individually using Morison's equation with relative velocity formulation [130]. The added mass and drag forces (and moments) are scaled according to the proportion of the volume that is submerged in water.

$$F_w = \frac{V_w}{V}(\rho V a_w + C_a \rho V a_r) + \frac{V_w}{V}\left[\tfrac{1}{2}\rho A C_d |V_r| V_r\right] \qquad (3.8)$$

$$H_w = \frac{V_w}{V}(I\alpha_w + I_a\alpha_r) + \frac{V_w}{V}\left[\tfrac{1}{2}\rho BC_m|W_r\|W_r|\right] \quad (3.9)$$

where, F_w is the fluid force on a segment

H_w is the fluid moment on a segment

V is the total volume of the cylinder

V_w is the instantaneous wetted volume of the cylinder

ρ is water density(kg-m^3)

ρV is the displaced mass of water(Froude-Krylov Force term)

a_{w} is the fluid linear acceleration vector at the wetted centroid of the segment

C_{a} is the segment added mass coefficient

a_{r} is the fluid acceleration relative to the body

A is the drag area of the segment

C_{d} is the segment drag coefficient

V_{r} is the fluid velocity relative to the body (velocity of local water isobar minus the velocity of the cylinder)

I is the displaced moment of inertia (Froude-Krylov moment)

α_{w} is the angular acceleration vector of the local water isobar at the wetted centroid of the segment

I_a is the added mass moment of inertia

α_{r} is the fluid angular acceleration vector relative to body

B is the drag area moment

C_m is the drag moment coefficient

W_{r} is the fluid angular velocity relative to the body (angular velocity of local water isobar minus the angular velocity of the cylinder)

Any buoyancy variation due to wave is accounted for by applying a load corresponding to the wetted volume given by $\rho V_w g$. Any additional load due to damping, F_d is also scaled by the proportion wet as ($\frac{V_w}{V} \times F_d V_r$). These fluid loads are applied at the instantaneous centroid of the wetted volume of the spar. The wetted

volume V_w and its centroid are computed from the volume of the cylinder when it is truncated by the water surface. It must be remembered that the load matrix is 6-dimensional, 3 for representing the force vectors and three for representing the moment vectors. At each time step, the instantaneous wetted surface of cylinder is calculated and the component forces due to drag, added mass and damping are calculated for the submerged parts. Thus, the system geometry is recalculated to account for all geometric non-linearities, including the spatial variation of both wave loads and contact loads.

The geometry of the spar and its segments is used to determine the buoyancy forces, considering the instantaneous position of the water surface and its slope. Since the software computes the forces on each segment individually, the program requires an area (normal and axial) and coefficient (normal and axial) for each segment. As was recommended, since the slices used for modelling were thin, the values for the hydrodynamic properties (drag, inertia and damping) appropriate for whole shape (for lower spar and upper spar) was considered and not the individual slice. These were discretised in six dimensions with user supplied coefficients. These values were chosen empirically according to the guidelines in OrcaFlex manual [125]. The values for drag coefficients were chosen from Hoerner [131]. A normal drag coefficient value of 0.8 was chosen for the segments of the upper spar and a value of 0.825 was chosen for the lower spar segments. An axial drag coefficient of 0.8 was applied to bottom-most segment. The value for axial drag area at the segment intersection between the upper and bottom spar was quite small and hence axial drag co-efficient was almost zero for this section. For selecting the appropriate added mass co-efficients for the segments, reference was made to Newman [132]. The ratio of diameter to length of the cylindrical segment (*D/L)* for the upper spar as well as lower spar was less than 0.3. For the upper spar, a normal added mass coefficient of 0.89 and axial value of 0.07 was chosen from ellipsoid approximation for the reference volume. The corresponding values for the lower spar were 0.92 and 0.06 respectively. Added moments for the discretised buoy are automatically computed by OrcaFlex from the distribution of hydrodynamic forces along the buoy axis. Figures 3.17 & 3.18 show the drag and added mass menu for the stepped spar in OrcaFlex. In order to decide if the model required any additional damping forces, still-water

vibration tests were carried out. The time history of displacements was recorded for the heave and pitch response. A comparison was made with experimental results and

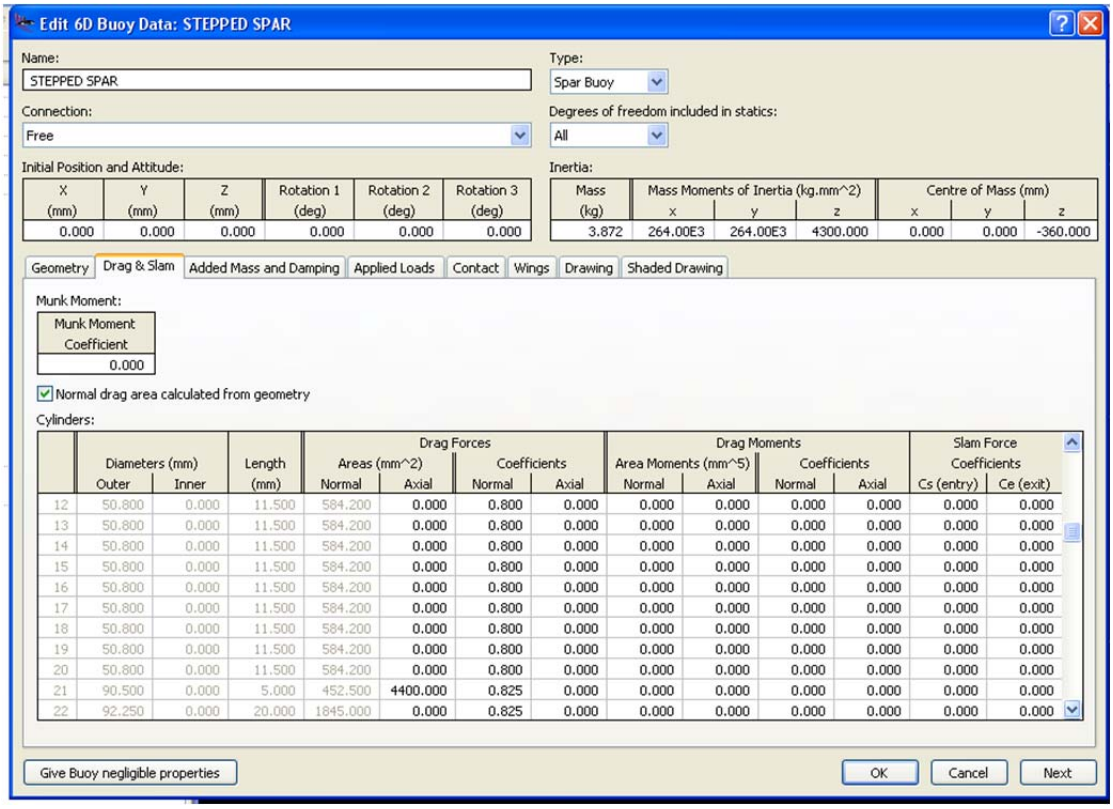

Fig. 3.17 Drag coefficient data of the spar as entered into Orcaflex

the values were decided by trial and error adjustments (refer to Section 3.3.1).

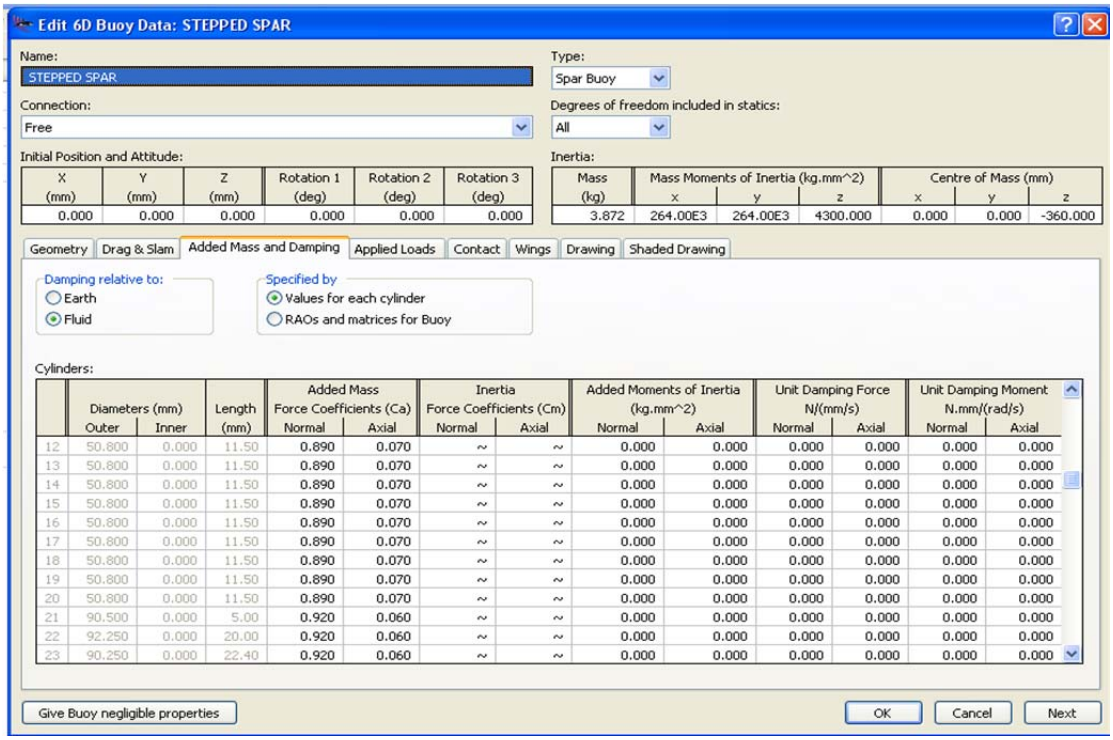

Fig. 3.18 Added Mass and Damping data

3.6.2 Modelling the mooring lines

The mooring line dynamics in OrcaFlex is handled by a 3D finite element model. Lines are discretised as lumped mass elements that are connected to visco-elastic spring-damper segments to model the axial, torsional, bending stiffness and damping. Figure 3.19(a) shows the discretisation of a line where, n_{xyz} represents the nodal co-ordinate system and s_{xyz} represent the segmental co-ordinate system.

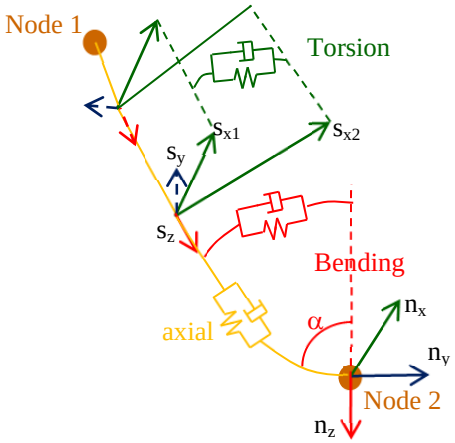

(a)

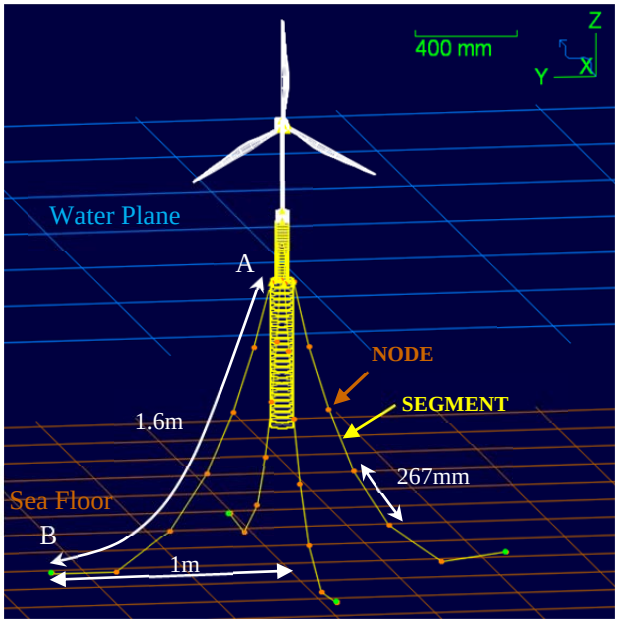

(b)

Fig. 3.19 Mooring line modelling in OrcaFlex (a) Mooring line segment and node discretisation reproduced from[125] (b) Line model in OrcaFlex

The axial stiffness and damping components (shown in yellow colour) tend to apply an equal and opposite effective tension force to the nodes 1 & 2. Likewise, torsional and bending spring and damper elements (shown by green and red colour respectively) apply equal and opposite moments to the nodes at each end of the segment. Four mooring lines each 1.6m in length were arranged 90º apart. Each line was divided into 6 nos of 267mm long segments that were connected by 7 nodes. The selection of number of segments was a compromise between the simulation time and accuracy. The beginning of a line, for example (denoted by node (A) in Fig. 3.19(b)) was attached to the top of lower spar and the end node (B) was attached to an anchor point that was 1m along the y axis from the centre position . Each segment is divided into two halves and the non-structural properties (weight, drag etc) of each half-segment are lumped to the node at that end of the segment. To decide on the line type, OrcaFlex offers a variety of cable configurations and to enable fast and accurate analysis of catenary systems. Steel wire rope data from the 'line type' wizard was customised to match the inertia properties of the lines that were used in the experimental set-up. The line structural properties are defined in Table 3.4.

Item/Description	**Units**	**Value**
Line type	-	Steel wire rope
Nominal outer diameter	mm	2
Weight in air	kg/mm	$16x10^{-6}$
Displacement	kg/mm	$2.011\ x10^{-6}$
Weight in water	kg/mm	$14\ x10^{-6}$
Diameter/Weight Ratio	mm/(kg/mm)	$114.71\ x10^{3}$
Axial stiffness	kN	161
Torsional stiffness	Nmm^2	$80\ x10^{9}$
Normal drag coefficient	-	1.2
Axial drag coefficient	-	0.08
Normal Added mass co-efficient	-	1.0
Numerical damping	-	0.3
Poisson ratio	-	0.5

Table 3.4 Line structural properties

Torsional stiffness was not modelled as twisting was allowed for catenary configuration. The line hydrodynamic effects are modelled using Morison equation. The line static calculations are performed to compute the starting shape of the line (allowing for weight, buoyancy, drag) and the full equilibrium position for the model. For the dynamic simulation at the beginning of a time step, OrcaFlex computes the total load on each node as the sum of structural and non-structural loads (weight, drag, added mass etc.,). The structural loads include the line tension (rate of change of segment length between nodes), bending moments spanning between the node and segment axes and shear forces. OrcaFlex then calculates the resulting accelerations of the node, and then applies forward integration to obtain the velocity and position at the next time step. The line-seabed interaction is modelled by a modified coulombic friction element model that includes for hysteresis characteristics. The lateral friction is modelled by a coulombic element with an empirical friction coefficient.

3.7 Simulating the sea states and motion response

A simulation in OrcaFlex can be analysed with full graphical and numerical representation of the parameter being analysed. An animated display of the simulation in real time is available which is useful to correlate with physical model behaviour. As a first step, static analysis was run to ensure that the computed equilibrium position in still water matched with the displacement and draft in the model tests. Dynamic time response simulation in the presence of waves was then carried out by subjecting the model to regular and irregular seas. For modelling the design seas, OrcaFlex offers a variety of wave field models based on wave theory and spectral representation. A sea state at any given time is obtained by superposition of wave trains each defined by a direction modelled using single wave component (regular waves) or multiple wave components (irregular waves). The measured time series for the regular waves were input to the numerical model. Nineteen regular wave trains were simulated using the wave time series generated during the experiments. The response time histories for surge, pitch and heave motions were extracted and Fourier transformed to compute the response amplitude operators for each wave period.

Irregular waves were modelled based on the measured time series for JONSWAP spectrum. To generate the incident wave spectrum, 281 sinusoidal wave components, each with an amplitude, phase and frequency were extracted from the measured wave spectrum and input to the numerical model. The range of frequencies between 0.5Hz and 1.59Hz were chosen as the bandwidth within 2-minute duration. The program then synthesises a wave time history based on the superposition of the linear wave components. Figure 3.20(a) shows the screenshot of the model in still water. Figure 3.20(b) shows the model subjected to regular waves with the plots for time histories of motion response.

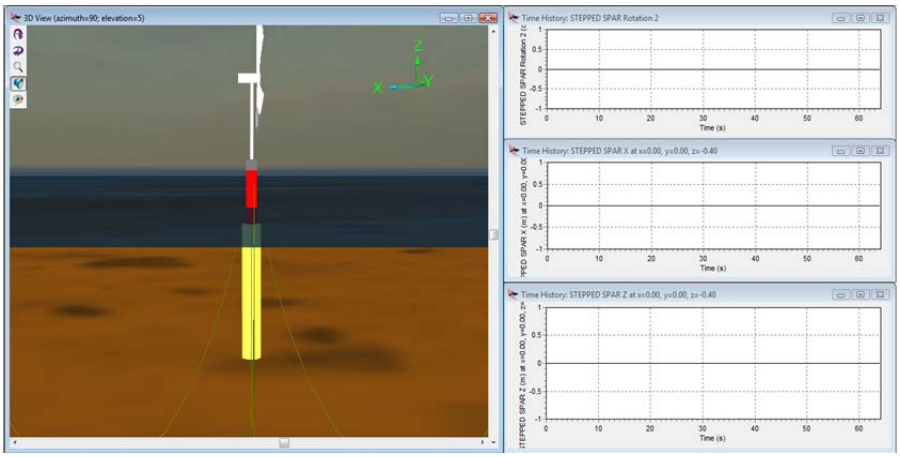

(a)

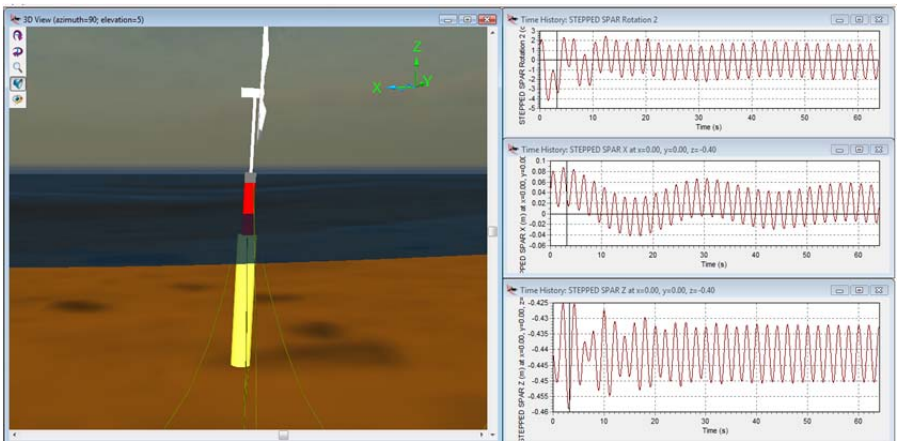

(b)

Fig. 3.20 Screenshots of the model in OrcaFlex (a) Model in still water (b) Model in the presence of waves

The simulations were run for the sea states of interest (refer Table 3.3). The simulation time origin and duration were so chosen that principal wave group passed within the simulation time. The wave repeat period used in the study was 128 sec. Sufficient time was allowed for the waves to build up to avoid starting transients. The response spectrum in surge, pitch and heave were computed from the simulated time histories using an in-house Matlab function (refer to APPENDIX-A) which is based on the Welch's averaged periodogram method[10].

3.8 Summary

An overview of the modelling aspects and the theoretical basis were presented for the experimental and numerical models of a 1:100 scale model stepped spar wind turbine. The hydrodynamic behaviour of the system for the static and dynamic conditions was experimentally determined and used to calibrate the FEM-based numerical model in OrcaFlex. As a first step, the system natural frequencies were calibrated. Other aspects that were calibrated include wave surface elevation profiles and motion response at the centre of mass and nacelle. The measured hydrodynamic responses were evaluated as Response Amplitude Operator (RAO). The next chapter presents the results of the comparison between experiments and numerical models.

[10] Welch's method is an improvement on the standard periodogram method for spectrum estimation: it reduces noise in the estimated power spectra in exchange for reducing the frequency resolution.

Chapter 4

Part-I Results and Discussions

4.0. General

This chapter presents the results for the hydrodynamic responses of a 1:100 scale model floating spar wind turbine under regular and irregular waves measured by experimental and numerical techniques as described in the previous chapter. The surge, heave and pitch motions of the spar model were experimentally measured using an optical tracking system both at its centre of mass and nacelle. The same motions are also simulated numerically using OrcaFlex under identical wave conditions. A comparison of wave elevation profiles and motion responses is presented to demonstrate the accuracy of calibration. The response amplitude operator derived from both experiments and numerical model are compared to establish the model validity.

4.1. Results

The traditional approach for testing offshore structures has been by subjecting them to long-crested uni-directional seas. This approach is based on the assumption that most severe vertical plane responses occur in uni-directional head seas and the most severe lateral plane responses occur in uni-directional beam seas. Although wave directionality can have an influence on the responses, designing structures based on unidirectional seas usually provides first-hand estimates on the system behaviour that can serve as a good starting point to determine their feasibility. Therefore, for the present work, as a conservative design case, only head seas (along surge direction) were simulated in both experiments and numerical model. The study mainly considered surge, heave and pitch responses, while sway, roll motions and other derived responses were not relevant.

4.1.1. Wave elevation profile and motion response for regular waves

The spar model was subjected to a series of regular, periodic unidirectional progressive waves for the purpose of investigating the linear and quasi-linear quantities namely motion responses and relative wave elevations. The wave heights varied from small (30mm), medium (60mm) to large waves (90mm), each with a set of 19 frequencies between 0.5-1.6Hz in steps of 0.0625Hz. The motion responses and wave elevation records were measured from experiments and numerically reproduced by OrcaFlex. The results were processed by Fourier analysis and expressed as transfer functions (RAOs) as defined in Chapter 2.

The time histories for wave elevation profiles and motion response in regular waves for one of the low (0.5Hz) and high frequencies (1.44Hz) tested are shown in Fig.4.1 & Fig.4.2. These results correspond to a wave height, H=30mm. Pitch and surge responses were observed to be in phase with each other in experiments as well as in simulations. However, since the experimental records for wave elevation and motion response were manually synchronised, time delay during the measurements was inevitable. This explains for the phase lag that existed between the computations and experiments. Although some differences between measured and simulated responses is obvious from plots in Fig. 4.1 & Fig. 4.2 which represent lower and higher frequency limits, the time-histories for measured and simulated records for several other frequencies close to the tank optimal frequency (1Hz) showed a good match (For e.g. surge, heave and pitch responses as shown in Fig. 4.3).

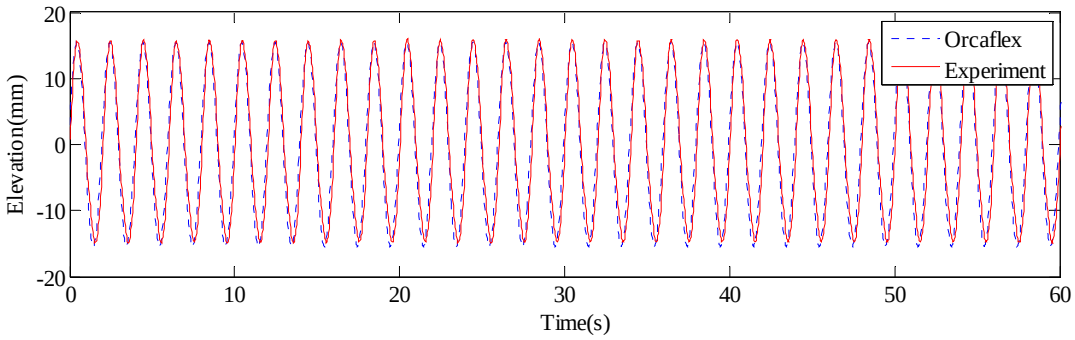

(a)

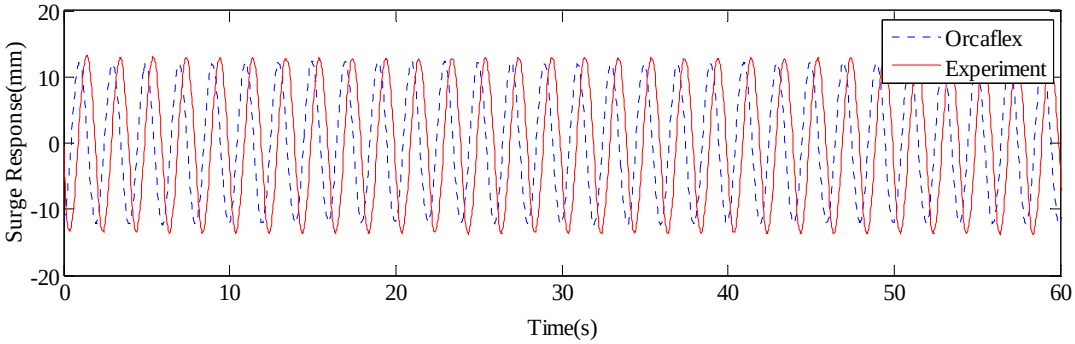

(b)

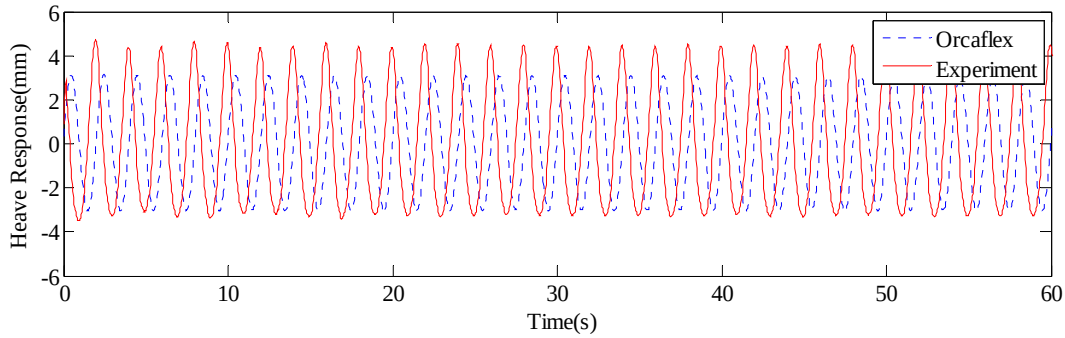

(c)

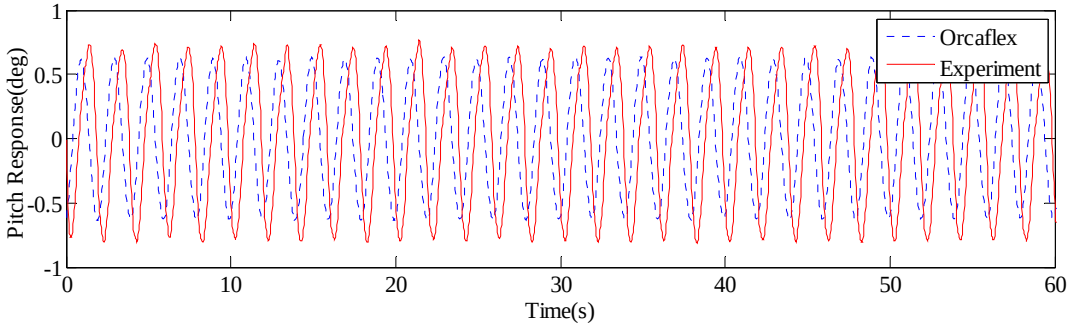

(d)

Fig. 4.1 (a) Wave elevation time history for 1 minute duration (regular wave, *H*=30mm, *f*=0.5Hz), (b) Surge response time history, (c) Heave response time history(d) Pitch response time history for 1 minute duration . All responses are at C.O.M.(Centre of Mass).

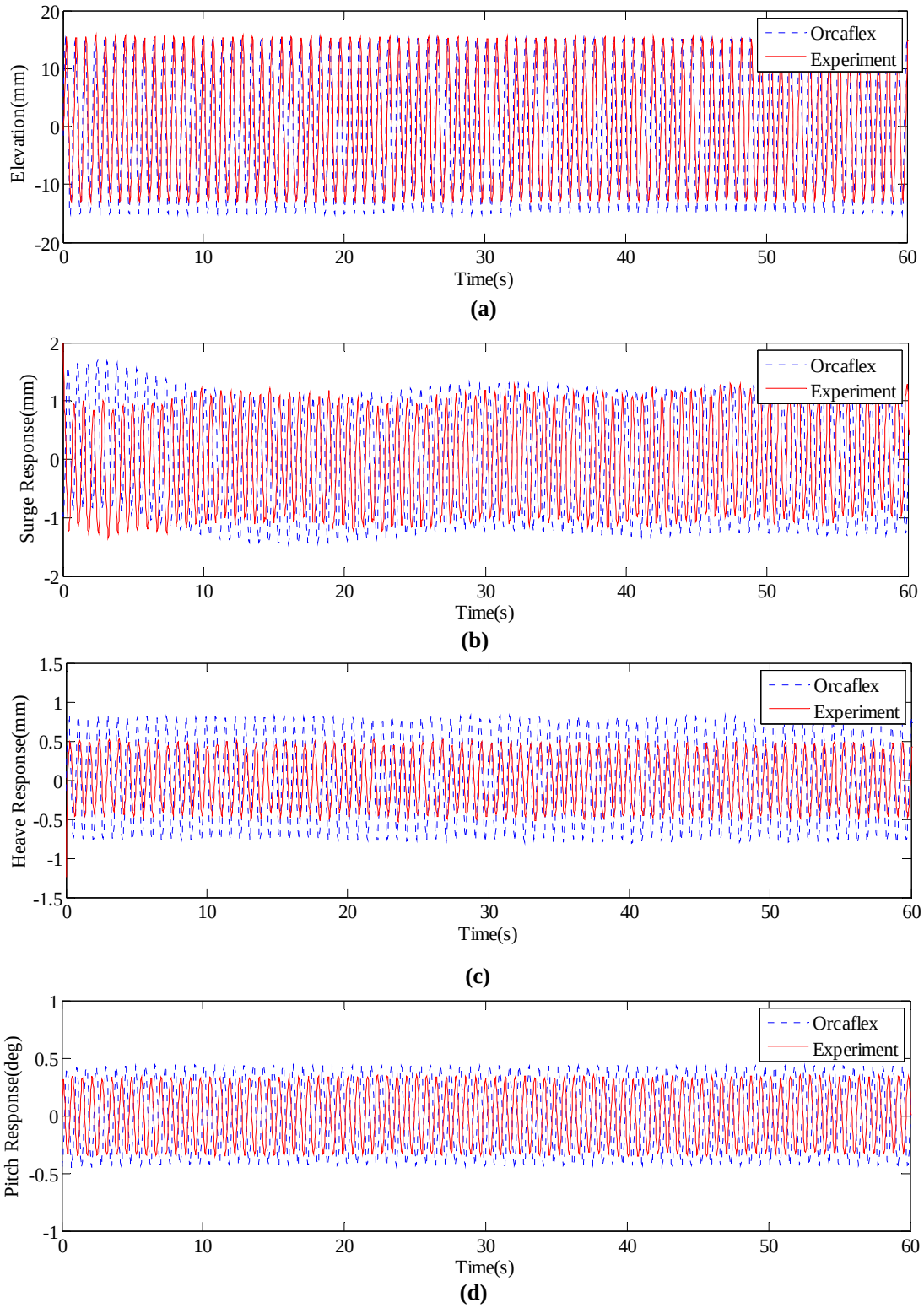

Fig. 4.2 (a) Wave elevation time history for 1 minute duration (regular wave, *H*=30mm, *f*=1.44Hz), (b) Surge response time history, (c) Heave response time history and (d) Pitch response time history. All responses are at C.O.M.

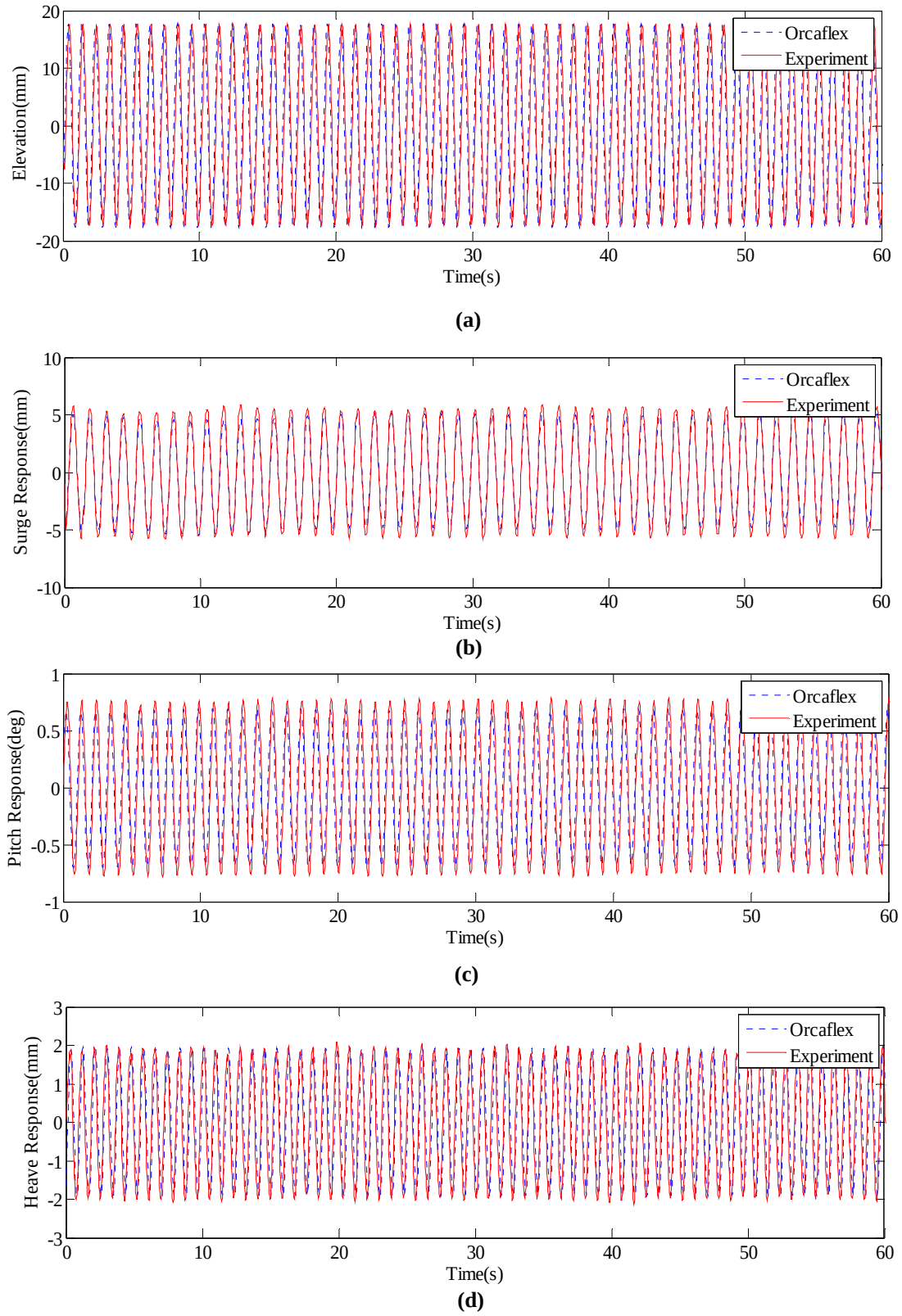

Fig. 4.3 Wave Elevation time history for 1 minute duration (regular wave, *H*=30mm, *f*=1 Hz), (b) Surge Response History, (c) Heave response time history and (d) Pitch response time history. All responses are at C.O.M

Fig. 4.4 to 4.6 show the RAO plots for the surge, heave and pitch motions plotted with scattering parameter, *ka*. These were computed both at the centre of mass and at the nacelle. At model scale, RAOs for pitch response were obtained by normalising the angular displacement on millimetre of incident wave amplitude (refer to equation 2.1, Chapter 2). To interpret the results at full scale, these values must be proportionally scaled by a factor of 100. The RAOs for the linear motions (surge and heave) are unaffected by scaling. The experimentally determined results were found to generally agree with the trend predicted by the numerical model. However, the presence of reflections in the wave tank caused the experimental points to oscillate about the theoretical mean predicted by OrcaFlex. Maximum deviation from the theoretical mean was noted for frequencies between 0.875Hz and 1Hz (corresponding to the range $0.065 < ka < 0.09$). The reflected waves either interacted constructively to amplify the response (points above the numerical curve) or destructively to diminish the response (points below the numerical curve). An earlier study by Payne *et al*.,[120] gives a detailed account on this ripple noise phenomenon. This effect was further exacerbated by low frequency noise that was present in the measured time series for the heave and pitch motions.

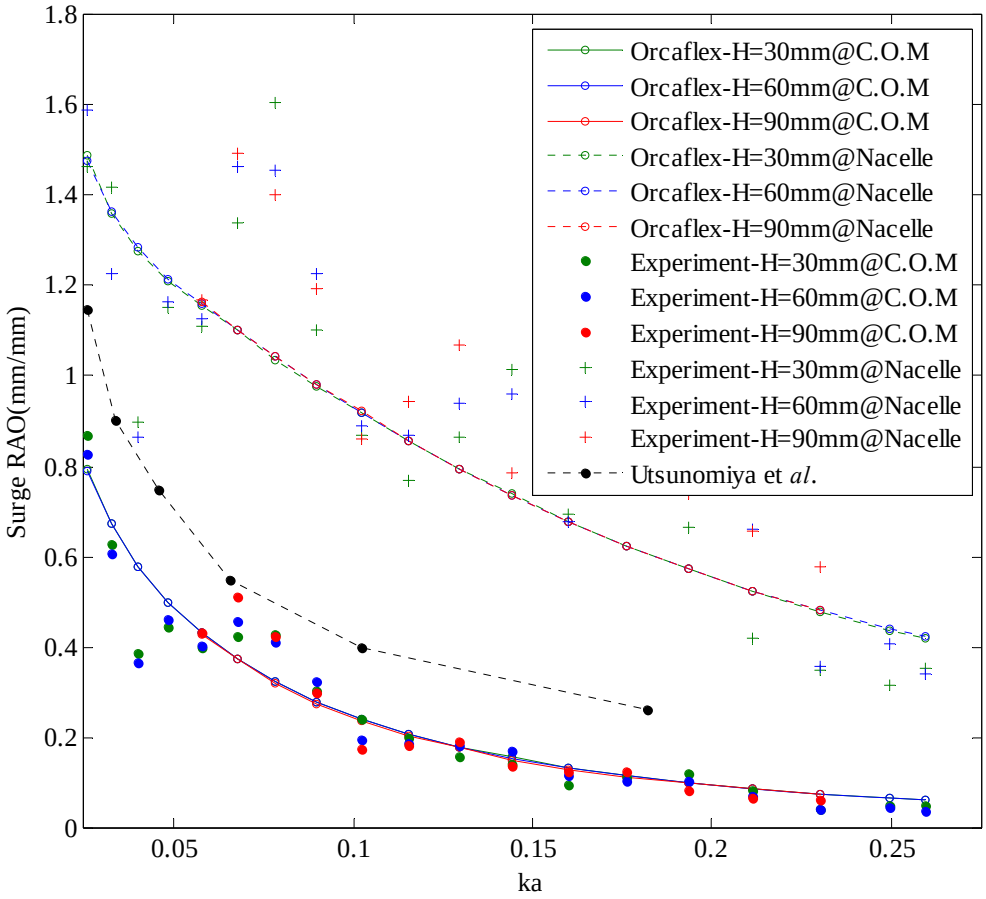

Fig. 4.4 Surge Response amplitude operator for regular waves of height *H*=30mm, 60mm and 90mm.

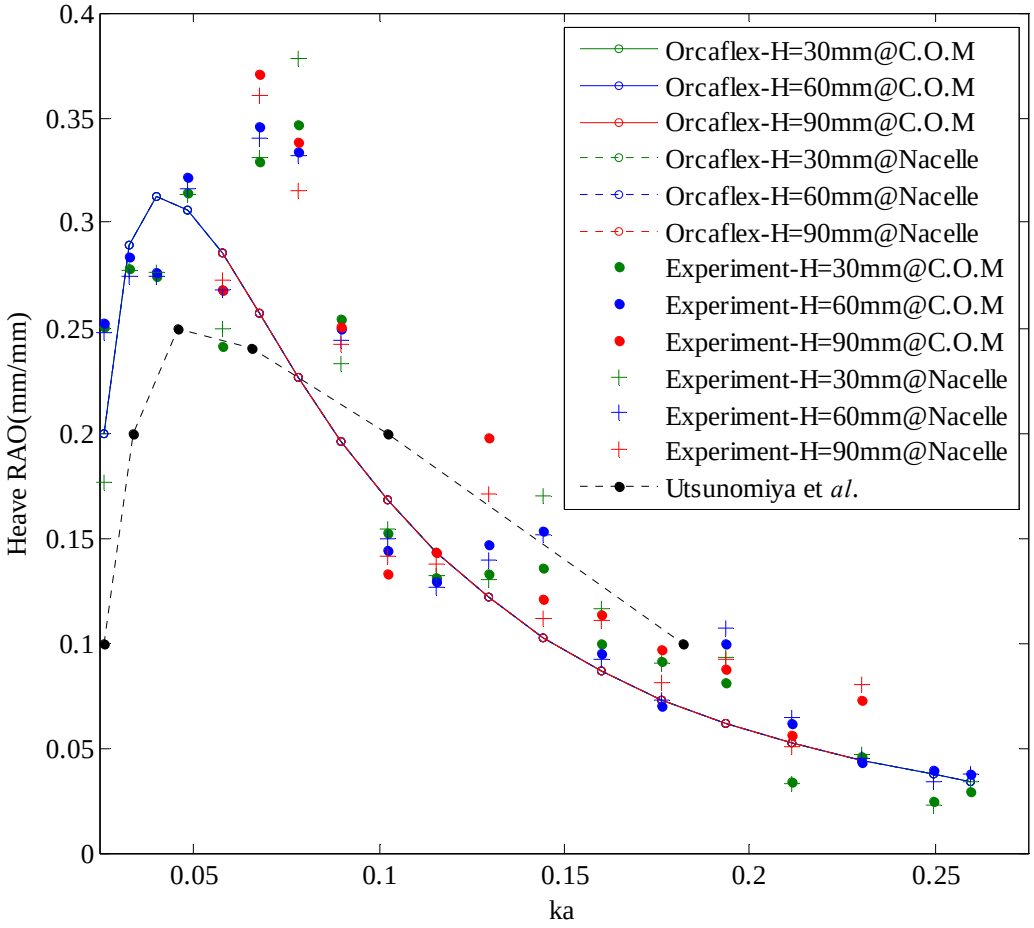

Fig. 4.5 Heave Response amplitude operator for regular waves of height *H*=30mm, 60mm and 90mm.

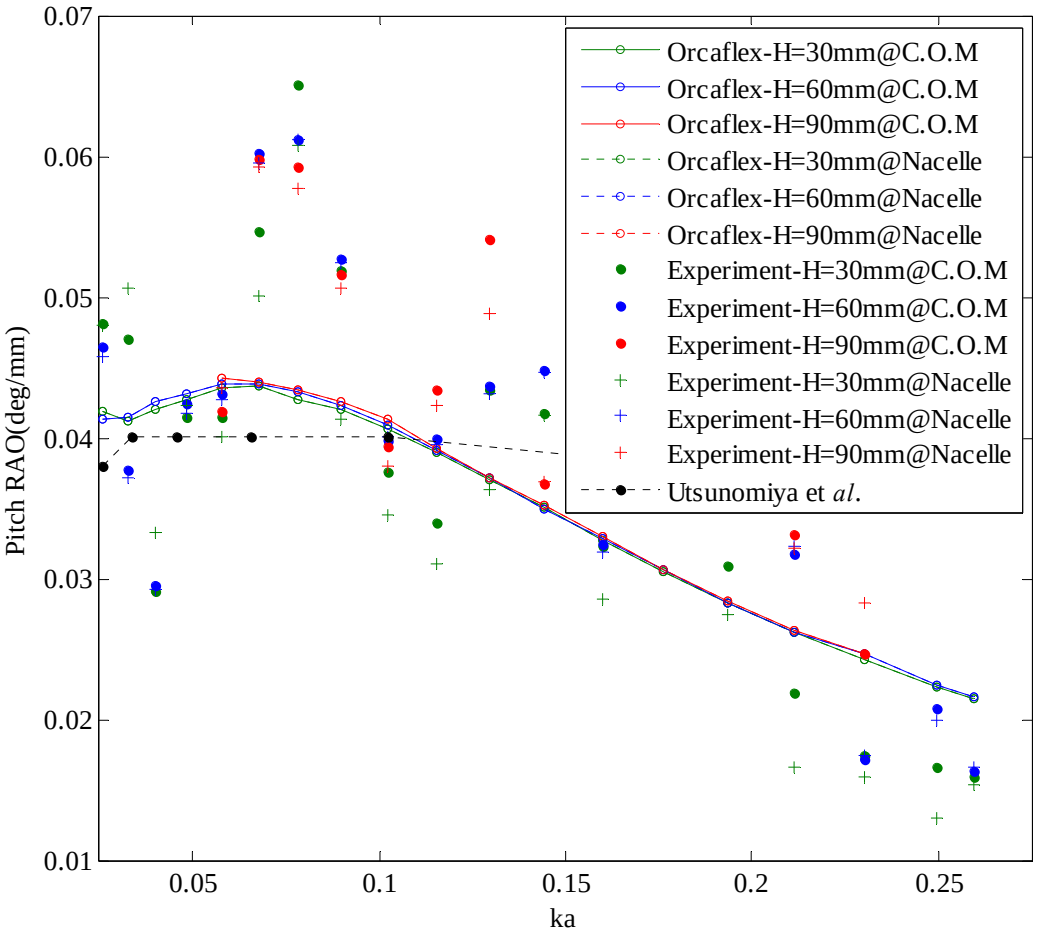

Fig. 4.6 Pitch Response amplitude operator for regular waves of height *H*=30mm, 60mm and 90mm.

In the computations of the response at the nacelle, it was assumed that the tower was structurally rigid and the effect of structural deformation was negligibly small. The validity of the assumption was confirmed by the fact there was no appreciable

change in the pitch motion measured at the nacelle and at the C.O.M. Heave motion was also preserved at the nacelle.

4.1.2. Pitch-coupled surge component- Nacelle Magnification Factor

Significant magnification of surge was observed at the nacelle. Assuming that the spar pitches about the centre of gravity (see Fig. 4.7), the pitch coupled component of surge, denoted by δx is infinitesimal at the centre of mass. This increases as we move away from C.O.M towards the nacelle. This scaling effect is illustrated in the Fig. 4.7

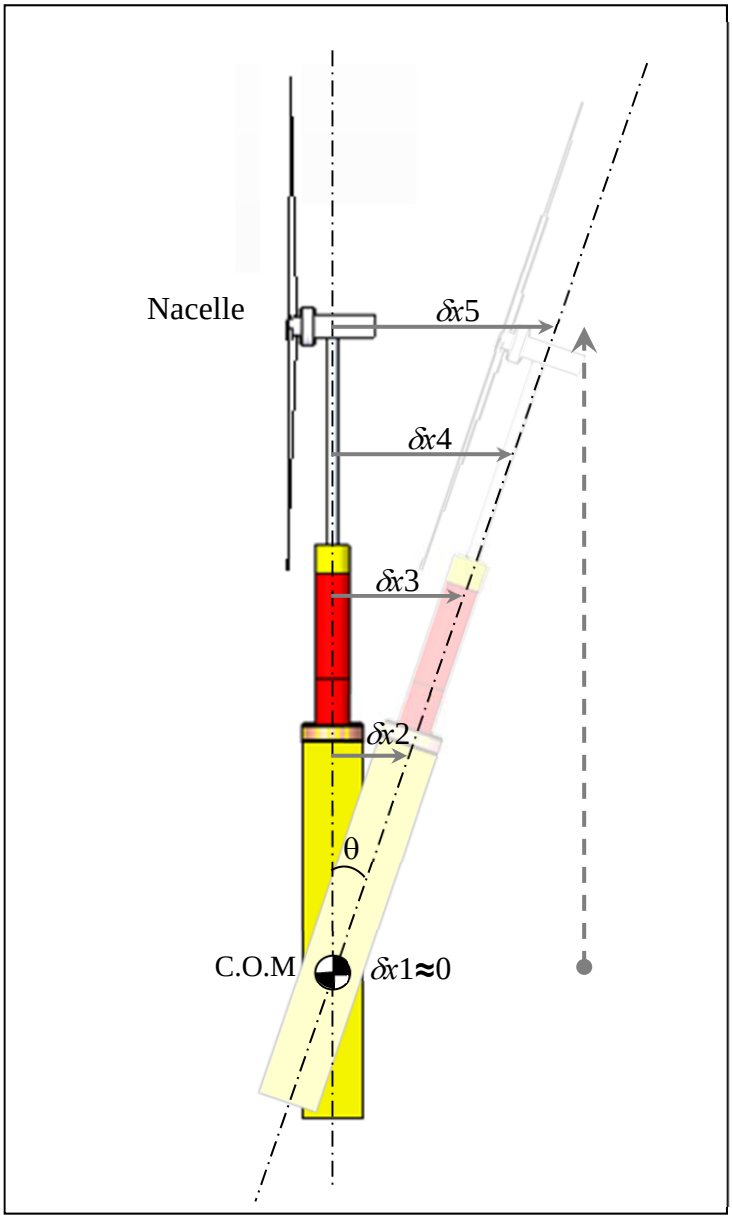

Fig. 4.7 Dynamic scaling effect of pitch coupled surge response.

The percentage contribution of this pitch coupled component, δx depends on the frequency of the exciting wave and the damping mechanics of the system. To understand the surge behaviour at nacelle, a term "*Nacelle magnification factor*", *NMF* is defined as the ratio of the response amplitude operator at nacelle to the response amplitude operator at the C.O.M. The magnification factor for any given frequency can be calculated using

$$NMF(\omega) = \frac{RAO(\omega)_{NACELLE}}{RAO(\omega)_{C.O.M}} \tag{4.1}$$

The coupling effect of pitch motion resulted in a significant increase in surge response at the nacelle with *NMF*s in the range 1.5-8.5. The coupling effect also made the dispersive distribution of the experimental points more pronounced at the nacelle. The average pitch coupled component of surge motion, δx (computed as the difference between the surge RAOs at the nacelle and C.O.M.) was 0.64 and 0.59 for the experimental and numerical models respectively. The dotted line in Fig. 4.8, shows the numerically computed surge response at the nacelle assuming a steady pitch component with negligible damping (a value of 8 was assumed to be the magnification factor). However, the inherent pitch damping at lower frequencies minimises this coupling effect and hence closes the gap between C.O.M values and that of the nacelle. The response for the heave and pitch motions were preserved at the nacelle, giving the *NMF* close to unity. It is believed that the knowledge of nacelle magnification factor for a given floater configuration will be useful to understand the overall behaviour and help decide the hub height that ensures lowest nacelle displacement.

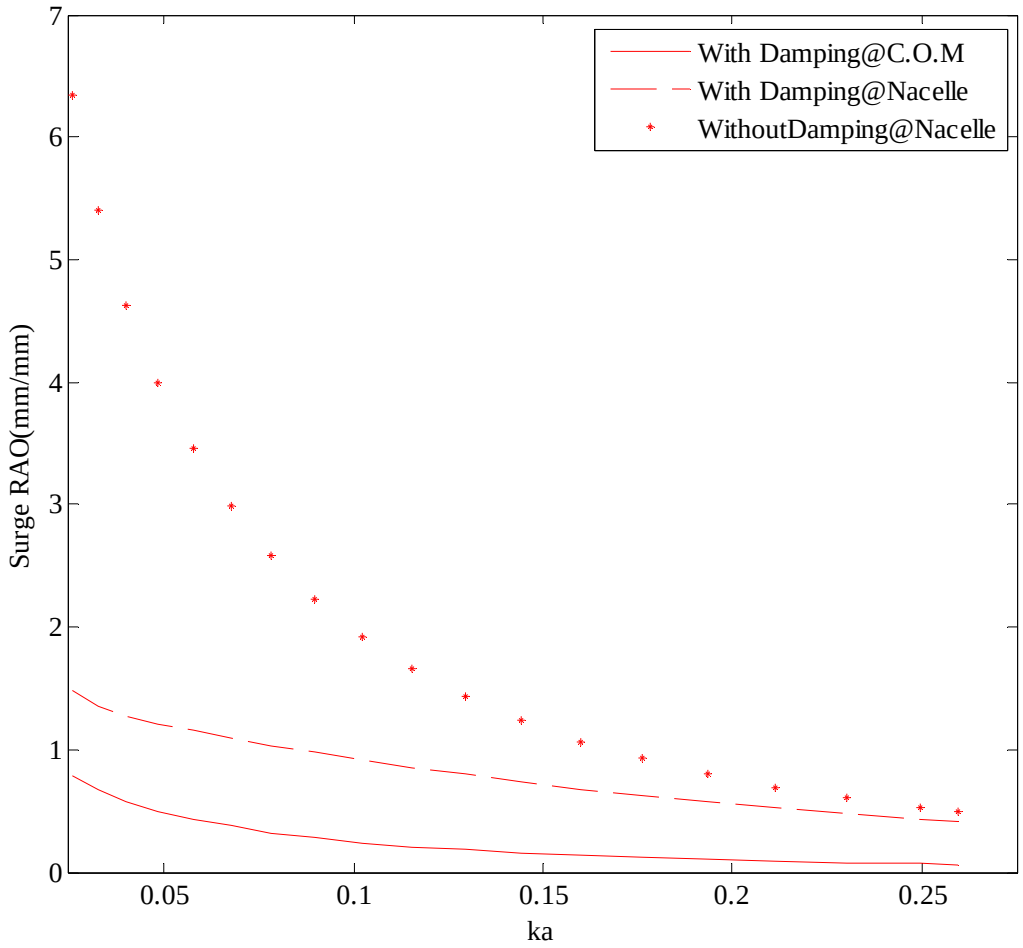

Fig. 4.8 Surge response with and without damping of pitch induced surge motion (computed numerically from OrcaFlex simulations)

Testing for the remaining two wave heights (i.e., 60 mm and 90 mm) confirmed the behaviour observed in 30 mm seas. In order to inspect the accuracy of the present results with literature, a comparison was made with the results computed at the C.O.M for a similar configuration previously studied by Utsunomiya *et al*.,[36]. The RAOs for surge, heave and pitch motions corresponding to 30 mm wave heights were extrapolated from Utsunomiya *et al.,*[36] and re-interpreted as a function of scattering parameter, *ka* and superimposed in Figures 4.4, 4.5 & 4.6. The pitch RAOs were suitably scaled for consistency with units used in this study. A closer inspection of results from the two studies was useful in making a few interesting observations. Results reported in the present study confirmed the lower dynamic heave and pitch motions as was predicted by Utsunomiya *et al*.,[36]. However, the surge response computed in this study was noticeably lower. Although a lower centre of gravity

could be one of the reasons, the damping effects from the four-point mooring configuration cannot be disregarded. The surge RAO plot for C.O.M was concave-up and lower than unity in the low frequency region. This may be attributed to the 4-point mooring system that introduces appreciable damping. Discarding the spurious peaks ($0.0675 < ka < 0.9$) in the experimental points obtained in this study, the RAO plots for the heave motion followed the standard shape (i.e. an upward sloping trend up to a certain peak at 0.6875Hz, $ka = 0.046$ and downward sloping trend beyond this point). The heave response curve predicted in this study was more right-skewed with comparatively higher response for the frequencies below 0.875Hz ($ka = 0.078$) and lower response for subsequent frequencies. The response was below the 0.5 mark in both the cases for the range of frequencies considered. Pitch response also showed a downward sloping trend unlike a flatter curve reported by Utsunomiya *et al*., [36]. This clearly demonstrates the need to include the non-linearities and dynamic uncertainties introduced by the mooring.

4.1.3. Wave elevation profiles and motion response for irregular waves

For the tests with more realistic wave conditions, waves in both the experiment and simulation were based on a target JONSWAP spectrum. Three sets of irregular wave tests were used for validating the OrcaFlex model consisting of a significant wave height of 30mm, 60mm and 90mm with peak-spectral frequencies between 0.6-1.6Hz. The irregular wave elevations measured during the experiments were used as input to the numerical time domain model in OrcaFlex. The motion responses measured from the experiments and numerical simulation were processed to compute the response spectrum.

A close match was observed between wave elevation time histories (Fig. 4.9) and wave spectra (Fig. 4.10) computed from the experiment and the numerical model. This showed that the numerical model accurately reproduced experimental testing conditions. Therefore the accuracy of the numerically generated and measured waves is not expected to affect the comparison between the experimental data and numerical results.

The time response of motions in irregular waves predicted by OrcaFlex was found to generally agree with the model response in experiments except for the period between 65-80 seconds where erroneous peaks were observed in the OrcaFlex simulations (Fig.4.11).

Figures 4.12-4.17 show the response amplitude operators computed for irregular waves for significant wave height (H_{m0}) of 30 mm. Testing for different peak frequencies in irregular waves showed consistency in response for the majority of the wave frequencies, except in the low frequency region (ka < 0.0675) where poor reproduction of waves resulted in large variations and spurious peaks in the experimental points. The differences were considerably larger for peak spectral frequencies above 0.8Hz. Since the wave field model in OrcaFlex was based on the measured wave spectrum, the numerical model also exhibited this low frequency anomaly. The oscillating pattern in experimental points was found to recur and was more evident for pitch motion. The RAOs computed for regular waves of similar wave height (H = 30 mm) were superimposed on the Figures 4.12-4.17 (denoted by black dots and line) for comparison. A careful look at the plots indicates that the experimental and numerical results for irregular seas were consistent with the trend predicted for regular seas for majority of frequencies that were tested (ka > 0.0675). Similar trend was noted for significant wave heights of 60 mm and 90 mm. For these wave heights, for the purpose of comparison with regular waves, the range was limited to 0.7Hz-1.3Hz and the results are presented in Figures 4.18-4.29. The motion response RAOs in 60mm and 90mm wave heights were observed to be very similar to 30 mm waves. It may however be noted from the RAO results that the oscillating pattern in experimental points for pitch response(that were originally present for 30mm wave height) become less prominent at greater wave heights. The maximum values for the surge and pitch RAO were consistent with those predicted at 30mm wave height implying the consistency in the performance. For the purpose of discussions, the motion responses for 30mm wave height are explored further in detail in the following sections.

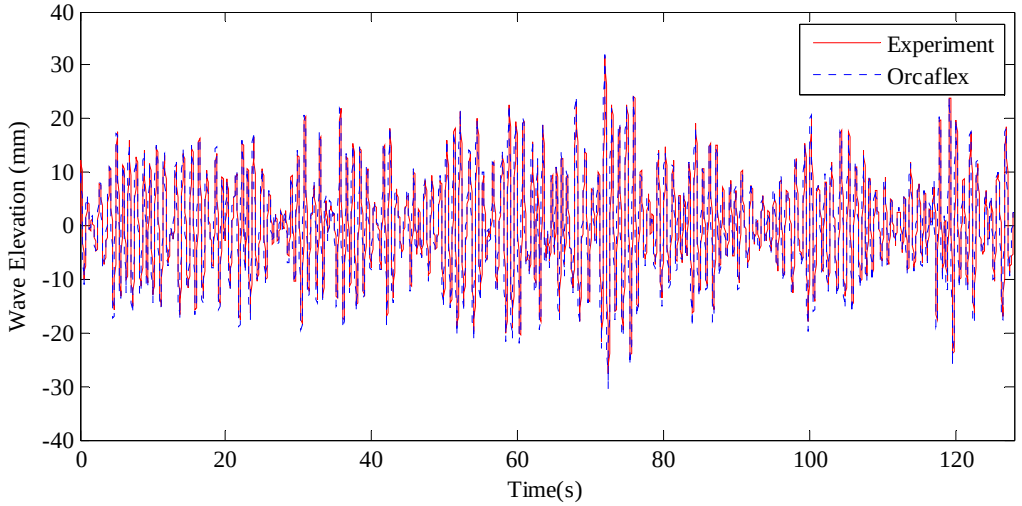

Fig. 4.9 Wave elevation time history for a duration of 128sec(irregular wave, H_{m0}= 30mm and f_p=0.8Hz).

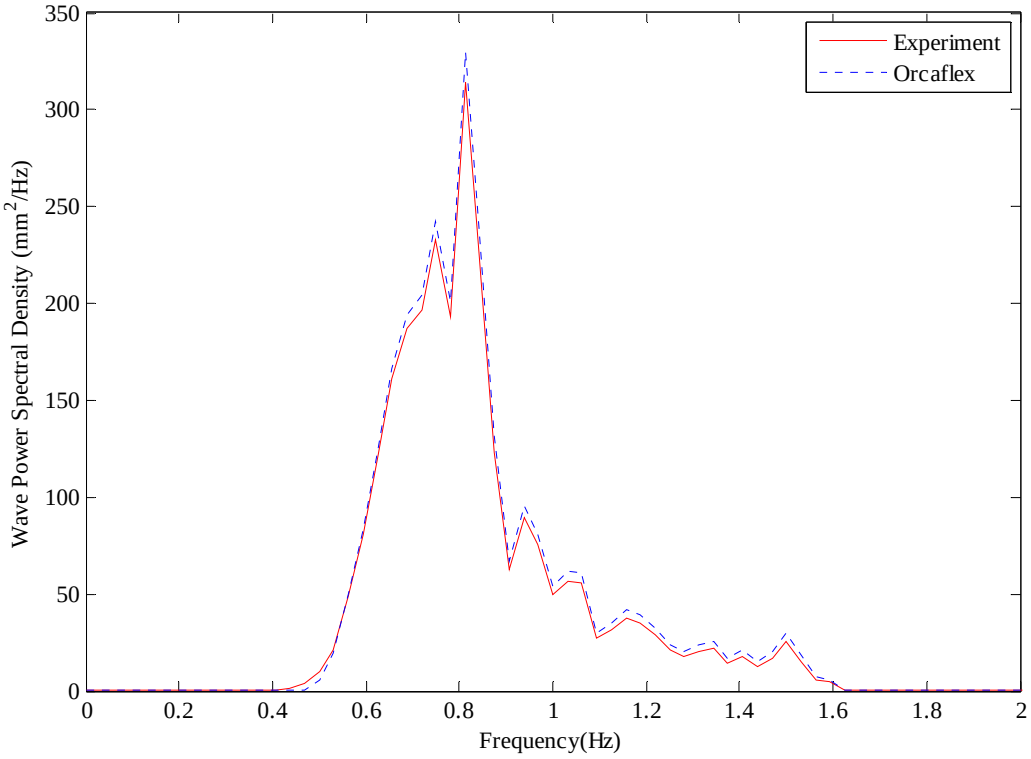

Fig. 4.10 Wave spectrum computed from experimental measurements and OrcaFlex simulations(irregular wave, H_{m0}= 30mm and f_p=0.8Hz)

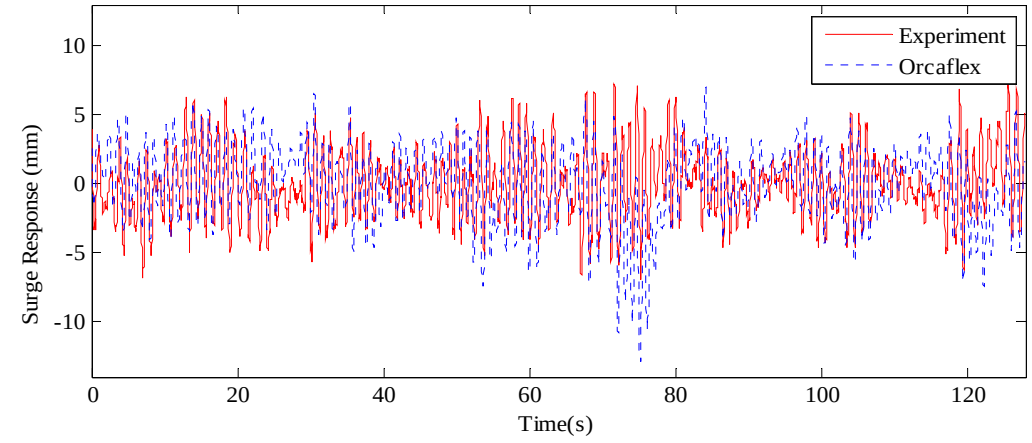

(a)

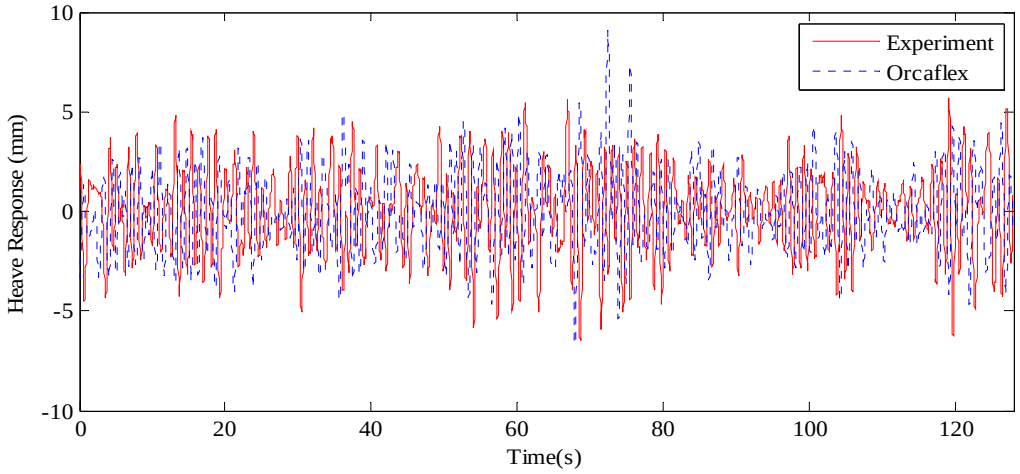

(b)

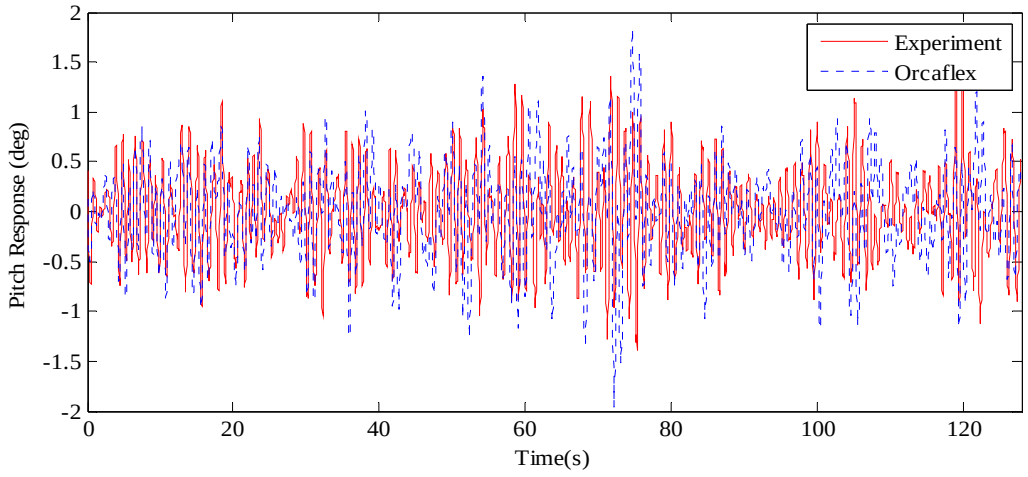

(c)

Fig. 4.11 (a) Surge response time history (b) Heave response time history (c) Pitch response time history. All response time histories were recorded at the C.O.M for duration =128sec (irregular wave based on JONSWAP spectrum, H_{m0}=30mm and f_p=0.8Hz).

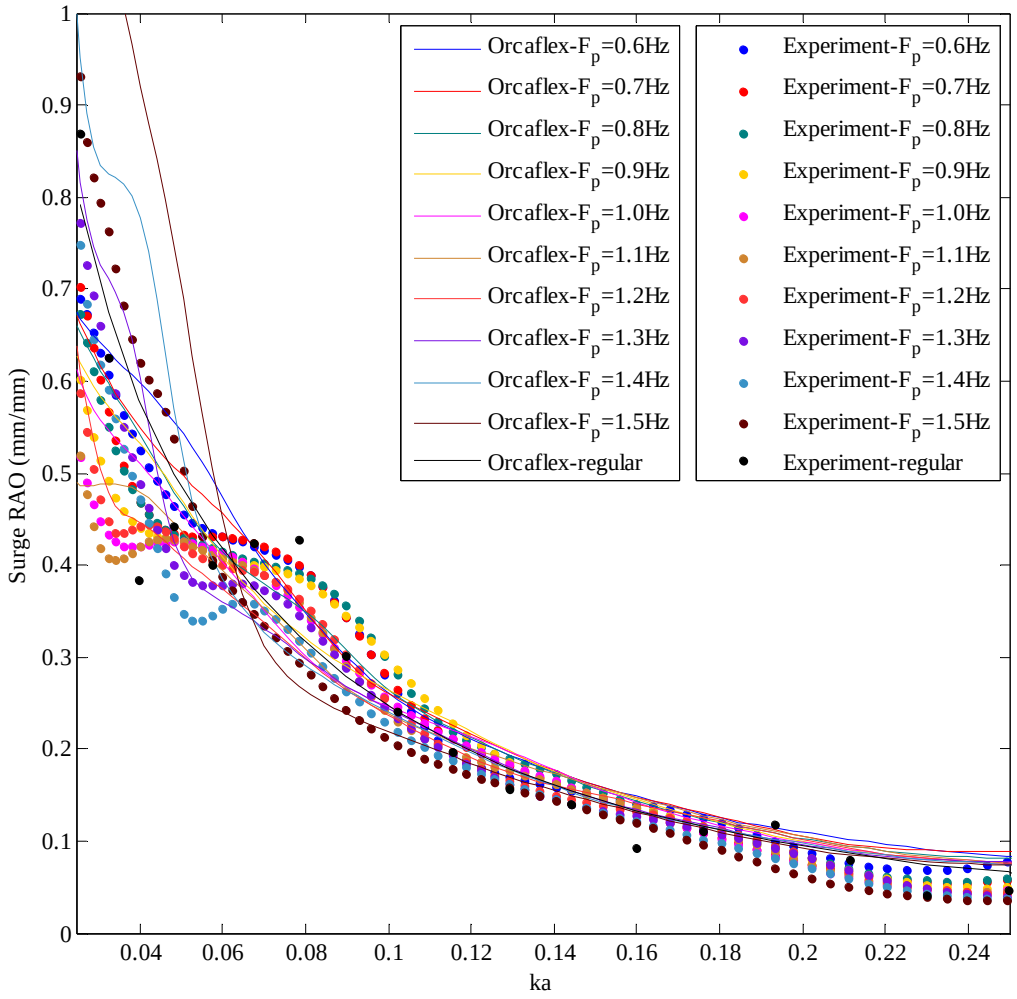

Fig. 4.12 Surge Response Amplitude Operator computed at the C.O.M for irregular waves defined by JONSWAP spectrum, H_{m0}=30mm.

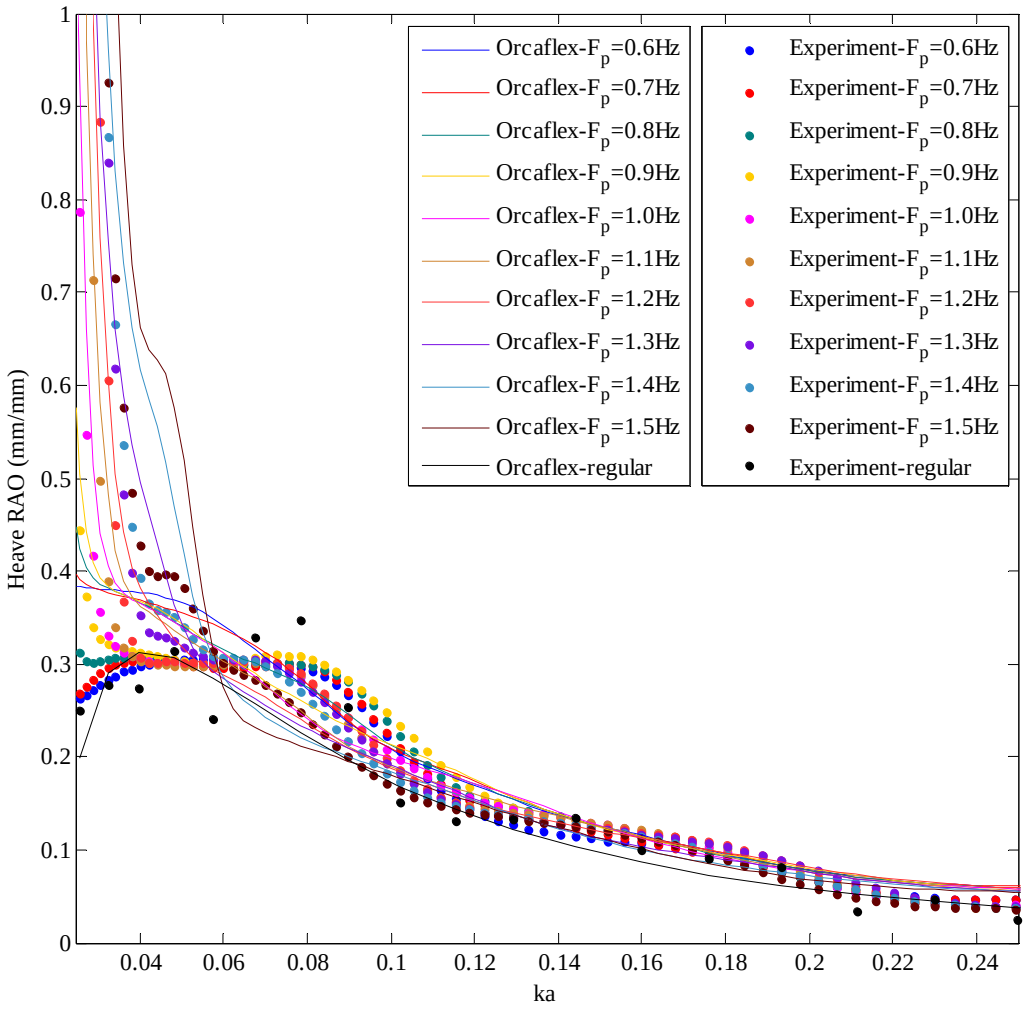

Fig. 4.13 Heave Response Amplitude Operator computed at the C.O.M for irregular waves defined by JONSWAP spectrum, H_{m0}=30mm.

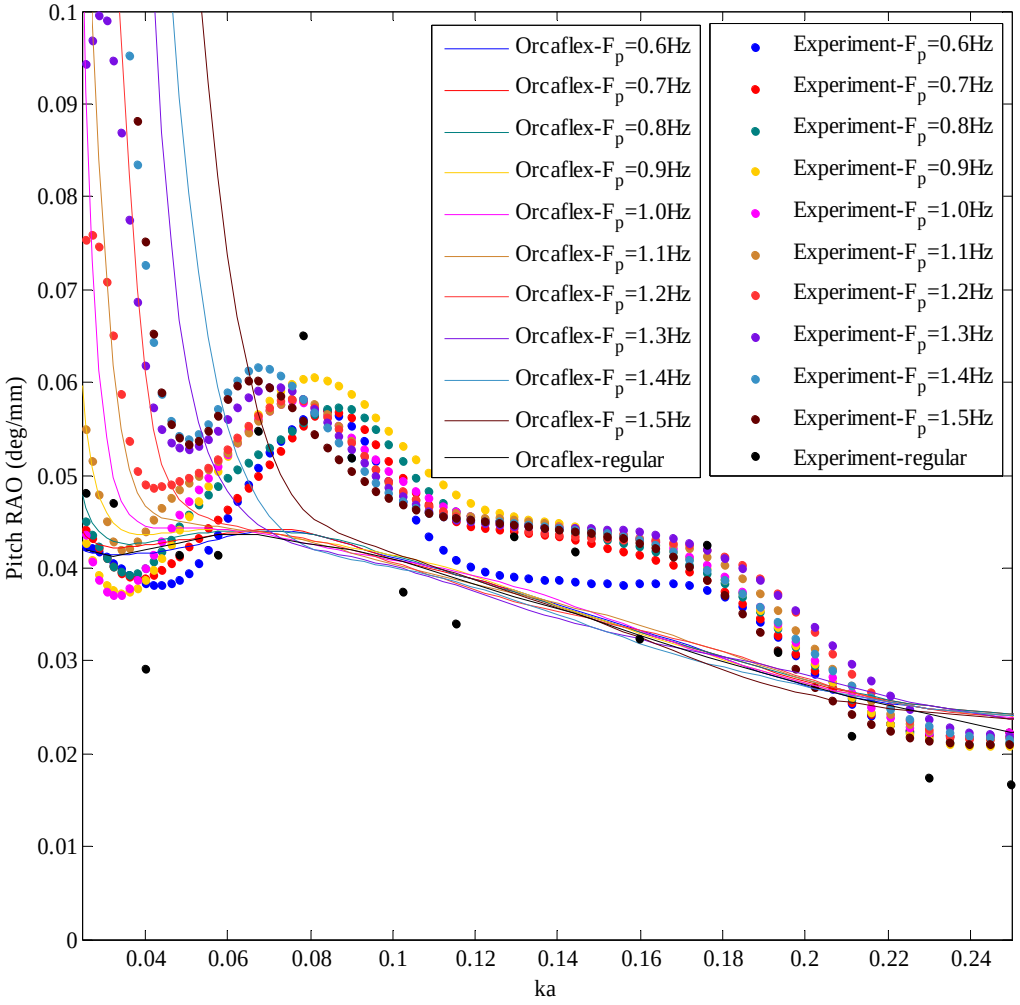

Fig. 4.14 Pitch Response Amplitude Operator computed at the C.O.M for irregular waves defined by JONSWAP spectrum, Hm0=30mm.

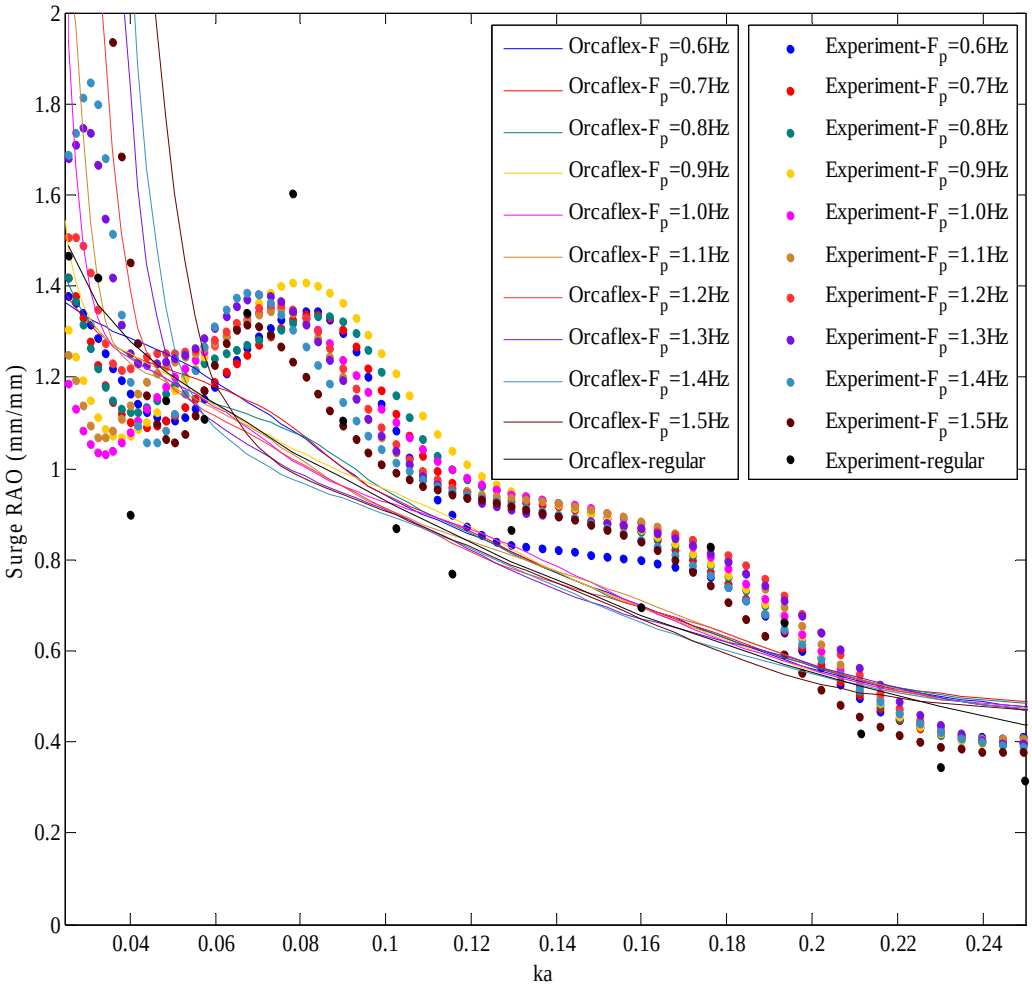

Fig. 4.15 Surge Response Amplitude Operator computed at the nacelle for irregular waves defined by JONSWAP spectrum, Hm0=30mm.

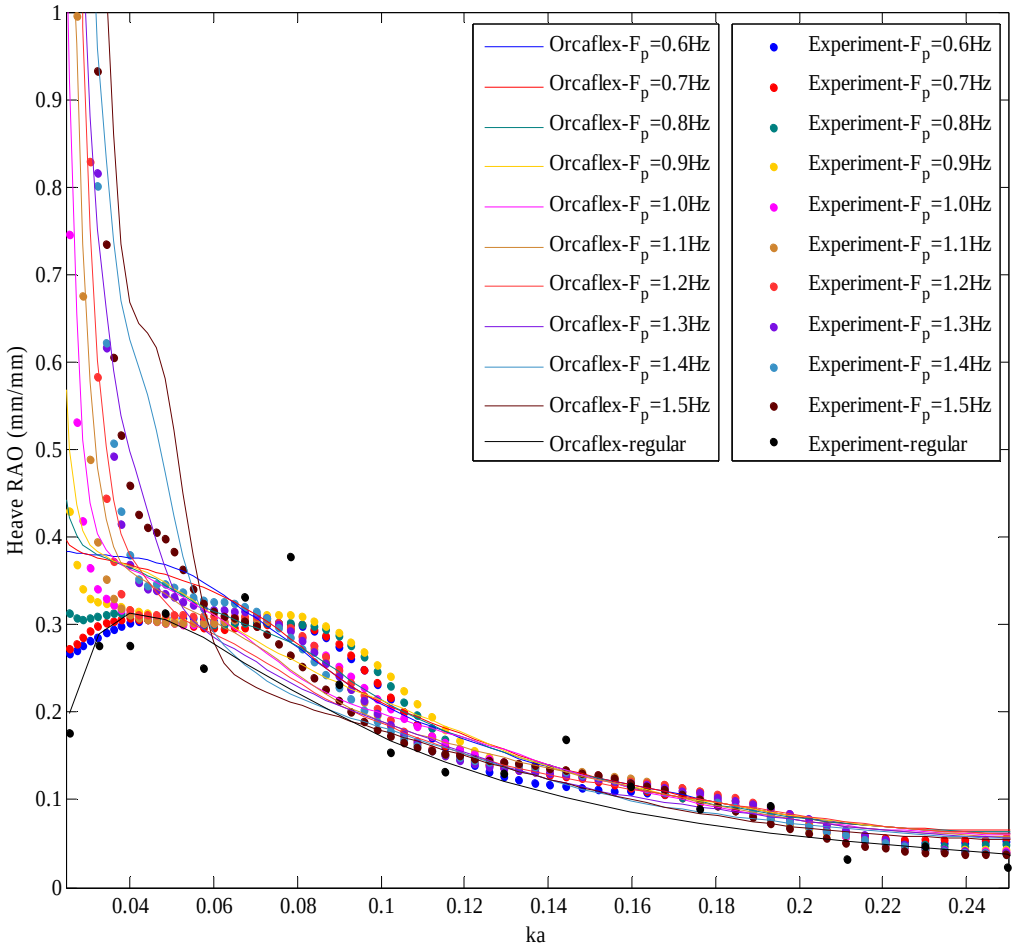

Fig. 4.16 Heave Response Amplitude Operator computed at the nacelle for irregular waves defined by JONSWAP spectrum, H_{m0}=30mm.

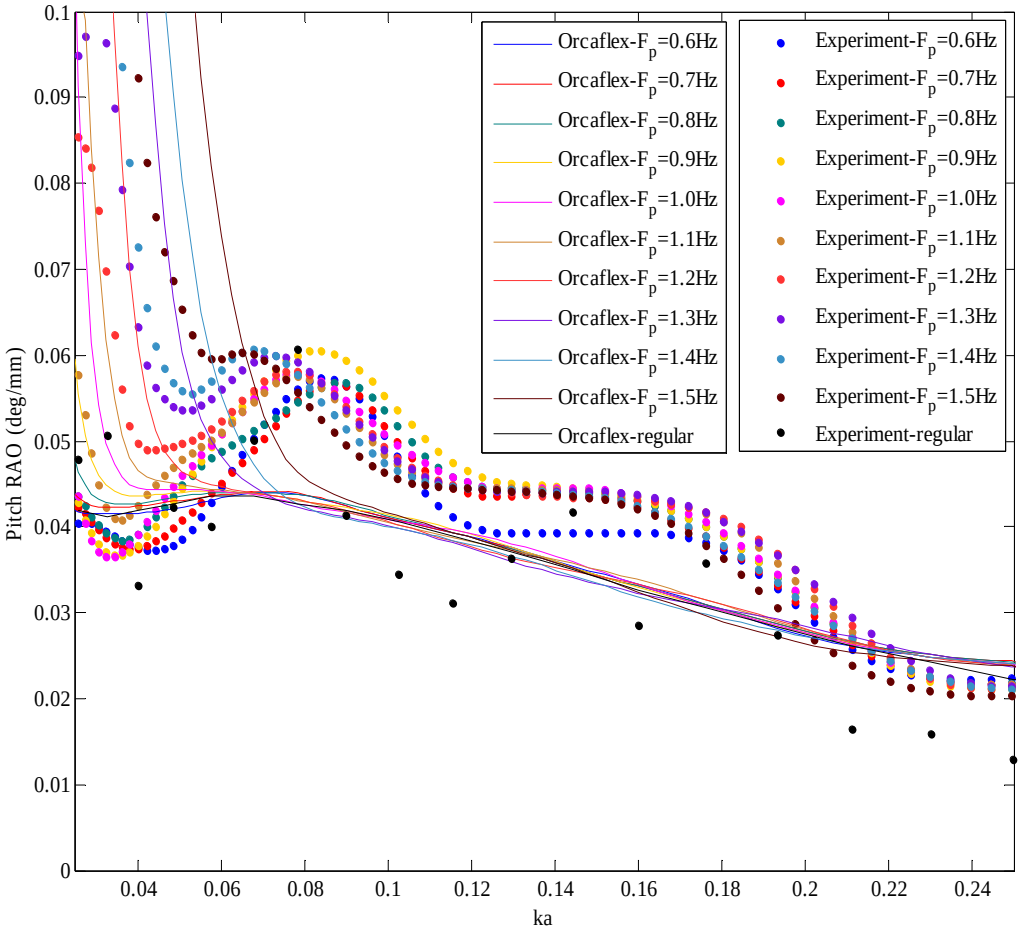

Fig. 4.17 Pitch Response Amplitude Operator computed at the nacelle for irregular waves defined by JONSWAP spectrum, H_{m0}=30mm.

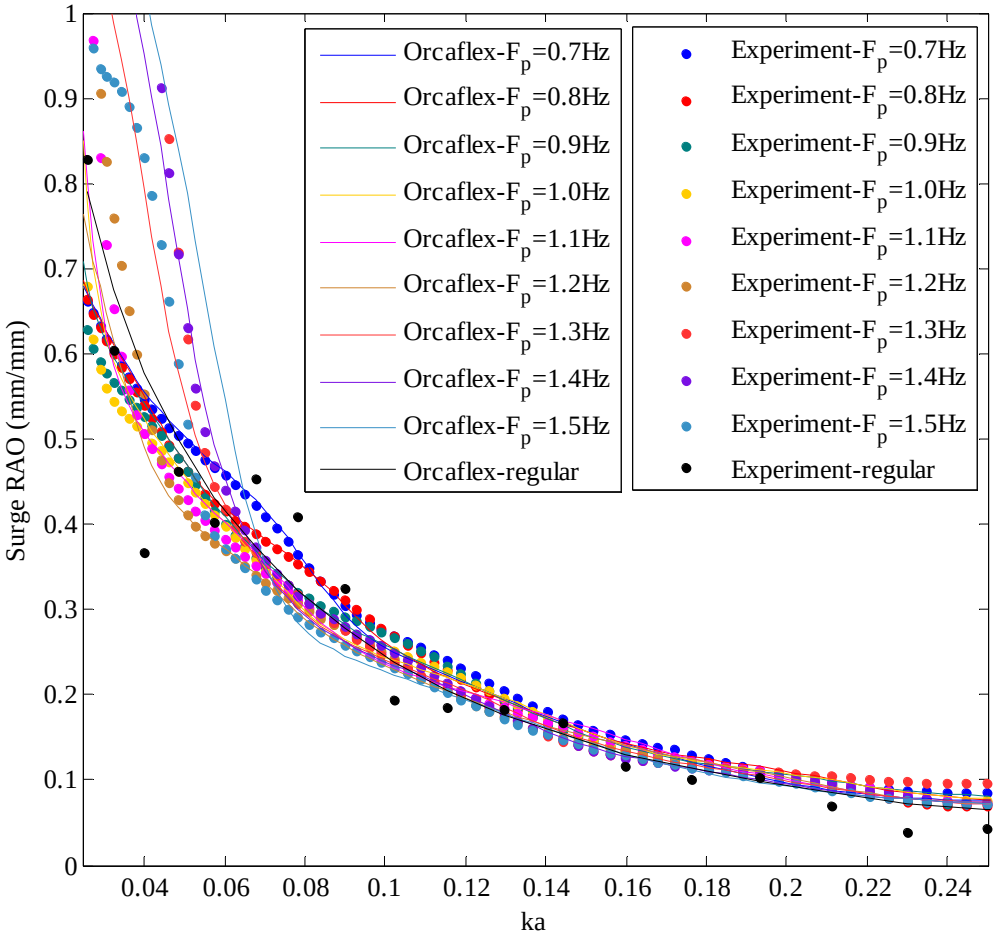

Fig. 4.18 Surge Response Amplitude Operator computed at the C.O.M for irregular waves defined by JONSWAP spectrum, H_{m0}=60mm.

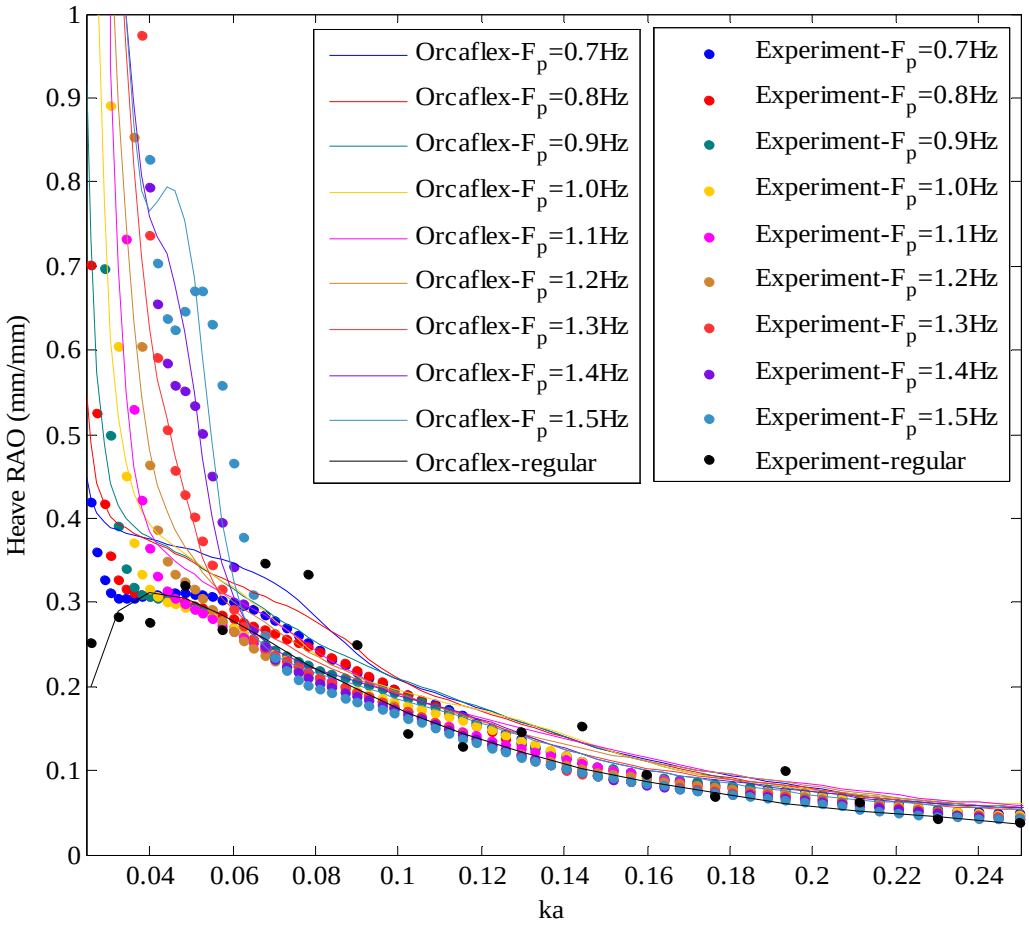

Fig. 4.19 Heave Response Amplitude Operator computed at the C.O.M for irregular waves defined by JONSWAP spectrum, H_{m0}=60mm.

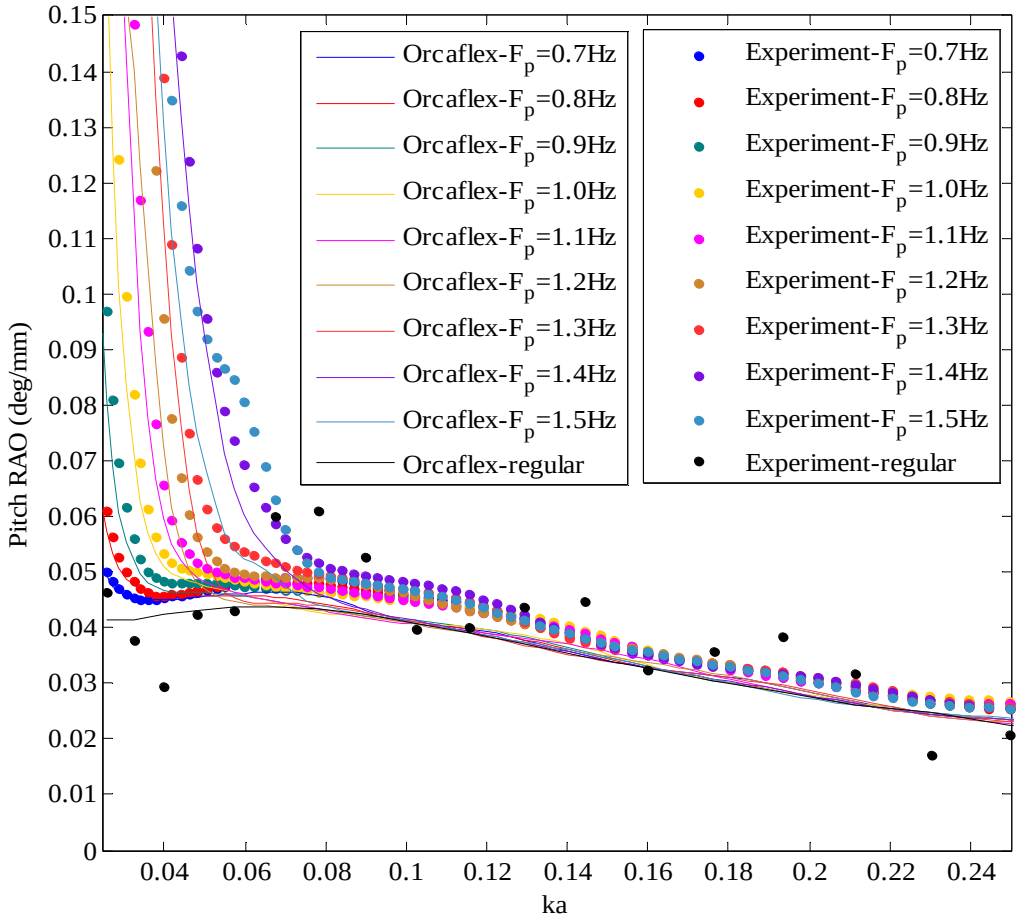

Fig. 4.20 Pitch Response Amplitude Operator computed at the C.O.M for irregular waves defined by JONSWAP spectrum, H_{m0}=60mm.

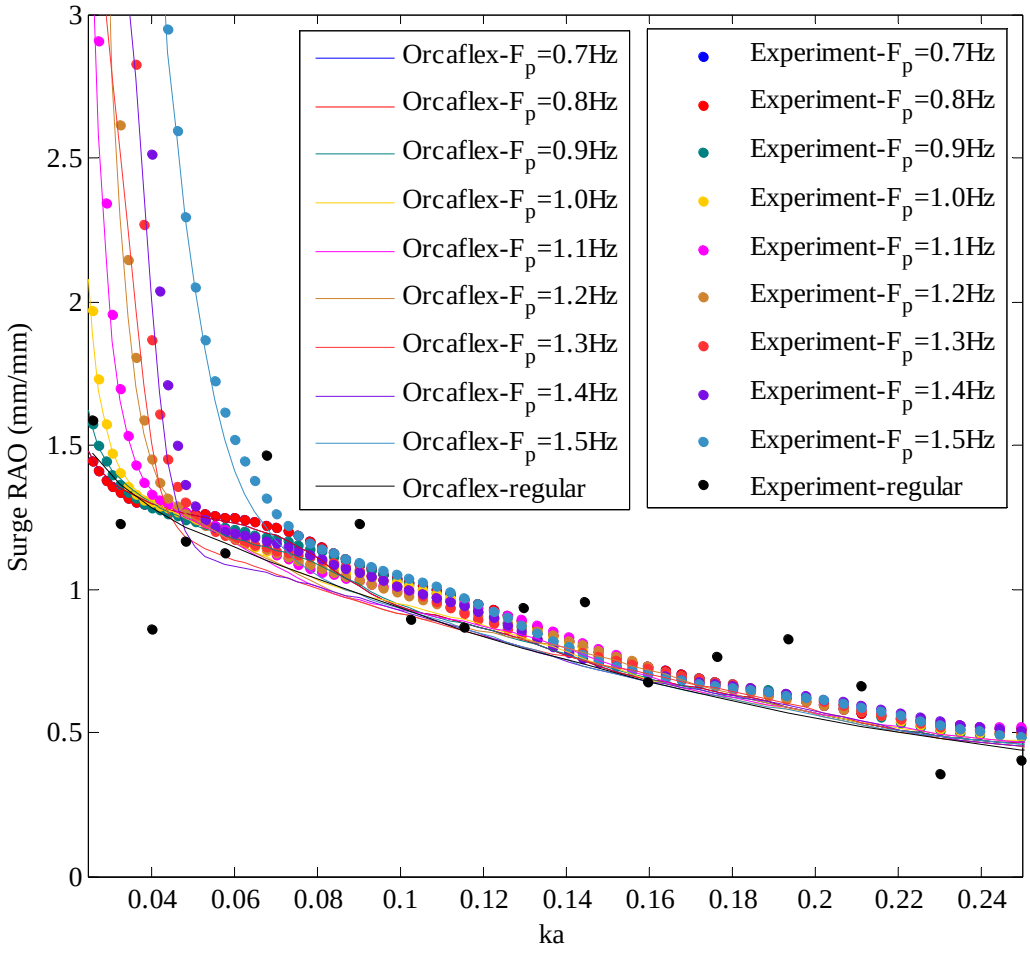

Fig. 4.21 Surge Response Amplitude Operator computed at the nacelle for irregular waves defined by JONSWAP spectrum, H_{m0}=60mm.

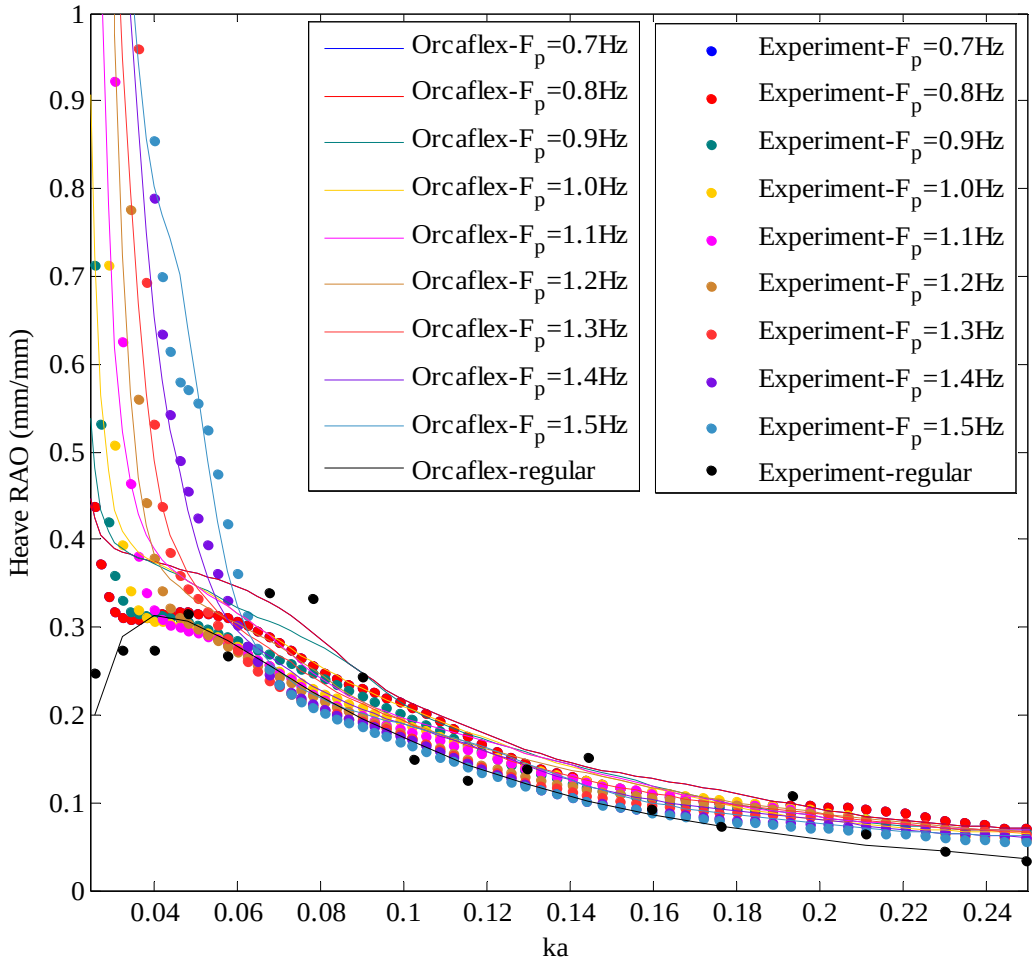

Fig. 4.22 Heave Response Amplitude Operator computed at the nacelle for irregular waves defined by JONSWAP spectrum, H_{m0}=60mm.

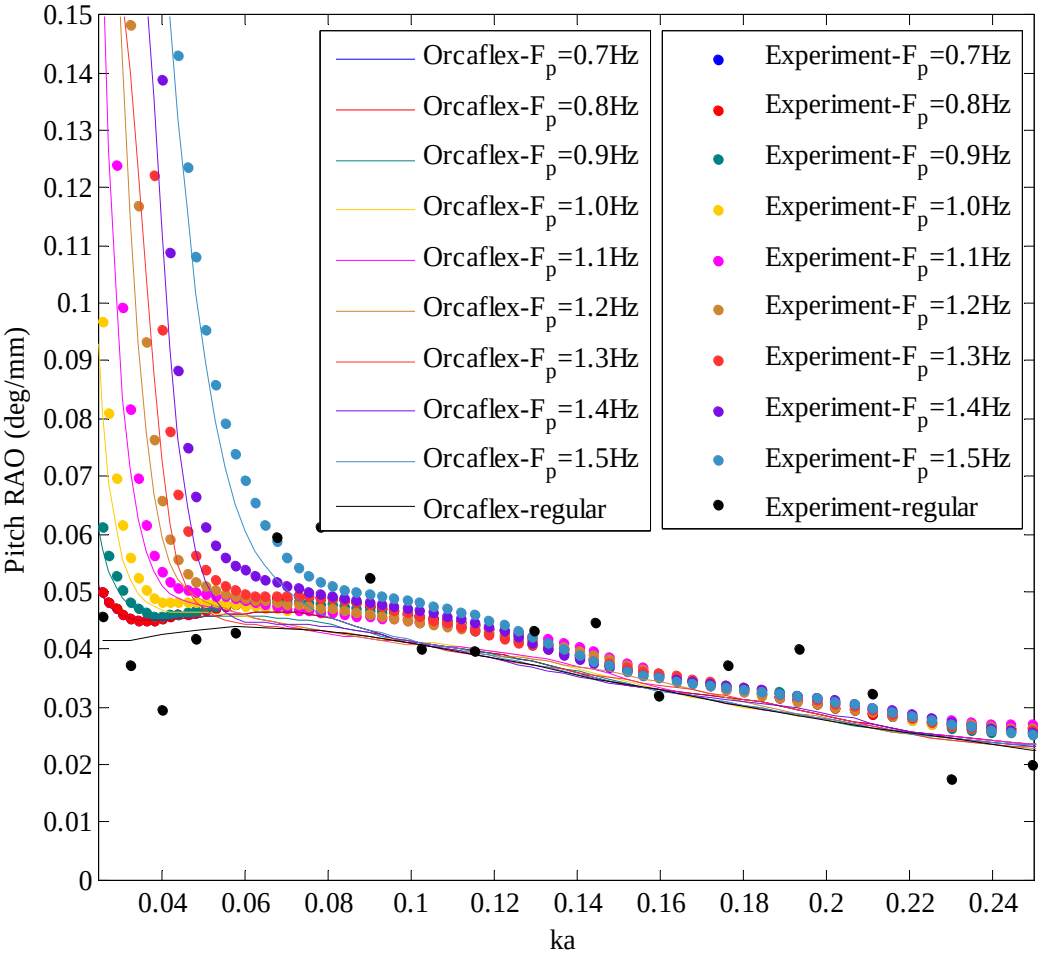

Fig. 4.23 Pitch Response Amplitude Operator computed at the nacelle for irregular waves defined by JONSWAP spectrum, H_{m0}=60mm.

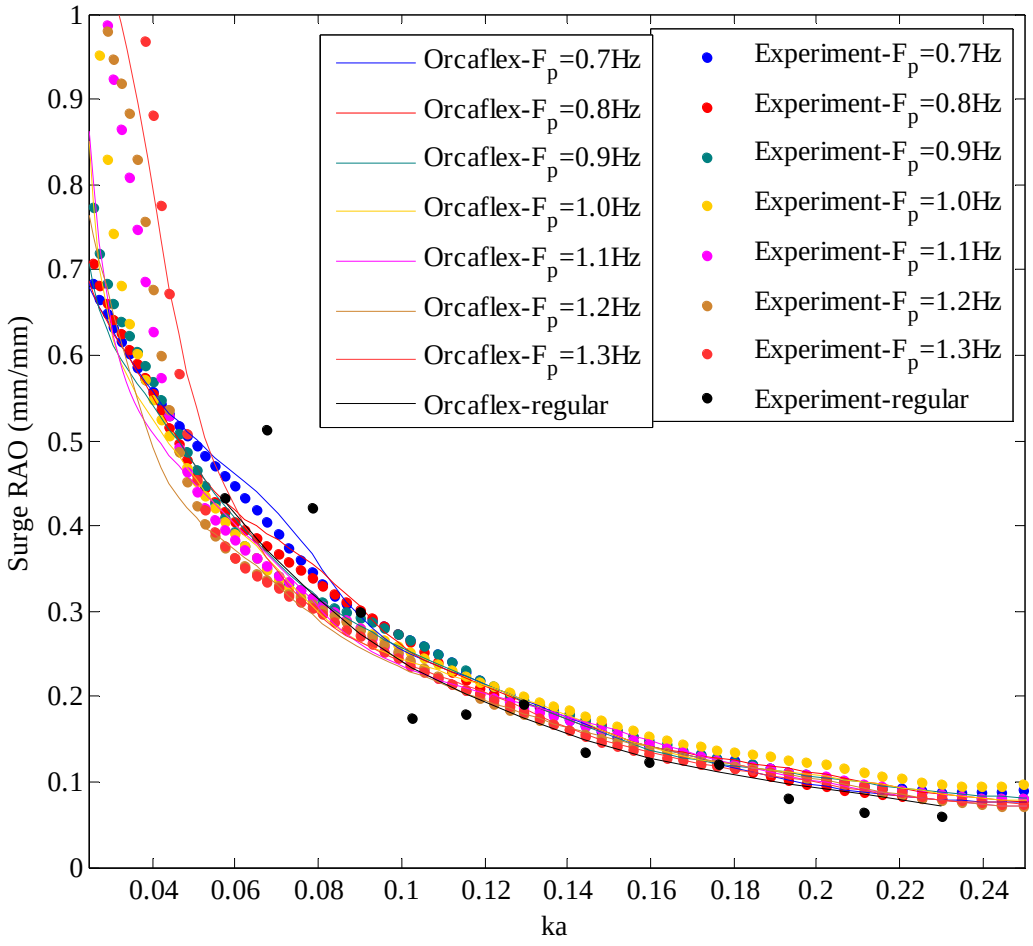

Fig. 4.24 Surge Response Amplitude Operator computed at the C.O.M for irregular waves defined by JONSWAP spectrum, H_{m0}=90mm.

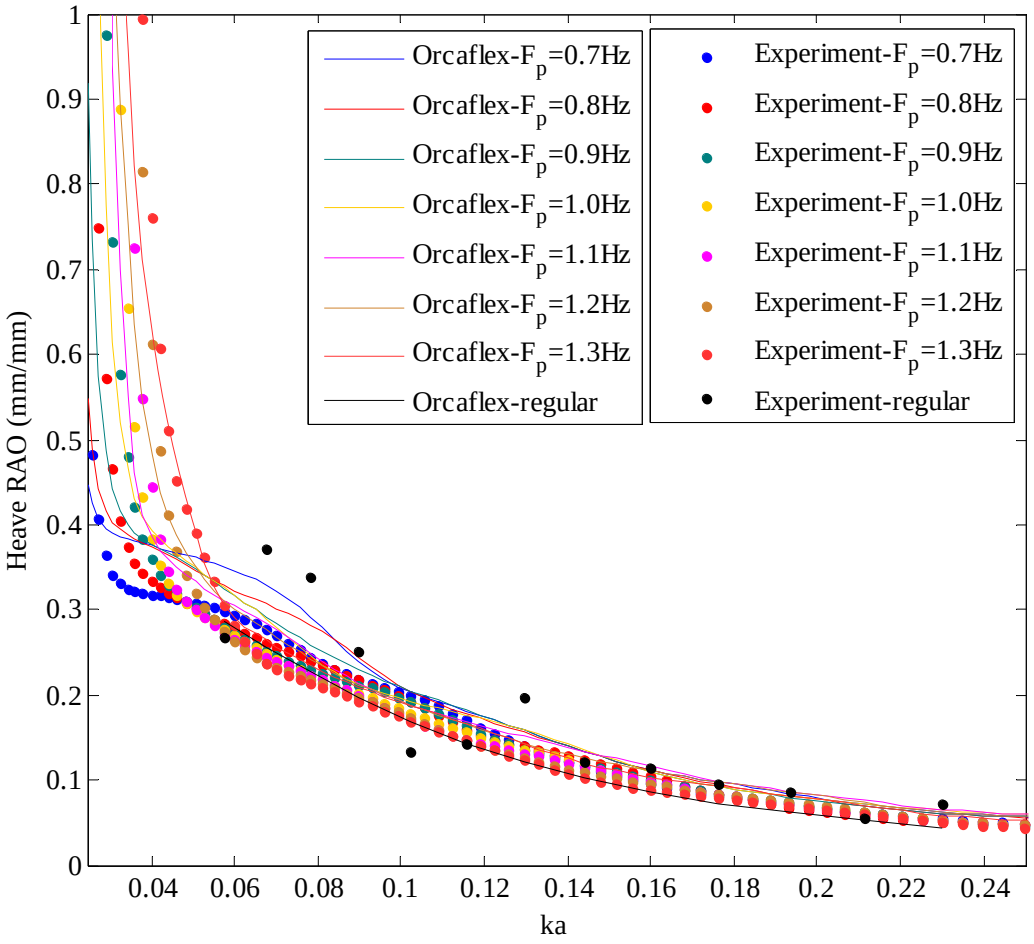

Fig. 4.25 Heave Response Amplitude Operator computed at the C.O.M for irregular waves defined by JONSWAP spectrum, H_{m0}=90mm.

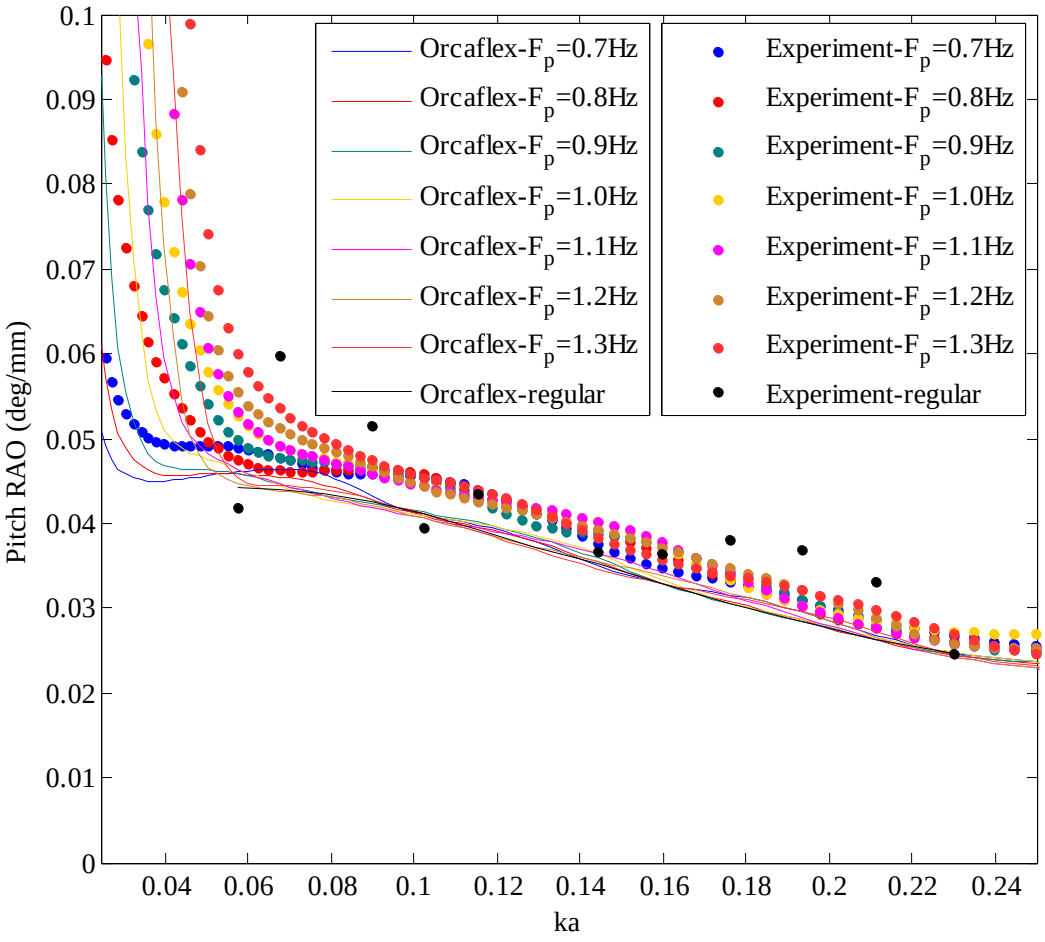

Fig. 4.26 Pitch Response Amplitude Operator computed at the C.O.M for irregular waves defined by JONSWAP spectrum, H_{m0}=90mm.

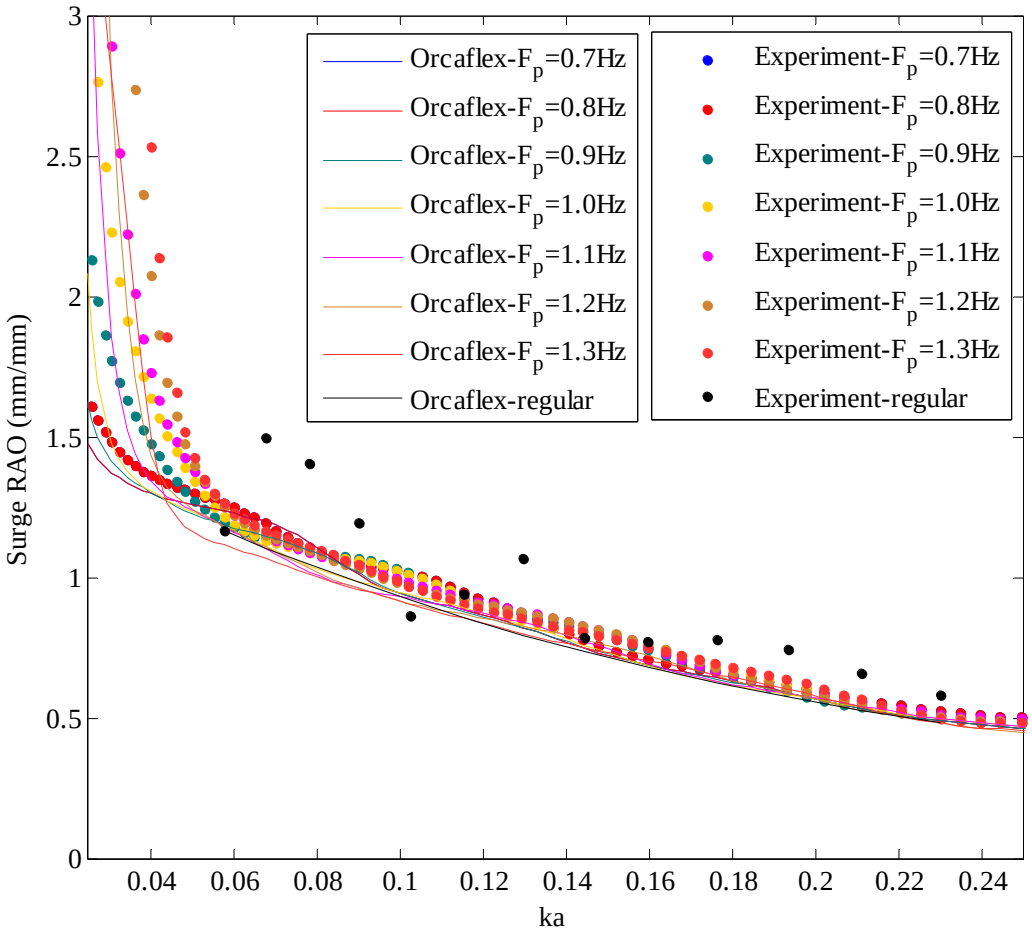

Fig. 4.27 Surge Response Amplitude Operator computed at the nacelle for irregular waves defined by JONSWAP spectrum, Hm0=90mm.

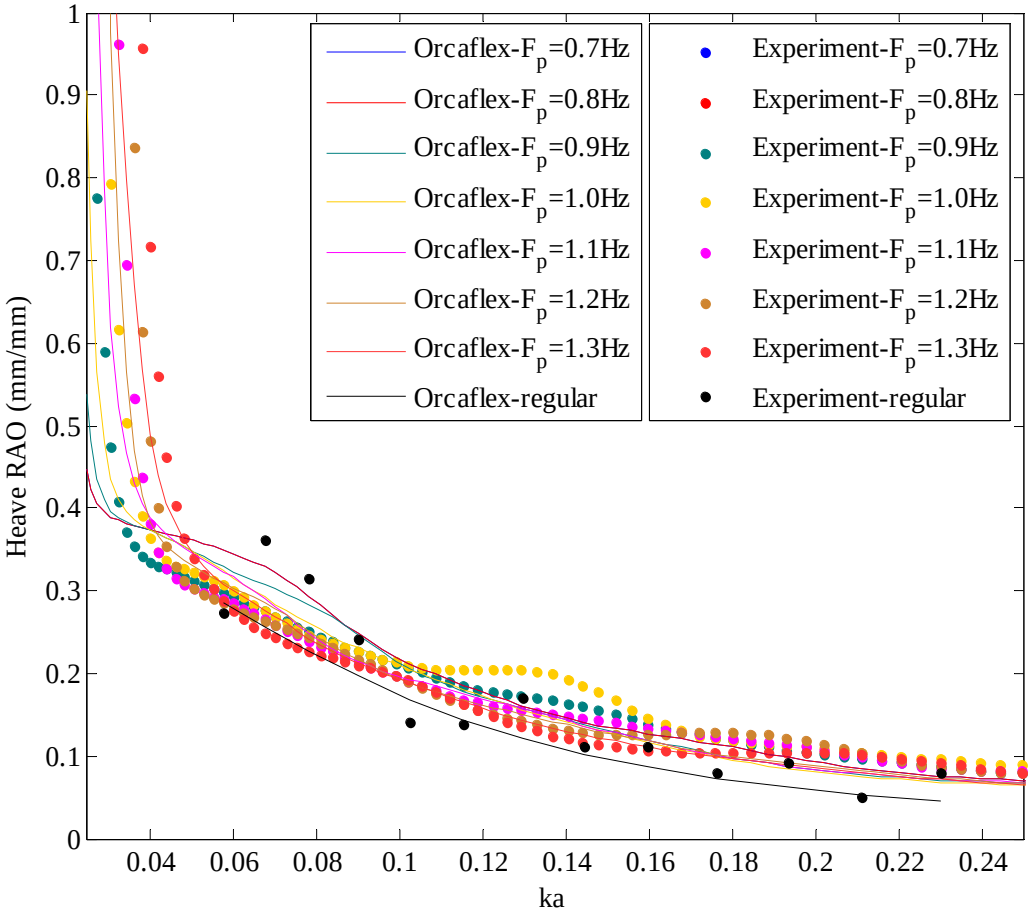

Fig. 4.28 Heave Response Amplitude Operator computed at the nacelle for irregular waves defined by JONSWAP spectrum, H_{m0}=90mm.

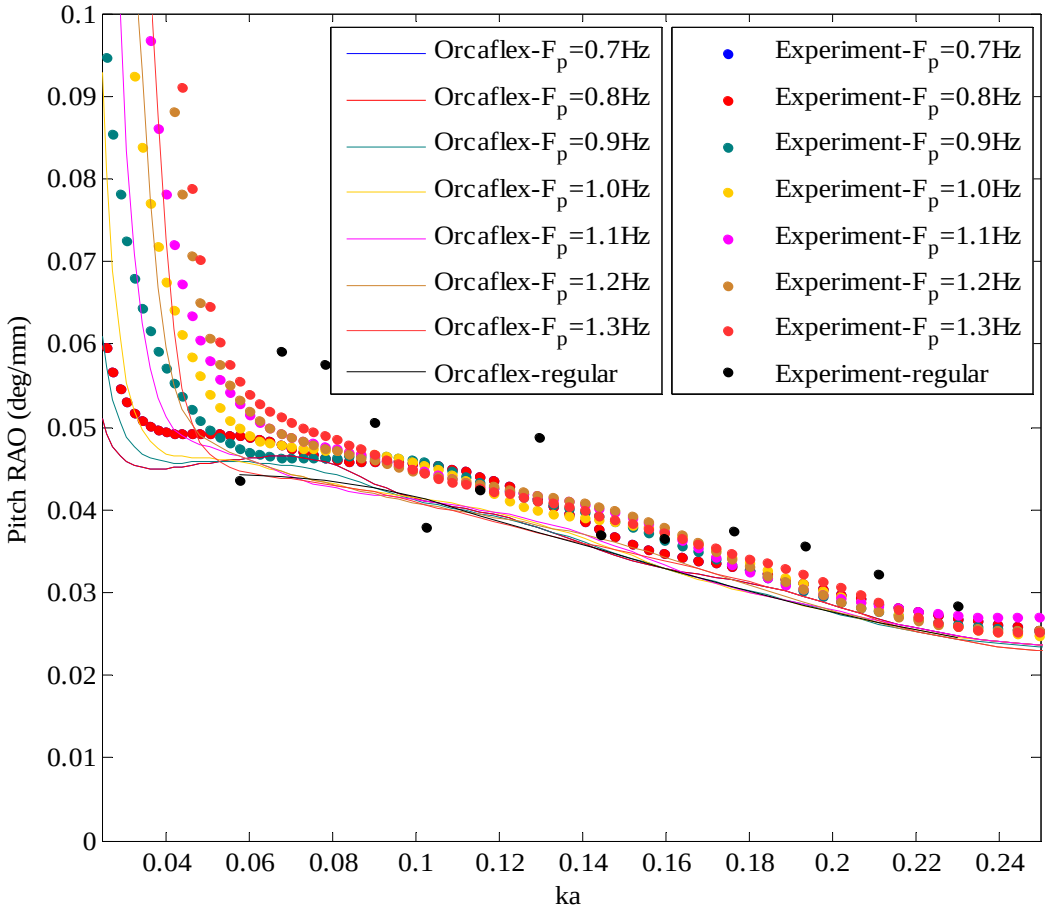

Fig. 4.29 Pitch Response Amplitude Operator computed at the nacelle for irregular waves defined by JONSWAP spectrum, H_{m0}=90mm.

Spectral responses of the platform computed at the C.O.M and the nacelle are presented in Figures 4.30 to 4.32. The resonance bandwidth predicted by OrcaFlex is consistent with the experimental results. The OrcaFlex time domain predictions for the surge spectrum (Fig. 4.30) contain more energy near the surge resonance peak frequency (0.0625Hz). Both experiments and simulations envisage a considerable

amount of surge energy at the nacelle that is pitch induced. This is attributed to the distance of the nacelle from the centre of mass. A good agreement in response peak was observed at the wave frequency.

The heave spectrum (Fig. 4.31) computed from numerical simulations shows slightly higher energy around the heave natural frequency as compared to experiments. The OrcaFlex estimates for the nacelle and the C.O.M are unchanged. The difference in heave spectral energies determined from experimental measurements may be attributed to the wave reflections and errors in measurement. Fig. 4.32 shows that the surge induced pitch motion is relatively small in terms of energy content. Similar to the heave spectrum, the experimentally determined pitch resonant peak at the nacelle is lower than that computed at the C.O.M.

In general, these results present a good idea about the model behaviour for the range of sea states considered in the study. The input data for the numerical model and results presented in this work were based on physical model tests in an experimental wave basin where it was impractical to control all the conditions. Factors such as scale effects could alter the accuracy and hence the sensitivity of the results to those factors should be considered. The results must therefore be examined with care and good sense of engineering judgment.

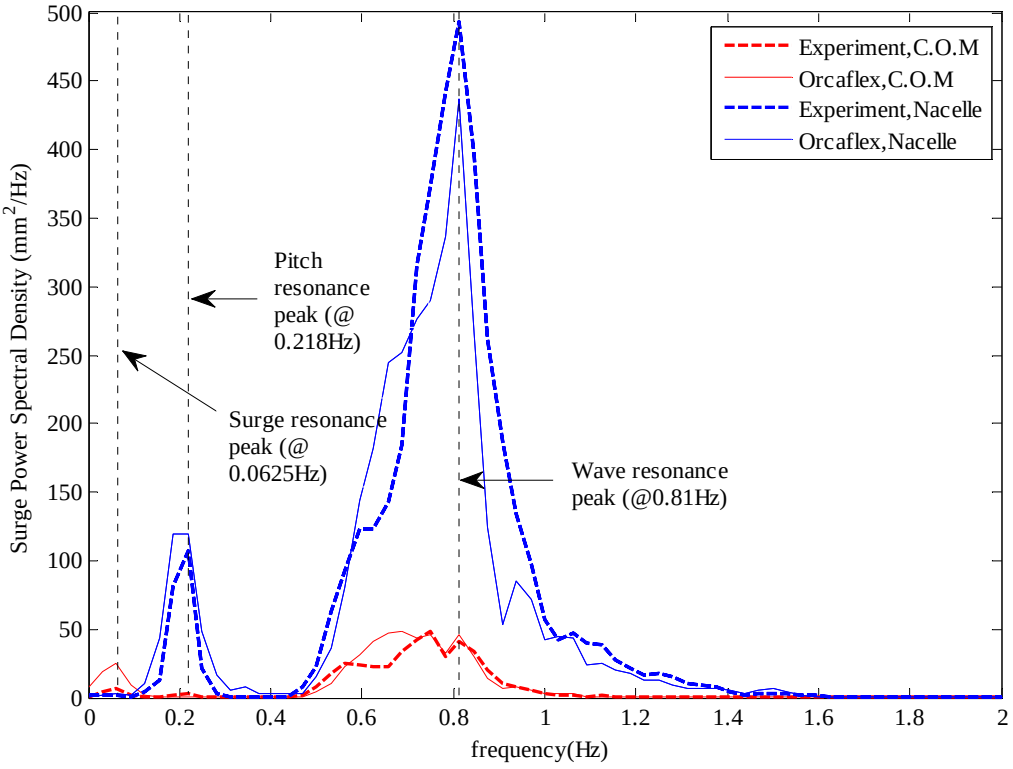

Fig. 4.30 Surge response spectrum computed at the C.O.M and nacelle based on Welch's averaged periodogram method for JONSWAP wave spectrum, H_{m0}=30mm, f_p=0.8Hz.

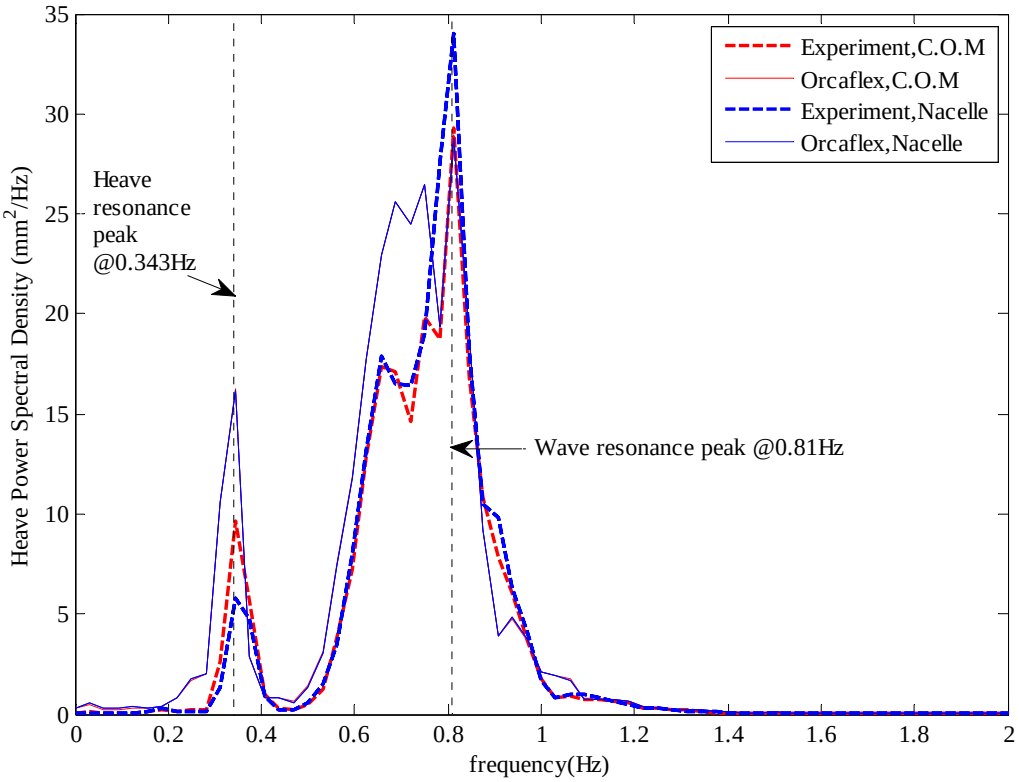

Fig. 4.31 Heave response spectrum computed at the C.O.M and nacelle based on Welch's averaged periodogram method for JONSWAP wave spectrum, H_{m0}=30mm, f_p=0.8Hz.

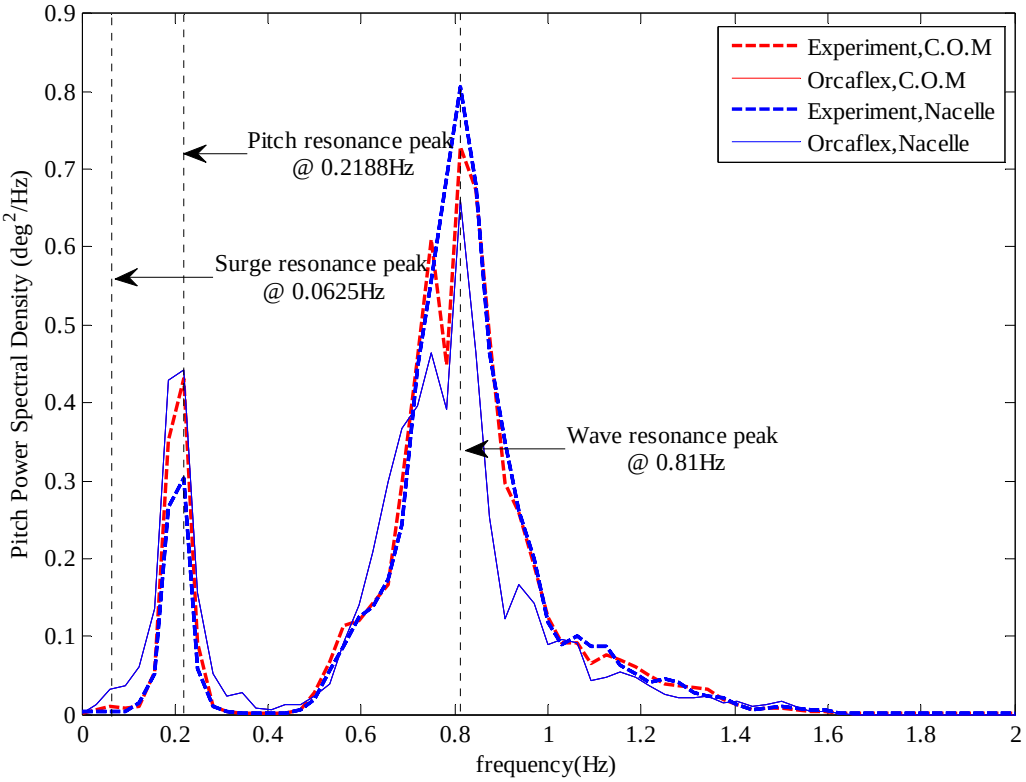

Fig. 4.32 Pitch response spectrum computed at the C.O.M and nacelle based on Welch's averaged periodogram method for JONSWAP wave spectrum, H_{m0}=30mm, f_p=0.8Hz.

4.2. Summary – Part I

Part-I of the research set out to evaluate the hydrodynamic behaviour of a spar-buoy type wind turbine by a new approach, involving improved mooring line modelling. For the purpose, a set of nine tasks identified in Chapter 1 were accomplished systematically. The empirical results from laboratory tests and numerical simulations on a 1:100 scale model of the stepped spar floating wind turbine for regular and irregular sea states provided better understanding and evidence to support the findings which are presented as follows:

- A good agreement with the experimental results confirmed the validity of the FEM-based OrcaFlex model in accurately reproducing the physical model behaviour as well as the testing conditions
- The dynamics of the mooring lines was better captured by the FEM-based numerical model that provided with more realistic profiles for the motion response.
- The hydrodynamic behaviour of the system reported using response amplitude operators for both regular as well as irregular waves confirmed the feasibility of the stepped-spar concept.
- Four-point mooring is beneficial in minimising the surge response, while maintaining the yaw motions at acceptable levels suggesting a likely increase in contribution to damping from the mooring lines.
- In general, the presence of pitch-coupling effect in surge response is greatest at the nacelle. For the stepped spar system, this effect is considerably lower at the nacelle corroborating the presence of active pitch damping mechanics at lower frequencies.
- Examining the RAOs at the centre of mass as well as the nacelle provided a new design parameter, *Nacelle Magnification Factor (NMF)* that provides a greater understanding of the surge behaviour at the nacelle.

The above findings were limited by the fact the input data and analysis were entirely from the physical model tests at laboratory scale where measurement errors due to scale effects are invariably present. Therefore interpretation of results at full scale must be done with care and good sense of engineering judgment. Notwithstanding

these limitations, Part-I has been instrumental in providing new knowledge and enhancing the general understanding of the coupled dynamic behaviour of the stepped-spar floating wind turbine. As the next step in the course of investigation, the results from Part-I will be used as inputs to Part-II to examine the impact of floater motions on the integrity and dynamics of the drive-train.

Chapter 5

Part-II Structural Integrity of a Direct–drive generator for a FWT

5.0 General

This chapter initiates the Part-II investigations by providing an assessment of the structural integrity of a direct-drive radial flux permanent magnet generator in response to nacelle motions in a FWT system. The structural integrity of the generator design is verified from the stability of the air-gap between the rotor and stator. Measures for air-gap management and their possible design implications on the overall system are examined. Nacelle motion responses were obtained from the Part-I studies on a 1:100 scale FWT model. ANSYS suite was used to estimate the structural deformations of the generator and the changes in the air-gap distribution. A simplified analytical model was then used to compute the resulting changes in flux density and force distribution along the rotor periphery. The results were then evaluated to identify the design of a direct-drive generator that best preserves the integrity of the overall system. This study was aimed at offering some early guidelines for designing direct-drive systems, particularly deciding the strength requirements of generators that are better suited for wind turbines with floating supports.

5.1 Introduction

The nacelle acceleration is a key performance index for a floating wind turbine, so that the objective of any design is to minimize that value for all sea states. Previous research suggests that a value less than $0.3g$(i.e $2.94 m/s^2$,where g is the acceleration due to gravity) can guarantee satisfactory performance[42]. Since larger nacelle motions can damage equipment or degrade turbine performance, it is important to

verify the equipment performance in relation to nacelle motions. Consequently this can help verify the overall adequacy of the design and help identify the best control measures. For the direct-drive technology to be implemented for a FWT system, the structural integrity of the components must be demonstrated to be at an acceptable level in response to the various loads endured during their operation.

5.2 Generator structural integrity

The most critical component of the direct-drive technology is the generator. These generators operate at low speeds, are very large and require massive support structures. In a PM generator, the stator and rotor are physically separated by a small air-gap measuring a few millimetres (for a certain generator diameter D, the air gap distance is typically $D/1000$ [133]). Figure 5.1(a) shows the stator inner surface and rotor external surfaces separated by a certain air-gap distance, g_a. For simplicity, the slotting on stator and magnets on the rotor are not shown here. If the axis of rotation is defined by the x-axis, then g_a refers to the nominal air gap measured in the radial direction in the y-z plane. There always exists an attractive magnetic force (normal component of Maxwell stress) between stator and rotor that serves to close this air-gap. Since, the quality of power conversion for these generators depends on the uniformity of this air-gap, maintaining the air gap in proper deflection against the attractive forces imposes stiffer structural requirements.

Non-uniformity of the air-gap (also termed as eccentricity) can result from a variety of sources such as structural deflection, incorrect bearing positioning during assembly, shaft misalignment, shaft deflection or bearing wear. Large air-gap results in poor torque output while a small air-gap magnifies the output voltage and a non-uniform air-gap can cause fatigue loads on the generator. The stability of this air-gap qualifies the structural integrity of the generator which is related to the stiffness of the rotor and stator support structures as well as that of support shaft bearings in effectively countering the loads that act to close the gap. Direct-drive generators for wind turbines can successfully operate as long as eccentricity is limited to $\pm$10% of the nominal air-gap length[133, 134] . The electromagnetic and structural models of the PM generator are tightly integrated. The normal air-gap closing loads include the

radial attraction forces of magnets, the self-weight/gravitational force and thermal expansion due to heat. For a generator with adequately designed support structures, there exists a uniform distribution of the magnetic forces (shown by arrows of equal vector lengths in Figure 5.1(a)). If the support structures are not adequately designed, then deflections in the structure contribute to air-gap deformation and imbalance in the magnetic forces. Figures 5.1 (b)-(d) shows deformed rotor and stator structures with an imbalance in magnetic forces (shown by unequal vector lengths) along the periphery, with maximum forces in region with the lowest air-gap and vice versa. For a certain air-gap deflection caused by support structure of the generator, δ_s, the structural stiffness is important to achieve such that the necessary condition for equilibrium is:

$$F_{structure} - F_{mag} \geq 0 \tag{5.1}$$

where, $F_{structure}$ is the generator structural stiffness, F_{mag} the magnetic stiffness. Compliance in the shaft and bearing supports can contribute further to eccentricity. An external load such as wind or wave in addition to the normal gap closing forces complicates the air-gap problem. If the bearing stiffness is not adequate, then the shaft carrying the rotor may be further pulled towards the stator, thereby creating an imbalance in magnetic forces and de-stabilising the air-gap. Fig. 5.2(a) shows a shaft-hub assembly supported by two bearings. The shaft is displaced from the normal concentric arrangement, by a distance, δ_b. Fig. 5.2(b) shows a concentric rotor and Figure 5.2(c) illustrates the eccentricity induced by shaft displacement. Therefore, in the presence of external load (such as waves/wind); eccentricity may be induced by support structure deflection of the generator (δ_s) as well as shaft displacement or deflection (δ_b) caused by bearing compliance. A necessary condition for equilibrium in such a case would be

$$\sum F = F_{structure} + F_{bearings} - F_{mag} - F_{Ext} = 0 \tag{5.2}$$

Where F_{ext} is the external load (for e.g.: nacelle acceleration due to buoy motion), $F_{bearings}$ is the restoring forces from bearings. Thus, the first index for an eligible drive-train design would be its structural integrity (i.e., the stability of the air-gap between the rotor and stator in response to the nacelle accelerations). Any additional

design measures to ensure the air-gap stability must be treated carefully with an assessment of its possible design implications on the overall system. For example, an increase in structural stiffness results in additional mass at the nacelle, thus requiring modifications to the tower or foundation design.

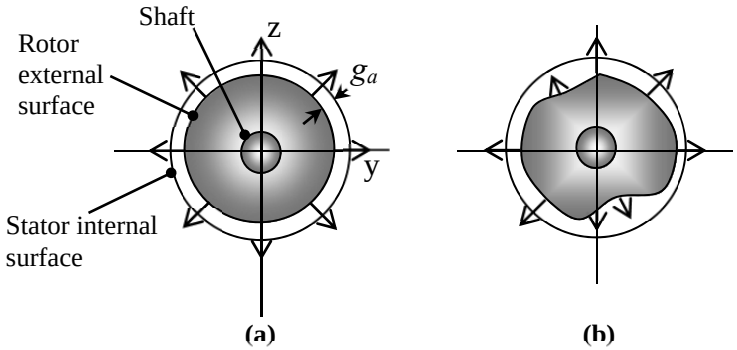

Fig. 5.1 Eccentricity due to structural deformation (a) No eccentricity (b) Deformed Rotor (c) Deformed Stator (d) Deformed Rotor & Stator

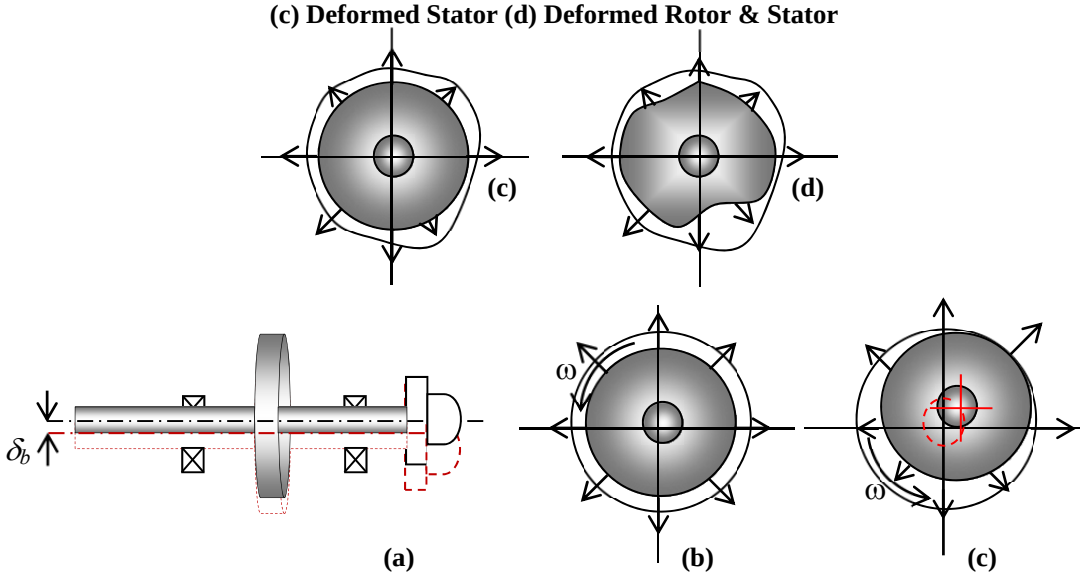

Fig. 5.2 Eccentricity due to bearing Tolerance (a) Shaft Displacement(Exaggerated) (b) Concentric Rotor (c) Eccentric rotor.

In order to evaluate the overall integrity of direct-drive generator, it is necessary to examine both these effects. In this study, these effects were examined independently. As a first step, the air-gap behaviour due to structural deflection is examined in response to waves. Firstly, the various loads that appear at the nacelle as a result of wave action were computed. Then, the structural strength of the generator in response to these loads was verified. As a subsequent step, contributions from shaft

displacements/bearing tolerances were examined. The implications on the overall system were also checked.

5.3 Methodology

The main aim of this study was to verify the structural requirements of a direct-drive generator for a given FWT system. This required the computation of nacelle loads as determined by the hydrodynamic response of the floater. It was decided to utilize the results from Part-I for making further investigations; more than three separate numerical tools were used. The steps involved in the analyses as illustrated in Fig. 5.3 are described as follows:

- A structural model for a 2MW radial flux permanent magnet generator of internal rotor construction is considered.
- The Part-I results for hydro-dynamically induced nacelle motions of a spar-buoy FWT are treated as load inputs for generator structural analysis.
- The structural stability and air-gap behaviour of the generator is examined in response to the nacelle motions by transient structural analysis in ANSYS.

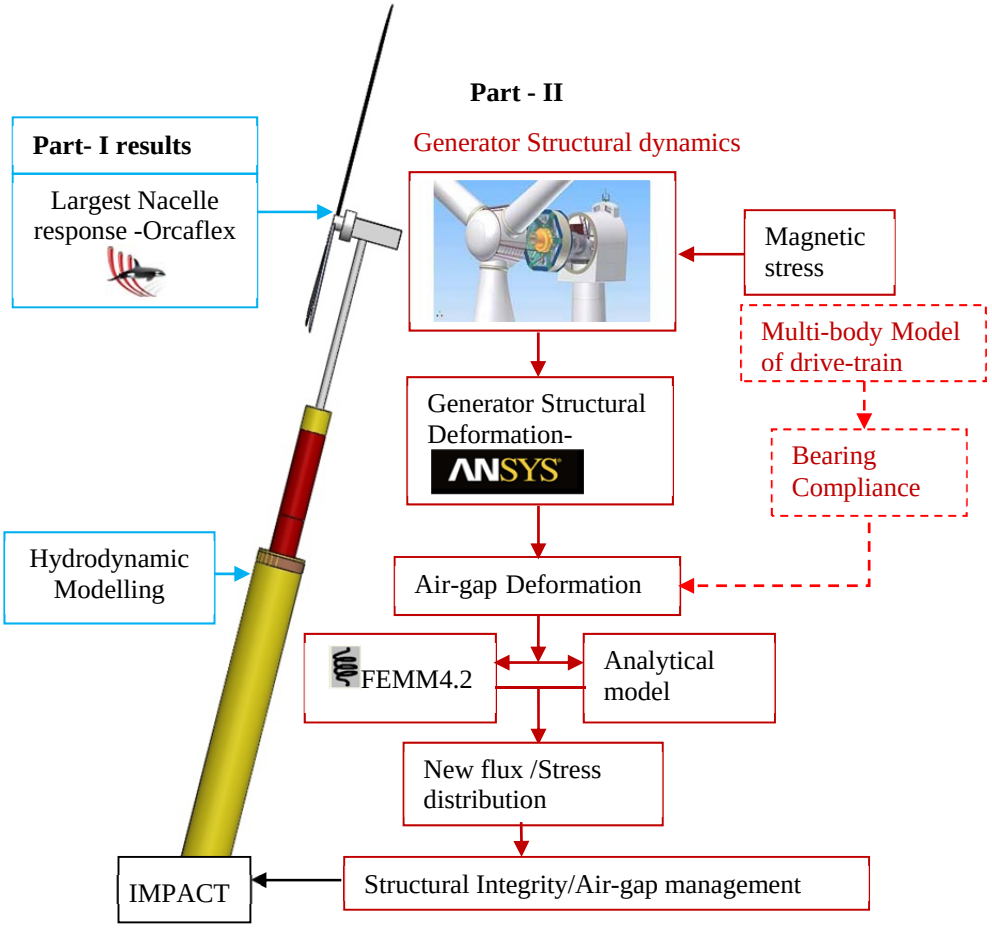

Fig. 5.3 Assessment Methodology

- Possible influences on air-gap response due to bearing support compliance are also investigated by multi-body simulation[135, 136].
- An analytical model is presented to evaluate the generator structural integrity. This is validated by numerical simulations in FEMM [137].
- Finally, the suitability of the generator is assessed based on its impact on the rest of the FWT system.

5.4 The Floating wind turbine -full scale model

For the generator structural analysis, it was sensible to consider the full scale properties of the spar-buoy wind turbine. These were obtained by applying Froude's dimensional scaling to the experimental model defined in Table 3.1 of Chapter 3. The model properties at full-scale for the stepped spar buoy system are listed in Table 5.1. During the stability calculations, the tower top mass was calculated to be 156 tons. This was computed based on the estimates for the main equipment masses for turbine, nacelle frame and the generator from a reference downwind turbine design with a 2MW direct-drive generator [81]. A further 20 tons was assumed as a design margin to provide for variability in the type of direct-drive topology and associated auxiliary equipment (e.g.: power electronic converter, transformer, cabling, switchgear, brake disk & callipers, cooling system, yaw drive, brake and bearing) . This mass scales down by a factor of 10^{-6} to 0.156 kg for the experimental model. Further details of the model can be found in Chapter 3.

Item/Description	Units	Values
Total mass	ton	3870
Turbine Rating	MW	2
Turbine Rated speed	rpm	18
Turbine 1P frequency	Hz	0.3
Generator	-	Direct-drive
Nacelle Mass (tons)	ton	156
Centre of Gravity(from keel)	m	29.5
Meta-centric height	m	4.3
Surge Natural frequency	Hz	0.00625
Pitch natural frequency	Hz	0.02188
Heave Natural frequency	Hz	0.03438

Table 5.1 Properties of a stepped-spar floating wind turbine scaled for prototype model.

Item/Description	Units	Weight
Nacelle+ frame Mass	ton	34*
Rotor Mass	ton	42*
Generator mass	ton	60*
+Design margin for generator topology and other miscellaneous equipment	ton	20
Total	ton	156

Table 5.2 Tower top mass estimate used for stability calculations (* Data from [81]).

5.5 Nacelle motions

In response to wave action, the nacelle of a FWT system generally experiences 6 DOF motions along the three axes defined by the orthogonal co-ordinate system (say x, y & z axis). The motions are coupled and dependent on the direction of incident waves. For example, a wave acting along a particular-direction displaces the structure horizontally in that direction (surge), vertically (heave) and also produces a tilt motion (pitch). In practice, all of these motions occur simultaneously with a phase lag between them. These result in accelerations and velocities at the nacelle that are cyclic in nature with repeat periods determined by the resonance properties of the system for each degree of freedom. The spar motions for this study were extracted from OrcaFlex simulations.

Since this study was aimed at examining the structural behaviour of the generator, the effect of turbine rotation and control system action were initially not considered. In order to determine the generator loads, the nacelle motions were obtained from Part-I studies. The OrcaFlex time response simulations for 3 m, 6 m and 9 m wave heights (on 1:100 scale) gave the position, orientation, velocity and accelerations of the nacelle along the 3 co-ordinate axes for surge, heave and pitch motions. Assuming consistency in lift/drag coefficients, these responses were upscaled to represent full-scale conditions by applying Froude's laws for geometric similitude. For the scale factor, λ =1/100, the accelerations were scaled by a factor of 1, velocity by $\lambda^{1/2}$ and mass by λ^3. Typical nacelle accelerations predicted for a 9 m regular wave height by OrcaFlex are shown in Fig. 5.4. These accelerations included the gravity component. The highest nacelle accelerations(particularly along surge

direction) were observed for a wave period of 6.9 s (frequency = 1.44Hz) and this was chosen as the worst possible load condition that would be seen by the generator and hence considered for further investigation as described in Fig. 5.3.

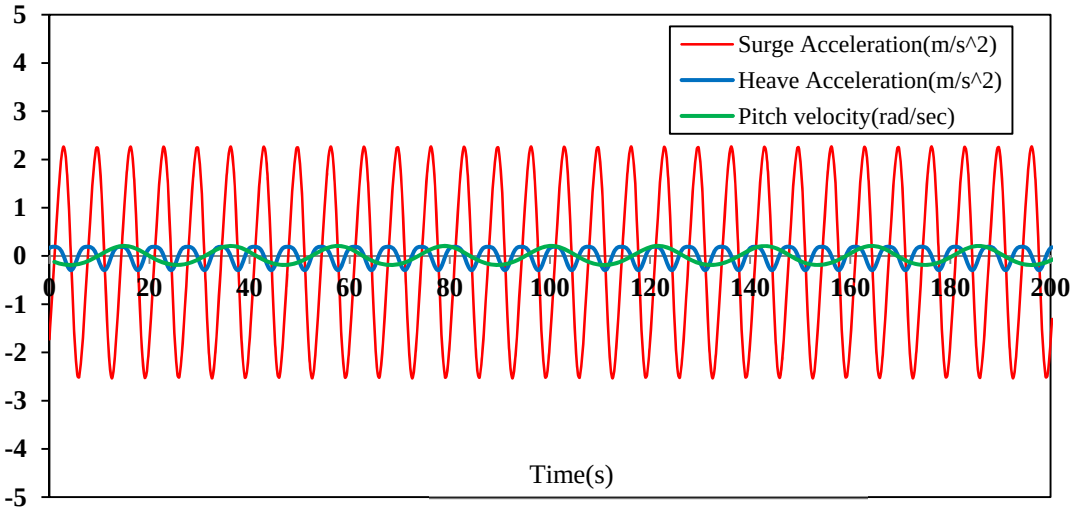

Fig. 5.4 Nacelle acceleration and pitch velocity components for regular wave of height of 9 m and wave period 6.9 s (from OrcaFlex)

5.6 Generator Model

The generator considered for this study is a radial flux permanent magnet synchronous generator (PMSG) rated 2MW. Different configuration choices exist for radial flux PMGs for the rotor type, location, generator-hub interface options [90]. To allow for a quick modelling and analysis time, a simple design representative of a standard construction developed by [138, 139] was chosen. The rotor and stator structures have a spoke-arm construction (refer to Fig. 5.5). The rotor pole width was assumed to be 80% of pole-pitch [140].

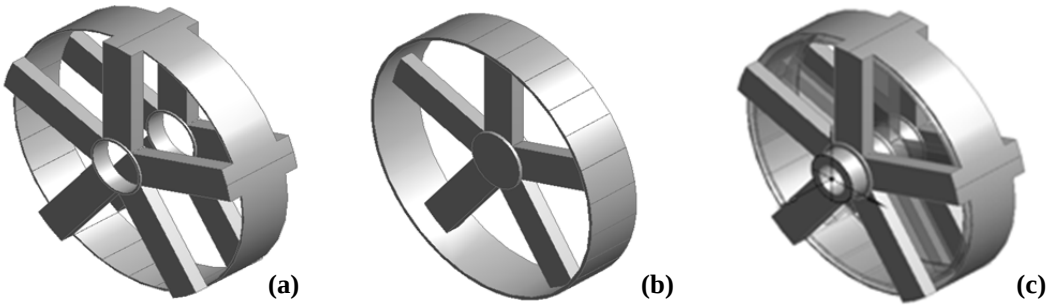

Fig. 5.5 Generator support structures (a) Stator with spoke arm (b) Rotor with spoke arm (c) Complete assembly with shaft

The generator shaft was assumed to be supported by a double-bearing arrangement which gives it a high stiffness/mass ratio. The assumption of high stiffness was applied for the purpose of capturing only structure induced eccentricities.

The electromagnetic parameters were derived based on the design model presented in reference[140]. The detailed structural parameters were computed using the analytical models presented in [109] and [138] to reach a minimum feasible structure. Table 5.3 gives the design parameters for the generator. For the chosen structure, the total mass of the generator including those of magnets, windings, bearings, shaft (refer to Table 5.4) was estimated at 50 tons using the mass models from [141, 142]. As this mass was practically consistent with the value considered for computing the nacelle mass during the initial stability calculations, no attempt was made to optimise the structure.

Air gap Diameter, D_g	4.34
Axial Length, L_s	0.869
Air gap length, g_a	0.00434
Magnet height, h_m	0.0108
Stator diameter, D_s	4.35
Slot pitch, τ_s	0.033
Pole pitch, τ_p	0.099
Pole pairs, p	69
Magnet width b_p	0.0792
Slot width, b_s	0.0148
b_s/τ_s	0.45
Tooth width, b_t	0.0181
Slot height, h_s	0.0787
Stator yoke thickness , h_{sy}	0.040
Rotor yoke thickness , h_{ry}	0.050

Table 5.3 Electro-magnetic and structural design data for generator (ALL Dimensions are in m)

Item	**Mass (ton)**
Permanent Magnets	0.68
Copper	3.10
Steel	3.33
Rotor Structure	13.82
Stator Structure	23.17
Shaft	4.45
Bearing	0.54
Total mass	**49.12**

Table 5.4 Generator Mass data based on [141]

5.7 Evaluation of Structural integrity of the generator

For a direct-drive generator in the steady-state condition, the normal air-gap-closing loads [134] are constant so that inertia and damping effects are less significant. The resulting stresses and deformations are only a function of space, i.e. identified with respect to the location of interest around the periphery of the rotor and stator. Therefore the air-gap problem is treated by simple static structural analysis. However, in the presence of external load such as wave action, although the rotor is not rotating, the external loads are continuously varying and time-dependent causing the system to move. The air-gap problem can therefore be treated as a dynamic system under steady-state. Because of the dynamic nature of the loads, the resulting stresses, deformations and air-gap distribution vary both spatially and temporally. It therefore becomes necessary to perform a time-history analysis to solve the structural dynamics problem.

In order to examine the structural integrity of the generator design, finite element methods were used. The transient structural analysis module in ANSYS was chosen to compute the deformations of the generator stator and rotor structures. To understand the possible contributions from shaft/bearing compliances, a separate study was carried out using multi-body simulation tools [135, 136].

For the transient structural analysis, it was required to determine all the loads that would be seen by the generator and also identify the location where these loads act. The motion loads, accelerations and velocity were extracted from the OrcaFlex simulations (Step 1, in Fig. 5.3) and applied at the centre of gravity of the generator. Assuming a uniform air-gap at start, the force due to the magnetic field develops an evenly distributed pressure load acting radially outward of the rotor and inward to the stator yoke. The length of the measured air-gap, denoted by g_a, was constant throughout. If the air-gap is non-uniform, it must be expressed as a function of angular position where it is measured. To estimate the values of air-gap and field distribution along the rotor periphery, the stator bore and rotor surface were divided into 25 equal segments, each having a particular area, dA for every 14.4 degrees of the stator bore. The nodes within each segmental area were grouped together and each segment was identified by the angle, θ it subtended with the x-axis varying from 0^o to 360^o. The number of segments (areas) was decided from the initial simulations in ANSYS that showed that the nodes within the surface mesh covering this segmental area underwent similar deformation.

A simplified analytical tool was developed to compute the new air-gap flux density and the magnetic stress distribution for the deformed structure. The analytical model was validated by 2D magneto-static finite element simulations in FEMM [137]. The newly estimated stresses together with the motion loads were then fed back into ANSYS simulations(step 2 in Fig. 5.1) to examine the short-term and long-term magneto-elastic stability of the generator by means of an iterative procedure. It was assumed that the nacelle motion loads remained unchanged throughout the simulations. The strength of the generator (i.e. mass/structural requirements) was determined by its ability to maintain a stable air-gap between the rotor and stator against structural deflection caused by these loads. As long as the load cycles are below the fatigue limit and if the nacelle accelerations are limited to 0.3*g*, the preliminary results (Section 5.10) suggest that structural stability of the generator is more sensitive to magnetic forces. In this regard, two approaches to air-gap management (Section 5.14) were studied:

a) Increasing the stiffness (inactive structural material) and

b) Increasing the design air-gap (active magnetic material).

The adequacy of the structural design was verified by examining the impact of the drive-train design on the rest of the system. To preserve the structural integrity of the drive-train and the platform, the following criteria were examined;

(i) Air-gap deflections are within 10% limit for the generator and

(ii) With the rest of the nacelle mass assumed to be fixed, the total generator mass and hence the tower top mass does not exceed the minimum value stipulated by hydrostatic stability by a large margin (to ensure static pitch angles are within 10º). This also served to verify if the system eigen frequencies were affected.

The two approaches were compared based on the results for the measured air-gap length (g_a) normalised to the design air-gap (g_{nom}).

5.8 Analytical model

Eccentricity is a phenomenon that causes the generator rotor and stator structures to deform due to unbalanced magnetic forces. Some common causes include stator core ovality, incorrect rotor/stator positioning while commissioning, bent shafts, mechanical resonances or bearing wear. The generator structure of a PMSG must be sufficiently stiff to withstand the resulting stresses. Estimation of the magnetic forces in a PMSG is a critical subject particularly when the intended application is a floating wind turbine as it can have a detrimental impact on the overall stability of the given design. In the case of FWTs, sources of rotor eccentricity can not only come from manufacturing tolerances, but also external load such as wind and waves.

Several analytical models exist to compute the air-gap, flux density distribution and the resulting forces for different types of eccentricities [143-146]. These models deal with the familiar effects of static and dynamic eccentricity caused by radial relative displacement of rotor with respect to stator. The flux models considered for static eccentricity are generally one-dimensional (function of space) as the position of minimum radial air-gap is fixed in space and does not change with time. Dynamic

eccentricity models on the other hand are 2-dimensional (i.e., a function of space and time), as the minimum air-gap revolves with the rotor. In the present study, we investigate an eccentric condition, possibly caused by external load when the rotor is stationary. The stator and rotor are assumed to be perfectly concentric with no relative displacement between them. The rotor is not rotating, but an external time-dependent wave load causes the nacelle and generator structure to accelerate in different directions. Such loads, if of reasonably large magnitude can disturb the air-gap equilibrium if the structures are not stiff enough.

For the first step, it was intended to capture particularly the structure induced eccentricities (δ_s), so the generator support structures were only modelled. As for the parked rotor condition, it was assumed that shaft displacements due to bearing compliance in the radial direction (δ_b) were negligible. For the purpose of simplicity, it was assumed that the bearing support stiffness was sufficiently high. So that for a support structure that is inherently light, the structural stiffness is more important to achieve such that the necessary condition for equilibrium is considered to be:

$$\sum F = F_{structure} - F_{mag} - F_{ext} = 0 \tag{5.3}$$

where, $F_{structure}$ is the generator structural stiffness, F_{mag} the magnetic stiffness and F_{ext}, the external load (nacelle acceleration due to buoy motion). It would be reasonable to assume a 2D model for flux distribution (time and space as variables) as it is expected to vary spatially with a time-dependent external load. In this section, a simplified analytical approach is proposed to estimate the radial forces and its distribution for such a case. The proposed analytical model can be used in conjunction with 3D finite element structural analysis tools such as ANSYS to assess the structural integrity of a PMSG. The following assumptions were made to compute the instantaneous values of air-gap flux density:

- Only motion loads due to waves were considered. All other loads, shaft or bearing displacements are not included. No eccentricity was assumed to previously exist;
- Rotor's centre of rotation is the same as the geometric centre of the stator. Stator and rotor symmetrical axes coincide, i.e., $O_s = O_r$ (O_s and O_r are the symmetry centres for stator and rotor respectively);

- Stator and rotor laminations are infinitely permeable, therefore the flux lines are perpendicular to the iron surface in a typical machine that is unsaturated; The 2-dimensional magnetic field was assumed considering only the radial component of flux density(tangential flux can be neglected);
- Space harmonics of the magnetic flux density distribution in the air-gap were ignored; Only the peak of the fundamental flux density was considered;
- Magnets do not undergo any distortion;
- No skewing of magnets or stator slots was assumed;
- Flux leakage and fringing effects were ignored;
- The rotor is assumed to be stationary. No stator excitation(armature reaction field) was considered;

The air-gap was assumed to vary only along the circumferential direction. Therefore it was sufficient to assume a polar coordinate system when referring to the rotor and stator surfaces ignoring the generator depth. Since a two-dimensional solution for the magnetic field was assumed, flux density was expressed as a function of position (θ) and time(t). The instantaneous value of peak flux density, $\hat{B}_g$ in the air-gap was primarily due to the open-circuit field produced by the permanent magnets given by

$$\hat{B}_g(\theta,t) = B_{magnet}(\theta,t) \tag{5.4}$$

Assuming linear demagnetization characteristics for the magnets, the peak flux density above the magnet in the air-gap can be calculated using Ampere's circuital law, considering flux continuity [147].

$$B_{magnet}(\theta,t) = B_r\left(\frac{h_m}{h_m + \mu_r g_{eff}(\theta,t)}\right) \tag{5.5}$$

where, B_r is the remnant flux density, h_{m} is the length of the magnet along the direction of magnetization, μ_{r} is the relative recoil permeability of magnets and g_{eff} is the effective air-gap length which is generally large for a radial flux permanent magnet machine. It is given by

$$g_{eff}(\theta,t) = K_{sat}K_{Cs}\left(g_a(\theta,t) + \frac{h_m}{\mu_r}\right) \tag{5.6}$$

where, K_{sat} represents the effect of saturation(i.e. reluctance of iron) in the magnetic circuit, K_{Cs} is the Carter factor for the stator slots computed using [148]. The value carter coefficient was close to unity ($K_{Cs} \approx 1$). The effect of saturation was considered to be negligible as the effective air gap is much larger due to the low permeability of the magnets. Let $g_a(\theta)$ represent the air-gap measured in the non-eccentric case, and $g_a(\theta,t)$ be the instantaneous value of mechanical air-gap for the eccentric condition measured at each segment calculated using the two-point formula (refer to Fig. 5.6):

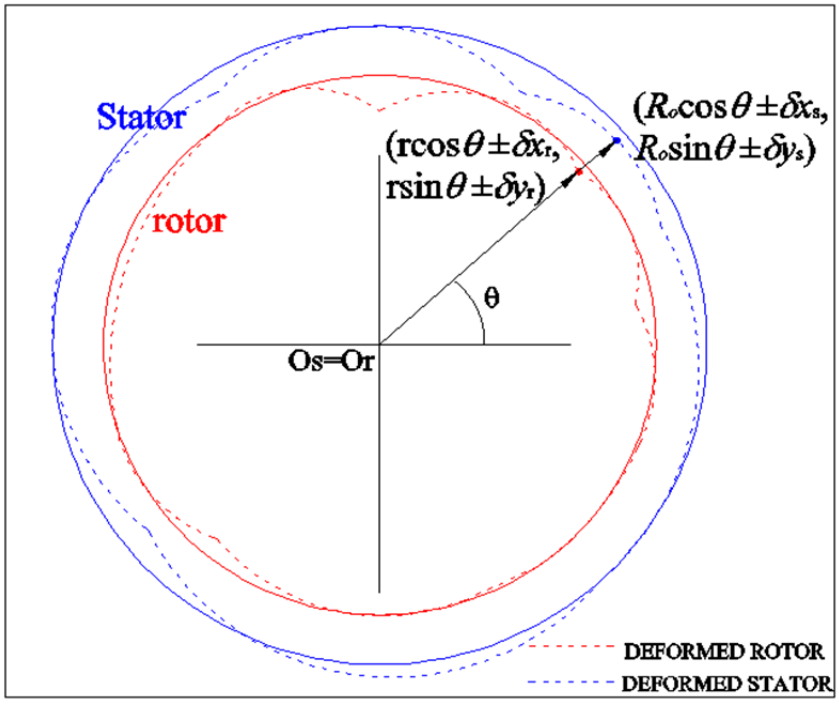

Fig. 5.6 Air gap computation from deformed rotor and stator profiles

$$g_a(\theta) = \sqrt{\left(R_o \cos\theta - r\cos\theta\right)^2 + \left(R_o \sin\theta - r\sin\theta\right)^2} \tag{5.7}$$

$$g_a(\theta,t) = \sqrt{\left(\left(R_o \cos\theta \pm \delta x_s\right) - \left(r\cos\theta \pm \delta x_r\right)\right)^2 + \left(\left(R_o \sin\theta \pm \delta y_s\right) - \left(r\sin\theta \pm \delta y_r\right)\right)^2} \tag{5.8}$$

R_o is the inner radius of the stator

r is the outer radius of the rotor

δx_r and δy_r are rotor deformations measured at a node (r, θ) located on the rotor at

time, t

δx_s and δy_s are stator deformations measured at a node (R_o, θ) located on the stator at time, t

The deformations of all nodes within a given segmental area were assumed to be constant. The magnetic stress, σ, acting on each segmental area can then be computed using the Maxwell stress tensor equation given by

$$\sigma(\theta,t) = \frac{1}{2\mu_0}\hat{B}_g^2(\theta,t) \tag{5.9}$$

where, μ_o is the permeability of free space. Thus, equation (5.8) was used to calculate the instantaneous values of air-gap length and equation (5.9) was used for computing the stresses due to magnetic field.

5.9 Modelling in FEMM

To validate the analytical model proposed in Section 5.8, a 2-D model of the generator was constructed in FEMM 4.2, an open-source 2-D finite element software for magneto-static simulation [137]. The aim of this model was to verify the trend of flux density and the resulting stresses predicted by the analytical model as the rotor and stator structures were deformed. The stator and rotor geometries for the generator were modelled for the design data furnished in Table 5.3. The various parts were drawn as planar two-dimensional components defined using nodes connected by line and arc segments available in the pre-processor. To guarantee a unique solution for the magnetic field, the dirichlet boundary condition was enforced by setting the magnetic vector potential to zero at the stator outer radius. An open slot geometry was considered; so materials were assumed to exhibit linear behaviour. The stator iron was assumed to have a zero electrical conductivity, so that eddy currents are neglected. The magnet material was assumed to be Neodymium-Iron-Boron (NdFeB) with nominal energy product of 40 MGOe. Because, this study deals with simulating the flux density due to permanent magnets and the stresses, no attempt was made to model the stator windings (for armature reaction). Nevertheless the effect of armature reaction on unbalanced magnetic pull is expected to be small [149] and hence was neglected. The winding was therefore modelled as air. The

FEMM program discretises the solution space using a triangular mesh and utilises a set of Maxwell's equations to solve the electromagnetic problem. Field solutions of these problems are generally available in the form of contour and density plots (refer to Fig. 5.7(a)). The flux density in the air-gap was extracted from the plots of field quantities produced along these contours. Fig. 5.7(b) shows the plot for air-gap flux density over one pole-pair computed by FEMM, with the flat-topped value of flux density giving a value of 0.955 Tesla. The flat top value assumes that the maximum flux density under a tooth is used. The values for peak flux density from the analytical model and FEMM plots (not shown in the figure) were 0.783 Tesla and 0.8 Tesla respectively, which indicates that the analytical model worked well. This gave

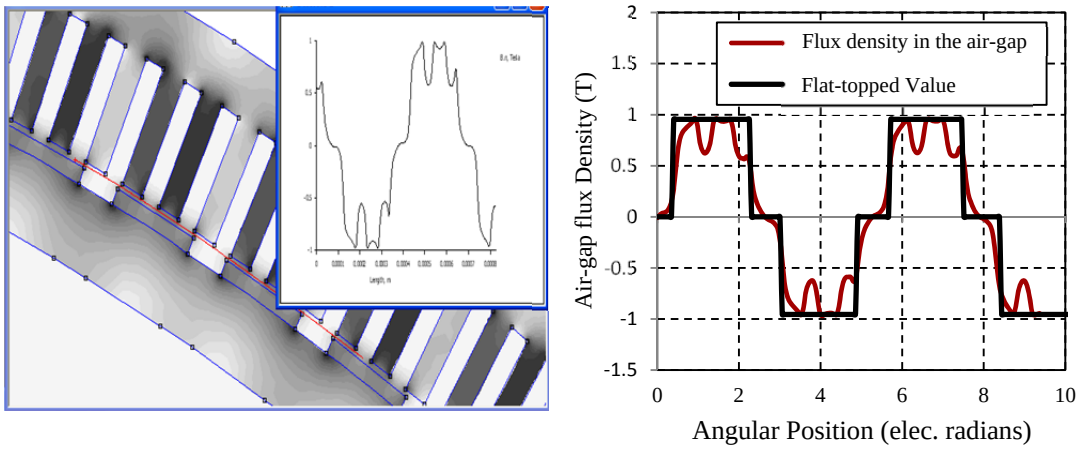

(a) **(b)**

Fig. 5.7(a) Flux density contour plots from FEMM; (b) Radial air gap flux density variation per pole-pair

confidence in using the peak value for the fundamental flux density from analytical model to compute the stress values for the deformed structures.

5.10 Structural dynamic analysis in ANSYS

After estimating the magnetic force and its distribution (from Section 5.8), a 3D transient finite element simulation in ANSYS was employed to visualize and calculate the structural deformations of the rotor and stator. This allowed the simulation of dynamic loads or any combination of static and dynamic loads as in the present case. For the analysis, the loads that were considered to act on the generator

were due to magnetic pressure and nacelle motions. The structural integrity of the design was then evaluated.

For carrying out the analysis a length of simulation time had to be chosen. After several trials, 200 seconds was chosen as the reasonable length of the time that can cause significant deformation that was also stable for the measured amount of time. The time sub-step chosen for the analysis was 0.3125s. Deformations were computed for every sub-step at each nodal location identified by their co-ordinates(r and θ). It was observed during the simulations that within the simulation time, the nodal deformations at a given sub-step, 't' were close to sub-step 't+1' (refer Fig. 5.8), therefore it was sufficient to extract the deformations at the end of the simulation time.

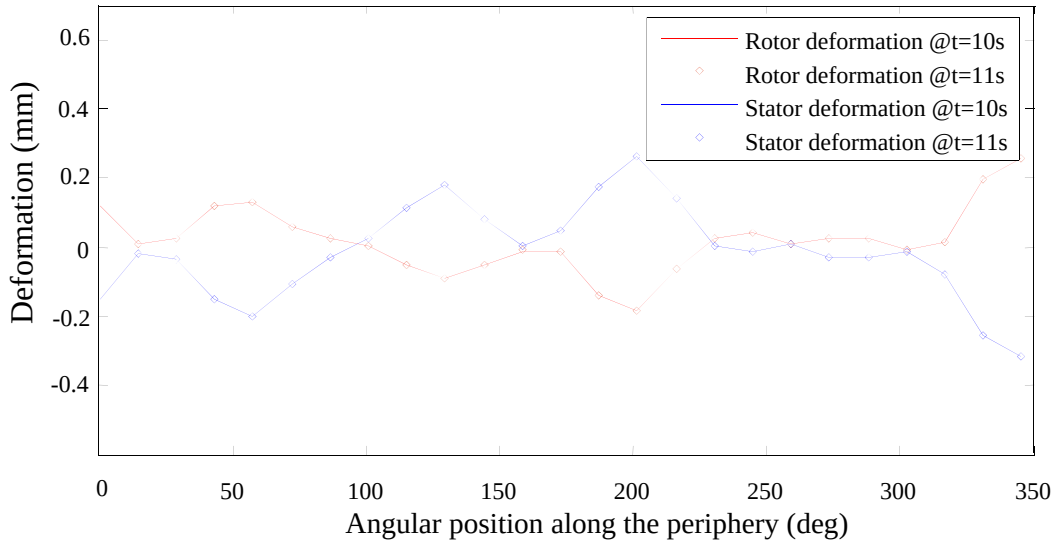

Fig. 5.8 Stator and rotor deformation profiles along the periphery

To understand the impact of various loads on the air-gap of the generator, time history simulations were run separately for three cases namely;

(i) Magnetic field only,

(ii) Nacelle motions only and

(iii) Load combination (Nacelle motions+ Magnetic field)

These load cases were used to examine the structural integrity of the generator and validate the adequacy of the platform. The generator was constrained in all degrees of freedom at the centre where it was imagined to be attached to the shaft. For the first design analysis, bearing supports were assumed to be of very high stiffness. To

understand the influence of bearing stiffness and shaft displacement, the basic theory and some preliminary results for a multi-body model are presented. In all of the cases described in detail below, the nacelle axis was assumed to be parallel to the wave direction (i.e. along z-axis, refer to Fig. 5.9).

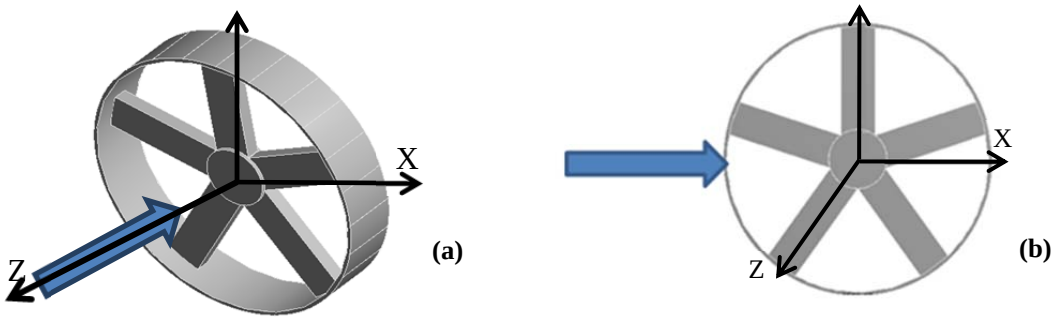

Fig. 5.9 Nacelle alignment (a) Nacelle aligned with wave direction (b) Nacelle perpendicular to wave direction

5.10.1 Magnetic Field only

The normal magnetic stress calculated using equation (5.9) was 0.244 MPa. This force was assumed to act as a uniformly distributed pressure load over each of the 25 segments of the exterior and interior surfaces of the rotor and stator. This load is relatively constant subjecting the rotor and stator structures to constant tension and compression respectively. The self-weight of the structure was modelled by defining the material density and acceleration due to gravity, 9.81 m/s^2. The new air-gap, g_a, was computed using equation(5.8) where, θ varied between 0º and 360º and t = 200 s. Fig.5.10 shows the results for the air-gap distribution, g_a normalised with the rated air-gap under normal condition, g_{nom}. The values were found to vary between 0.869 and 0.985.

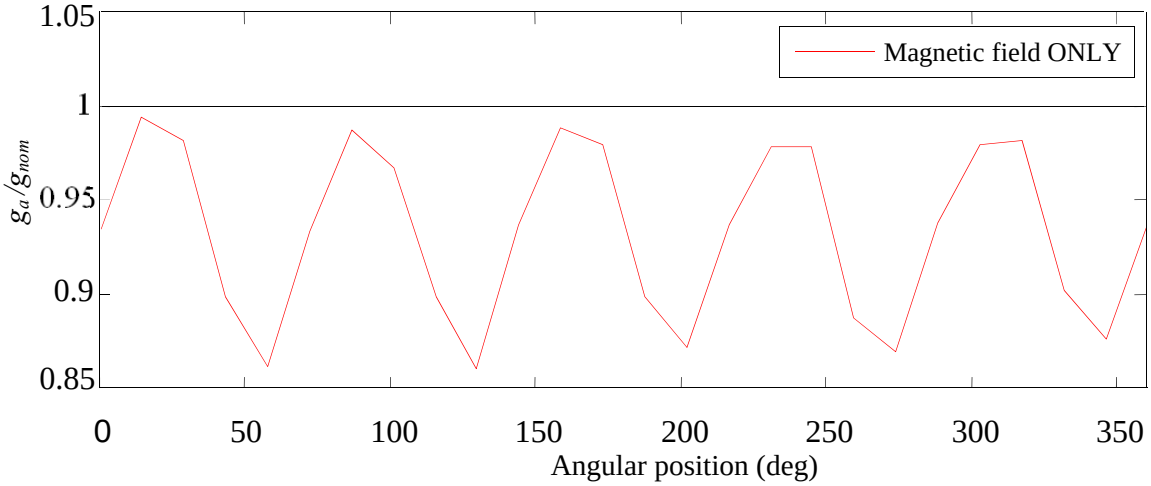

Fig. 5.10 Air-gap variation due to magnetic field only

5.10.2 Nacelle Motions Only

The wave loads considered for this study were assumed to be regular, periodic and of constant amplitude. The corresponding motion loads, i.e. the accelerations and velocity appearing at the nacelle of the wind turbine were cyclic and therefore subject the generator structures to repeated compressive and tensile loads that alternate with time. The OrcaFlex predicted values for surge, heave accelerations and the pitch rotational velocity were applied along the z, y axes. These values corresponded to a wave height of 3m with a repeat period of 6.9s. The gravity component of acceleration was not modelled separately since the acceleration components computed by OrcaFlex were obtained by the resolution of vectors, $\ddot{a}_i$ - g_i, where, $\ddot{a}_i$ is the acceleration measured along an axes of interest and g_i is the component of gravity acting along the axis of interest. The attractive forces from the permanent magnets were assumed NOT to be present. Fig.5.11 shows the air-gap deformation (g_a) observed under wave loads only, normalised over the rated air-gap under normal condition (g_{nom}). Less than 0.03% variation was observed. Fig.5.12 shows the corresponding values for the nacelle motions that were applied. It may be observed that the wave induced motions are not large enough to have significant impact on the structure. This confirmed the stiffness of the structure against external

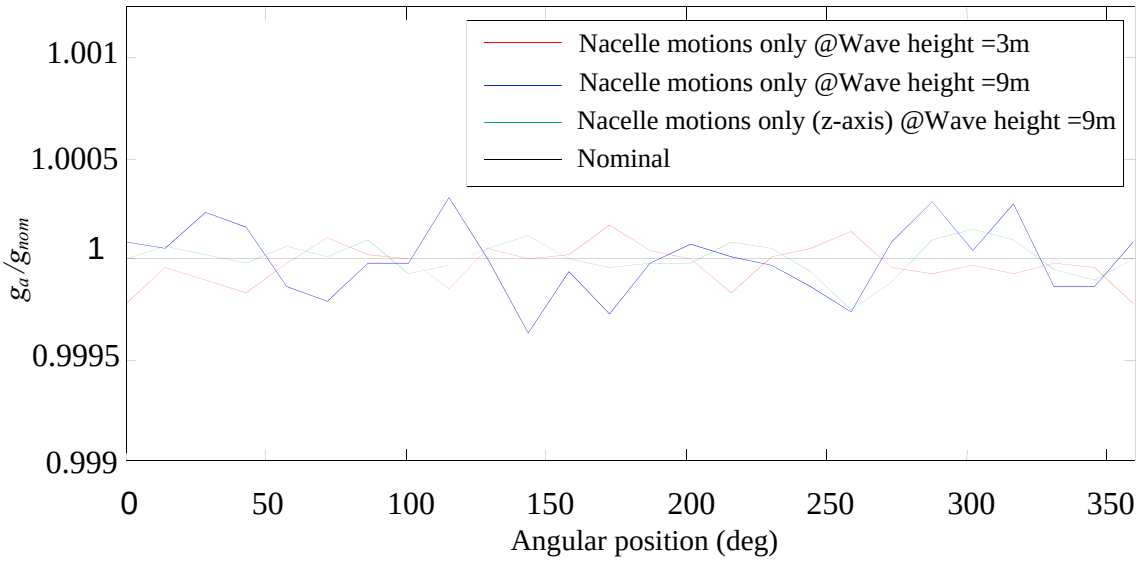

Fig. 5.11 Air-gap variation due to Nacelle motions only

load. It is however important to estimate the impact with different wave heights and wave direction as they can result in higher nacelle accelerations. For this reason, motion loads due to 9 m waves were considered to act along the x and z-axes (refer to Fig. 5.9(b)). For the case where wave loads were assumed to act along the x-axis, any axial variation of eccentricity (non-uniform rotor eccentricity along the axial length of the rotor) was also examined. The deformations were extracted for every 100 mm of the axial length of the rotor and stator structures (refer to Fig.5.13).

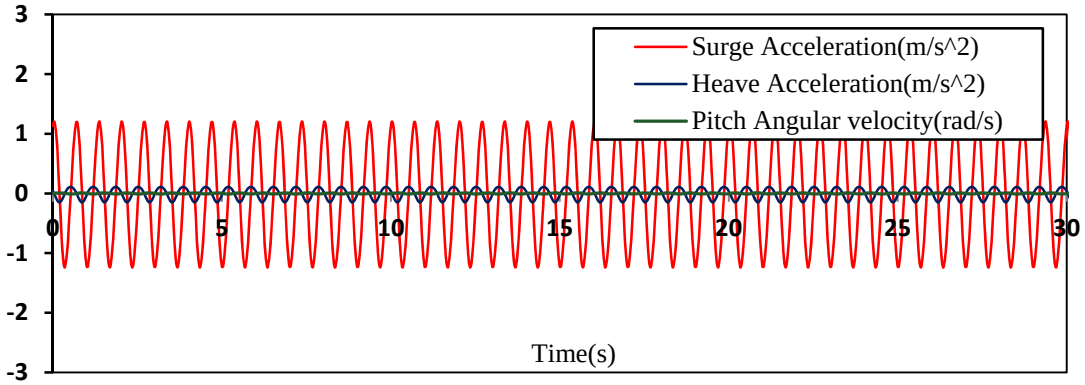

Fig. 5.12 Nacelle acceleration and pitch velocity components for regular wave of height, H=3m and wave period 6.9s (From OrcaFlex).

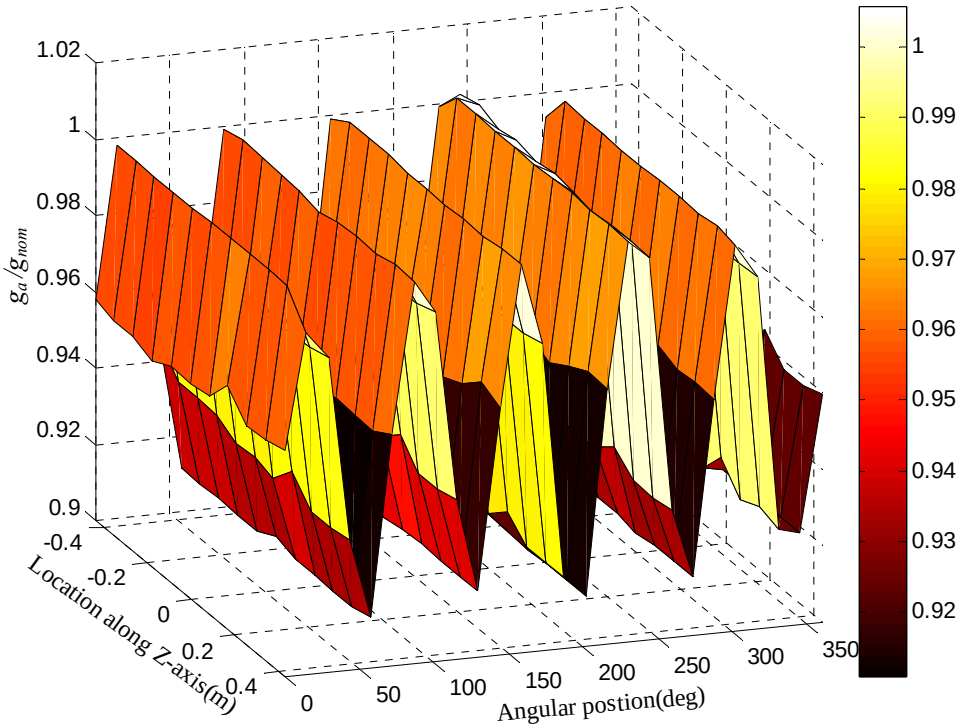

Fig. 5.13 Axial and radial variation of air-gap

It may be noted that negligible variation occurs laterally and this confirmed the initial assumption of no axial variation in air-gap. Also, no major difference was noted between the deformations computed for 3m and 9m wave heights.

5.10.3 Load combination

The effect of a combination of static & dynamic loads (Nacelle motions and normal component of magnetic stress) on the air-gap is important particularly from the point of view of stress analysis and fatigue life of structures. Any change in load direction or magnitude causes a change in stress distribution. As the elastic behaviour of the structure varies with the type of load, it is important to examine the structural response to a combination of axial, radial and torsional loads. For this load case, the alternating motion loads were superimposed on a static pressure load due to magnetic field. Data plotted in Fig. 5.14 show that the distribution of air-gap follows the trend set by the normal magnetic stress load (Fig. 5.10) indicating that the magnetic stress dominates the dynamics of air-gap.

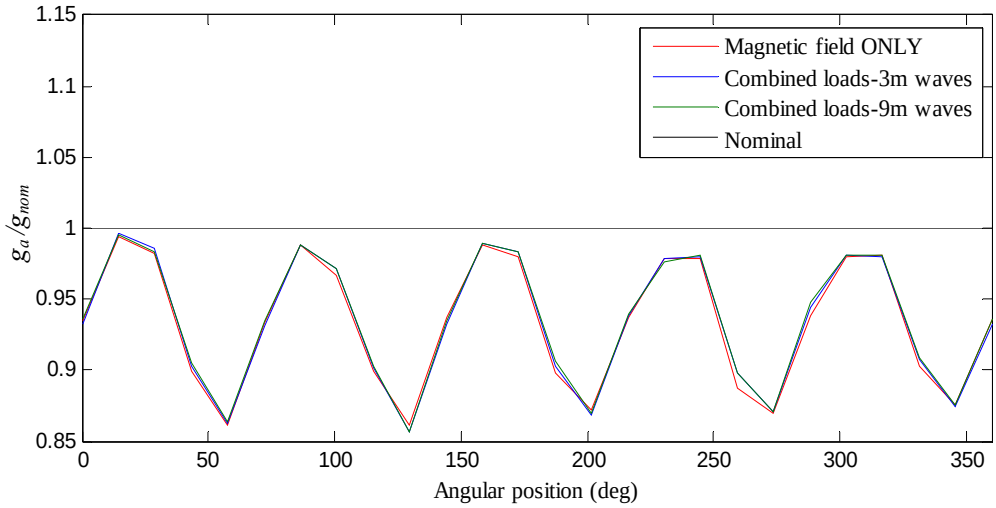

Fig. 5.14 Air-gap variation due to Load combination (Magnetic field+ wave loads)

The above study was useful in isolating the important load endured by the direct-drive generator. Assuming no wind and when the rotor is stationary, wave loads (with different heights, different directions) do not induce any observable structural deformation over a reasonably short time of application, assuming a high stiffness for the bearing supports. The generator structure was inherently less stiff than what was

required to maintain the air-gap within the 10% deflection limit and the normal magnetic stress was the single dominant force. In terms of hydrodynamic response, the floating turbine system exhibits very low accelerations (< 0.3*g*) even for wave heights of up to 9 m. The magnitudes of motion response were therefore not high enough to cause the generator structure to deform excessively implying a good design. The results also suggest that for a given light-weight structure, the air-gap instability is primarily brought about by the magnetic system. The common methods of dealing with such air-gap instability are by increasing the structural stiffness i.e., adding extra mass to minimise the deflection or by increasing the design air-gap. These methods are explored later in Section 5.14.

5.11 Contributions to air-gap eccentricity from bearing compliance

It is a common tendency for drive-train designers to favour stiffer shaft designs to maximise damping, stability and effective torque transfer. In the above study cases, the shaft was assumed to be rigidly supported. However, in practice there exists a certain degree of compliance in the shaft as well as from bearing supports which contribute to air-gap eccentricity. For a FWT system, shaft displacements can be large if the support stiffness is not carefully designed. It is important to understand the impact of bearing stiffness and shaft displacements on eccentricity. To understand and model these effects, multi-body simulation tools such as HAWC2[135] and SIMPACK [136] were required. Therefore a more comprehensive research was carried out independently; only the analytical model and few results are presented here for the purpose of understanding. Detailed results on drive-train investigation are presented in Chapter 7.

5.11.1 Bearing stiffness Versus Magnetic stiffness-theory

A simple mechanical model of the shaft–bearing arrangement for the radial flux PMSG is shown in the Figure 5.15(a). The generator rotor is attached to the shaft that is supported by two bearings. The system has six degrees of freedom permitting translational and rotational displacement of the shaft along the three co-ordinate axes. Let x- axis represent the axis of rotation, for a shaft supported by bearings with radial stiffness value for the y and z directions. If an external wave load radially

displaces the shaft, by a certain distance, δy, at time, t, this alters the air-gap distribution. This change in air-gap contributes further to the unbalanced magnetic pull (UMP) on the periphery of the rotor (Fig. 5.15(b)), in addition to any pre-existing generator structural deformation.

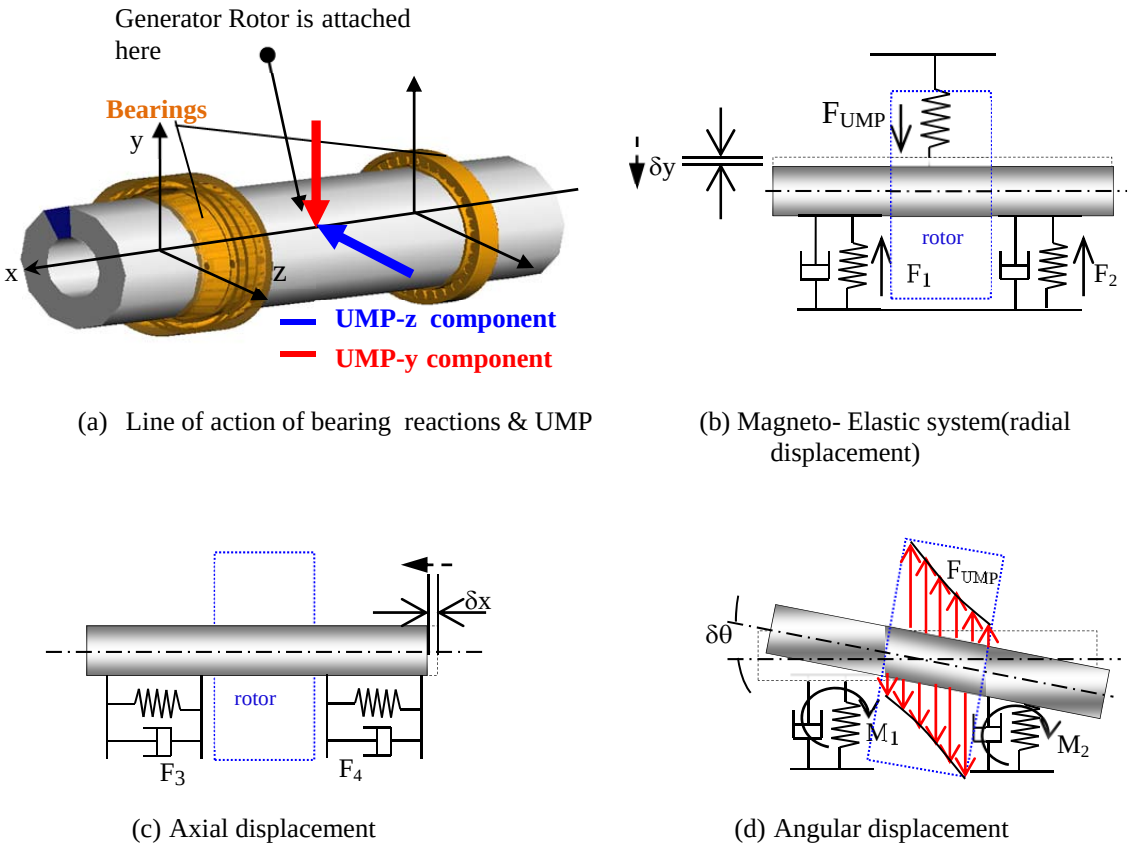

(a) Line of action of bearing reactions & UMP

(b) Magneto- Elastic system(radial displacement)

(c) Axial displacement

(d) Angular displacement

Fig. 5.15 Shaft-bearing arrangement

It must be noted that the shaft can undergo axial displacement (by a certain distance δx as shown in Fig. 5.15(c)) or angular displacement (δθ, as shown in Fig. 5.15(d)) and corresponding reaction forces (F_3 & F_4) and moment components (M_1 & M_2) are generated at the bearings. While a uniform axial displacement does not disturb the magnetic equilibrium, a rotational displacement creates a UMP load which has a distribution depending on the air-gap distance (maximum load in the region with lowest air-gap and vice-versa). In order to simplify the problem, for the present study, contributions to UMP were assumed to arise only from radial displacement of the shaft. The effects of UMP due to shaft tilting were ignored. An approximate

linear model was used to relate the change in air-gap caused by radial shaft displacement to unbalanced magnetic forces, F_{UMP_SHAFT} as

$$F_{UMP\_SHAFT} = A\frac{g_{ash}}{g_{nom}} + B \tag{5.10}$$

where, g_{ash} is the measured air gap change due to an incremental shaft radial displacement(bearing deflection) in the y and z-directions (denoted by δy and δz respectively) computed as

$$g_{ash} = \sqrt{\delta y^2 + \delta z^2} \tag{5.11}$$

where, A and B are force co-efficients that can be determined from magneto-static simulations in FEMM for certain pre-defined amount of eccentricity. The UMP forces will have two components (for the y and z directions respectively). A detailed model for UMP forces due to shaft displacements will be presented later in Chapter 7. The UMP forces due to structural deformation can be obtained by integrating equation (5.9) about the circumference of the rotor. The net force due to UMP in the radial direction, F_{UMP_RADIAL} can be either additive or subtractive depending on the nature of structural deformation or the direction of shaft displacement given as

$$F_{UMP\_RADIAL} = F_{UMP\_SHAFT} \pm F_{UMP\_STRUCTURE} \tag{5.12}$$

The resulting forces are assumed to act at the centre of the shaft where the rotor is attached (refer to Fig. 5.15(a)) and tend to displace the shaft further. The forces act in a direction opposite to the restoring forces from the bearings. In general, the forces due to UMP can be imagined as a mechanical spring with negative stiffness (denoted as k_{mag}). The magnitude of this magnetic stiffness, if comparable to the mechanical bearing stiffness, tends to weaken the restoring forces provided by bearings. Referring to Fig. 5.15(b), if F_1 and F_2 represent the restoring forces from the bearings along the y-direction, then for a displacement δy, the y-component of magnetic stiffness, k_{Ymag} is obtained by dividing equation (5.12) by δy giving, $k_{Ymag} = \frac{F_{UMP\_RADIAL}}{\delta y}$. The bearing mechanical system acts as a spring-damper system with certain stiffness and damping. Unlike the bearing mechanical system, no

damping is assumed for the magnetic system. The total stiffness of such a magneto-elastic system (Fig. 5.15(b)) consisting of two mechanical springs (stiffness k_1 and k_2) and the magnetic force (with negative stiffness, k_{mag}) acting in parallel can be written as

$$k_{total} = k_1 + k_2 - k_{mag} \tag{5.13}$$

The structural equilibrium is maintained by the main shaft bearings that must be designed to withstand the thrust loads and absorb any deflection due to shaft bending or displacement caused by off-axis loads. A necessary condition for mechanical stability of the drive-train system, for the axial, radial and tilt displacements can be expressed by the following force and moment balance equations:

$$\sum F_{Axial} = F_{axial\_Structure} + F_{axial\_bearing} - F_{ext} = 0 \tag{5.14}$$

$$\sum F_{Radial} = F_{radial\_Structure} + F_{radial\_bearing} - F_{UMP\_RADIAL} - (F_{ext} \pm F_{inertia}) = 0 \tag{5.15}$$

$$\sum M = M_{Structure} + M_{bearing} - M_{UMP} - M_{ext} = 0 \tag{5.16}$$

Where, $F_{axial\_Structure}$ and $F_{radial\_Structure}$ represent the stiffness of the generator support structure in the axial and radial directions, F_{UMP_RADIAL} represents the forces due to unbalanced magnetic pull caused by radial shaft displacements, F_{ext} represents the forces due to external load (for e.g.: wave induced motions in the case of FWT), $F_{axial\_bearing}$ and $F_{radial\_bearing}$ are the total restoring forces from the bearings in the axial and radial directions and $F_{inertia}$ is the inertia of the rotor-shaft-turbine assembly. $M_{Structure}$ and $M_{bearing}$ are the bending stiffness of the support structures and bearing, M_{ext} represents an external moment load and M_{UMP} is the moment component of UMP generated due to shaft tilting (which can be derived for the distributed load in Fig.5.15(d)). It may be noted that UMP term appears only for the radial and tilt displacements. In practice, since the shaft can undergo translational as well as rotational displacements; the stiffness of the support structure and bearings must be carefully chosen to ensure mechanical stability for all conditions. For simplicity, the discussion focuses on radial part of the force balance equation. In general, the generator support structure is designed to have an elastic stiffness that is great

enough to balance the magnitude of magnetic stiffness. If the generator body is assumed to be perfectly rigid in radial direction, then the stability of the system depends on the restoring forces from the bearings. Thus equation (5.15) reduces to:

$$F_{radial\_bearing} - F_{UMP\_RADIAL} - (F_{ext} \pm F_{inertia}) = 0 \qquad (5.17)$$

A necessary condition for air-gap stability requires that $F_{radial\_bearing} >> F_{UMP}$ for all load conditions. This implies that the stiffness ratio, say ε, between the bearing stiffness, $k_{radial\_\text{bearing}}$ and the magnetic pull constant k_{mag} must be large ($k_{radial\_bearing} >> k_{mag}$ for all load conditions) so that when the external load reaches a certain threshold, defined as the $F_{critical}$, the magnetic stiffness becomes comparable to mechanical stiffness and the system loses its stability. Dividing equation (5.17) by displacement, δy, gives the relationship for critical stiffness, $k_{critical}$

$$k_{radial\_bearing} - k_{mag} = k_{critical} \qquad (5.18)$$

Thus, the bearing mechanical system for a FWT must be optimally designed to not only resist deflection due to normal loads but also be stiff enough to overcome the negative stiffness from UMP and the external loads in a FWT.

5.11.2 Sensitivities of air-gap eccentricity to bearing compliance

The following discussions are based on a preliminary work on sensitivity study for air-gap eccentricity and UMP to bearing stiffness in a radial flux PMSG for a FWT system carried out using SIMPACK. This study was carried out on a multi-body drive-train model for a 5MW machine considering wind loads, rotor rotation, buoy motions as well as control system action, with the stiffness data for bearings provided by the bearing manufacturer (refer to APPENDIX-B). The complete details of the mechanical model will be described later in Chapter 6. This study analysed the forces due to UMP caused only by radial shaft displacements using equation (5.10). Therefore, the generator structure was assumed to be rigid. In the following, the results for four cases of bearing stiffness (drive-train flexure) are discussed. Case 1 is a base case with a relatively rigid system with an equivalent bearing radial stiffness

at 3.81×10^{10} N/m and Case 2 was 20 % less stiffer in the radial direction with a stiffness value of 3.175×10^{10} N/m. Cases 3 and 4 were less stiffer than the base case by 25% and 30% respectively. Case 1 represents the ideal case with eccentricity restricted to below 10% and Case 2 demonstrates a more realistic scenario. Cases 3 & 4 were treated as supplementary problems for examining the stability and validity of the model. For all the cases,10% damping from bearings was assumed in the radial direction as per the recommendations in [150]. These stiffness models were implemented for a 5MW direct-drive system and one-hour simulations were carried out at a mean wind speed of 25m/s (representing the highest wind speed at which the 5MW wind turbine may be operated) and a wave height of about 6m. The air-gap length for this machine was 6.36 mm. Complete details of the mechanical model and the methodology used for these simulations is presented in Chapter 6.

Sample time histories of measured change in air gap due to shaft displacements (g_{ash}) for Cases 1-3 are shown in Fig. 5.16. It may be noted, that shaft system in Case-1 remains relatively stable and non-compliant. Case 2 with 20 % less stiffness still results in a tolerable behaviour with displacements limited to below 2mm. With significantly larger displacements and the possibility of air-gap closure, Case 3 is not practicable.

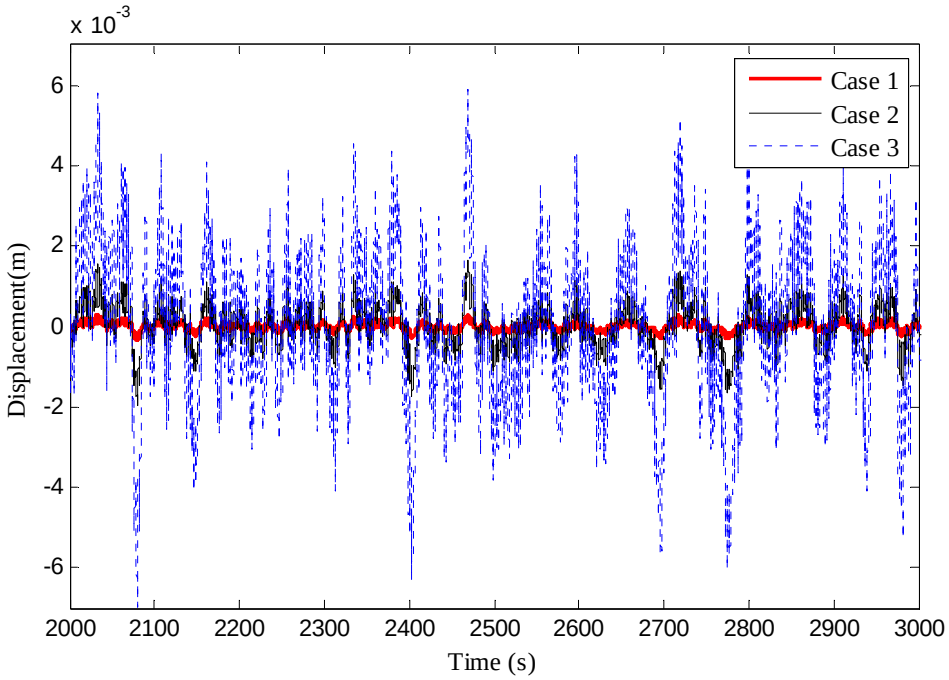

Fig. 5.16 Shaft radial displacements (g_{ash}) measured for different bearing stiffness

A reduced bearing stiffness also suggests a greater unbalance of magnetic forces within the generator as a result of increased eccentricity. This manifests itself as an additional bearing load. The UMP forces were computed for the measured shaft displacements using the equation 5.10. The time histories of the main bearing radial load(y-component) and the y-component of UMP are shown from Figures 5.17 to 5.20. These plots show a general increase in F_{UMP_SHAFT} from 20kN for Case 1 to as high as 2MN for Case 3. Case 4 at 30 % lower stiffness results in an extreme case where the magnetic stiffness and bearing stiffness become comparable, the system completely loses its stability and becomes inoperable. Thus Cases 1 and 2 yielded most promising results. A closer examination of the Cases 1 and 2 will be useful in deciding the optimal stiffness for the bearing system.

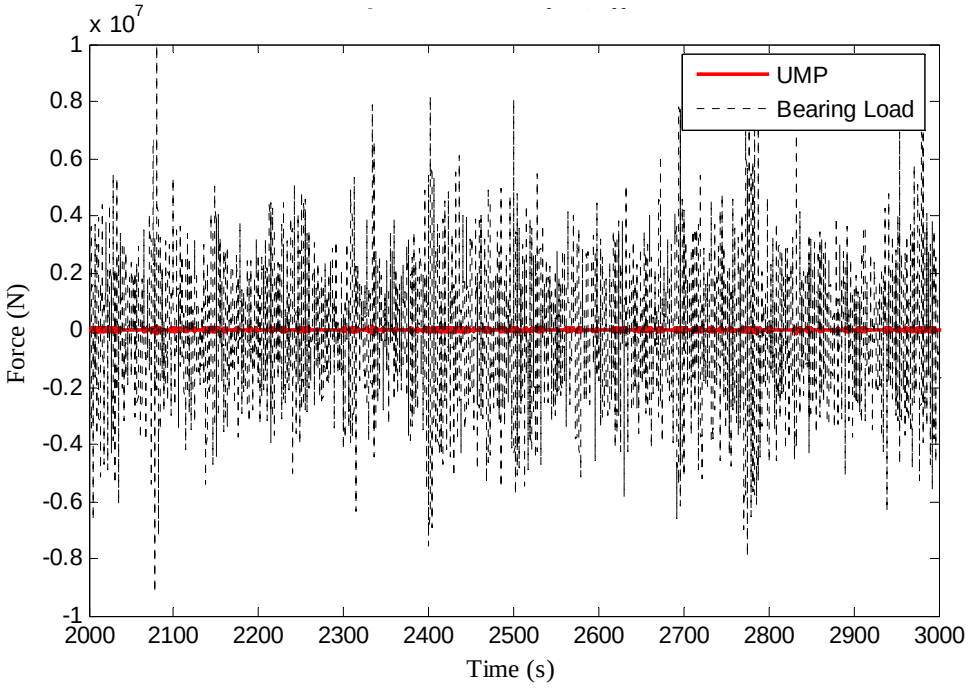

Fig. 5.17 UMP and bearing forces for Stiffness Case 1

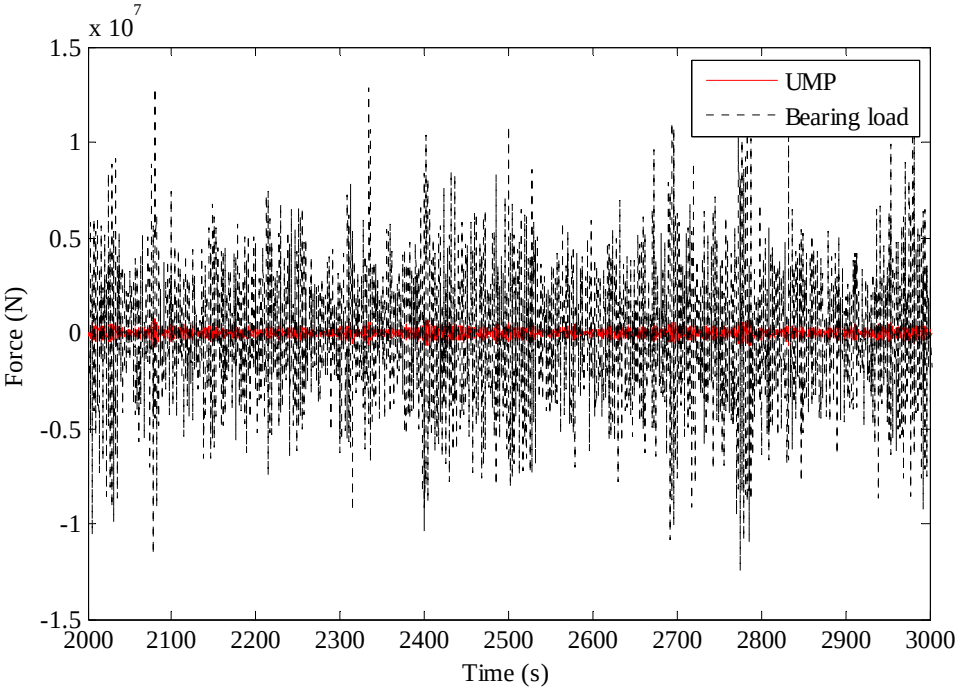

Fig. 5.18 UMP and bearing forces for Stiffness Case 2

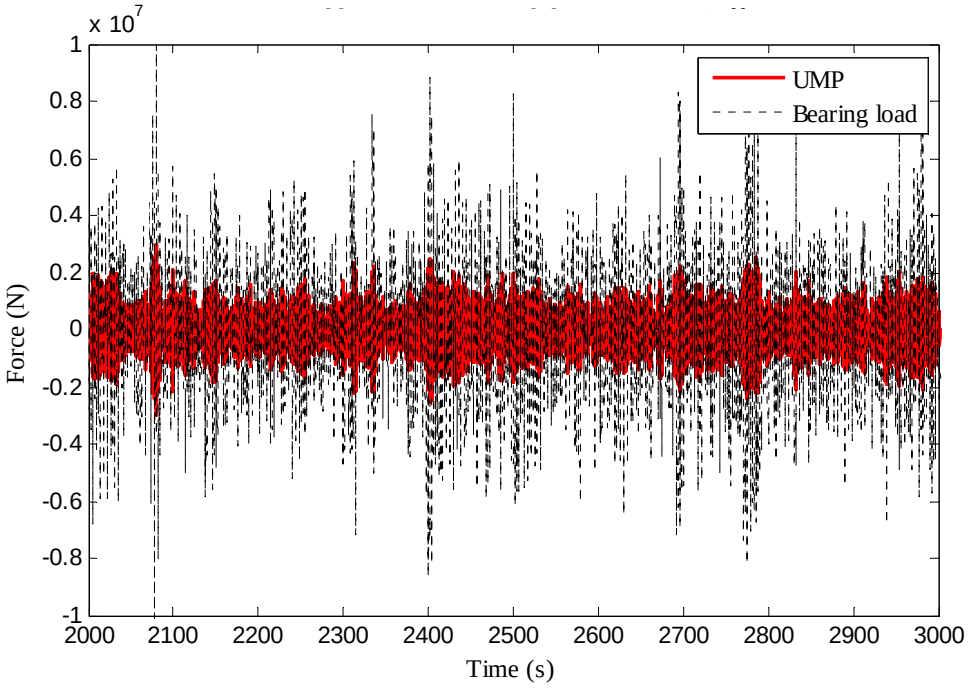

Fig. 5.19 UMP and bearing forces for Stiffness Case 3

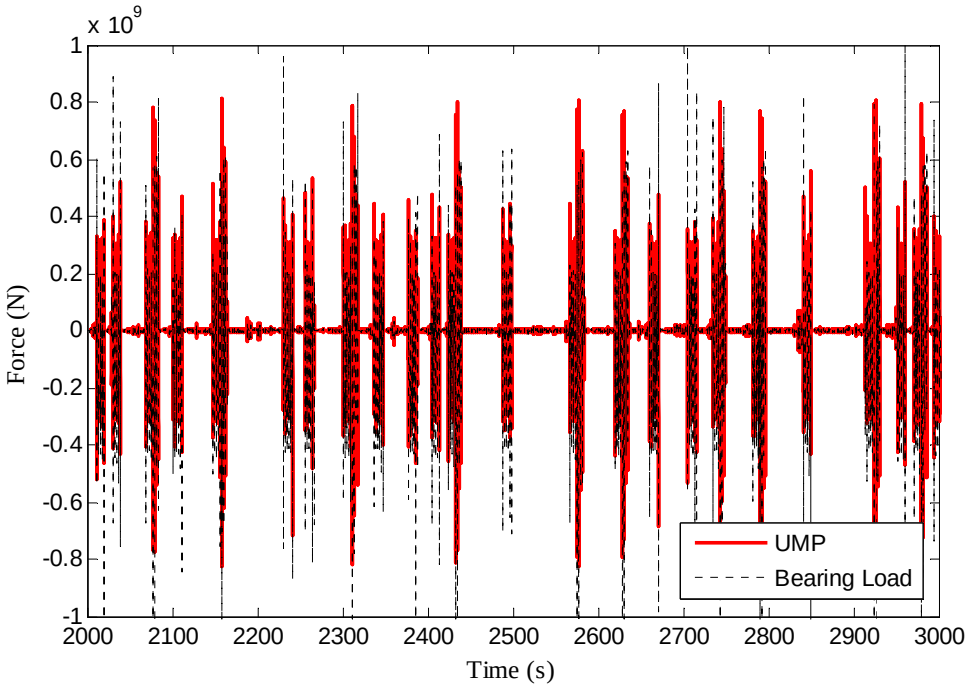

Fig. 5.20 UMP and bearing forces for Stiffness Case 4

Cases 1 and 2 were further tested for a range of wind speeds from 4-25m/s and wave heights from 1.96-5.88m. The percentage of eccentricity due to shaft displacement was computed as a ratio of shaft displacement to nominal air-gap $\left(\frac{g_{ash}}{g_{nom}} \times 100 \right)$.

Fig. 5.21 shows a general increase in mean values of shaft induced eccentricity with increasing wind speeds and wave heights for both the cases. It may be noted that shaft system with higher radial stiffness (Case 1) can however help limit the mean eccentricity induced by shaft displacements to 2%. The above results show that bearing stiffness must be sufficiently high to limit the eccentricity from shaft compliance to acceptable levels. At the same time, higher bearing stiffness would imply a higher natural frequency of drive-train transverse vibrations. A full eigen analysis can point towards possibilities of mechanical resonance.

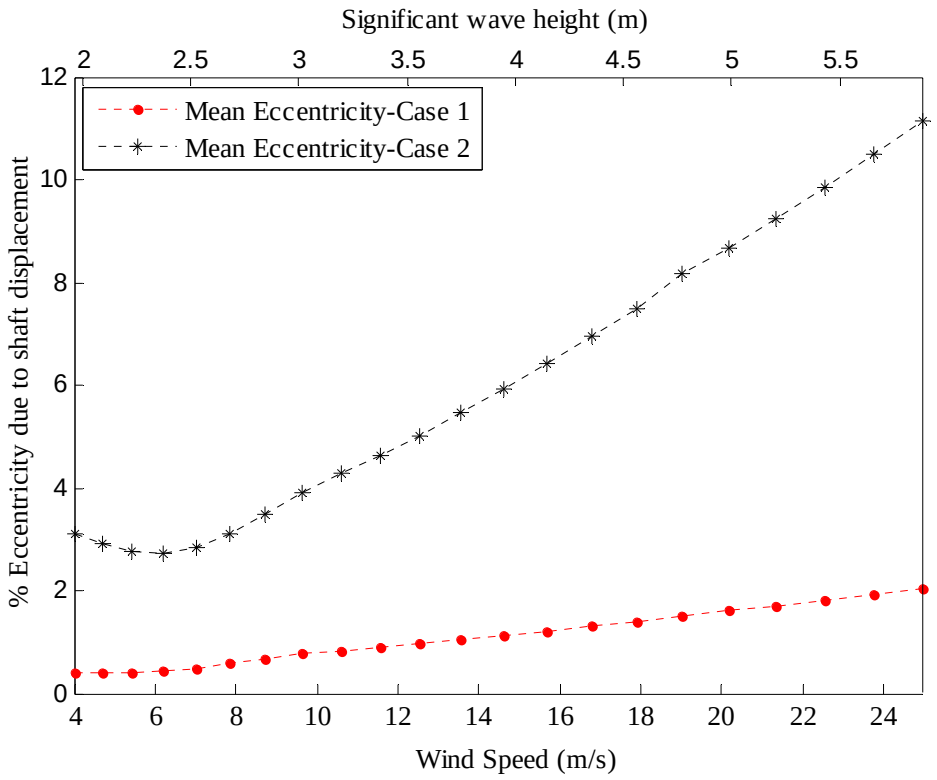

Fig. 5.21 Shaft Induced Eccentricity at different wind speeds for FWT system

Results from Sections 5.10 and 5.11 only emphasize the need for a careful evaluation of stiffness for generator support structure and drive shaft (bearing system) for the FWT system so as to limit the overall air-gap eccentricity to below 10%. There is yet no hard and fast rule for determining the optimal bearing stiffness, but in general, decision on bearing stiffness is a compromise with generator support structure stiffness in the need to limit the overall eccentricity to 10%. The following sections proceed with the investigations on the generator support structure and its design implications.

5.12 Magneto-elastic stability of the generator - Secondary deflection

Structural deflection causes the air-gap to decrease (or increase) and the flux density in the air-gap to increase (or decrease) accordingly. As the eccentricity persists for longer periods, there will be secondary deflection caused by negative magnetic stiffness [151]. Depending on the structural stiffness, the secondary deflection either stabilises with time or continues until the rotor touches the stator and eventually no

longer operable. For a typical design, the allowable deflection is only 10% of the air gap clearance otherwise the air-gap flux density will increase significantly leading to an increase in normal stresses and even greater deflection[134]. In order to ensure that the eccentricity does not exceed 10%, it is necessary to determine the optimal generator design by examining its magneto-elastic stability for a sustained period. For this purpose, an iterative procedure similar to what was suggested in reference [138] was implemented using the analytical model proposed in this study (Fig. 5.22). The motion loads and the stresses due to the magnetic field were assumed to act for a period of 200s for the first iteration and the deformations were extracted. As can be expected of secondary deflection, as time elapses and loads persist, the variation in air-gap around the periphery results in a re-distribution of magnetic field. For the next iteration, the stresses due to magnetic field have to be re-evaluated for the new air-gap and re-applied on the already deformed structures. It is assumed that the motion loads remain unchanged during this period. Also the impact of generator behaviour on the platform motion was not assessed. For the purpose of assessing the long-term structural stability, air-gap instability was allowed to be sustained for a relatively longer period of time. However, for a design air-gap of 4.34mm, secondary deflection causes the air-gap to close after the 4th iteration (after sustaining 800s of eccentric condition). Figures 5.23 & 5.24 show the polar and surface plots for the air-gap normalised for each iteration. Fig. 5.25 shows the corresponding plot for stresses normalised by actual stress on un-deformed structures. It was observed for the region where the air-gap closed (129°) that each successive iteration introduced a 50% increase in deflection on an average.

This study considered only the impact of cyclic loading from the wave induced motions, with the number of load cycles lower than the fatigue limit. As the structure failed to maintain the air-gap after 800s, there was no opportunity to investigate the effect of longer load cycles for the lightweight structure. Also the presence of wind/control system action was not considered. If such conditions are included, the possibility of progressive and localized structural damage cannot be ruled out.

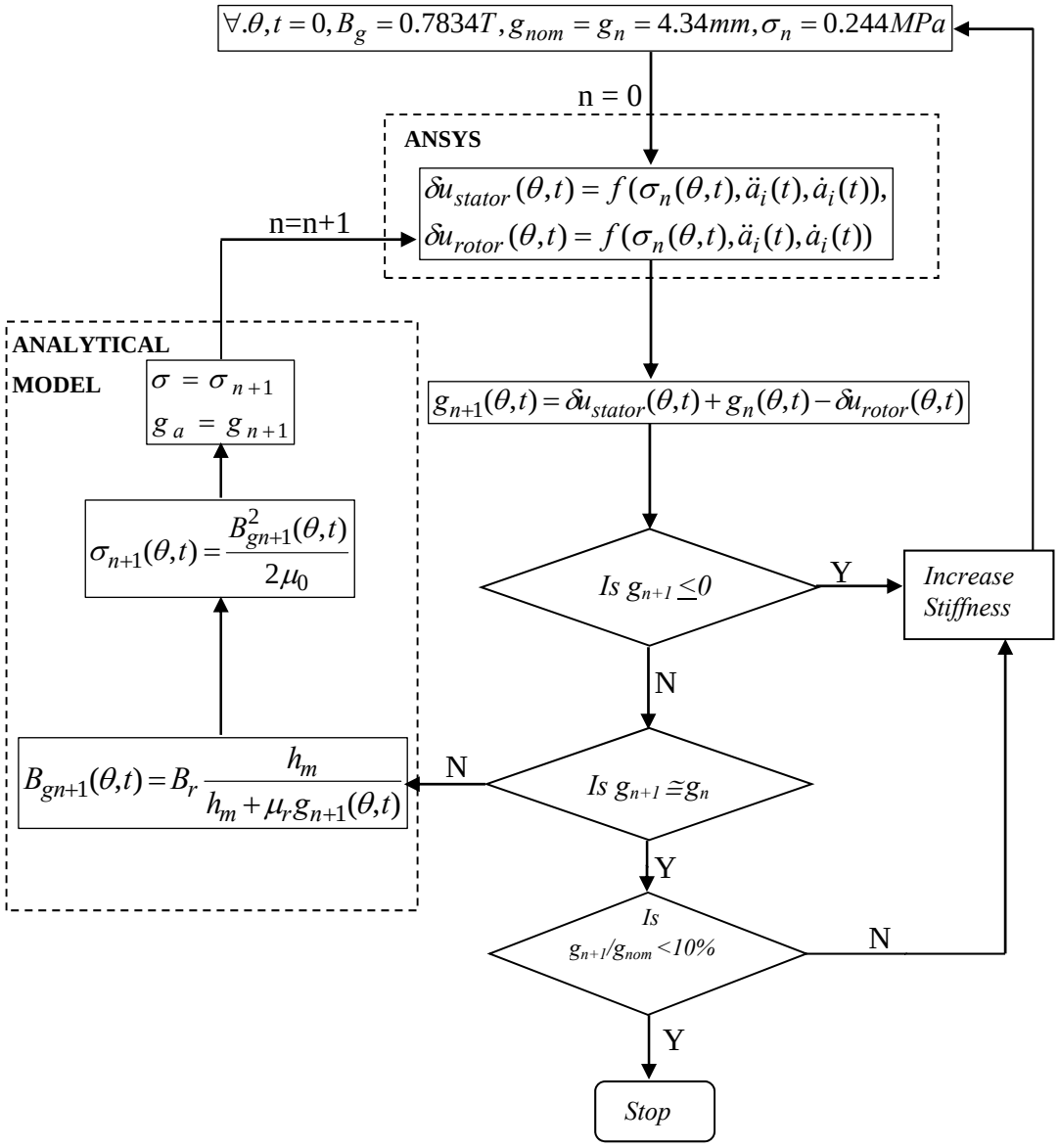

Fig. 5.22 Iterative procedure for air-gap deflection for radial flux PMSG (based on the analytical model from section 6.8)

where, $\ddot{a}_i(t)$ - Nacelle Acceleration component

$\dot{a}_i(t)$ -Nacelle Velocity component

n- Iteration number

$\delta u_{rotor}(\theta,t)$–Rotor radial deflection measured at node (r,θ) at time, *t*

$\delta u_{Stator}(\theta,t)$–Stator radial deflection measured at node (R_o,θ) at time, *t*

Note: The deflections are computed by applying the magnetic stress, nacelle acceleration and velocity loads in ANSYS

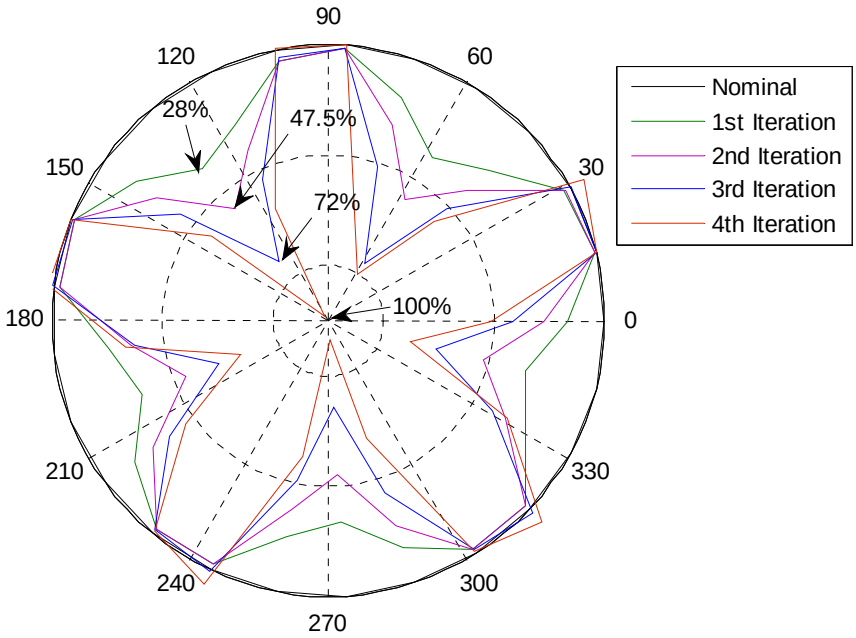

Fig. 5.23 Percentage air-gap reduction after each iteration

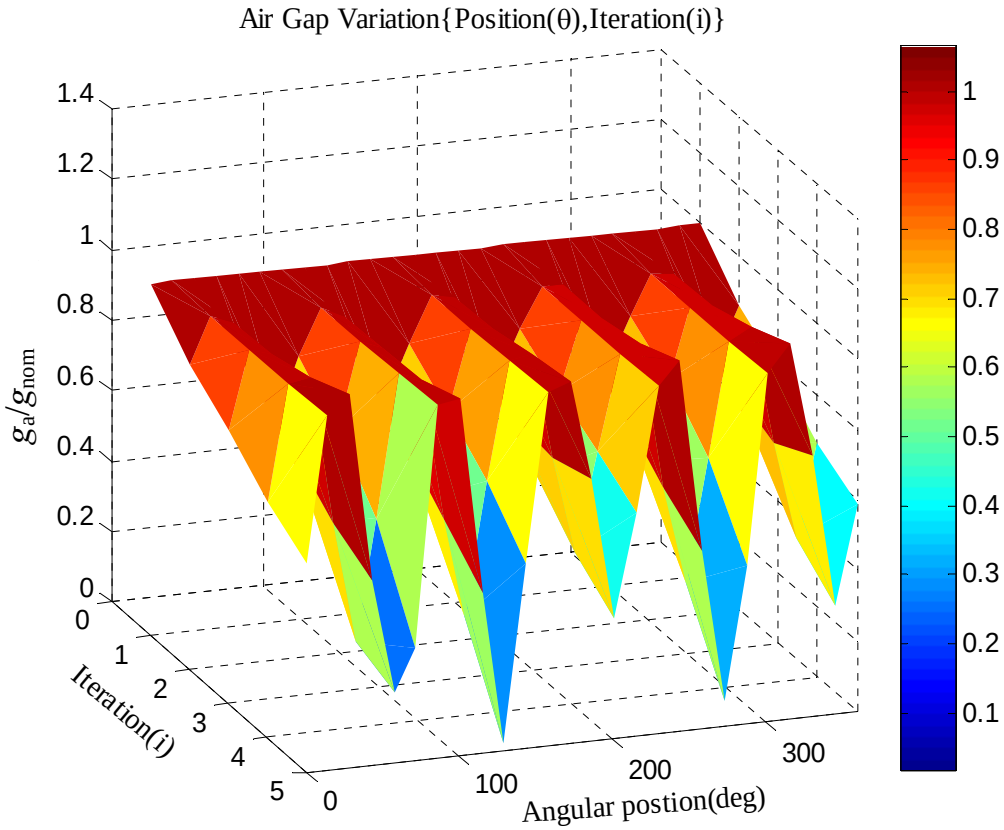

Fig. 5.24 Air-gap variation as a function of position and iteration

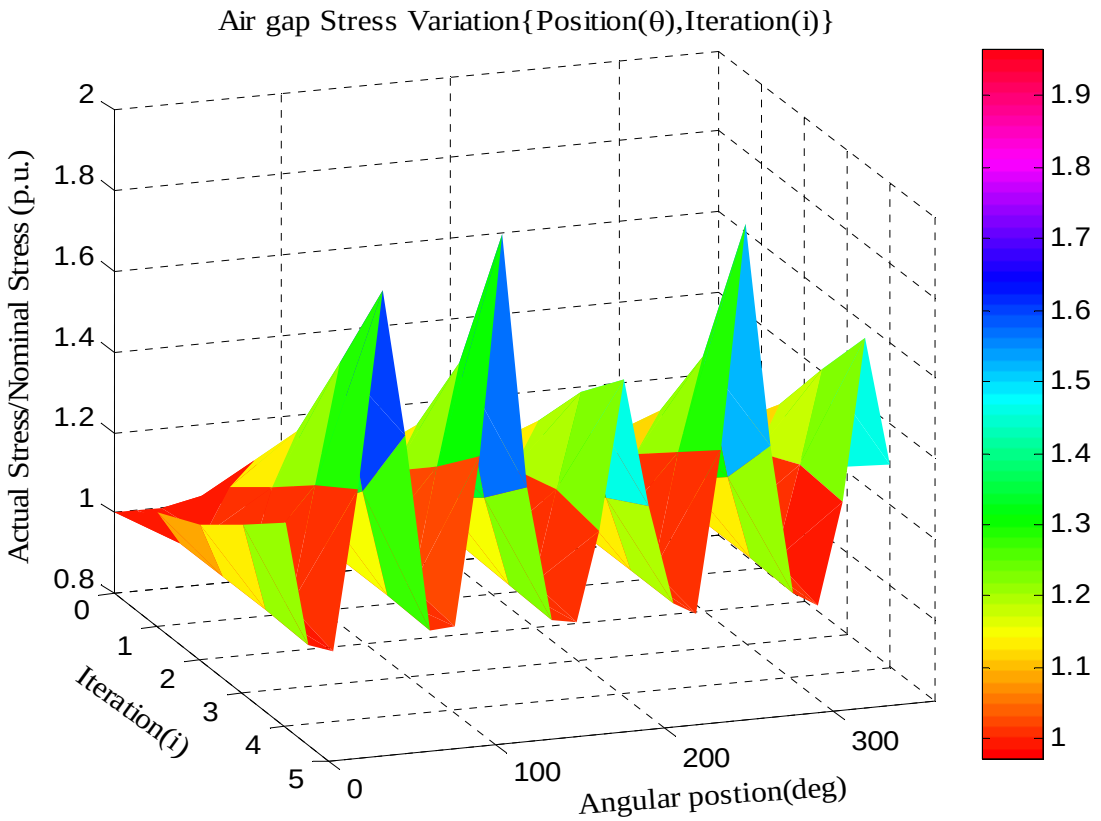

Fig. 5.25 Stress variation as a function of position and iteration

5.13 Comparison of results with FEMM

The nature of the electromagnetic problem in this study is dynamic. However, analyses in FEMM are for mechanically static configurations. In order to be able to make inferences on the dynamic behaviour of the magnetic field, a quasi-static approximation will be required. A series of simulations of static configurations were carried out. The static configuration of every simulation represented the final state of the generator after it had undergone deformation. To simulate the eccentric condition observed after each iteration, the elements that define the rotor and stator structures were grouped together to represent the 25 segments that were previously defined in the analytical model (Section 5.8). Each group was then incrementally shifted by a known amount deflection δ_x and δ_y estimated for each iteration by ANSYS simulations. Fig. 5.26 shows the flux contour plots for each iteration as obtained from FEMM simulations corresponding to a region along the periphery, where the air-gap was reduced significantly.

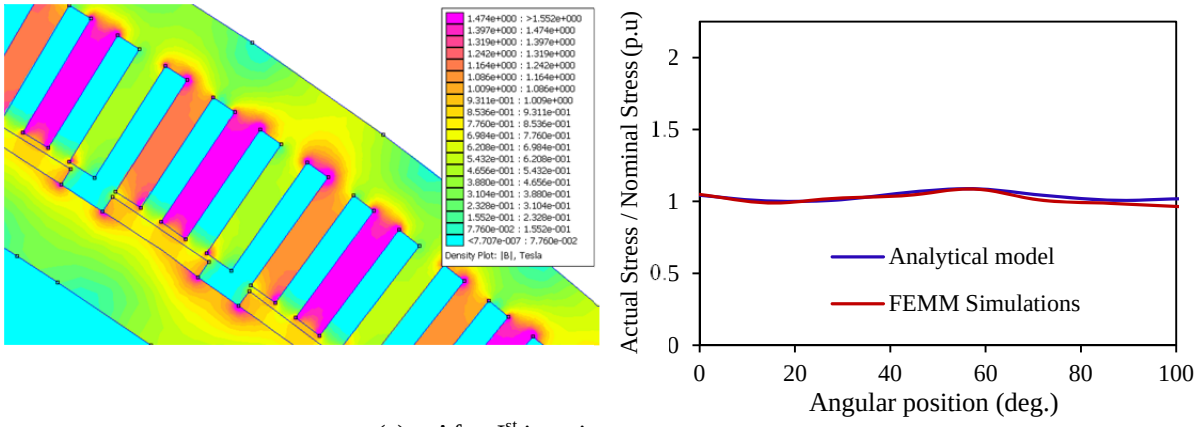

(a) After I[st] iteration

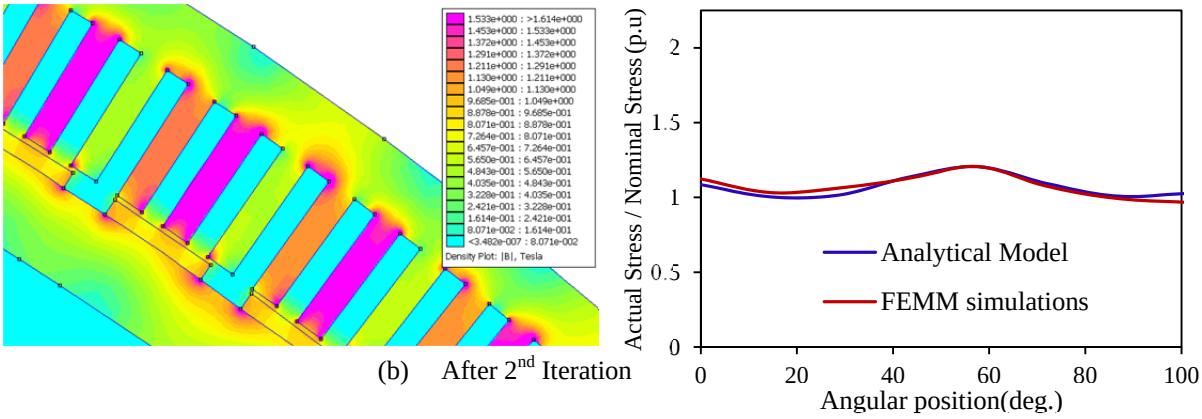

(b) After 2[nd] Iteration

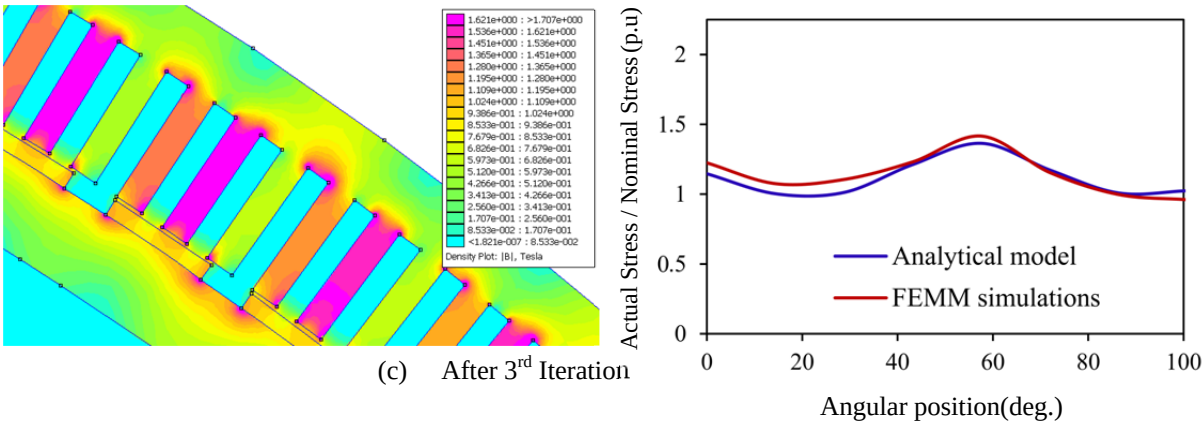

(c) After 3[rd] Iteration

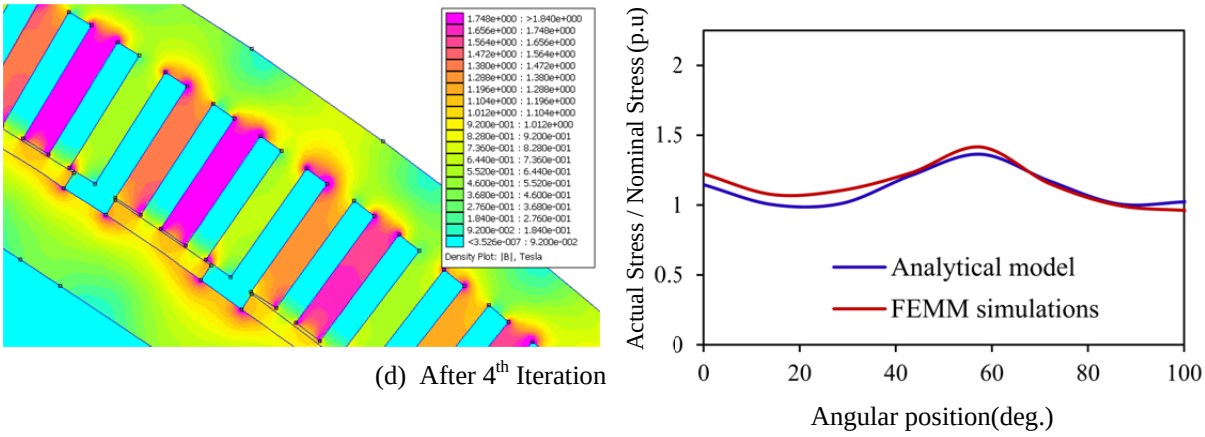

(d) After 4[th] Iteration

Fig. 5.26 Flux contour and variation of normalised stress between 0°-100° along the periphery

It may be observed from these plots that as the rotor deformed, magnets moved closer to the stator teeth causing an increase in air-gap flux density. Referring to the pink contours on these plots, the range of highest flux densities increases from 1.47 Tesla for the 1st iteration(refer legend of Fig. 5.26(a)) to 1.74 Tesla for the 4th iteration(refer legend of Fig. 5.26(d)). The corresponding plots for normalised stresses show the stress values peaking at the location of 57.6º. These values almost double after the 4th iteration. The trends show a very good agreement between the analytical model and the FEMM simulations. However, a small difference exists as the analytical model does not account for leakage flux effects (Refer Table 5.5). It may also be noted that the difference increases with the iteration. Since the effect of fringing which becomes negligible with smaller air-gap, the flux-density in the air-gap is greater and better captured by FEMM simulations. However, this effect is not captured by the analytical model, as a result, the difference increases with the iteration as the air-gap becomes smaller.

Iteration number	Analytical	FEMM
1st Iteration	1.088	1.08
2nd Iteration	1.205	1.206
3rd Iteration	1.364	1.41
4th Iteration	1.856	2.06

Table 5.5 Comparison of normalised stresses computed using the analytical model and FEMM simulations

5.14 Possible Solutions for prevention of air-gap from closing

To prevent the air-gap from closing, two design options were investigated. In the first design option, the structures were made stiffer to limit the radial deflection to 10% of the nominal air-gap. In the second option, the design air-gap was increased with a corresponding increase in active magnetic material. In these studies, attempts were made to identify the extent to which the generator weight and the design air-gap had to be increased in order to meet with the 10% deflection criteria. The possible implications on the rest of the system were also investigated.

5.14.1 Design Option I -Increasing Structural Stiffness

In order to investigate the effect of increased stiffness, eight design cases were considered and the corresponding results are included in Table 5.6. The rotor and stator yoke thicknesses (h_{yr} and h_{ys} respectively) were progressively increased to restrict the maximum radial deflection to < 3% after the first iteration, so that the secondary deflections from successive iterations do not exceed the 10% limit. This increased the overall generator mass to 90 tons for Case 8. As was done previously for the base case, the magneto-elastic stability of the structure was investigated using the iterative analytical procedure (described in Section 5.12) for the heaviest structure (Case 8)**.**

Fig. 5.27 shows the percentage reduction in air-gap after each iteration for the base case and case 8. It was noted that the stiffer structure in case 8, almost retained its shape even after the 4th iteration, with a maximum deflection of 6.9%. It is expected that the structure will remain stable irrespective of the duration for which it endures the loads. In all of the design cases, the motion responses were assumed to be unchanged. However, the motion response of a system with an increased nacelle mass is expected to be different from the values that were considered earlier (from Step 1, Fig. 5.3). A detailed investigation of the impact of generator structure on nacelle response was not in the scope of the investigation. However, the results are useful in making a preliminary assessment of the design needs of a direct-drive generator for a FWT.

This study provides a useful initial estimate on the overall mass of the generator if the radial deflection limits were to be satisfied. In reality, the observed increase in generator mass and hence the tower top mass has direct implications on the overall system inertia, resonance, hydrostatic properties and therefore the stability of the system.

Component Mass (ton)	**Case 1**	**Case 2**	**Case 3**	**Case 4**	**Case 5**	**Case 6**	**Case 7**	**Case 8**
	h_{yr}=50mm, h_{ys}=40mm	h_{yr}=100mm, h_{ys}=90mm	h_{yr}=120mm, h_{ys}=110mm	h_{yr}=150mm, h_{ys}=150mm	h_{yr}=200mm, h_{ys}=200mm	h_{yr}=250mm, h_{ys}=250mm	h_{yr}=300mm, h_{ys}=250mm	h_{yr}=300mm, h_{ys}=300mm
Permanent Magnets	0.68	0.68	0.68	0.68	0.68	0.68	0.68	0.68
Copper	3.10	3.10	3.10	3.10	3.10	3.10	3.10	3.10
Steel	3.34	3.37	3.37	3.37	3.37	3.37	3.37	3.37
Rotor Structure	**13.83**	**17.92**	**19.51**	**21.56**	**25.71**	**29.56**	**33.01**	**33.01**
Stator Structure	**23.18**	**27.62**	**29.37**	**32.11**	**37.22**	**41.12**	**41.12**	**45.10**
Shaft	4.45	4.45	4.45	4.45	4.45	4.45	4.45	4.45
Bearing	0.54	0.54	0.54	0.54	0.54	0.54	0.54	0.54
Total Mass	**49.12**	**57.68**	**61.02**	**65.82**	**75.07**	**82.82**	**86.27**	**90.26**
Maximum % deflection after 1st iteration	**28**	**11**	**8.9**	**6.5**	**4.6**	**3.65**	**3.4**	**3**

Table 5.6 Generator mass and air-gap deflection for design Cases 1-8

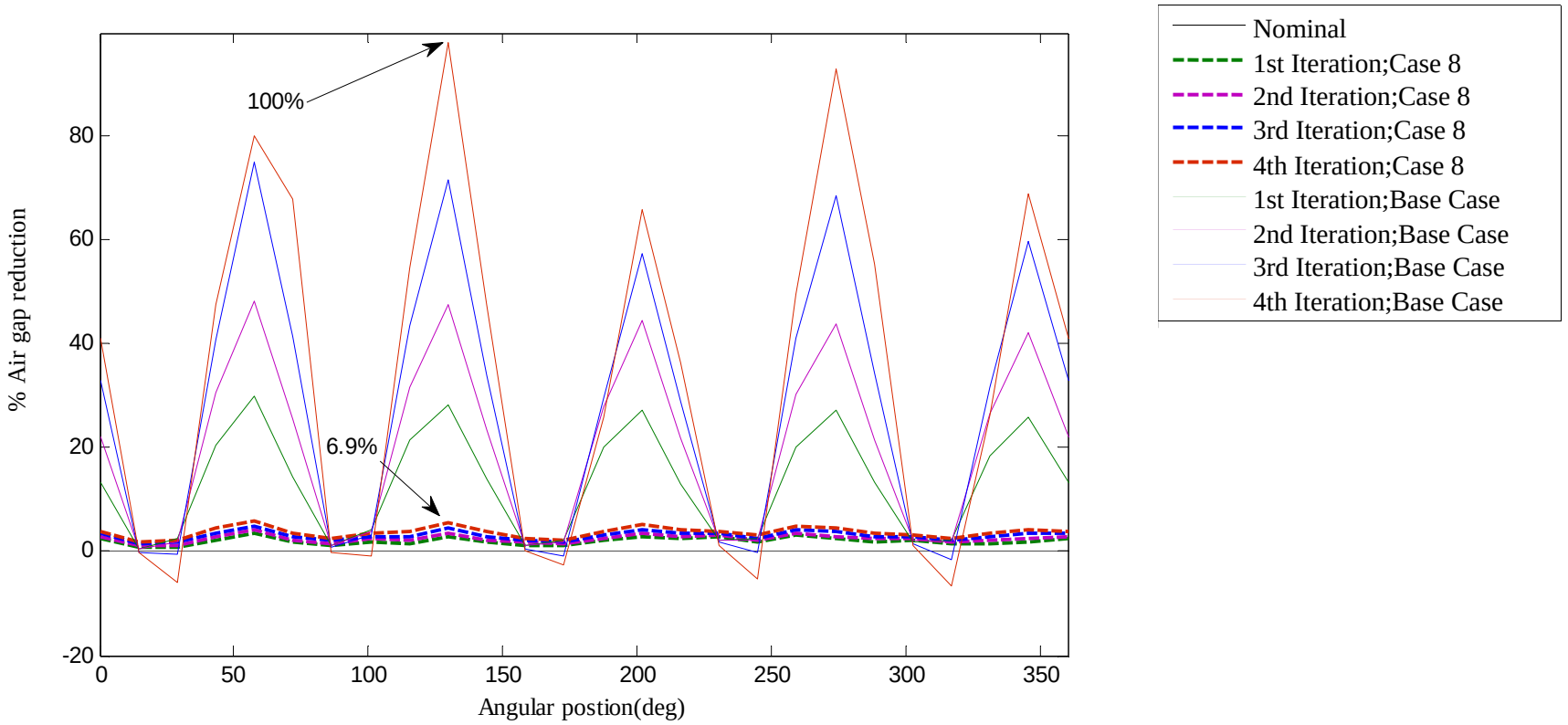

Fig. 5.27 Percentage reduction in air-gap after each iteration

The obvious change will be an increase in draft and displacement of the structure. A 40 ton addition to the nacelle displaces an equivalent weight of water, increasing the depth of submergence of the structure from 70 to 72 m. As the tower top mass and the draft increase, the centre of gravity also moves up closer to the centre of buoyancy thereby reducing the transverse meta-centric height of the system by 1.5 m. Table 5.7 shows the comparison of hydrostatic properties for the base structure (Model A) and Case 8 (Model B).

Item	**Units**	**Model A**	**Model B**
Generator mass	ton	50	90
Tower top mass	ton	156	196
Overall mass	ton	3870	3910
Centre of gravity	m	29.5	31.3
Centre of buoyancy	m	33.8	34.1
Meta-centric height	m	4.3	2.80
Draft	m	70	72
Heave Natural frequency	Hz	0.03438	0.0328

Table 5.7 Effect of Generator (Nacelle) Mass on Hydrostatic and resonance properties of the floating wind turbine

A lower value of meta-centric height causes the turbine to heel quickly. Assuming the same hydrostatic stiffness (K) a marginal decrease in the natural frequencies (ω_i) of the system in surge, heave and pitch can also be expected with increase in tower top mass (δM) as one can see from equation (5.19),

$$\omega_i = 2\pi\sqrt{\frac{K}{M+\delta M}} \tag{5.19}$$

For example, the heave natural system for Case 8 reduces to 0.0328 Hz from 0.03438 Hz for the base case. If the tower top mass increases further, then the system's natural frequency reduces further where the wave frequencies begin to dominate. The increased draft reduces the available hub height for power capture

requiring taller and heavier tower, making installation much more difficult and expensive. It is evident from the above study that the need to satisfy the deflection criteria increases the generator mass and compromises the overall stability of the system. A report by Vestas [75] suggests a 50% increase in foundation costs if the tower top mass increased from 156 tons to 192 tons with monopile foundations. The costs may be much higher for floating foundations [152]. The above discussions clearly highlight the difficulty in negotiating the optimal generator mass for a direct-drive generator against the structural requirements and overall costs of a floating wind turbine system.

5.14.2 Design Option II -Increasing the design air-gap

As a second study case, it was decided to explore any opportunity in avoiding air-gap closure without increasing the structural mass. In general, an increase in air-gap length results in light-weight structures with reduced volume of structural support [139]. However, in order to be able to generate the same flux as that of a machine with smaller air-gap, the volume of magnetic material must be increased. For the machine considered in this study, no attempt was made to alter the machine volume along the axial direction, as this might shift the location of centre of gravity of the generator at the nacelle. Also, the aspect ratio L_s/D_g (where, L_s is the axial length of the machine and D_g is the air-gap diameter of the machine) was already below unity which precluded any opportunity to reduce the axial length of the machine further. The stator diameter was retained at 4.34m, while the rotor diameter was progressively decreased to achieve a larger design air-gap without altering the slot and pole numbers. The reduced rotor diameter constrained the amount of radial space available for placing the magnets. Consequently the only possible means of preserving the flux density was to increase the magnet height. The pole pitch was correspondingly reduced to accommodate the same number of poles on a smaller radial space. In order to identify the design that can best comply with the 10% limit on radial deflection, a number of design cases were examined using the iterative procedure earlier suggested in Section 5.12. The air-gap was progressively increased from 4 mm to 14 mm in steps of 2 mm resulting in 5 different structures (see Table 5.8). The rotor diameter was accordingly decreased for every 2 mm increase in

air-gap. In every case, the ratio, $\left(\frac{h_m}{g_{nom}}\right)$ was preserved at 2.5 [140], so that the peak air-gap flux density for the first iteration remained at 0.78 Tesla. Then, ANSYS simulations were carried out for the first iteration and the new air-gap deformations were computed. Results of air-gap deformation and generator mass data for these structures are presented in Table 5.8. Results from the FEMM simulations (shown in Fig. 5.28 for base case, 8 mm and 12 mm design air-gaps) revealed the problem of flux leakage around the magnets as the air-gap increases and as the pole pitch (magnet width) reduces.

In order to compute the new flux densities and stress values for the deformed structures, the FEMM model was preferred over the analytical model as it accounts for the losses due to flux leakage. After performing successive iterations, it was discovered that the structures with higher air-gap experienced lower magnetic stresses and hence lower deformation compared to the base case structure. This could be attributed to greater losses due to flux leakage effects. Referring to Fig.5.29, the highest deflection for the structure with 8 mm air-gap was located at 345.6º. Despite successive iterations, the highest deflection was 33.8% which was still only a third of the values observed for the base case (for which the air-gap closes at 129º), as can be seen in Fig. 5.29. Fig. 5.30 shows the variation of normalised stresses as a function of air-gap after the first iteration. The trend observed here confirms the results presented in [108] for stresses in permanent magnet machines with larger air-gap. It appears that the relationship between the air-gap and the stress levels can be best described by a 3rd order polynomial (shown by red-dotted line). It may also be noted that increasing the design air-gap beyond 12mm, i.e. to 14mm does not bring considerable reductions to the stress levels.

Air-gap(mm) / **Mass(ton)**	**4.34**	**6**	**8**	**10**	**12**	**14**
Permanent magnets	0.68	0.95	1.26	1.58	1.90	2.21
Copper	3.10	3.09	3.09	3.08	3.08	3.08
Steel	3.34	3.34	3.34	3.34	3.34	3.34
Rotor Structure	**13.83**	**13.81**	**13.74**	**13.66**	**13.59**	**13.51**
Stator Structure	23.18	23.18	23.18	23.18	23.18	23.18
Shaft	4.45	4.45	4.45	4.45	4.45	4.45
Bearing	0.54	0.54	0.54	0.54	0.54	0.54
Total	**49.12**	**49.36**	**49.60**	**49.84**	**50.07**	**50.31**
% reduction after 1st Iteration	**28**	**8.7**	**7**	**4.8**	**3.6**	**3.4**

Table 5.8 Generator mass and air-gap deflection for structures with larger air-gap

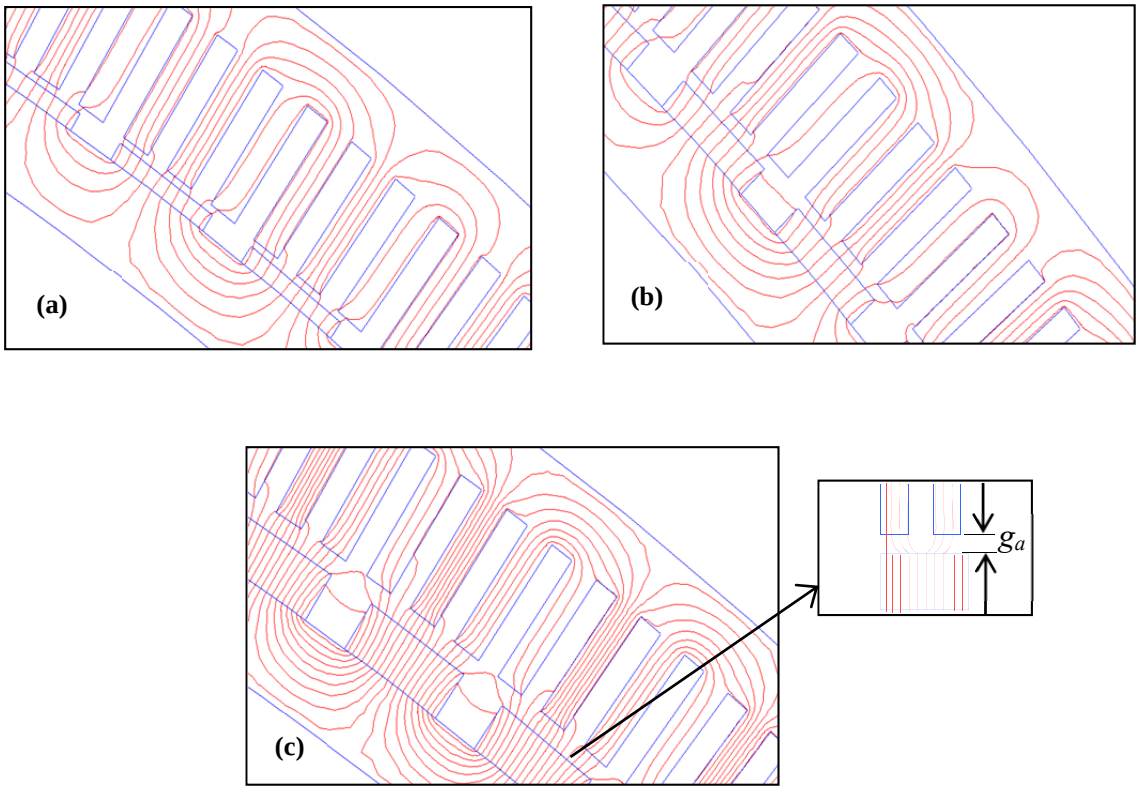

Fig. 5.28 Flux line plots for (a) Base case (b) 8mm and (c) 12mm air-gap designs

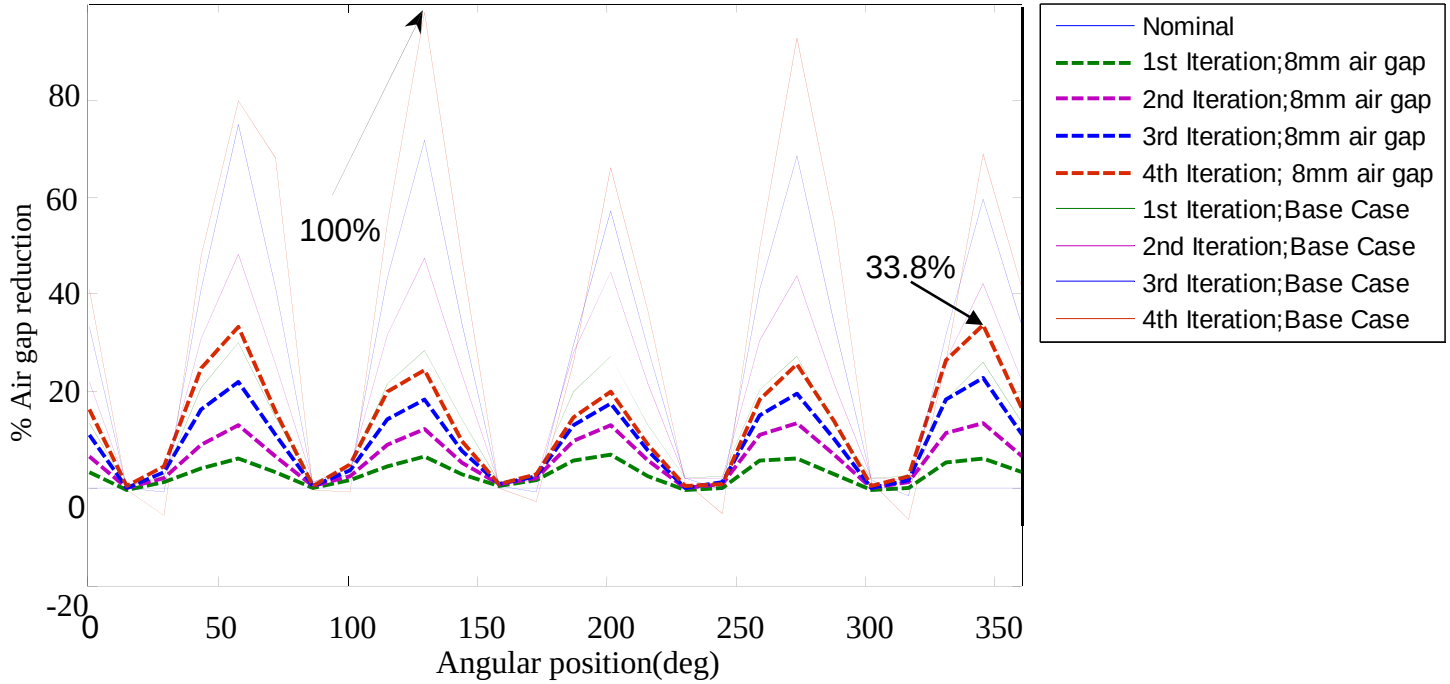

Fig. 5.29 Percentage reduction in air-gap after each iteration

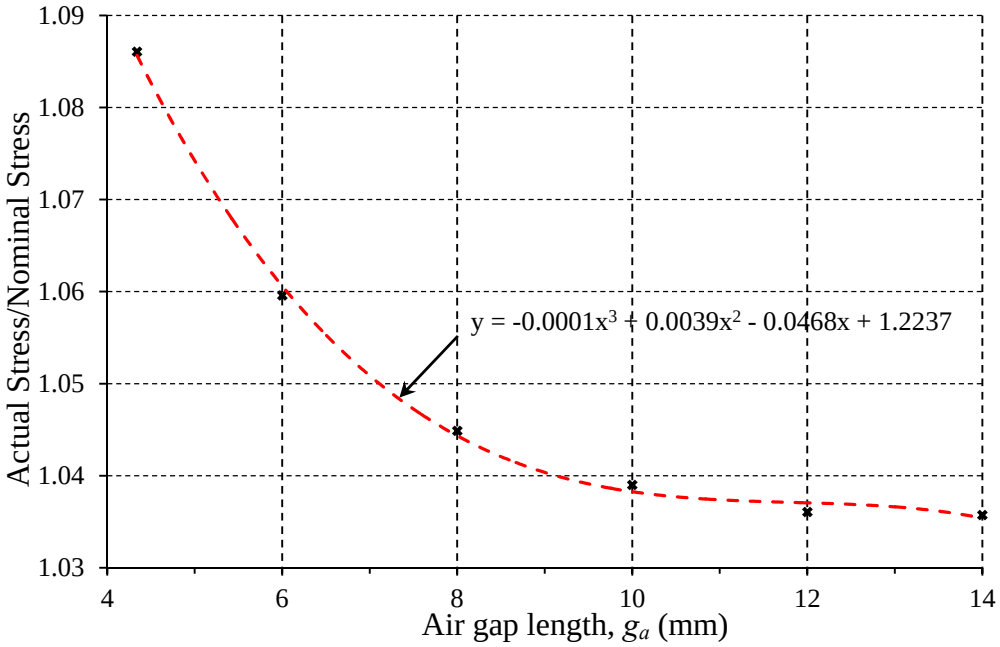

Fig. 5.30 Stress variation as a function of air gap length

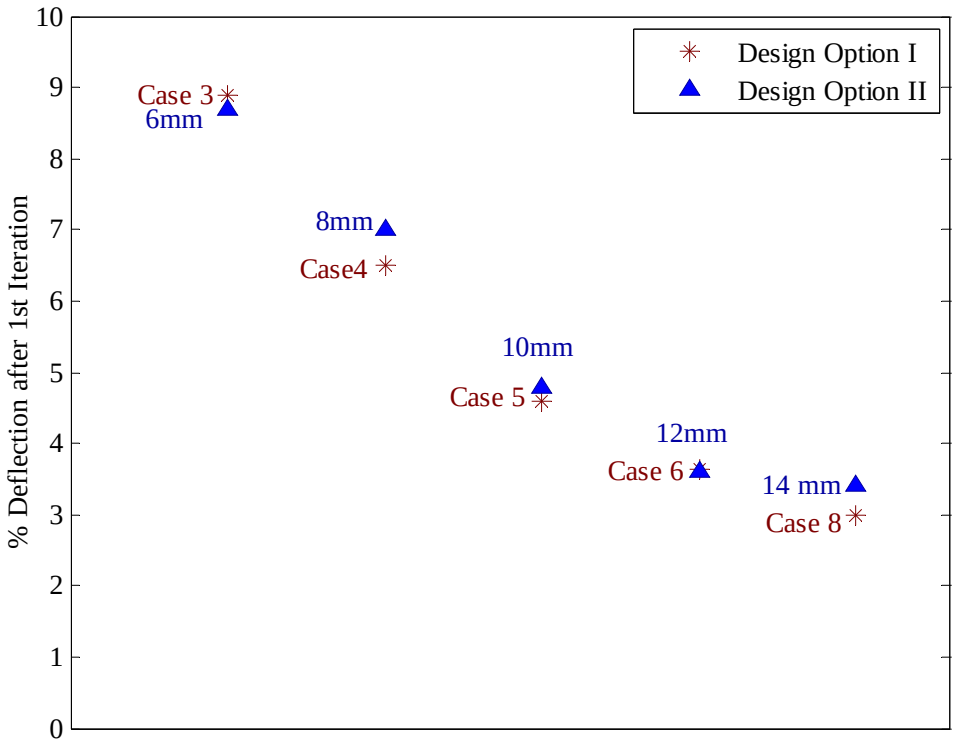

Fig. 5.31 Comparison of Stiffer structures (Design Option I)with structures of larger air-gap (Design Option II)

Interestingly, the addition of extra magnetic material altered the overall mass only very slightly (refer to Table 5.8). Even for the structure with 14 mm air-gap, the overall mass of the generator was still around 50 tons. If the 10% radial deflection is not a binding factor, then this study suggests that larger air-gap machines can still result in a structurally tolerable design in terms of stability requirements for floating wind turbines. As noted from Fig.5.31, a comparison of these designs against the cases with increased structural stiffness shows that large air-gap machines can demonstrate similar control over air-gap (for the first iteration). However, this comes at an extra investment on magnet materials that are already expensive.

The magnet volume necessary for proper excitation of a permanent magnet generator is a function of a number of factors that determine the quality of power production [153]. Despite being a structurally favourable option, large air-gap machines require greater magnet material making them more expensive to build. Minimising magnet consumption in these type of machines while also trying to achieve the necessary flux densities for optimal performance would be difficult to achieve; for example by the use of high energy density permanent magnets that make them more expensive [154, 155].

5.15 Discussions

Several other routes of air-gap management exist for lighter generator structures to compensate for the unequal flux distribution caused by structural flexure. For example, the use of passive actuator mechanisms [156, 157] or dedicated control system for monitoring and maintaining the clearance as in reference [158]. However, these systems further add to the complexity and hence may not be cost-effective.

The results of this study demonstrate the need for a new structural design philosophy for floating wind turbine system: One that incorporates greater knowledge of the rotor nacelle assembly (viz., drive-train technology) in the foundation design and their combined impact on the overall dynamics of the FWT system. With regard to the suitability of direct-drive radial flux permanent magnet generators for FWTs, questions still remain on optimal size, weight, costs and performance. All of these factors are basically determined by the need to limit the air-gap eccentricity to 10%

of the air-gap diameter. When designing machines for offshore wind turbines, designers generally set two different yardsticks to measure the adequacy of air-gap design [159]. Firstly, to ensure good power quality and fatigue requirements are satisfied, the operational deflections are limited to $\pm$10%. Secondly, for extreme load cases, when the turbine is not rotating, deflections are permitted to a level just enough to prevent the stator from touching the rotor. It is believed that the opportunities for newer design perspectives are greater, if the 10% limit is allowed to be relaxed when designing generators for FWT systems.

5.16 Summary – Part II

The structural integrity of a direct-drive radial flux permanent magnet generator was examined for a stepped-spar FWT system. The generator design was assessed based on its air-gap stability and its possible implications on the FWT system. Air-gap instability in a direct-drive generator can be caused by structural compliance as well as shaft-bearing compliance. In this study, these effects were examined separately. The nacelle response for a 1:100 scale model were up-scaled and applied as motion loads on a 2MW radial flux PMSG. As the wave loads were time-dependent, 3D transient FE simulations were carried out using ANSYS to compute the structural deformations of the stator and rotor. A simplified analytical tool was developed to estimate the new air-gap flux density distribution and force distribution for eccentricity caused by external wave loads. The estimated force distribution was then re-used in ANSYS simulations to examine the elastic stability of the structure by means of an iterative procedure. In a separate study, a multi-body simulation on a drive-train model was carried out to examine the effect of shaft displacements on eccentricity. The results of these studies offer some early guidelines for designing direct-drive generators for FWTs:

1. The generator structure for parked rotor condition is structurally stable in the presence of wave loads provided the shaft support stiffness is sufficiently high. This corroborates the importance of restricting nacelle accelerations to $< 0.3g$ from the point of view of nacelle component design. This also confirms the adequacy of platform design.

2. Magnetic forces are the most dominant loads that have to be structurally endured by the direct-drive generator. In a design that is inherently less stiff/lighter, secondary deflection due to eccentricity effects can surpass the 10% deflection limit causing the air-gap to close.
3. Practically, in a FWT system, in addition to generator structural deflection, bearing compliance/shaft displacements can further accentuate the air-gap problem. Preliminary results emphasize the need for high bearing stiffness to limit the shaft induced eccentricity to acceptable levels. The decision on optimal bearing stiffness is a compromise with generator support structure stiffness in order to limit the overall eccentricity to 10%. This has obvious implications on the drive-train resonance behaviour.
4. With regard to generator structural design, methods of managing the air-gap are critical:
    - Generators with stiffer support structures exhibit a good control over the air-gap, but these designs come with a large weight penalty, causing stability, and resonance problems demanding more expensive foundation systems.
    - Generators with large air-gap can demonstrate similar air-gap behaviour as that of generators with stiffer structures. These designs are structurally more favourable, but require additional magnetic material adding to cost penalty.
5. The results presented in this work are valid for the spar buoy configuration. Interpretation of results for other configurations must be done with care and good sense of engineering judgment.

These initial observations suggest that implementing direct-drive radial flux permanent magnet generators for FWTs is fundamentally challenged by the difficulty in achieving the optimal weight and costs without compromising air-gap tolerances. The need for an amendment to design standards becomes clearly intuitive to recognise the design challenges of FWTs. A detailed investigation on the dynamics of the drive-train, considering shaft and bearing loading will be useful in assessing the performance and reliability of the system when applied for FWT systems. These aspects will form the Part-III investigations in the subsequent chapters.

Chapter 6

Aero-hydro-servo-elastic model of a FWT with a direct-drive generator

6.0 General

The results from Part-II investigations highlighted the structural design challenge with direct-drive generators; yet, a more accurate assessment of their performance would be possible with the help of a fully coupled dynamic analysis involving the interactions of the various elements with the drive-train. This chapter forms the basis of Part-III investigations aimed at exploring further challenges and opportunities in implementing a direct-drive generator for FWT. The work presented herein provides preliminary specifications for a fully-coupled aero-hydro-servo elastic model of a floating wind turbine with a 5MW direct-drive generator. The properties of the drive-train, including mass and mechanical properties, layout of the nacelle, adjustments to tower and platform properties are discussed. The development of the variable speed-variable pitch control system suitable for the direct-drive system including modifications to avoid negative damping is presented. The validity and behaviour of the model was examined for the various wind and wave conditions.

6.1 Introduction

Ensuring competitiveness, reliability and robust operation of a direct-drive generator for a FWT system requires a good understanding of detailed dynamic behaviour of the drive-train considering the aero-dynamic interaction, platform motions and control system response. Preliminary studies on a 2MW radial flux PM generator (RFPMG) in Chapter 5 supported this viewpoint and identified some of the structural challenges in implementing the direct-drive technology for FWTs. As commercial scale wind turbines are moving towards multi-MW level, it would be relevant to examine, validate and interpret the results for FWTs with larger turbine ratings. The dynamics of the direct-drive generator, its impact on and the interactions with the

rest of the FWT system can be best understood by numerical modelling techniques that help assemble the various elements together, simulate the loads properly, accurately capture the kinematics and physical interactions. So far, the most common method for detailed drive-train investigations is to use a wind turbine simulation software and specialised drive-train analysis software in linear combination [160, 161]. State of the art techniques use multi-body simulation tools as they accurately describe the interactions between elastic body deformations of, for e.g., blades and large rigid body motions[162]. Firstly, a global model of the FWT system must be developed in order to:

- enable a fully coupled aero-hydro-servo-elastic simulation and obtain the global response loads for determining the drive-train design loads and component strength and
- identify any special structural requirements, design adjustments that might be necessary for accommodating a direct-drive generator

For parameterisation of this global model, properties of turbine, tower, foundation, mooring system, control system and drive-train are required. Secondly, another simulation model must be developed for detailed drive-train investigations, because the global model generally ignores the internal loading within the drive-train. This can be subsequently used to verify the design loads, component durability and validate any assumptions for global load simulation (e.g. stiffness, mass).

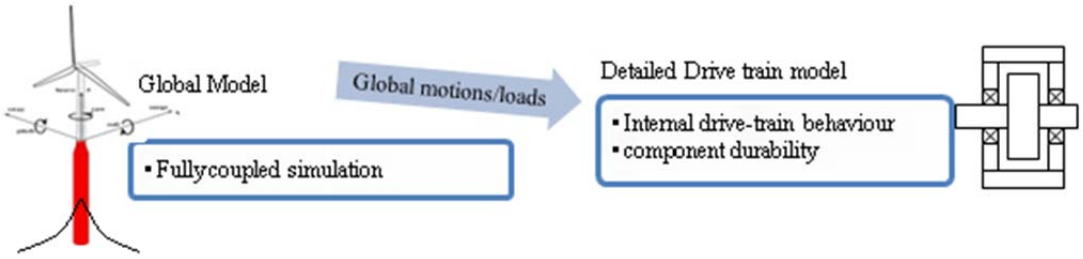

Fig. 6.1 Drive-train analysis methodology

To facilitate early conceptual studies, preliminary design specifications were developed for a 5MW FWT system that could support a radial flux PMG (henceforth referred to as FWTDD system). A fully coupled aero-hydro-servo-elastic model was developed for dynamic response analysis for design verification. The model presented here shall be used for performing fully-coupled time-domain analyses

using multi-body simulation codes such as HAWC2 [135] and SIMPACK [136]. Details of the drive-train, including mass and mechanical properties, layout of the nacelle, control-system properties are presented. The important challenges in dealing with large nacelle mass, adjustments to tower and platform properties and the rationale behind development of the optimal system are discussed. It is verified that the spar with the direct-drive generator has expected behaviour in different wind and wave conditions.

6.2 A fully-coupled mechanical model

Different configuration choices exist for radial flux PMGs for bearing types and arrangements, shaft/axle load supports, rotor type, location, generator-hub interface options [90, 94]. Generally, the drive-line arrangement and the mechanical parameters are highly design-specific and not consistent with the configurations; moreover such information is scarce in the public domain and is available only for selected configurations for example, references [90, 163]. As detailed information on the drive-train parameters for the chosen radial flux topology was not available at the time of the study, it was decided to develop these parameters to enable a fully coupled aero-hydro-servo-elastic analysis. The model for a 5MW geared system developed by [47] was adapted with changes to the drive-train (section 6.3.1), nacelle (section 6.3.2) and control system properties(section 6.6) to allow the integration of a direct-drive generator. 5MW was chosen as the design rating as it is expected to be the level of production that is useful to validate the competitiveness of the design. The aerodynamic and blade structural properties for the turbine and hub design were retained as the NREL offshore 5-MW baseline wind turbine [47, 164]. The mooring system did not require alterations, but modifications to the tower and support platform properties and controller were necessary. The following sections provide details of the drive-train and document the preliminary specifications for the important elements of the FWTDD system in the same order as described by [47]. Wherever appropriate, the properties for the baseline system are listed alongside to highlight the differences between the two systems. Where the properties are not listed, the relevant values from the baseline system [47] shall hold.

6.3 Direct-drive generator topology

The direct-drive generator considered for this study is a low speed radial flux permanent magnet generator of the interior rotor construction that was obtained from a previous optimisation study [141]. The rotor is a cylinder of disc type construction; stator is also a cylinder with double spider arrangement. Fig. 6.2 provides an illustration of the rotor nacelle assembly for the direct-drive generator and constructional details (clearances). The detailed machine parameters and dimensional details are available in reference [165], with the main properties summarised in Table 6.1. It was assumed that the hub was integrated onto the main shaft which carries the generator rotor. The turbine-rotor and the shaft are supported by means of two roller bearings BR1 and BR2 that are housed on generator stator support structures. The shaft/hub loads are transferred to the stator through BR1, BR2 and stator support arms. The stator is integrated to the bedplate that is coupled to the tower by

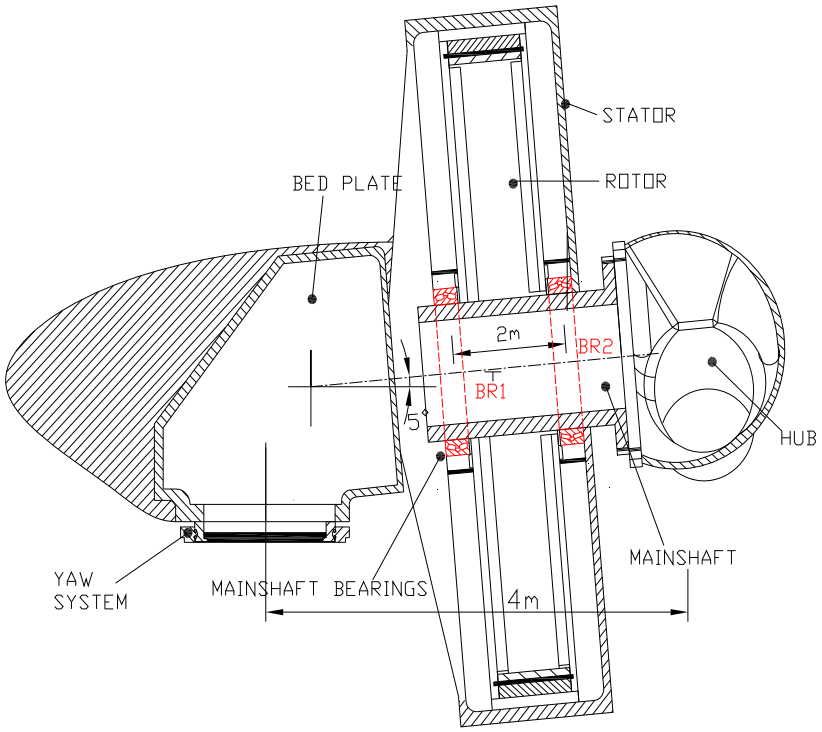

Fig. 6.2 Rotor Nacelle Assembly of a direct-drive generator

means of a yaw system. Hub thrust, shear, and bending moments are transferred to the nacelle bedplate by the main bearings via the stator support structure. With

regards to the driveline arrangement, there are some similarities with the MTorres design [166]. BR-1 is a cylindrical roller bearing (CRB) designed to take radial loads; BR-2 is a double row tapered roller bearing with inner race (TDI) designed to carry both the axial loads and radial loads. This arrangement is expected to be structurally more efficient in terms of stiffness to mass ratio [167]. The choice of the bearing configurations and stiffness was based on the recommendations from bearing manufacturer(TIMKEN [168], refer to APPENDIX-B). It is emphasised that the bearing arrangement/locations were tentative and not optimised for the design. For simplicity, any other components of drive-train mounting system such as suspension or shaft coupling elements are not shown.

Item	Units	Value/Description
Generator type	-	Radial Flux PMSG, interior rotor
Generator nominal power	MW	5.56
Rated Torque	MN-m	4.38
Efficiency	%	96.6
Rotor diameter	m	6.36
Stator diameter	m	6.37
Axial length	m	1.72
Air-gap length	mm	6.36
Magnet height	mm	15.9
Rotor mass	kg	51,440
Stator mass	kg	77,040

Table 6.1 Generator Properties

6.3.1 Modelling the direct-drive generator

The direct-drive generator can be modelled with varying levels of detail depending on the type of analysis, the component being analysed, the control algorithm and the size/rating of the machine. These vary from a simple mass spring-damper system (one-mass, two-mass oscillator models), to very complex higher order systems containing flexible bodies (blades) and super-elements (three-mass, 6-mass models)[169]. The higher order models are computationally time - intensive and are

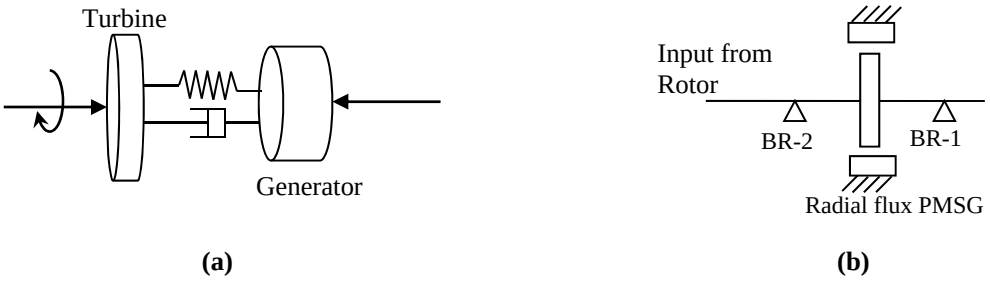

Fig. 6.3 (a) Simple mechanical model of a direct-drive generator (b) Direct-drive generator Topology

generally preferred where unequal blade torque loading is important. For the present study, the implemented control algorithm regulates the generator torque and the rotor speed, therefore the first eigen mode for torsional compliance in the drive-train (i.e. variable rotor speed and drive-shaft flexibility) was of most interest. This encouraged the consideration of a lower order model represented by a single DOF torsional spring-damper system for the global response analysis using fully-coupled aero-elastic simulation (refer to Fig. 6.3(a)). The remaining modes whose eigen frequencies were higher than the wind turbine, were therefore not included in the global analysis. It must be remembered that the torsional model does not consider the stresses on the drive-train imposed by the aerodynamic, gravitational and inertial loads. Nevertheless, previous studies considering torsional model for global analysis have shown to be adequate for most calculations providing reasonable conclusions about the overall dynamic behaviour [21, 52]. The shaft and the generator rotor are treated as rigid bodies with their mass moment of inertia and damping lumped to that of the low-speed shaft. This single-degree of freedom model was considered sufficient to provide an insight into the dynamic behaviour of the system, allowing time efficiency at an acceptable modelling precision.

6.3.2 Development of drive-train mechanical properties

This section provides a description of the 1-DOF equivalent drive-train properties for the direct-drive generator. The 5-MW baseline wind turbine drives a low speed radial flux permanent magnet generator. Results of the optimisation study by [141] were used to obtain the generator mass and dimensions. The generator inertia about the shaft was taken to be 3.7961×10^5 kg-m^2. This value was comparatively lower

than the equivalent geared drive-train value reported by [47], which is intuitive because of the absence of gearbox. In the determination of the mass and dimensions of the rest of the components of the drive-train, a number of reports on drive-train design were reviewed [90, 170-172]. In general, shaft and bearing arrangement are design variables that directly depend on the generator design. Because several arrangements are possible, there is no standard formula available to estimate the dimensions of the shaft. The main shaft can either be tapered or uniform cross-section depending on the generator design. However, it is intuitive to expect the shaft to be smaller in length compared to a conventional geared drive-train. This required making a preliminary engineering design.

The parametric design models [90] and scaling law model [170] for the direct-drive generator offered some initial ideas about the shaft dimensions and component weights although the estimations in [90] considered a direct-drive generator with inner rotor design and one-sided stator support. The data for the 5MW geared drive-train were interpreted from [171, 172]. These served as a reference to estimate the component mass and dimensions for the model developed for this study. Table 6.2 summarises the mass estimated from the various models. The shaft model considered by [90] was a 2-piece structure with the rotor attached to a gudgeon shaft that rested on bearings over a stationary main shaft. The analytical model for weights provided no information about the shaft diameter and length.

In determining the shaft properties, few assumptions on construction had to be made with reference to [171]. The shaft mass for the direct-drive system was estimated by extrapolation [90] as 9.4 tons. Assuming a shaft outer diameter of 1m diameter and shaft inner diameter of 0.5m, this gave a total shaft length of 2.03m which appeared to be insufficient for the present direct-drive model having a total generator axial length of 2.0m (including stator spider support). Therefore a clearance of 0.5m on either side of generator was a reasonable assumption to make, resulting in an overall shaft length of 3m. The outer and inner diameters of the shaft were retained at 1m and 0.5m in line with the geared drive-train, to endure similar stress and fatigue levels. The shaft was assumed to be a uniformly hollow cylindrical steel tube made from high-strength characteristic yield of 828 MPa and modulus of rigidity of 79

GPa. This gave an estimated shaft mass of 13.24 tons. The values for generator housing mass predicted by both [90] and [170] were identical and were therefore adopted for the model considered in this study. The structural adequacy of the shaft was verified by performing a finite element analysis using SolidWorks [173]. The shear stresses at the outer surface were found to be less than the allowable stress, for the largest loads possible on the drive-train. Table 6.2 presents the main dimensions and mass properties for the drive-train.

Item/Description	**Units**	**NREL, 5MW baseline [170-172]**	**Scaling law model for direct-drive system [170]**	**Parametric design data (extrapolated for 5MW direct- drive) [90]**	**Estimated dimensions /weights for FWTDD system**
Shaft mass	ton	17.38	-	9.4	**13.24**
Shaft Length	m	3.76	3.78	2.03	**3**
Shaft outer diameter	m	1	-	1	**1**
Shaft inner diameter	m	0.5	-	0.5	**0.5**
Generator Housing Mass/Mainframe mass	ton	28.24[170]	15.53	15.33	**15.33**
Main shaft bearing mass	ton	2.7	2.7	0.1	**2.7**

Table 6.2: Drive-train mass and dimensions

In computing the equivalent drive shaft mechanical constants, contributions to torsional stiffness come from the drive shaft and the generator rotor with negligible stiffness due to electromechanical torque. The magnetic coupling between rotor and stator (grid) of a synchronous generator can be described by a mechanical torsion spring. The damping is so small that it can be virtually neglected[174]. Therefore these generators are characterised by the dominant torsionally-elastic behaviour. The torsional twist of the shaft while transmitting power was limited to a value determined by its equivalent torsional stiffness, K_{ls}. This value was determined as:

$$\frac{1}{K_{ls}} = \frac{I}{K_{shaft}} + \frac{1}{K_{gen\_rotor}} \tag{6.1}$$

where K_{gen_rotor} is the generator rotor structural stiffness in torsion determined from the natural frequency of vibration in torsion(which was 41.25Hz) and K_{shaft} is the

shaft torsional stiffness determined from the elastic torsion formula for hollow shafts[175] as

$$K_{shaft} = \frac{GI_p}{L} \tag{6.2}$$

where, G is the modulus of rigidity of steel (GPa), I_p is the polar moment of inertia (m^4) and L the length of shaft (m). This gave an equivalent drive-shaft torsional stiffness of 2.17 GN-m rad^{-1}. The structural-damping ratio was 5% of critical for the free-free mode of the drive-train (i.e. rigid generator and rigid rotor). With a moment of inertia of 373,279 kg-m^2 in the torsional mode, the equivalent drive-shaft torsional-damping coefficient was computed as 2.85 $MNms^{-1}rad^{-1}$. A large torsional stiffness in the system (approximately 2.5 times larger than the geared system) resulted in larger natural frequencies in the torsional mode. The natural frequencies of the torsional mode for the free-free condition (with a rigid rotor) and fixed-free mode (if the generator DOF is disabled)were computed as[176]

$$f_{n\ (free\text{-}free)} = \frac{1}{2\pi}\sqrt{\frac{K_{ls}}{I_{Turbine}} + \frac{K_{ls}}{I_{gen}}} \tag{6.3}$$

$$f_{n\,(fixed\text{-}free)} = \frac{1}{2\pi}\sqrt{\frac{K_{ls}}{I_{Turbine}}} \tag{6.4}$$

where, $I_{Turbine}$ and I_{gen} are the turbine and generator inertias about the low speed shaft. The values computed using equations (6.3) and (6.4) were 12.1 Hz and 1.24 Hz respectively. The total mass of the generator (including magnets, windings and steel) plus the shaft and bearings and generator housing was estimated to be about 160 tons. No effort was made to size or optimise the rest of the elements of the drive-train; the mass of the rest of the drive-train were estimated from existing models [79] and commercially available designs [177]. Although these values may appear to be overstated and not represent the true case, they were useful for initial investigations. Approximately 50 tons (based on values suggested in reference [79]) was assumed for ancillary equipment such as brake disk & callipers, hydraulic and cooling systems, yaw drive, brake, bearing and nacelle cover that make up the rest of the nacelle mass. The output of the generator is connected to a dedicated power

conversion and high voltage transmission and distribution equipment (Figures 6.4(a) and 6.4(b) show the typical nacelle and component layout for a direct-drive wind turbine).

Item/Description	**Units**	**FWTDD system**	**NREL, 5MW baseline system**[47, 164]
Turbine Power	MW	5.0	5.0
Rated Rotor Speed	rpm	12.1	12.1
Generator Speed	rpm	12.1	1173.7
Generator Rated Torque	MN-m	4.3	0.043
Rotor System layout	-	3-bladed Upwind	3-bladed Upwind
Drive-train	-	Low speed, Direct-drive, radial Flux, PMG	High speed, Multiple stage, Gearbox, Induction generator
Electrical Generator efficiency	%	96.6	94.4
Generator Inertia about the shaft	kg-m^2	3.79x10^5	5.07 x10^6
Turbine Inertia about the shaft	kg-m^2	3.54x10^7	3.54x10^7
Equivalent Drive-Shaft torsional-stiffness	Nm/rad	2.17 x10^9	8.67 x10^8
Equivalent Drive-Shaft torsional-damping constant	Nms/rad	2.85 x10^6	6.21 x10^6
Natural frequency in free-free mode for torsion	Hz	12.1	2.23
Natural frequency in fixed-free mode for torsion	Hz	1.24	0.78
Major Equipment Masses			
Power distribution equipment/ cooling unit	ton	120	NA*
Generator mass	ton	131	15.22
Shaft & Housing mass	ton	28.5	NA
Turbine mass	ton	110	110
Brake disk, Hydraulic system, Yaw drive, Nacelle frame	ton	50	NA*

* Not available

Table 6.3 Drive-train properties and mass of major equipment

A further 120 tons was considered for the power transmission and distribution equipment and other auxiliaries (heat exchanger, heaters, UPS) based on the 5MW prototype design by DARWIND [177]. The baseline arrangement had the generator converter and transmission equipment at the nacelle [47, 171]. If a similar arrangement was to be adopted for the direct-drive system, then this would result in

an overall nacelle mass of 330 tons. Table 6.3 presents the drive-train properties with column 4 presenting the properties of the baseline system as reference.

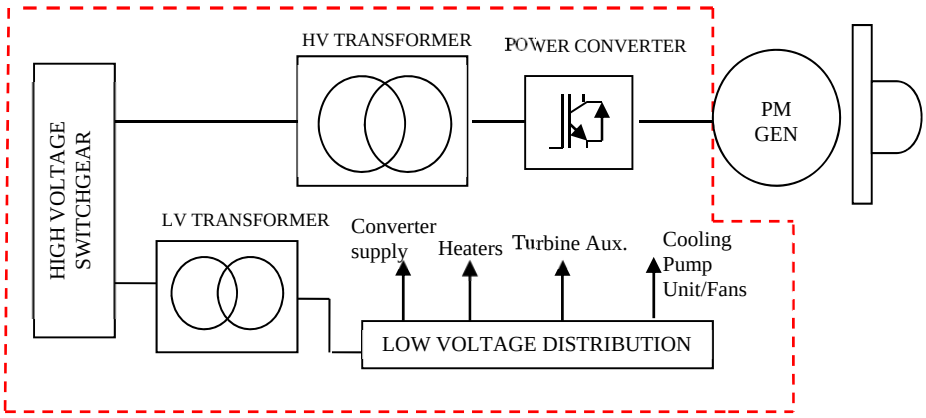

Fig. 6.4 (a) Typical Nacelle layout for a direct-drive generator[177]

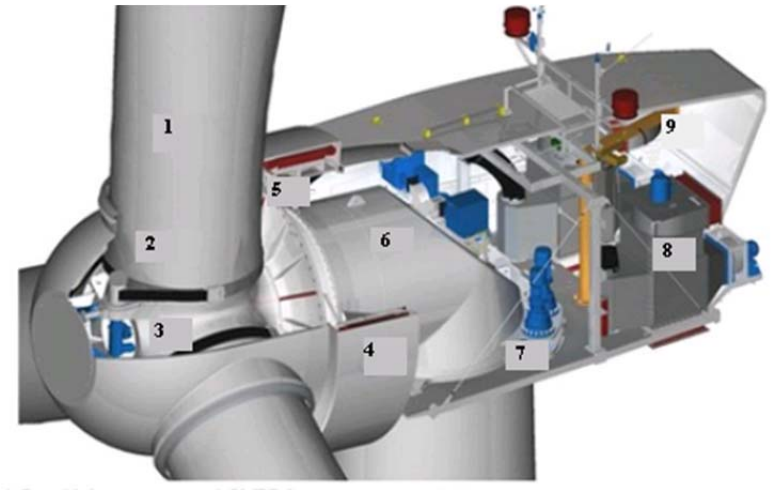

1. ROTOR BLADE
2. TOOTH BELT PITCH
3. HUB
4. PMDD GENERATOR
5. ROTOR GENERATOR BEARING
6. BASEFRAME
7. YAW SYSTEM
8. HEAT EXCHANGER
9. AUXILIARY CRANE

Fig. 6.4 (b) Typical Component layout at the nacelle of a direct-drive generator [178]

6.4 Hub and Nacelle Properties

The hub of the wind turbine was located 4 m upwind of the tower centre line at an elevation of 90 m above the ground. The vertical distance from the tower top to hub was 2.09m. The elevation of the yaw bearing, shaft tilt of 5° were retained as in the original baseline system. The vertical distance along the yaw axis from the tower top to the shaft is 1.82m. The distance directed along the shaft from the hub centre to the main bearing BR2 was taken to be 0.65 m. The hub mass and inertia were retained

from the baseline model. Initial estimates for the total nacelle mass excluding the turbine exceeded 300 tons, with the centre of mass (C.O.M) at 0.65 m upwind of the yaw axis and 1.5 m above the yaw bearing. The nacelle inertia about the yaw axis was 2,115,474 kg-m^2. Fig. 6.5 shows the main dimensions at the nacelle.

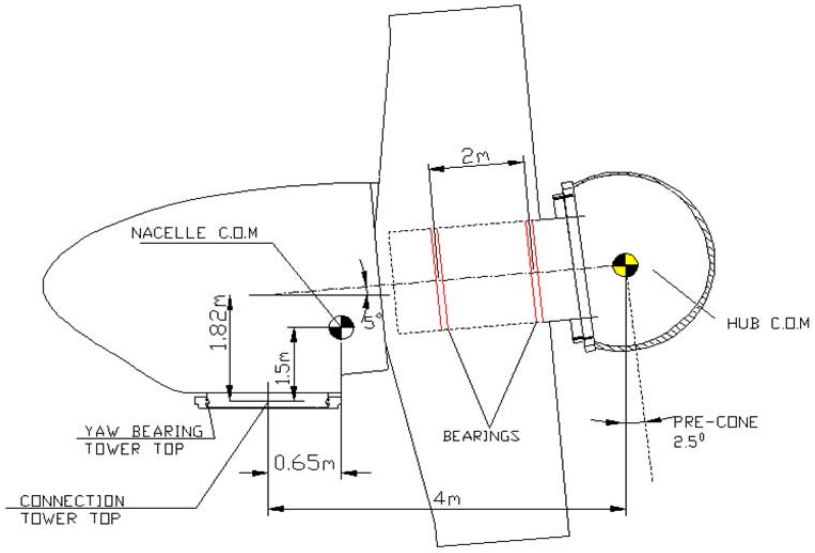

Fig. 6.5 Main dimensions at the nacelle

This was computed as the inertia about its nacelle C.O.M and translated to the yaw axis using the parallel-axis theorem with the nacelle mass and upwind distance to the nacelle C.O.M. The nacelle-yaw actuator had a natural frequency of 3 Hz and a damping ratio of 2% critical. The equivalent nacelle-yaw-actuator stiffness and damping properties were retained as the baseline design. Table 6.4 summarizes the nacelle and hub properties discussed in this section with properties of the baseline system as a reference.

Item/Description	Units	FWTDD system	NREL, 5MWbaseline system[47, 164]
Elevation of Yaw Bearing above Ground	m	87.6	87.6
Vertical Distance along Yaw Axis from Yaw Bearing to Shaft centre	m	2.0	1.96
Distance along Shaft from Hub to Yaw Axis	m	4	5.01
Hub mass	kg	56,780	56,780
Hub Inertia about low speed shaft	kg-m^2	115,926	115,926
Turbine mass	kg	53,233	53,233
Nacelle inertia about yaw axis	kg-m^2	2,115,474	2,607,890
Nacelle centre of mass from yaw axis	m	0.65[1] upwind	1.9 downwind
Nacelle C.O.M location above Yaw Bearing	m	1.5[1]	1.75
Main Bearing separation	m	2	NA*
Shaft tilt angle	deg	5	5
Distance along Shaft from Hub Center to Main Bearing 1	m	0.65	NA*
Distance along Shaft from Hub Center to Main Bearing 2	m	2.65	NA
Nominal Nacelle-Yaw Rate	deg/s	0.3	0.3

[1]initial estimates *Not Available

Table 6.4 Hub and Nacelle properties

6.5 The floating spar system

A spar-type FWT system was designed to support the proposed 5MW direct-drive generator design for the purpose of examining the dynamic behaviour of the drive-train. This is a ballast stabilised catenary moored spar system with the basic design mentioned in [47, 179], with three mooring lines with fairleads located on the spar circumference. The mooring lines assume a delta configuration and serve for station-keeping in surge and sway. The delta mooring layout provides extra yaw stiffness and the clumped weights increase the pre-tension in the mooring lines. The pitch and roll motions of this FWT system are primarily ballast-stabilised. For the evaluation of the spar properties and ballast requirements, the super-structure (tower, nacelle) design has to be determined. With the knowledge of the nacelle and turbine mass

(Section 6.4), it was decided to estimate the tower properties as the first step. Knowledge of the tower properties was then used to determine the overall structural requirements of the platform and the system response properties.

6.5.1 Tower and platform properties

It was intended to achieve the same draft and ensure similar natural periods of rigid body motions so that the global motion response characteristics for the geared and direct-drive FWT system were similar. At 330 tons, the nacelle of the direct-drive FWT was heavier than the geared system by 90 tons. Typically for every ton of extra mass at the nacelle, the tower mass increases by 2 tons. As a result the tower dimensions for the original 5MW turbine needed to be upgraded. It was intended to achieve the same fatigue life as that of the tower for a geared FWT. For this purpose, 22 short-term uni-directional responses from 4m/s to 25m/s for the geared FWT were computed to determine the short-term fatigue lives in turbulent wind field and irregular wave condition. The wind and wave climates were correlated by a method described by Johannessen *et al.,* [180]. A wind probability distribution(assuming Rayleigh distribution[181]) was then applied to calculate the long-term fatigue life for each of these 22 short-term responses. The same procedure was repeated for the FWTDD system. This resulted in a substantial increase in tower structural requirements and subsequently increased the overall inertia, the draft and altered the natural periods of the system. Column 4 in Table 6.5 shows the increase in tower mass and system natural periods, when attempting to match with the tower fatigue life as that of the geared system.

The ideal solution must ensure minimal change to platform design, mooring system design, system natural frequencies, motion response and the cost. Three options were considered so as to support the direct-drive generator: using heavier ballast, increasing the draft of the spar and increasing the spar diameter. It was observed that increasing the draft or spar diameter would bring major changes to the design and also add to a huge cost penalty. Increasing the spar draft increased the pitch stiffness and inertia. The tower height also had to be increased to see similar wind speed at the hub height. While using a heavier ballast (for e.g.: if steel is considered instead of gravel or water) can ensure minimal change to overall system design, it might prove

to be expensive. Table 6.5 presents a comparison of properties with the spar length increased to 150m and diameter increased by 1m. Therefore, all of the above three options proved to be practically infeasible. The quickest approach to matching the geared system must seek to minimise the difference in nacelle mass to below 20 tons. The largest contributors to the heavy tower top mass for the FWTDD system include the generator, turbine, power transmission equipment. It was decided to retain the properties of the turbine to replicate the aerodynamic behaviour, therefore other options to reduce the nacelle mass were investigated for the FWTDD system.

Item	**Units**	**Geared FWT [47, 182]**	**Designing for tower fatigue strength**	**Using Denser ballast**	**Increasing Spar length(draft)**	**Increasing spar diameter**
Surge natural period	s	125	124.67	124.67	139.9	137.4
Heave natural period	s	30.8	31.62	31.62	35.39	34.92
Pitch natural period	s	29.1	47.87	35.37	44.8	37.48
Total platform mass including ballast	ton	7460	7130	7130	9270	11,026
Mass of Tower	ton	249.7	608.8	608.8	608.8	608.8

Table 6.5 Resonance properties for different configurations

6.5.2 Mass Adjustments for the nacelle

The radial flux topology of the generator initially considered during the mass estimation was obtained from an optimisation study [141]. More structural solutions do exist [109] and point towards a further reduction of weight. Alternative design topologies such as air-cored axial flux machines, transverse flux machine, machines with magnetic bearings and super-conducting generators show significant weight-saving potential [110, 183-185]. However they introduce complexities(viz., manufacturing, dynamic balance for air gap). Therefore it was decided not to disturb the generator topology. The next choice was removing some mass from power distribution and transmission equipment (~120 tons). The size and mass of the conversion equipment generally depends on the generation voltage of the generator. The obvious choice for 5MW generator was medium voltage as in [177] as it

eliminates the need to install a transformer in the nacelle and heavy and expensive low-voltage cables that have to run down the tower. The converter can be compact and lighter. Further, the transmission equipment (transformer, switchgear etc.,) can be located at the bottom of the tower. Critical electrical equipment can be protected from vibrations generated by the platform motion that is considerably lower at the tower bottom of a FWT. Considering these advantages, it was decided to relocate some mass (the transmission equipment) to the bottom. This resulted in a nacelle mass of 255 tons which was comparable with the geared system (240 ton). Table 6.6 summarises the platform hydrostatic and resonance properties of the spar buoy wind turbine supporting the direct-drive generator. The nacelle C.O.M was thus shifted to be 2.5m upwind of yaw axis. Fig. 6.6 shows the location of the nacelle C.O.M.

Item/Description	**Units**	**FWTDD system**	**NREL,5MW baseline system [47, 182]**
Nacelle mass	ton	255	240
Nacelle centre of Mass from yaw axis	m	2.5 upwind	1.9 downwind
Nacelle C.O.M Location above yaw Bearing	m	1.9	1.75
Centre of gravity of the entire system	m	-77.56*	-78.61*
Surge/sway natural period	s	125.6	125
Heave natural period	s	31.4	30.8
Roll/Pitch Natural Period	s	29.9	29.1
Yaw Natural Period	s	7.57	5

*Negative sign indicates measurement below water plane

Table 6.6 Spar properties

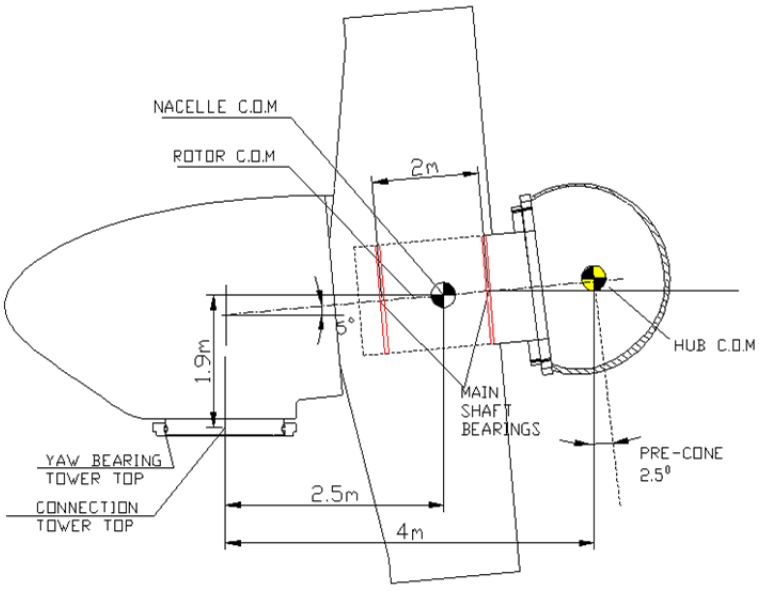

Fig. 6.6 C.O.M location for the adjusted system

6.5.3 Tower structural properties

The main dimensions of the tower were not altered, but in order to account for the additional 15 tons in the nacelle and to match the fatigue life of the baseline system the tower thickness was adjusted by about 9%. This increased the overall tower mass by 128 tons against the baseline system[47]. The un-displaced position of the base and the tower top were located at 10m and 87.6 m above the SWL respectively. The corresponding thickness at base and top levels were 0.0381 m and 0.027 m. The mechanical steel properties of the tower were retained as mentioned in [47]. The radius (and thickness) of the tower was assumed to be linearly tapered. Table 6.7 and 6.8 give the un-distributed and distributed tower structural properties. The entries in the first column of Table 6.8, HtFract are the fractional height along the tower centre line from the tower base to the tower top. The description for the remaining terms is listed below Table 6.8.

Item/Description	**Units**	**FWTDD system**	**5MW Spar system [179]**	**NREL, 5MW baseline [47]**
Elevation to Tower Base (Platform Top) Above SWL	m	10	10	10
Elevation to Tower Top (Yaw Bearing) Above SWL	m	87.6	87.6	87.6
Overall (Integrated) Tower Mass	kg	377,564	347,460	249,718
CM Location of Tower Above SWL Along Tower Centreline	m	38.36	NA*	43.4
Tower Structural Damping Ratio (All Modes)	%	1	1	1

* Not available

Table 6.7 Undistributed Tower Properties

HtFract	**TMassDen**	**TwFAStif**	**TwSSStif**	**TwGJStif**	**TwEAStif**	**TwFAIner**	**TwSSIner**	**TwFAcgOf**	**TwSScgOf**
(-)	(kg/m)	(Nm^2)	(Nm^2)	(Nm^2)	(N)	(kg-m)	(kg-m)	(m)	(m)
0	6104.43	6.65+11	6.65E+11	5.12E+11	1.50E+11	27469.9	27469.9	0	0
0.1	5713.10	5.79E+11	5.79E+11	4.46E+11	1.41E+11	23916.0	23916.0	0	0
0.2	5334.62	5.02E+11	5.02E+11	3.86E+11	1.31E+11	20718.0	20718.0	0	0
0.3	4969.00	4.32E+11	4.32E+11	3.32E+11	1.22E+11	17851.3	17851.3	0	0
0.4	4616.24	3.70E+11	3.70E+11	2.85E+11	1.14E+11	15292.4	15292.4	0	0
0.5	4276.32	3.15E+11	3.15E+11	2.42E+11	1.05E+11	13018.3	13018.3	0	0
0.6	3949.27	2.66E+11	2.66E+11	2.05E+11	9.75E+10	11007.2	11007.2	0	0
0.7	3635.06	2.23E+11	2.23E+11	1.72E+11	8.98E+10	9238.1	9238.1	0	0
0.8	3333.72	1.86E+11	1.86E+11	1.43E+11	8.23E+10	7690.7	7690.7	0	0
0.9	3045.22	1.53E+11	1.53E+11	1.18E+11	7.52E+10	6345.8	6345.8	0	0
1.0	2769.58	1.25E+11	1.25E+11	9.65E+10	6.84E+10	5185.0	5185.0	0	0

Table 6.8 Distributed Tower Properties

HtFract - fractional height along the tower centreline from the tower base to the tower top;
TmassDen – Tower Section Mass Density;
TwFAStif- Tower fore-aft Stiffness;
TwSSStif- Tower Side-to-Side Stiffness;

TwFAIner - tower section fore-aft inertia per unit length;

TwGJStif – Tower torsional stiffness

TwEAStif- Tower Extensional stiffness
TwSSIner- tower section side-to-side inertia per unit length
TwFAcgOf - Mass offset measured from the tower centreline in the fore-aft direction
TwSScgOf - Mass offset measured from the tower centreline in side-to-side directions

6.5.4 Platform structural properties

The main dimensions of the platform, including the tapered conical section remain the same as the baseline system. The draft was maintained at 120 m. The mass of the platform including ballast was 7365 tons. The CM of the floating platform, including ballast, is located 93.2 m along the platform centreline below the sea water level. The roll and pitch inertias of the floating platform about its centre of mass are 7.335×10^{10} kg-m^2 and the yaw inertia of the floating platform about its centreline is 1.037×10^{8} kg-m^2. These inertias were calculated using a mass distribution appropriate to the floating platform. Table 6.9 presents the platform properties for the FWTDD system with the values for the baseline system for reference.

Item/Description	**Units**	**FWTDD system**	**NREL, 5MW baseline [47]**
Depth to Platform Base Below SWL (Total Draft)	m	120	120
Elevation to Platform Top (Tower Base) Above SWL	m	10	10
Depth to Top of Taper Below SWL	m	4	4
Depth to Bottom of Taper Below SWL	m	12	12
Platform Diameter Above Taper	m	6.5	6.5
Platform Diameter Below Taper	m	9.4	9.4
Platform Mass, Including Ballast	kg	7365000	7466330
CM Location Below SWL Along Platform Centreline	m	93.21	89.91
Platform Roll/Pitch Inertia about CM	kg-m^2	7.33×10^{10}	4.22×10^{9}
Platform Yaw Inertia about Platform Centreline	kg-m^2	1.03×10^{8}	1.64×10^{8}

Table 6.9 Platform Structural properties

6.5.5 Mooring Properties

The layout and properties of the mooring system were retained from [179]. Three sets of mooring lines with fairleads located on the circumference of the spar form a delta configuration. Each line consists of three sections; a delta line made up of two segments that form a delta connection at the spar, an upper line connecting the delta

to a clump mass and a lower line that connects to an anchor on the sea floor. The mooring system characteristics namely the diameter, length and masses of the mooring segments were found to be sufficient for the FWTDD system, hence no modifications were required. The line stiffness and pretensions were consistent with [179]. Table 6.10 summarises the mooring system properties and Fig. 6.7 shows the schematic layout for the FWTDD system with mooring lines.

Item/Description	**Units**	**FWTDD system**
Number of Mooring lines	-	3
Angle Between Adjacent Lines	deg	120
Depth to Anchors Below SWL (Water Depth)	m	320
Depth to Fairleads Below SWL	m	70.0
Radius to Anchors from Platform Centreline	m	853
Radius to Fairleads from Platform Centreline	m	5.2
Un-stretched Mooring line length	m	902.2
Mooring Line Diameter	m	0.09
Clump mass	kg	17,253
Equivalent Mooring line mass Density	kg/m	42.5
Equivalent Mooring line weight in Water	N/m	381.8

Table 6.10 Mooring system properties

The overall mass of the FWTDD system including mooring lines was computed as 8396 tons, though further attempts on optimisation can result in further reduction in the weights. As may be noted from the Fig. 6.8, this compares well with some of the other spar designs that have been under research.

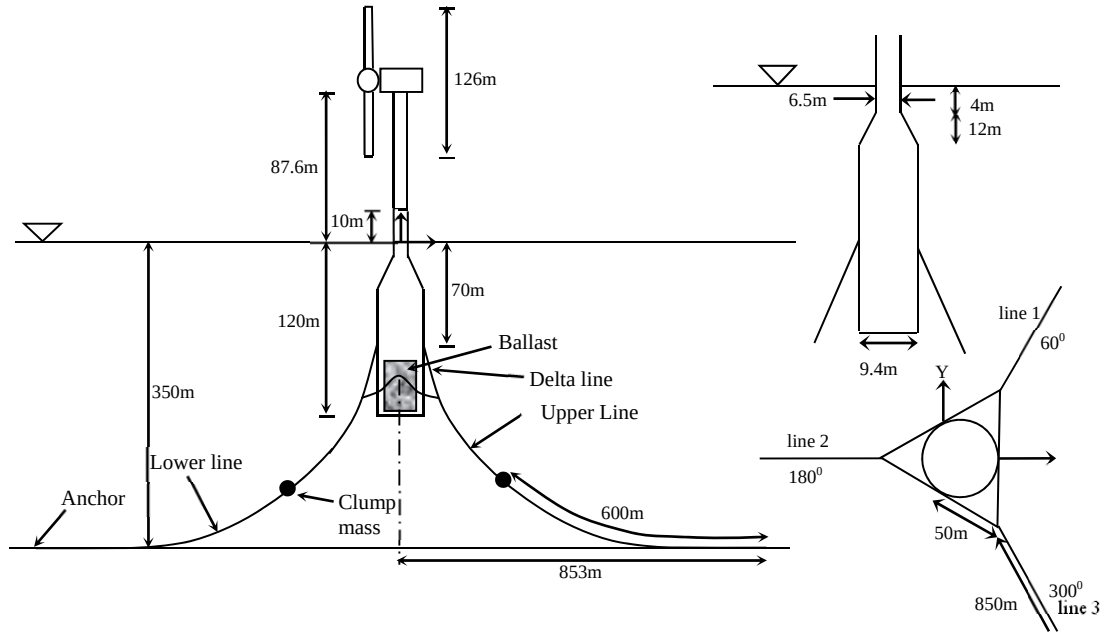

Fig. 6.7 Mooring layout of the FWTDD system

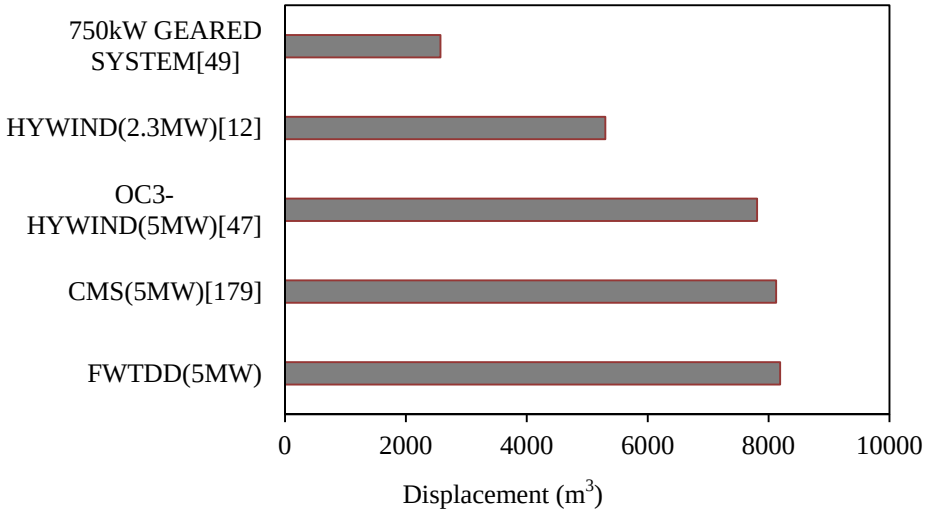

Fig. 6.8 A comparison of FWTDD system with existing designs (based on spar floaters)

6.6 Wind turbine Controller properties

The NREL 5-MW wind turbine is described by a quasi-static rotor model for controlling the aerodynamic efficiency. Variable speed operation of the wind turbine with power regulation can be achieved with direct-drive-wind generators either by active blade pitch control or stall control. However, active stall control places extra

demands on the generator, in terms of its efficiency and overload capability, thus making it much heavier and more expensive than the generator system for pitch control [186]. Therefore, the conventional variable blade-pitch control system was chosen and implemented using controllers for generator torque and blade pitch angle. The measured generator speed is filtered using a recursive low-pass filter before being fed as input to the controllers. The demand torque from the generator is established by a proportional-integral velocity controller, with control laws described in the following sections. The matching between the aerodynamic torque and the electromechanical torque of the generator determines the reference pitch angle rotor speed.

6.6.1 Generator-Torque Control

The control philosophy adopted for a direct-drive wind turbine is similar to the system implemented for the gear drive system[47, 164]; however the absence of gearbox in a direct-drive wind turbine requires high torque operation at lower speed, suggesting different dynamics for the control action. The control parameters defined in [47] were therefore modified to match the requirements of a direct-drive generator designed for the FWT. Depending on the measured generator speed, the wind turbine is operated according to five different control regions namely 1, 1½, 2, 2½ and 3 which are described as follows.

As may be noted from Fig. 6.9, the turbine start-up occurs in Region 1, for generator-speeds between 0 and 6.9rpm. In this region the generator torque is zero. Once the wind speed is sufficient for start-up, the pitch angle of the blades is changed from full feather (approximately 90°) to a pitch angle when the turbine operates in Region 2 (the run-pitch position, i.e 0°). Once the generator speed has accelerated to 6.9 rpm, the generator torque is switched ON and power is produced normally. The Region 2 torque curve is intended to keep the turbine operating at the peak of its Cp-λ curve and follows the square law:

$$T_{Gen\,2} = \left(\frac{\pi}{30}\right)^2 k_T \Omega^2 \tag{6.5}$$

where, T_{Gen2} is the commanded generator torque in Region 2, Ω is the filtered generator speed in rpm, k_T is the nominal Optimum torque control gain or the generator torque constant ($\text{Nms}^2/\text{rad}^2$) given by

$$k_T = \frac{1}{2}\rho\pi R^5 \frac{C_{p\max}}{\lambda_*{}^3} \approx \frac{P_{rated}}{\Omega_0{}^3} \tag{6.6}$$

Where R is the rotor radius, C_{pmax} is the maximum power co-efficient, λ_* is the tip-speed ratio at C_{pmax} and P_{rated} is the rated mechanical power of the turbine. To account for turbulence in wind speeds and maximise energy capture [187] , the torque gain is set to about 90% of the optimum. This allows the rotor to speed up more when the wind speed increases, thereby reducing the loads on the drive-train. For a rated mechanical power of 5.56MW and rated speed of 12.1 rpm (i.e. 1.27 rad/s), the torque gain was computed using equation (6.6) as $2.45\text{MN-ms}^2/\text{rad}^2$. This value was substantially higher than the baseline geared system by a factor of about 10^6. Region 1½ is a linear transition in the start-up region that spans the range of generator speeds between 6.9 rpm and 30% above this value (or 8.9 rpm). The minimum generator speed of 6.9 rpm corresponds to the minimum rotor speed used by the REpower 5MW machine [171]. Fig. 6.9 shows the optimal torque curve crossing the rated torque line at a higher rotor speed (rpm) than the rated speed (12.1 rpm). Using the same control law for generator torque results in a value below rated torque at rated speed (shown in black dotted line). In order for the generator torque to be equal to rated torque at rated speed a new region 2½ is introduced such that the torque is described using equation(6.7) from[188]

$$T_{Gen\,2\frac{1}{2}} = T_1 + \left(\frac{T_{rated} - T_1}{\Omega_2 - \Omega_1}\right)(\Omega - \Omega_1) \tag{6.7}$$

Ω is the measured generator speed for which $T_{\text{Gen2-1/2}}$ is to be determined, T_1 is the generator torque at the rotor speed when this region starts (Ω_1) and T_{rated} is rated torque, and Ω_2 is the rotor speed at which rated torque is reached. In Region 3, for above rated wind speed, the control switches to a constant torque mode with active pitch control to avoid negative aerodynamic damping as per the recommendations in [28]. The constant generator torque in region 3, T_{Gen3} is set to be saturated to a

maximum of 10% of the rated torque (T_{rated} = 4.38MN-m) to 4.81 MN-m inorder to avoid excessive overloading of the generator such that

$$T_{Gen3} = 1.1\,T_{rated} \tag{6.8}$$

Above rated speeds, the blade pitch controller typically pitches the blades to feather, which decreases the aerodynamic angle of attack and compensates for the speed response. A variable power pitch control is achieved without the risk of any negative damping in the rotor-speed response. The generator is expected to be overloaded as

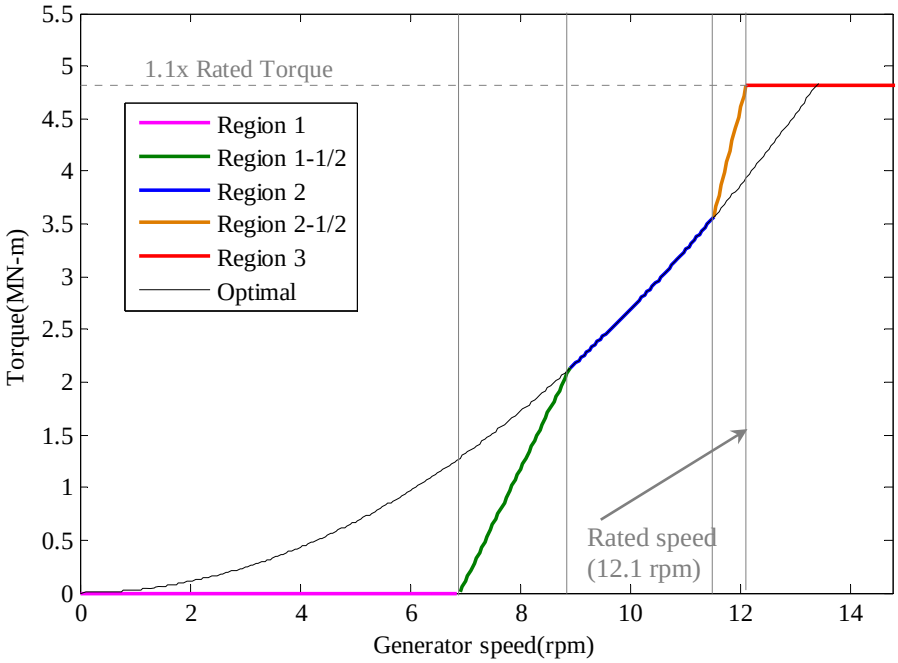

Fig. 6.9 Generator Speed-Torque Characteristics

power increases with rotor-speed. The generator torque is inferred from electrical measurements and measured rotor speed. Since the electrical system was not modelled, the generator torque is assumed to instantly follow the controller set-point assuming a faster dynamic response from electrical system. The present controller has not been optimised for all operating conditions. However because of a very low inertia of the generator rotor, a quick response is particularly important during start-up and when operating above the rated wind speed when aerodynamic torque increases rapidly and the generator torque must match the turbine to avoid damage due to over-speed. For this purpose, the maximum generator torque rate was imposed at $1x10^8$Nm/s.

6.6.2 Blade-Pitch Controller

The blade pitch control system is designed to be effectual on the torsional degree of freedom of the drive-train for wind speeds above rated. The servo system is implemented by a PI controller that provides a reference pitch angle depending on the measured generator speed. Above rated wind speed, the aerodynamic torque, T_{Aero} was linearised assuming negligible variation in rotor speed and greater sensitivity to pitch angle, θ. The blade pitch angle, $\Delta\theta$ is regulated by measuring the generator speed error using a PI controller [28] such that

$$\Delta\theta = K_P(\Omega - \Omega_{ref}) + K_I \int_0^t (\Omega - \Omega_{ref})\, dt \qquad (6.9)$$

Where, K_P and K_I are the proportional and integral control gains, Ω is the measured generator speed, Ω_{ref} is the reference speed, hence Ω-Ω_{ref} is the generator speed error. If φ is the integrated angle difference from the actual rotational speed and the measured generator speed, then the controller response assumes a second order system of the form given by

$$I\ddot{\varphi} + D\dot{\varphi} + K\varphi = 0 \qquad (6.10)$$

With a response frequency, ω_0, relative damping, ζ and damped natural frequency ω_d related by

$$\omega_0 = \frac{\omega_d}{\sqrt{1-\zeta^2}} \qquad (6.11)$$

The values for the constants are determined as

$$K_I = \frac{\Omega_0 I \omega_0^2}{\frac{\partial P}{\partial \theta}} \qquad (6.12)$$

$$K_P = \frac{2\zeta K_I}{\omega_0} \qquad (6.13)$$

where, $\frac{\partial P}{\partial \theta}$ is the sensitivity of aerodynamic power to rotor-collective blade pitch angle [47]. In reality, the gains and time constants vary according to the measured

value for the pitch angle; hence a gain-scheduling law was implemented to predetermine the set of tuning parameters. To eliminate the negative aerodynamic damping, the gains are tuned such that the controller response frequencies are lower than the natural frequencies of the FWTDD system [28, 189]. The natural frequency of the controller (0.0142Hz) was set to be lower than the pitch natural frequency (0.033 Hz) of the FWTDD system so that pitch control is slower than the tower motion. This value was chosen by verifying the controller stability in different wind conditions. Section 6.7 provides a discussion on controller performance and stability. The resulting properties are summarised in Table 6.11.

Item/Description	**Units**	**FWTDD system**	**OC3 Hywind 5MW**[47]
Corner frequency of generator-speed low pass filter	Hz	0.25	0.25
Peak power coefficient	-	0.482	0.482
Tip speed ratio at C_{pmax}	-	7.55	7.55
Rotor-Collective Blade-Pitch angle at Peak Power Coefficient	deg	0	0
Generator-Torque Constant in Region 2	Nms^2/rad^2	2455061.04	2.332
Generated rated power	MW	5.56	5.29
Rated generator torque	MN-m	4.38	0.043
Generator speed between 1 and 1½	rpm	6.9	670
Transitional Generator speed between regions 1½ and 2	rpm	8.9	871
Transitional Generator speed between regions 2½ and 3	rpm	11.9	1161.9
Minimum Blade Pitch for ensuring region 3 Torque	deg	1	1
Maximum Generator Torque	MN-m	4.8	0.047
Maximum Generator Torque Rate	MN-m/s	100	0.015
Proportional Gain at Minimum Blade-Pitch Setting	s	2.11	0.00627
Integral Gain at Minimum Blade-Pitch Setting	-	0.094	0.00089
Blade-Pitch angle at which the Rotor Power has doubled	deg	6.302	6.302
Minimum Blade-Pitch Setting	deg	0	0
Maximum Blade-Pitch Setting	deg	90	90
Maximum Absolute Blade Pitch Rate	deg/s	8	8

Table 6.11 Controller properties

6.7 Modelling the FWTDD system in HAWC2

The next step in the design process was to verify the FWTDD model specifications and to determine global response characteristics. For this purpose, a fully coupled aero-hydro-servo elastic model of the FWTDD system was implemented in HAWC2 for the specifications that were developed. HAWC2 is an aero-elastic simulation code developed by Risø National Laboratory [135] that can simulate the time domain response of a wind turbine subject to wind and control actions. The code is based on a multi-body formulation which uses the classic Timoshenko beam element considering Finite Element Analysis (FEA) for the structural dynamics and an advanced blade element momentum (BEM) theory for the aerodynamics. The various elements namely the tower, foundation, shaft/nacelle and rotor for the FWTDD system were modelled and assembled together by geometric sub-structuring technique. The turbine and nacelle were modelled as rotating substructures coupled to each other and the tower. The wind turbine blades and tower were modelled as long slender structures. Mooring lines use a simplified quasi-static force model implemented as DLL (Dynamic Link Library). The inertia and damping effects from mooring were ignored. This was because the mass of the mooring lines is small compared to the spar platform and damping (viscous forces) offer limited contributions to the global responses of the spar floater. Coupling in the surge/pitch and sway/roll directions were also included. The flexible elements of the drive-train were modelled as shaft elements with mass, structural stiffness and damping properties. A 1-DOF torsional spring-damper system was implemented. The generator is modelled as a separate rotational degree of freedom with the speed-torque characteristics and control algorithm modelled as a force element DLL. HAWC2 solves the equations of motion by a time integration scheme and presents the results as time series for loads and deformations.

6.7.1 Environmental loads

To characterise the wind and wave climate typically expected in deep-water conditions, a representative offshore site, Statfjord in North Sea was chosen. Statfjord is oil and gas field located at 59.7 N and 4.0 E, 70 km from coast of

Norway and operated by Statoil. Wind and wave data taken from site measurements between 1973 and 1999 were smoothed and fitted to analytical functions by the method described by Johannessen *et al*.,[180]. The 1-hour mean wind speed at 10-m height, *F(V)* was defined by a two-parameter Weibull distribution given by:

$$F(V) = 1 - \exp\left[-\left(V/\beta\right)^{\alpha}\right] \tag{6.14}$$

where, V is the mean 10-min wind speed at ten metres, with shape and scale parameters, α =1.708 and β = 8.426 recommended for the representative site. The average wind speed at hub-height was obtained by scaling the wind speed at 10m height using the power law with a power co-efficient of 0.147. To obtain the 10-min average wind speeds, 10% scaling was applied to 1-hour average wind speeds. The turbine cuts in at 4m/s and cuts out for wind speed above 25m/s. Blade pitch angle equals zero below rated and 90 degrees at cut-out.

The aerodynamic loads are derived from quasi-static theory using the BEM method with mean wind field effects including correction factors for induction; tip-loss, shear and tower drag and shadow effects (based on potential flow method). The turbulent part of wind was assumed to be homogeneous in space and generated according to Mann method[190]. Wind turbine blades are long and slender structures with wind flow at a given point assumed as two dimensional.

Wind generated waves were only considered; as a result wind and wave climates were correlated. The shape and scale parameters defined by Johannessen *et al*., [180] were used to obtain the formulae for the expected significant wave height, $E(H_{m0})$ and expected wave peak period, $E(T_P)$ [179] . These were obtained as a function of the mean ten minute wind speed at ten metres, V (m/s) using the following equations

$$E(H_{m0}) = \beta\Gamma\left(\frac{1}{\alpha} + 1\right) \tag{6.15}$$

where, $\alpha = 2 + 0.135V$ and $\beta = 1.8 + 0.1V^{1.322}$ and

$$E(T_p) = \left(4.883 + 2.68 H_{m0}^{0.529}\right)\left(1 - 0.19\frac{V - (1.764 + 3.426 H_{m0}^{0.78})}{(1.764 + 3.426 H_{m0}^{0.78})}\right) \quad (6.16)$$

Hydrodynamic load computation uses the strip theory based Morison formulation [130]. Wave kinematics at every time step uses airy theory, with wheeler stretching and the hydrodynamic forces are calculated considering the instantaneous position of every strip of the floater as

$$dF = \frac{\rho}{2} C_d D |u_r| |u_r| dZ + \rho \frac{\pi D^2}{4} C_a \dot{u}_r dZ + \rho \frac{\pi D^2}{4} \dot{u}_w dZ \quad (6.17)$$

where, dF is the wave force acting on a strip of length dZ, ρ the density of fluid, D the cylinder diameter, C_a the added mass coefficient, C_d the drag force coefficient, u_r the relative velocity of wave and cylinder and u_w the wave velocity. The values for C_a and C_d were 1.0 and 0.6 respectively considering a Keulegen-Carpenter number of 5 [191]. Since the Morison formula does not provide heave excitation and buoyancy forces, HAWC2 uses Archimedes plus static pressure integration methods over the bottom and conical sections of the spar to calculate the vertical forces [192].

The Joint North Sea Wave Project (JONSWAP) wave spectrum is used to represent the long-crested irregular waves. The spectrum, S_{JS} is described using [130] as

$$S_{JS}(f) = \frac{1}{5(0.065\gamma^{0.803} + 0.135)} \cdot S_{PM}(f) \cdot \exp\left(\frac{-(f - f_p)}{2\sigma^2 f_p^2}\right) \quad (6.18)$$

$$\text{With } \sigma = \begin{vmatrix} 0.07 & f \le f_p \\ 0.09 & f > f_p \end{vmatrix} \quad (6.19)$$

where, f is the wave frequency, f_p is the peak wave frequency, γ is the shape factor (chosen as γ =3.3), $S_{PM}(f)$ is the Pierson Moskowitz spectrum, σ is a constant that relates to wind speed and fetch length. For the turbine operational region that spans the wind speeds from 4-25m/s, 22 unidirectional wind and wave load cases were obtained using the empirical relations defined by equations (6.15) and (6.16). These

cases are presented in Table 6.12 where V_{mean} represents the 10 min-mean wind speed at hub-height, H_{m0} the significant wave height and ω_p the peak wave frequency obtained from equation (6.16).

V_{mean} (m/s)	H_{m0} (m)	ω_p (rad/s)	Status
4	1.96	0.646	Operating
5	2.08	0.645	
6	2.22	0.643	
7	2.36	0.641	
8	2.52	0.638	
9	2.68	0.634	
10	2.84	0.630	
11	3.01	0.626	
12	3.19	0.622	
13	3.37	0.617	
14	3.55	0.612	
15	3.75	0.607	
16	3.94	0.602	
17	4.14	0.597	
18	4.35	0.591	
19	4.55	0.586	
20	4.77	0.581	
21	4.98	0.576	
22	5.20	0.570	
23	5.43	0.565	
24	5.65	0.560	
25	5.88	0.555	

Table 6.12 Load Cases used for this study

6.7.2 Controller stability

Controller tuning and stability are important aspects that need to be evaluated carefully for a FWT system [28, 189]. The specifications of the controller properties defined in section 6.6 were incorporated into a control system dynamic link library (DLL) in the HAWC2 model. In order to evaluate the performance and stability of the controller, time response simulations were carried out where the turbine was subjected to deterministic wind speeds. The stability of the control system was first tested by observing the tower motion response to a linearly increasing wind velocity up to 16m/s. No waves were assumed to be present. Figures 6.10 (a-d) show the

simulation results for the shaft speed, blade pitch action and the rigid body tower surge motion for the FWTDD system. Rotor speed overshoots by 7% of the rated (i.e. 12.1rpm) to about 13rpm at 300s while the platform surges upto a maximum of 22m between 150-300s during which the wind ramp up occurs. It takes about 700s for the surge response to stabilise.

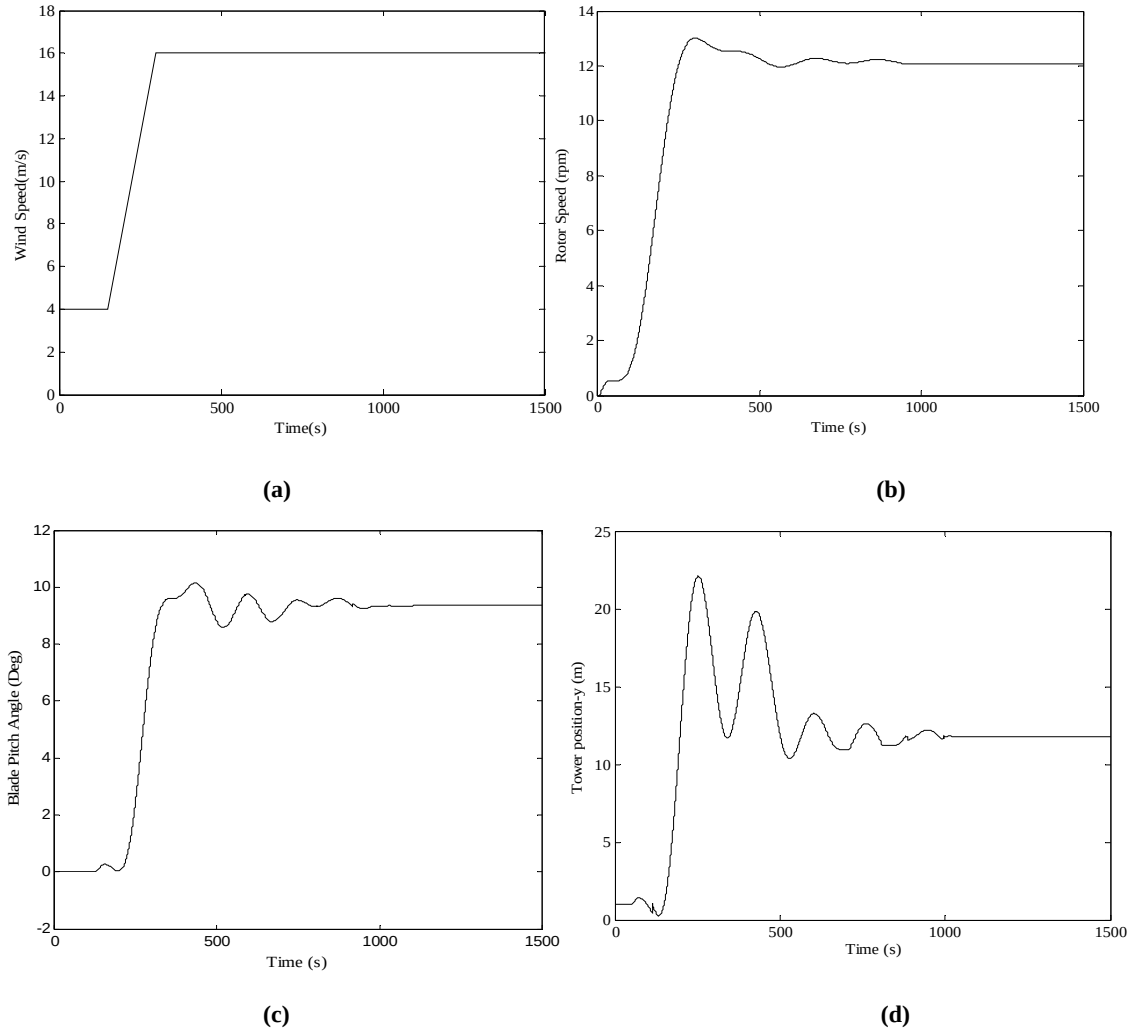

Fig. 6.10 Tower response and controller response for the FWTDD system for a deterministic wind speed (a) Wind Speed (b) shaft speed (c) blade pitch action and (d) platform surge motion

The controller performance was further tested in step winds. These step winds start at 11 m/s and ramp up to 25m/s at 600s. Both floating as well as land-based direct-drive wind turbine system (WTDD) were tested with the same controller. For the land-based system, the foundation and mooring lines were removed and the tower was

cantilevered to the soil floor. The results of the simulations are presented in Figures 6.11(a-e).

Overshoot in rotational speed was observed and was found to be below 10% for the land based wind turbine and 13% for the floating system. Moderate spikes are observed in the blade pitch response, every time the wind ramps up for the WTDD system. The oscillation in blade pitch response and shaft speed for the FWTDD system is induced by platform motions (particularly by pitch motion). Generator torque for both the systems is relatively stable except for two spikes at 94s and 188s respectively for the FWTDD system. The platform surges upto a maximum of 42m as the wind ramps up to 14m/s. The tower response for the WTDD system is solely provided as a reference in Fig. 6.11(e). It may be observed for the above wind conditions that the step change in wind speed was fast (and the duration for each wind speed was short, i.e. 40s) so that the spar (tower) motion response does not show a steady response for each wind speed. To examine the controller response more closely, simulations were run for a longer duration for each wind speed. Figures 6.12(a) shows the wind step increments from 11-13m/s. The controller response frequency was kept at 0.125 rad/s(or 50s). However, considerable pitch instability was observed after 700s of simulation causing fluctuations in generator torque and speed response. To ameliorate this problem, the controller response frequency was suitably adjusted until a more stable response was achieved for the given wind conditions (although the controller response was not optimised for all operating conditions). The controller response frequency was progressively reduced from 0.125 rad/s until 0.09 rad/s (or 70s) when a more stable response was achieved. Figures 6.13(a-e) show the response for the adjusted system.

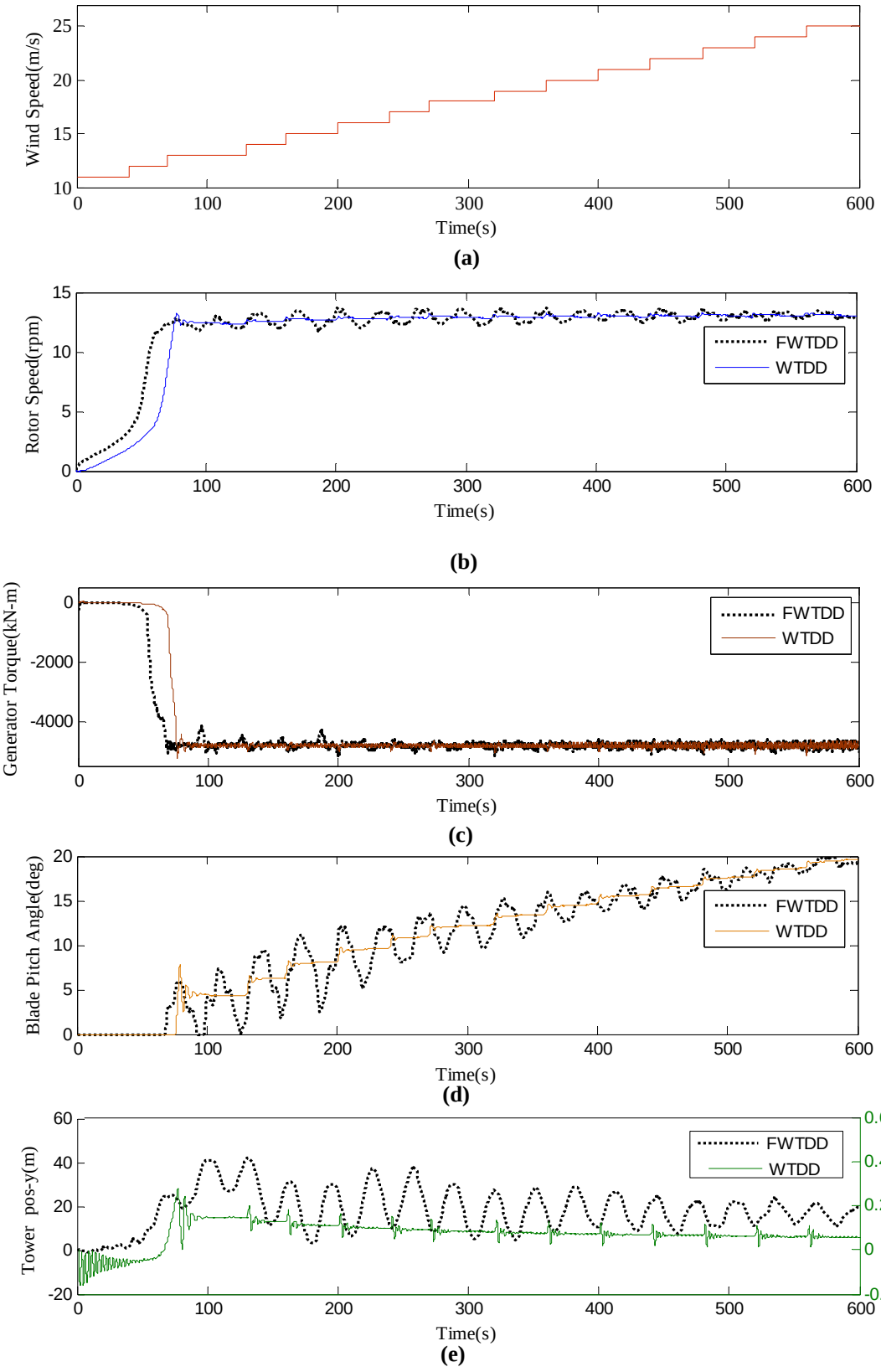

Fig. 6.11 Step response. (a) Wind speed (b) Shaft rotational speed (c) Generator Torque (d) Blade pitch angle (e) Tower position

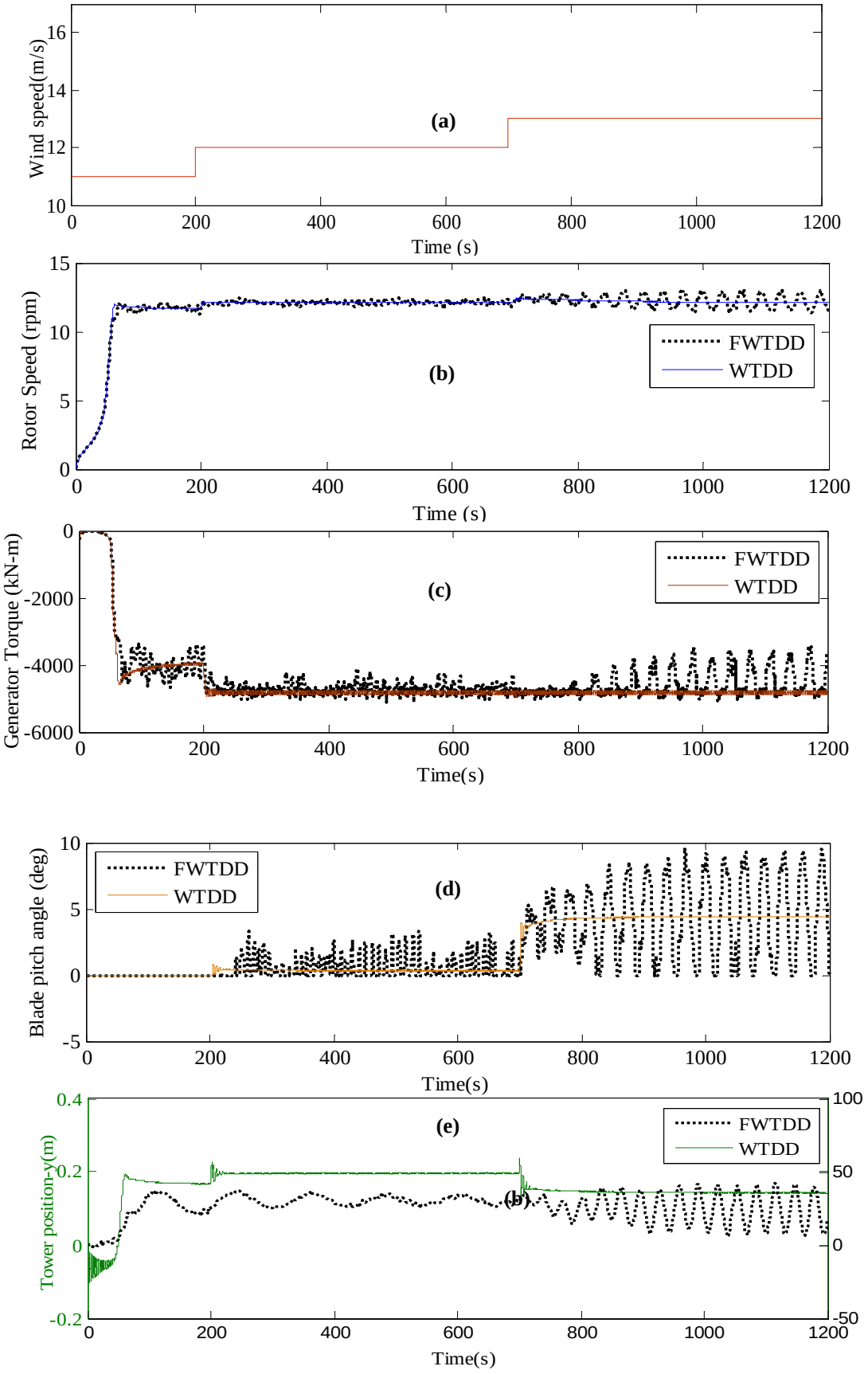

Fig. 6.12 Step response - longer duration. (a) Wind speed (b) Shaft rotational speed (c) Generator Torque (d) Blade pitch angle (e) Tower position

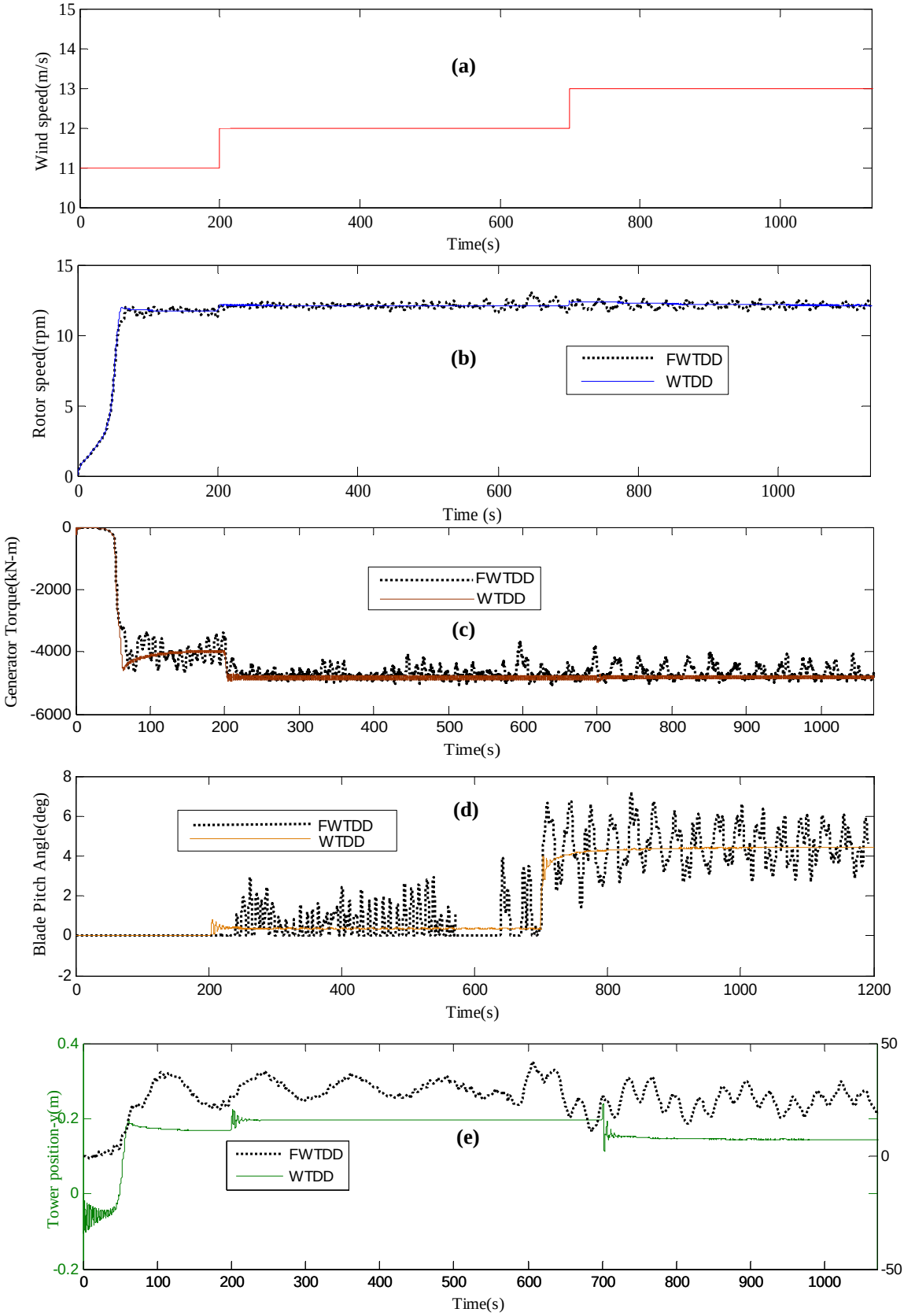

Fig. 6.13 Step response-adjusted (a) Wind speed (b) Shaft rotational speed (c) Generator Torque (d) Blade pitch angle (e) Tower position

6.7.3 Global motion response

22 one-hour simulations were carried out by subjecting the model to unidirectional wind and wave loads as defined in section 6.7.1 and the motion responses were extracted. A comparison of the motion responses was made with the 5MW geared FWT system that was modelled in HAWC2 using the specifications presented in [47]. Figures 6.14 (a) & (b) show the results for nacelle motion response statistics

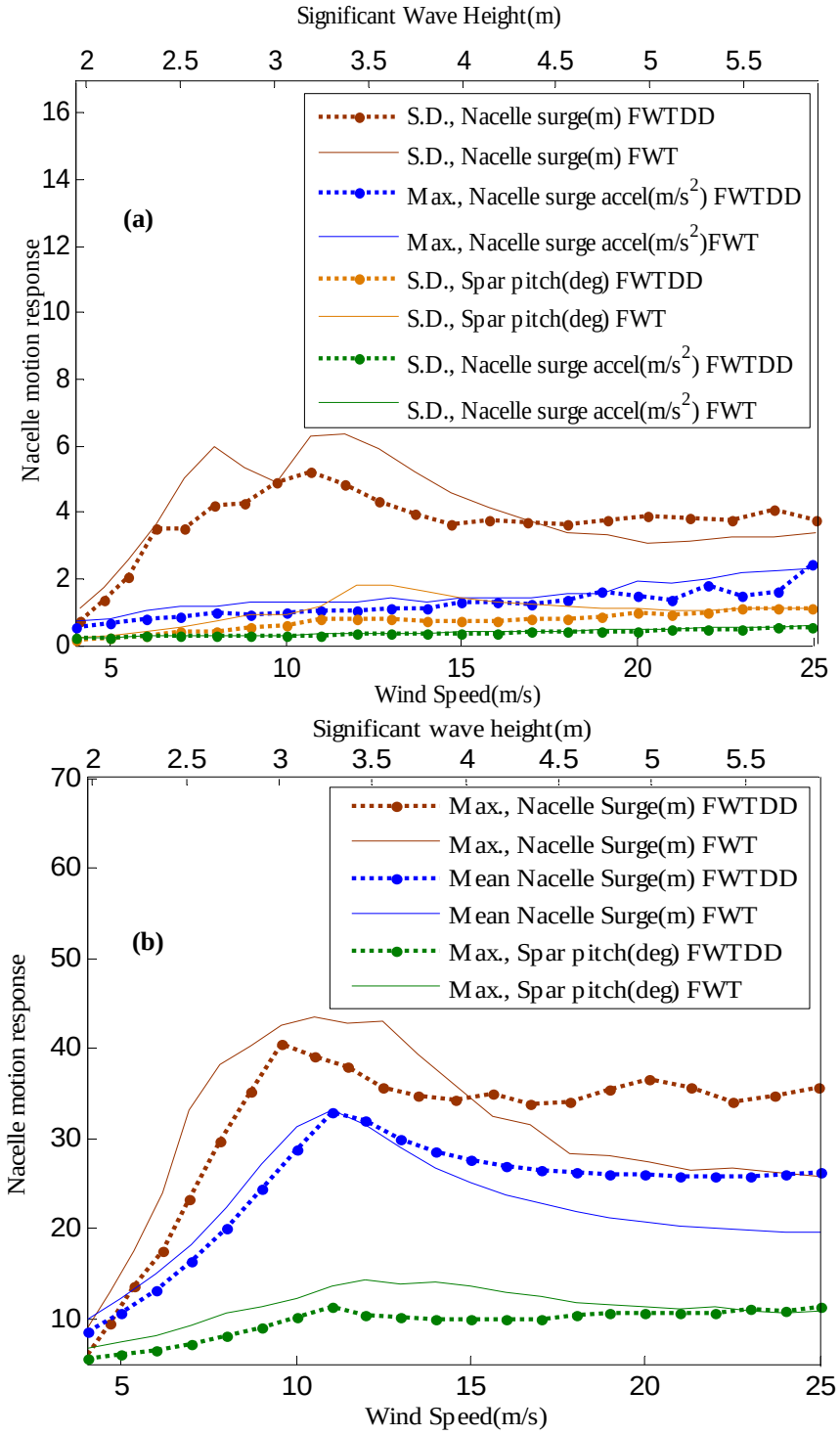

Fig. 6.14 (a) & (b) Nacelle motion response statistics from HAWC2 simulations

indicating a steady increase in surge and pitch responses upto 11m/s beyond which the responses begin to smoothen out. The maximum surge acceleration was 2.4m/s^2 (at 25m/s); maximum pitch angle was less than 8°. It can be inferred from the response characteristics that the behaviour of the FWTDD system closely resembled that of the geared FWT system.

Figures 6.15 (a) & (b) show the frequency spectra for the surge and pitch motions (computed for a wind speed of 20 m/s) indicating their respective contributions to the motion response. Since, one-hour simulations were considered, statistical uncertainty may be present for the below rated and above rated wind speed conditions.

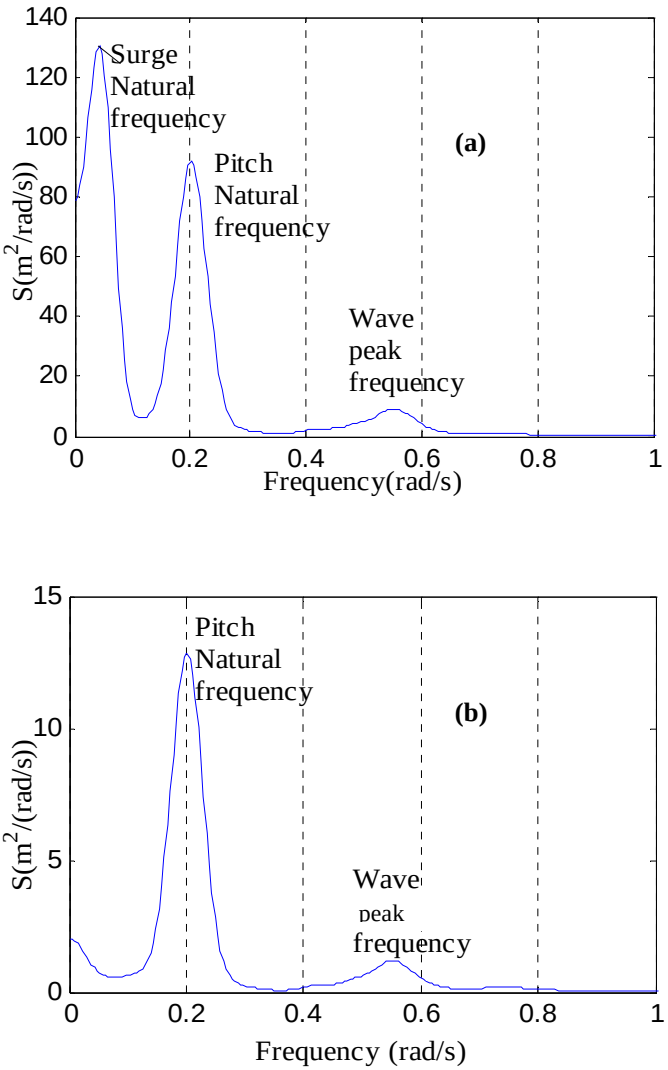

Fig. 6.15 Nacelle motion response spectra for FWTDD system (a) Surge (b) pitch response

6.7.4 Internal drive-train behaviour

Apart from the 6 DOF freedom motion response characteristics, HAWC2 also provides information on main shaft moments and forces. As a next step, to be able to assess the performance of the FWTDD system, dynamic behaviour of the drive-train must be evaluated. For this purpose, a two-step decoupled approach proposed by Xing *et al.,*[51, 52] shall be used. Fig. 6.16 shows the block diagram for this methodology. The global motion response and loads from HAWC2 are input to a detailed drive-train model in SIMPACK, a general purpose Multi-Body Simulation (MBS) software that enables kinematic and dynamic analysis of mechanical systems[136]. The SIMPACK model is a stand-alone system with the same drive-train model as described in section 6.3.2, but segregated from the tower, turbine and controller sections. The 6 DOF motion response variables for position ($p(t), \theta(t)$)), velocity ($v(t), \omega(t)$) and acceleration($a(t), \alpha(t)$) from HAWC2 are kinematic inputs. Shaft moments (M_{xyz}) and forces (F_{xyz}) are applied at the hub-end where the turbine is assumed to be attached. As the next step, the internal responses and loading of the drive-train shall be analysed in response to the applied loads in Chapter 7.

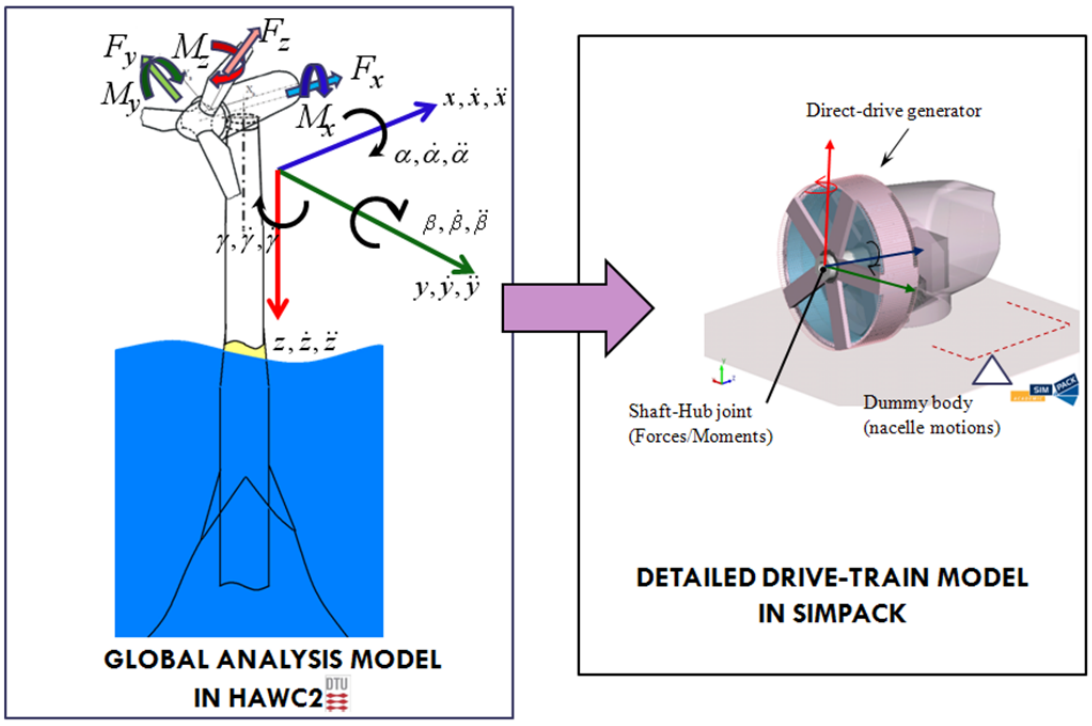

Fig. 6.16 Drive-train analysis methodology

6.8 Summary

The preliminary specifications for a floating version of 5MW wind turbine supporting a direct-drive generator was developed for the purpose of carrying out fully-coupled time-domain aero-hydro-servo-elastic simulations. The OC3-hywind model served as the main reference system to establish these specifications. Detailed drive-train properties including dimensions of the shaft, mechanical properties were developed to suit a radial flux permanent magnet generator topology that was obtained from previous optimisation studies. The direct-drive system made the nacelle heavier than the geared system requiring few adjustments to the design. The task involving adjustments to tower and platform properties revealed the challenge of maintaining the same draft as that of a geared system with larger nacelle mass. Yet it was possible to match the resonance properties with that of geared systems by manipulating the location of power distribution/auxiliary equipment. This resulted in a slightly heavier tower, although rest of the system did not require any major modifications. The overall mass of the developed FWTDD system is generally consistent with existing spar designs. The validity and behaviour of the model was tested for the various wind and wave conditions and the motion response behaviour was found to be generally consistent with the typical response characteristics observed for the spar buoy wind turbine. The properties for the controller were found to ensure a stable response, although the controller response was not optimised for all operating conditions. The next chapter proceeds with investigations on the internal drive-train behaviour and explores further challenges/opportunities of implementing the direct-drive model for floating wind turbines.

Chapter 7

Drive-train dynamics of a 5MW FWTDD system

7.0 General

This Chapter proceeds with investigations on a fully coupled model of 5MW FWTDD system that was presented in Chapter 6. First, the theory and methodology for investigating the behaviour of the direct-drive generator is identified. A preliminary study was carried out on a fully integrated land-based direct-drive wind turbine system using SIMPACK for this purpose. This study served to validate the 2-step de-coupled approach (as discussed in Chapter 6) as well as identify the important response variables such as eccentricity induced Unbalanced Magnetic pull (UMP) and vibrations that represented the main reaction forces in the direct-drive generator for a FWT. The land-based model served as a reference to model the drive-train for the FWTDD system.

7.1 Introduction

Ensuring the mechanical integrity of the drive-train, guaranteeing a reliable and robust operation under extremely demanding conditions in a FWT presents huge design challenges. In principle, when a direct-drive generator is implemented on a floating wind turbine, with fewer moving parts and half the number of components as that of the traditional geared system, it should present superior performance and greater reliability. Because the operational speeds of the generator are much lower, the generator is subjected to less wear, allowing a longer operational life and the capacity to handle larger operational loads. Yet, there isn't enough operational experience from existing offshore wind turbines with permanent magnet generators to corroborate this claim, designers are compelled to rely on experimental testing and numerical simulation techniques for making inferences on the dynamics of the drive-train.

7.1.1 Drive-train dynamics

Understanding the dynamic behaviour of the drive-train of a wind turbine is important for verification of design loads and strength requirements of machinery components. Drive-train dynamics involves the understanding of the behaviour of the component in response to the cyclic and stochastic loads imposed by various processes on the drive-train. Numerical simulation tools can provide a good insight into the dynamic loading of the drive-train and interfaces under all relevant loading conditions at relatively low expense. Most response states, failure modes/statistics and unexpected structural excitations can be identified. As the components perform both structural and mechanical functions at the same time, it is crucial to simulate loads properly and evaluate the response to predict their performance and reliability. The analysis of the direct-drive system for a floating wind turbine requires an accurate dynamic response model that includes its aero-dynamic interaction with the wind and control system, the nacelle accelerations, the torsional and translational responses of its mechanical components and the electro-mechanical interaction at the generator. Multi-body simulation (MBS) methods are widely used in the industry for this task [193]. MBS tools allow definition of these interactions and creation of a structural model of the drive-train with appropriate values of inertia, stiffness and damping properties to describe the motions and deformations in the system.

In recent years, numerous studies have been carried out on the internal drive-train dynamics of land-based and offshore wind turbines. The vast majority of these studies have been on geared drive-trains, aimed at improving the reliability of these systems, for example [194-197]. The first studies on the dynamics of a drive-train for floating wind turbines were reported by Xing *et al*., [51, 52]. On the other hand, the dynamic behaviour of direct-drive generators, have been less studied for wind turbines and reported in the public domain. The following section provides a discussion on this subject.

7.1.2 Dynamics of direct-drive generator

Direct-drive permanent magnet synchronous generators are designed with stringent manufacturing tolerances and are particularly sensitive to shaft misalignments that

lead to dynamic changes in air-gap and imbalances in magnetic forces. Possible consequences of these effects include vibrations, noise and bearing wear that can have an impact on the lifecycle of the drive-train components. It is important to understand these effects, verify component durability to be at an acceptable level and make any design changes if necessary before implementation in a FWT. Therefore, as a pre-requisite, dynamic analysis of the direct-drive generator must be carried out with an emphasis on electro-mechanical interaction and bearing loads.

Few investigations on dynamics of direct-drive generator have been carried out in the past. References [90, 159, 198] have analysed and optimised the structural and mechanical design of a radial flux direct-drive generator rated between 0.75-3.0 MW levels suitable for land-based or fixed bottom offshore wind turbines. Experimental tests on a 1.5MW design [159] showed no vibration problems with the generator, although up to 50% eccentricity was permitted during extreme loads. References [199-201] examined the vibration behaviour of the permanent magnet synchronous generator and quantified the excitations from cogging torque and torque ripple harmonics in the operational speed range of the turbine. The feasibility of direct-drive generators at larger scales for e.g.: 10MW is still being investigated [202]. References [163, 203] proposed the nacelle and hub design, examined the bearing life and structural adequacy for an outer rotor permanent magnet generator.

One of the first studies with a direct-drive generator for a horizontal axis spar-buoy FWT system was carried out by Boulder Wind Power [79]. Their drive-train uses a modular light-weight air-core design of a 6MW axial flux permanent magnet generator with a flexible support structure. Preliminary load analysis studies showed opportunities in nacelle weight reductions, promised reduction in extreme loads, savings in draft and tower structural requirements by about 10% and 15% respectively when compared to a geared FWT system. However, this came at the expense of larger heave displacements, resulting in modifications to the mooring design. The Boulder generator design has a low stiffness to weight ratio, which involves a greater degree of complexity in design and manufacturing. The robustness of the system relies entirely on the effectiveness of stator-rotor air-gap control, which can be difficult especially at higher magnitude nacelle accelerations. Reports on the drive-train behaviour are not

available in the public domain and the air-gap dynamics of the system has not been published yet.

In all of literature that was reviewed, the dynamic response of direct-drive generators has not been well established with regards to the electro-mechanical interaction. In order to make a realistic assessment for a FWT system, it is necessary to examine the dynamics of the direct-drive generator with special emphasis on the air-gap dynamics, unbalanced magnetic pull, bearing loads and lifetimes. This work aims to increase the general understanding of the behaviour of a direct-drive generator and continue the investigations on the fully integrated model of the FWTDD system that was developed in Chapter 6. Any further challenges/opportunities of implementing the model for a FWT are identified. To examine the drive-train dynamic behaviour, time-domain multi-body simulation tools namely HAWC2 [135] and SIMPACK [136] were used. A detailed description of HAWC2 was given in Chapter 6. SIMPACK is a multi-body simulation tool that allows detailed kinematic and dynamic analysis of wind turbine components by integrated wind turbine simulation, incorporating flexible Finite Element Methods (FEM) bodies, force and control elements.

The response characteristics of the drive-train were tested for the typical operational range of the wind turbine, i.e. 4-25m/s. The proposed drive-train model was first tested for land-based turbine model to identify and quantify reaction forces and possible feedback effects from the generator such as eccentricity induced UMP and vibratory torque. The investigation then proceeds with a 2-step de-coupled approach for the FWT drive-train analysis. The global motion response and drive-train loads (forces and moments) are obtained by 1-hour simulations in HAWC2. These are then fed to a detailed stand-alone multi-body model in SIMPACK. The drive-train was modelled with a flexible shaft with 6DOF supported by two main bearings with compliance and reaction forces due to eccentricity incorporated from kinematic measurements. The response statistics for shaft displacements, eccentricity, forces due to unbalanced magnetic pull, the main bearing reaction forces and tilting moments were computed and compared with a land-based wind turbine model. A standard bearing life model was used to predict the reductions in bearing life expectancies with the FWTDD system. The following sections introduce the theory and methodology for the analysis.

7.2 Theory and methodology

For the integrated dynamic analysis of the direct-drive generator, it was intended to adopt the two-step de-coupled approach proposed by Xing *et al.,*[51, 52] by the method discussed under section 6.7.4 in Chapter 6. This method is perfectly acceptable for geared drive-trains as the feedback forces are expected to be small and the gearbox response is of quasi-static nature with high frequency internal modes. However, before adopting this approach with confidence for a direct-drive generator, it is necessary to evaluate the significance of dynamic effects and feedback forces from the drive-train. Due to the low rotor speeds and high vibration sensitivity in direct-drive generators, reaction forces must be considered.

The approach to analysing a direct-drive power train was first validated after carrying out a preliminary investigation of the internal reaction forces in a direct-drive generator for a land-based wind turbine using SIMPACK. The preliminary investigation was intended to arrive at the drive-train model that best characterised the dynamic behaviour of a direct-drive generator and mainly served two purposes:

1) Internal drive-train reaction forces: To investigate the possible sensitivities of the drive-train to shaft misalignment and incorporate the necessary response variables into the drive-train model for the floating wind turbine.
2) Dynamic effects and Possible Feedback: To identify or quantify any unforeseen controller response action, due to the direct-drive generator reaction that has to be the included in the drive-train model for the floating wind turbine.

7.2.1 Internal drive-train response and feedback effects

In a floating wind turbine, the loads from the wind turbine coupled with the oscillatory motions at the nacelle can introduce high loads at the bearings and can cause shaft deflections. Typically the main shaft is susceptible to greater radial deflection or displacement, axial displacement and bending moments. The resulting interaction between assemblies in the drive–train results in additional vibration (for e.g: misalignment can cause excessive forces, torsion/bending vibration or resonance can occur). In a direct- drive permanent magnet generator, shaft displacement and rotor imbalance are serious issues that can cause increased vibrations, accelerated bearing

wear and lifetime consumption - and loss of revenue through increased O&M costs and standstill hours. Because, the probability of shaft misalignment is higher with FWTs, it is important to verify the impact on the internal drive-train behaviour and also feedback forces, if any from the direct-drive generator that can propagate to the wind turbine.

Possible reactions expected from the drive-train include (a) eccentricity induced unbalanced magnetic pull [143] and (b) shaft vibrations that manifest as bearing load [204] and torsional vibrations in the drive-train. Eccentricity effects particularly cause large stresses on bearings thereby reducing their lifetime. Torsional vibrations, on the other hand can trigger spurious pitch action and result in electrical power oscillations that can interact with the power system modes. The following sub-sections discuss these phenomena in detail.

7.2.1.1 Eccentricity induced unbalanced magnetic pull

The stator and rotor in a PMG are physically separated by a very small air-gap measuring a few millimetres. The non-uniformity of this air-gap (also termed as eccentricity) results in unbalanced magnetic pull (UMP) inside the machine. In a floating wind turbine, the probability of radial shaft misalignment is quite high which can be a major contributor to eccentricity. Chapter 5 introduced the basic theory and analytical model to compute the UMP caused by eccentricity due to shaft displacement.

If the generator structure is assumed to be perfectly rigid, then under normal conditions, the shaft is concentric with the stator, the length of the air-gap around the rotor is uniform and the forces in the air-gap are in equilibrium. Therefore the net radial load on the bearings only comes from the weight force of the shaft-rotor-turbine assembly. However, a radial shaft misalignment gives rise to an eccentric rotor causing dynamic changes in the air gap. This disturbs the equilibrium of the magnetic attraction forces that results in a periodical radial load on the bearings and depends on the rotor speed as well as the value of eccentricity. This also results in undesirable noise and vibration due to the increase in space harmonics as the air gap becomes non-uniform [145].

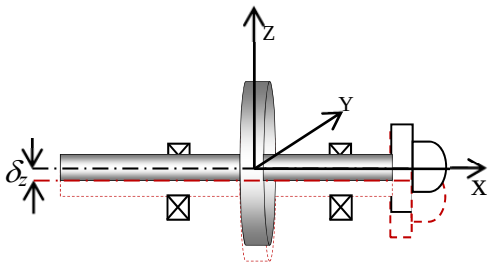

Fig. 7.1 Shaft Displacement

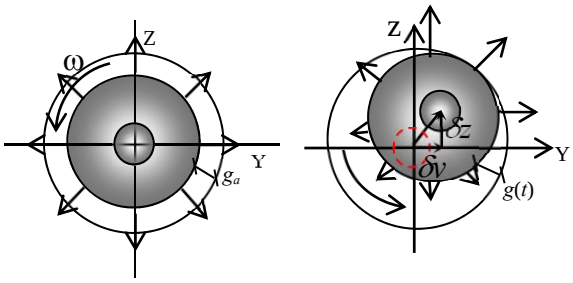

Fig. 7.2 (a) Concentric Shaft (b) Eccentric Shaft

Fig. 7.1 shows a shaft-hub assembly radially displaced from the normal concentric arrangement. Fig. 7.2(a) shows a uniform distribution of the magnetic forces (shown by equal vector lengths) for the case with concentric shaft. Figure 7.2(b) shows eccentricity caused by misaligned shaft (exaggerated), resulting in an imbalance in forces along the periphery. If shaft misalignment changes with time, then this results in dynamic eccentricity. As the shaft rotates, it also displaces from the centre as it rotates, the air gap distance is no longer spatially fixed but rotates with the rotor as well as the maximum and minimum force excitation, resulting in a dynamically asymmetric excitation of the generator. A greater pressure is observed along the region where the rotor has been displaced towards the stator whilst a less pronounced force is distributed in the opposite direction where the air gap length has increased. Intuitively, a dynamic unbalanced magnetic force results and manifests itself as a net dynamic radial load on the bearings.

The net load due to UMP caused by shaft eccentricity is determined using an approximate linear model that was introduced in Chapter 5 (equation 5.10 under section 5.11). The model relates the percentage change in air-gap (i.e. eccentricity) to unbalanced magnetic forces. With reference to Fig. 7.2(b), let $\delta y(t)$ and $\delta z(t)$ be the incremental shaft displacements, in the y-z plane, measured at any instant *t*. Then the dynamic change in air-gap, denoted as *g*(*t*) can be obtained from the incremental shaft displacement along the Y and Z axis as

$$g(t) = \sqrt{\delta y^2(t) + \delta z^2(t)} \tag{7.1}$$

The ratio of this value to the nominal air gap, g_a is defined as dynamic eccentricity, *e(t)* given by

$$e(t) = \frac{g(t)}{g_a} \tag{7.2}$$

The unbalanced magnetic forces due to eccentricity were computed using magneto static simulations in Finite Element Methods Magnetics software (FEMM)[137]. Static eccentricity simulations were carried out as they represented the worst possible conditions that can be experienced by the rotor. The rotor was displaced from 3% up to 90% of the nominal air gap length. The resultant force was obtained from the air gap flux density variation and was approximated as a linear function of the static rotor eccentricity ($e_{static} = g/g_a$) given by

$$F_{UMP\,STATIC} = 2291.8 \times e_{static} - 32.898\,kN \tag{7.3}$$

The above expression for force represents the eccentric condition in steady-state (refer to Figure 7.3). This model does not consider the effect of armature reaction on UMP as it is expected to be small [149]. A simple method of converting this force to represent dynamic eccentricity effects was used by accounting for the frequency of shaft displacements, ω_s. Together with dynamic eccentricity (equation (7.2), the two different components of the resultant dynamic force along the y and z-axis were then resolved as

$$F_y(t) = \{2291.8 \times e(t) - 32.898\} \cos \omega_s t \;\; kN \tag{7.4}$$

$$F_z(t) = \{2291.8 \times e(t) - 32.898\} \sin \omega_s t \;\; kN \tag{7.5}$$

The net dynamic UMP force is described using the following equation

$$F_{UMP\;\;NET} = \sqrt{F_y^2(t) + F_z^2(t)} \;\; kN \tag{7.6}$$

The frequency of shaft displacements, ω_s can be determined from the knowledge of static deflection and the natural frequency of transverse vibrations. This is explained in detail in the following section. It must be remembered that the linear model assumption ignores the normal deflection of the generator structure and induced secondary deflection that can further accentuate the loads due to eccentricity. It is also emphasised that in practice, the shaft can undergo translational as well as rotational displacements; resulting in a more complex UMP distribution. However for simplicity, only a radial misalignment of the shaft was assumed to contribute to UMP forces. The contributions from shaft tilting were assumed to be negligible. The equations (7.4) and (7.5) suggest that even at a non-eccentric condition there exists a residual force of

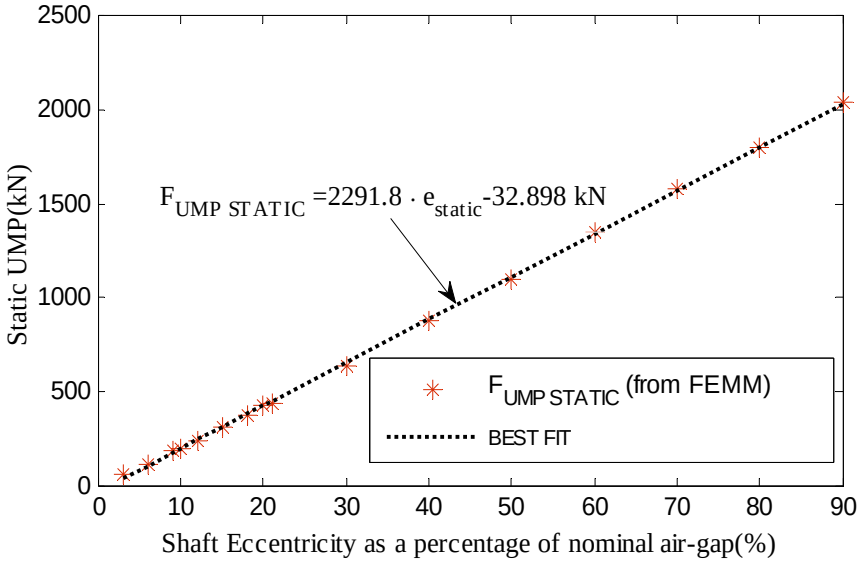

Fig.7.3 Eccentricity versus Forces due to UMP

32.89 kN. This residual force appeared because of modelling inaccuracies for the slots and pole pairs in the FEMM model. For a given shaft displacement the force

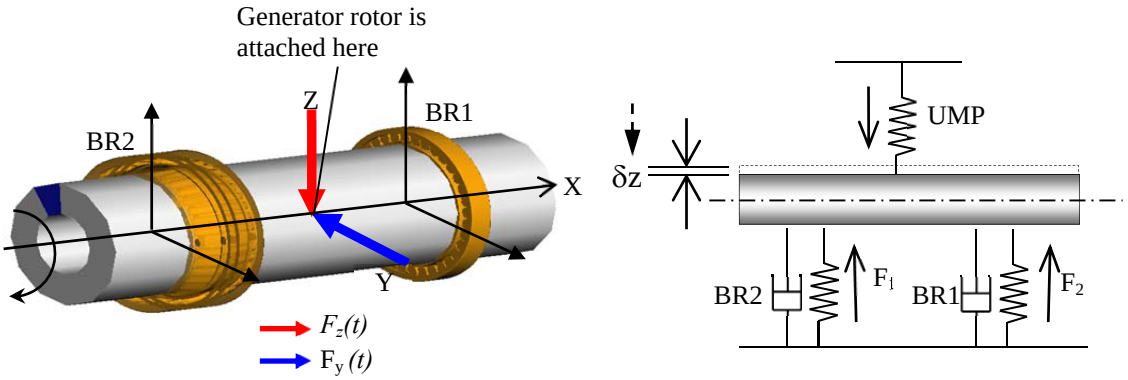

(a) Line of action of bearing loads & UMP **(b) Magneto-Elastic system**

Fig. 7.4 Shaft–Bearing assembly

components due to UMP are assumed to act at the centre of the shaft where the rotor is attached (blue and red arrow lines in Fig. 7.4(a)) and tend to displace the shaft further in the direction of original displacement. The forces due to UMP act like a spring with negative stiffness (k_{mag}), in a direction opposite to the restoring forces from the bearings (refer to Figure 7.4(b)). As with the linear model for UMP, the stiffness of the magnetic system is also assumed to exhibit linear characteristics.

7.2.1.2 Shaft displacement, vibratory torque and possible feedback effects

As the shaft of the wind turbine rotates, it is expected to undergo transverse displacements due to external loads. If the shaft displacements are large and frequent then this can instigate torsional vibration problems that can result in torque loss, if the generator torque controller response is not fast enough. If the shaft is out of balance or displaced from the centre, then the resulting centrifugal force will cause the shaft to vibrate. If the shaft rotates at a speed equal to the natural frequency of transverse vibration, then the shaft begins to whirl, causing it to resonate. This can be very damaging to the wind turbine generator; especially the bearings and can also trigger pitch action if measurable reductions in mechanical torque occur. Therefore efforts to understand this phenomenon must be taken to ensure the shaft is balanced and avoid the critical frequency while starting, stopping and during operation to avoid damage to the bearings and the turbine blades by avoiding spurious pitch action.

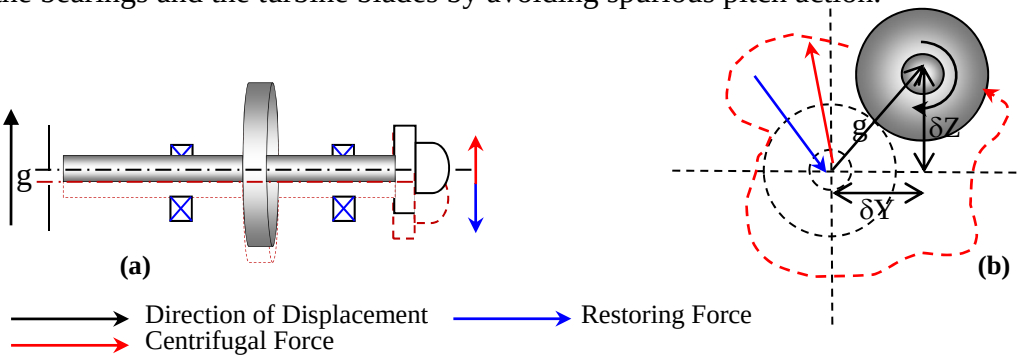

Fig. 7.5 Shaft Response (a) Radial displacement (b) Orbital motion

In the case of a rigid shaft, as the shaft is displaced away from the location of the centreline; the bearing stiffness constantly tries to restore the shaft back to the centre-line. Therefore the shaft orbits around the centreline as it rotates (the path shown by red dotted line in Figure 7.5(b) illustrates this effect. This can be imagined as a rotating mass that continually experiences a centrifugal force as it moves away from the centre of rotation(red arrow shows the direction of centrifugal force), and restored by inward pull from bearings(shown by blue arrow).

If the displacement of the shaft is measured at every instant, *t*, then let the distance by which the shaft is displaced from the centre be *g* (*t*) (equation 7.1). The centrifugal

force on the rotor shaft assembly is given by [205],

$$F_{centrifugal} = m\omega_s{}^2\left(g(t)+s\right) \tag{7.7}$$

where, ω_s is the frequency of the shaft displacement, s is the static deflection in steady state. If m is the mass of the rotor shaft assembly , then the restoring forces from the bearing with stiffness , k (ignoring damping term) must balance the centrifugal forces such that

$$m\omega_s{}^2\left(g(t)+s\right) = k \cdot g(t) \tag{7.8}$$

$$\omega_s = \sqrt{\frac{k \cdot g(t)}{m(g(t)+s)}} \tag{7.9}$$

$$\omega_s = \omega_{nat}\sqrt{\frac{g(t)}{(g(t)+s)}} \tag{7.10}$$

where, ω_{nat} is the natural frequency of transverse vibrations $\left(\omega_{nat} = \sqrt{\frac{k}{m}}\right)$. If the bearing stiffness is not high enough and the frequency of shaft displacement is too high, it can reduce the available torque from the generator considerably. The equation for available generator torque can be derived from first principles. Consider a mass with the rotational moment of inertia, I, rotating at an angular velocity, ω when a torque T is applied. As the shaft also undergoes displacement from the centre, some of the kinetic energy is lost in vibration. In order that rotational kinetic energy is conserved

$$Total\ \ Rotational\ \ Kinetic\ Energy = \frac{1}{2}I_1(\omega_1(t))^2 + \frac{1}{2}I_2(t)(\omega_2(t))^2 \tag{7.11}$$

where, I_1 the moment of inertia of the rotating mass, ω_1 is the angular velocity of the shaft, ω_2 is the frequency of shaft displacements, $I_2(t)$ is the moment of inertia of combined mass (shaft + rotor + turbine) displaced by a distance $g(t)$, from the centre given by

$$I_2(t) = m \times g^2(t) \tag{7.12}$$

To compute the instantaneous torque, equation 7.11 is first divided by time, t to get the total power as

$$Total\ \ Power\ = \frac{1}{2t} I_1 \omega_1^2(t) + \frac{1}{2t} I_2(t) \omega_2^2(t) \tag{7.13}$$

Dividing equation (7.13) by the intended frequency of rotation, ω, gives the expression for applied instantaneous torque, $T(t)$ as

$$T(t) = \frac{1}{2\omega t} I_1 \omega_1^2(t) + \frac{1}{2\omega t} I_2(t) \omega_2^2(t) \tag{7.14}$$

$$T(t) = T_1(t) + T_2(t) \tag{7.15}$$

where, $T_1(t)$ is $\frac{1}{2\omega t} I_1 \omega_1^2(t)$ and $T_2(t)$ is $\frac{1}{2\omega t} I_2 \omega_2^2(t)$. T_1 is the available generator reaction after the losses due to vibration induced torque T_2.

7.2 Modelling generator response

To estimate the effect of shaft displacements on UMP, the available mechanical torque and possible trigger of pitch action for the direct-drive system, a land-based model of a direct-drive wind turbine system (WTDD) was created in SIMPACK. SIMPACK allows for an integrated multidisciplinary simulation of wind turbine in time-domain. The various components can be modelled by rigid or flexible bodies interconnected by joints, constraints and force elements including nonlinear mechanics with active control and aerodynamics. In order to predict the kinematic behaviour, SIMPACK solves the dynamic Newton-Euler equations of motion for the mechanical system by variable-step time integration. A library of elements to model the excitations (torque/force), joints and control elements is available. Where these functionalities were not adequate, user-defined elements can be defined. Fig. 7.6 (a) shows the topology of the direct-drive generator modelled in SIMPACK. The tower assembly was modelled as an elastic body connected to the foundation by 0DOF joint. The foundation is connected to the ground by a three-dimensional bushing to simulate a visco-elastic ground. The nacelle was mounted on the tower by a yaw bearing with a revolute joint to describe the azimuth control. The nacelle contains the main components of the drive-element, i.e. the main shaft, generator rotor and the stator. The main shaft

supporting the generator rotor and the hub is modelled as a rigid body with a 6DOF joint to account for the axial, bending and torsional loads. Fig.7.6 (b) shows the graphically rendered version of the WTDD system.

A force element between rotor hub and main shaft was used to describe the torsional stiffness and damping of the rotor shaft. The generator stator and housing were modelled as rigid bodies with zero degrees of freedom with reference to the rest of the drive-train. The bearing elements were modelled using visco-eleastic element FE-41 which allows the definition of full stiffness matrices provided by bearing manufacturer. The stiffness matrices were linearised using symmetrical coupling terms and induced (radial load) axial force and moments to allow for extrapolation to a different load condition(refer to APPENDIX-B). About 10% damping was assumed from the bearing element. The bearing stiffness values were tuned further to be at a certain level by an initial sensitivity study (Chapter 5, section 5.11) so that eccentricity and induced UMP forces are not large enough to aggravate shaft displacements. Sensors were used to measure the instantaneous shaft displacements (in the Y and Z directions) and the shaft speed.

The controller interface DISCON is a Bladed-style dynamic Link library (DLL), similar to the one developed by Jonkman [21]. The controller was programmed using fortran subroutines, compiled and linked to SIMPACK as a user-defined force-control element. The controller for the direct-drive generator differs in the implementation of torque control by accounting for pulsatory behaviour of the shaft (defined in section 7.2.1.2). At every time step, the kinematic measurements of shaft displacements and generator speed are read as input variables from the sensors. Using equation 7.15, the vibratory torque is computed from the measured shaft displacements and deducted from the actual generator torque demanded for the five control regions of torque-speed curve (as defined in section 6.6 of Chapter 6). If $T_{Gen\text{-}i}$ is the demanded generator torque for region i (where i = 1,1½,2,2½,3) and T_{vib} represents the pulsatory torque measured at any instant , t, the set-point for generator torque after accounting for the losses due to vibration is described by

$$T_{available}(t) = T_{Gen-i}(t) - T_{vib}(t) \tag{7.16}$$

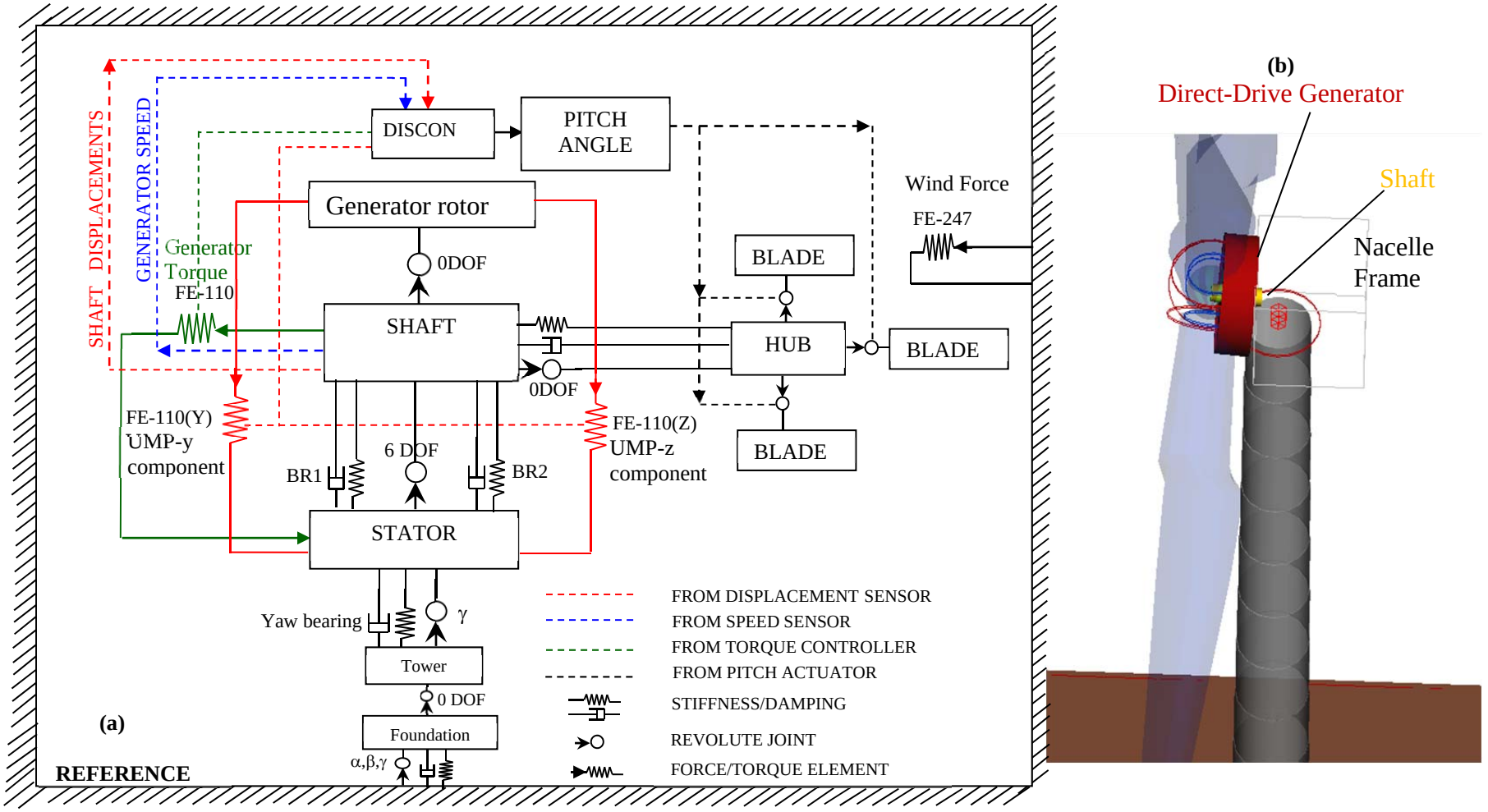

Fig. 7.6 A multi-body model of the direct-drive generator wind turbine (WTDD) in SIMPACK

The instantaneous values of shaft displacements are also used to compute the eccentricity and forces due to UMP as defined by equations (7.4) and (7.5). The generator torque and UMP forces are implemented using a proportional actuator element FE-110. This actuator element operates on the control element variable U_{set} (either force/torque from DISCON) with certain drive constants P and K such that the force (F) and torque(L) are obtained as

$$L = K \cdot (U_{set} + U_{pre\_set}) \tag{7.17}$$

$$F = P \cdot L \tag{7.18}$$

where, K is the torque multiplier constant (N-m) and P is the force multiplier constant (1/m). The values for P and K were chosen as unity and pre-set U_{pre_set} was zero. Thus output of the DISCON element provided three variables namely

(i) set-point of the generator torque (after accounting for torque pulsations) for the torque controller

(ii) blade pitch velocities (collective blade-pitch controller input) and

(iii) Force components due to unbalanced magnetic pull (Fy and Fz) acting between the rotor and stator.

The rotor blades were modelled as flexible bodies connected to the hub by a user-defined kinematic joint actuated by pitch control signal. Aerodynamic loads on the blades are generated by using the AeroDyn interface in combination with Turbsim [206] and applied using force element FE-227. This study was concerned with normal operation of wind turbine. For the purpose of simplicity braking action was not modelled. It was assumed that the blades will park while the torque controller demands no torque at wind speeds above 25m/s. A set of wind fields from 4-25m/s in accordance with the normal turbulence model as per IEC61400 [181] were created. Twenty-two one hour simulations were carried out and two parameters namely, vibratory torque and pitch angle were monitored. Fig.7.7 shows the time history of the vibration induced torque measured by SIMPACK for wind speeds of 4m/s and

12m/s. It was observed that the vibratory torque generally increased with increase in wind speeds.

Fig. 7.8 shows the vibratory torque expressed as a percentage of operating torque. The mean, standard deviation and maximum values remained below 0.4% of the operating torque, which was not significant enough to trigger pitch action.

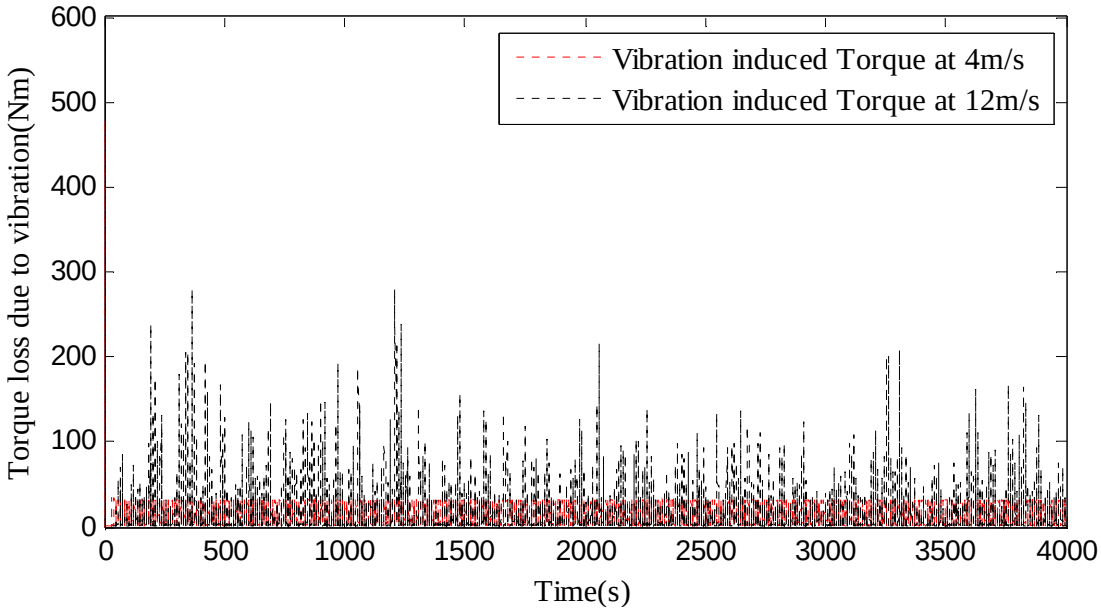

Fig. 7.7 Time history of Vibration induced torque measured by SIMPACK

This was verified by examining the blade pitch behaviour to detect any spurious control action due to pulsation. To validate the torque behaviour, comparison was made to the land-based HAWC2 model of the WTDD system (Section 6.7 of Chapter 6) which was treated as a hypothetical system with ideal torque and pitch control behaviour. The drive-train model in HAWC2 was implemented using a 1-DOF spring-damper system, for the specifications defined in Chapter 6. The drive-train was infinitely stiff in all modes except torsion. A quasi-static response was assumed from the generator, so that the feedback from the drive-train (speed) contained no spurious response. The generator torque-speed characteristics were modelled as a force element DLL. The HAWC2 model was tested in 22 similar wind conditions (4-25m/s) with a step increment of 1m/s and the torque and blade pitch angle time histories for one-hour simulations were extracted. A comparison of the results with

SIMPACK simulations was performed to detect any spurious pitch action from the direct-drive generator. Fig. 7.9 shows the percentage difference in mean values of

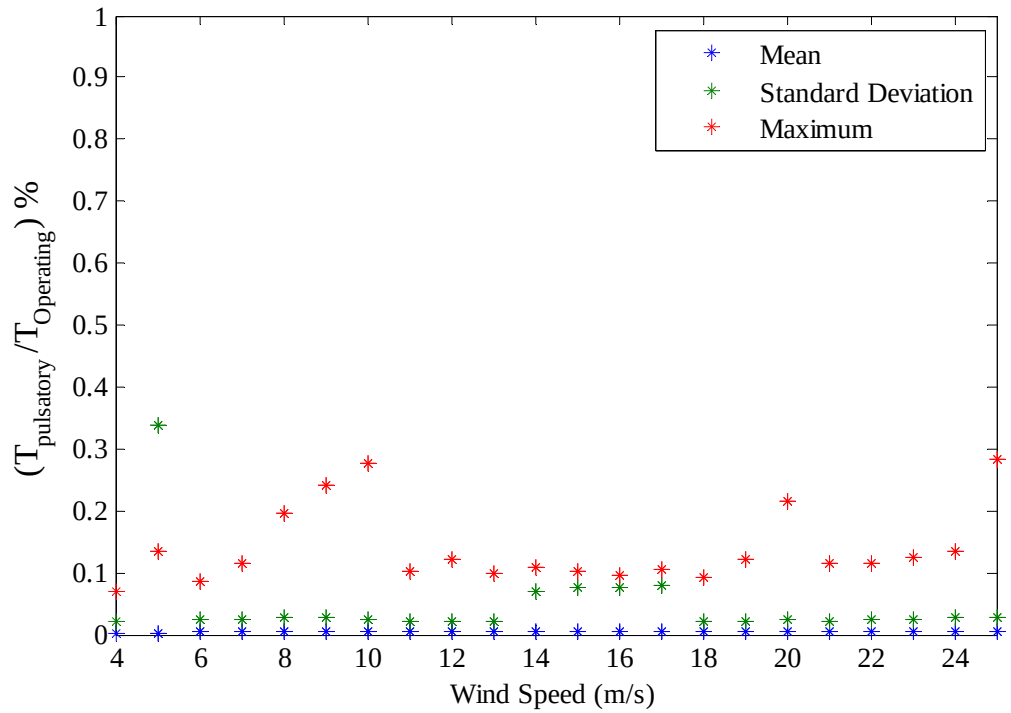

Fig. 7.8 Vibratory torque as a percentage of operating torque

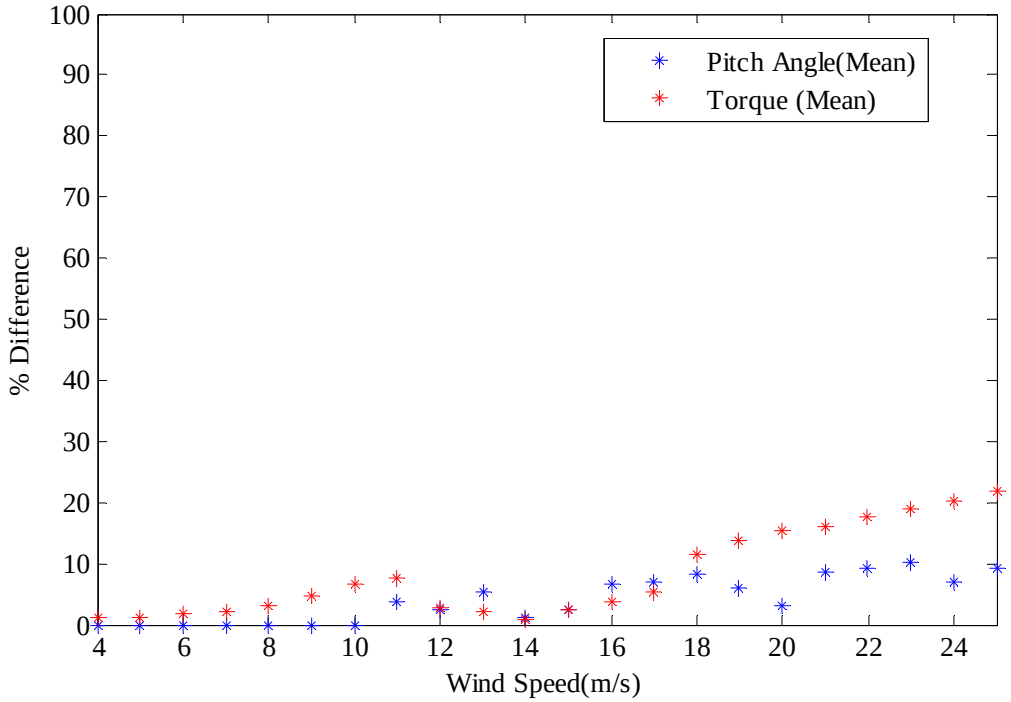

Fig. 7.9 Mean pitch response and torque at different wind speeds

torque and blade pitch angles computed from HAWC2 and SIMPACK simulations. As may be noted, no pitch action was predicted by both the models until about 10m/s of wind speed. At higher wind speeds about 10% difference existed between the two models. A maximum of 20% difference existed in the mean torque values.

To investigate the torque behaviour more closely, spectral analysis of torque was done to capture any unexpected excitations. The spectra at constant wind field (at 12m/s) for both models showed high frequency excitation at 19 rad/s, while the HAWC2 spectrum had an additional response peak at approximately 3P frequency at 3.8rad/s (Fig. 7.10). This was probably because of the tower shadow effects that were enabled in the HAWC2 model. The mean values of torque obtained from both the models were quite similar although SIMPACK model accounted for some whirling (4.82×10^6Nm from the HAWC2 model and 4.76×10^6 Nm from SIMPACK model). For turbulent wind field case, the comparison of frequency spectra (Fig. 7.11) shows large differences particularly at low frequencies(this was possibly due to differences in the turbulence models for the wind fields used by SIMPACK and HAWC2 HAWC2 uses the Mann model[190]).

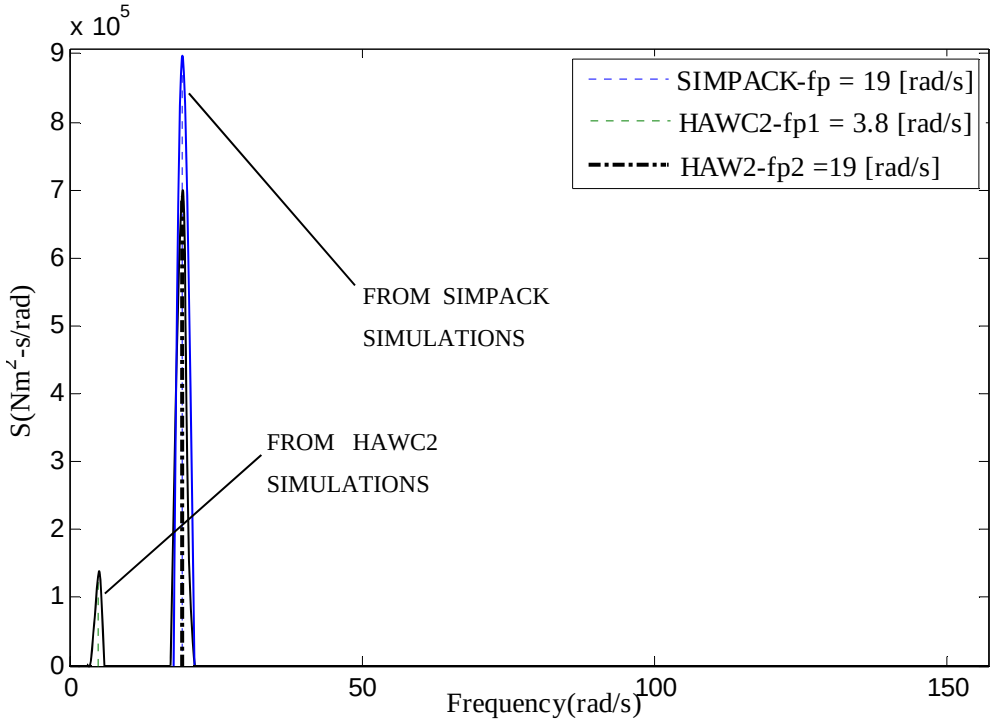

Fig. 7.10 Torque spectral density as obtained from SIMPACK and HAWC2 simulations under constant wind

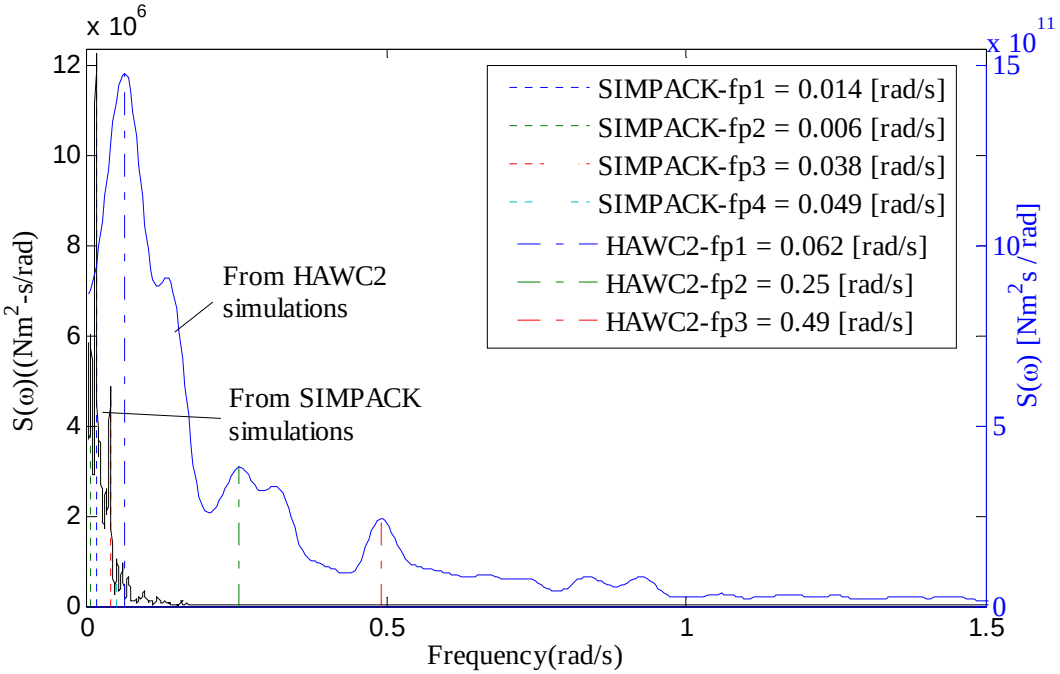

Fig. 7.11 Torque spectral density as obtained from SIMPACK and HAWC2 simulations under turbulent wind

In brief these results suggest that the pitch action for the 1-DOF WTDD system in HAWC2 was very close to the advanced SIMPACK model that includes the vibratory torque behaviour. This also helped to confirm that the presence of UMP or eccentricity was not significant enough to incite large shaft displacements or unnecessary pitch action in a direct-drive generator.

If the shaft is flexible, then any bending might introduce additional forces and vibrations due to whirling [205]. To investigate this effect, the shaft was modified as a flexible body in SIMPACK to estimate the amount of deflection that the shaft undergoes while in operation for the same range of wind speeds from 4-25m/s. The radial displacement of the shaft was measured at four nodes along the length of the shaft. Node 1 represents the hub connection and node 3 the generator rotor connection. Nodes 2 and 4 correspond to bearing supports. Fig. 7.12 shows the plots for the shaft nodal deflection versus the location of the deflection points for all the wind conditions. The results from SIMPACK simulations show that the wind induced deflection was very small with the arrangement of the main shaft mounted with two bearings spaced 2m apart. For the same loads, radial displacement of the shaft at the hub node 1 and the rotor node 3 is lower than 0.2mm.

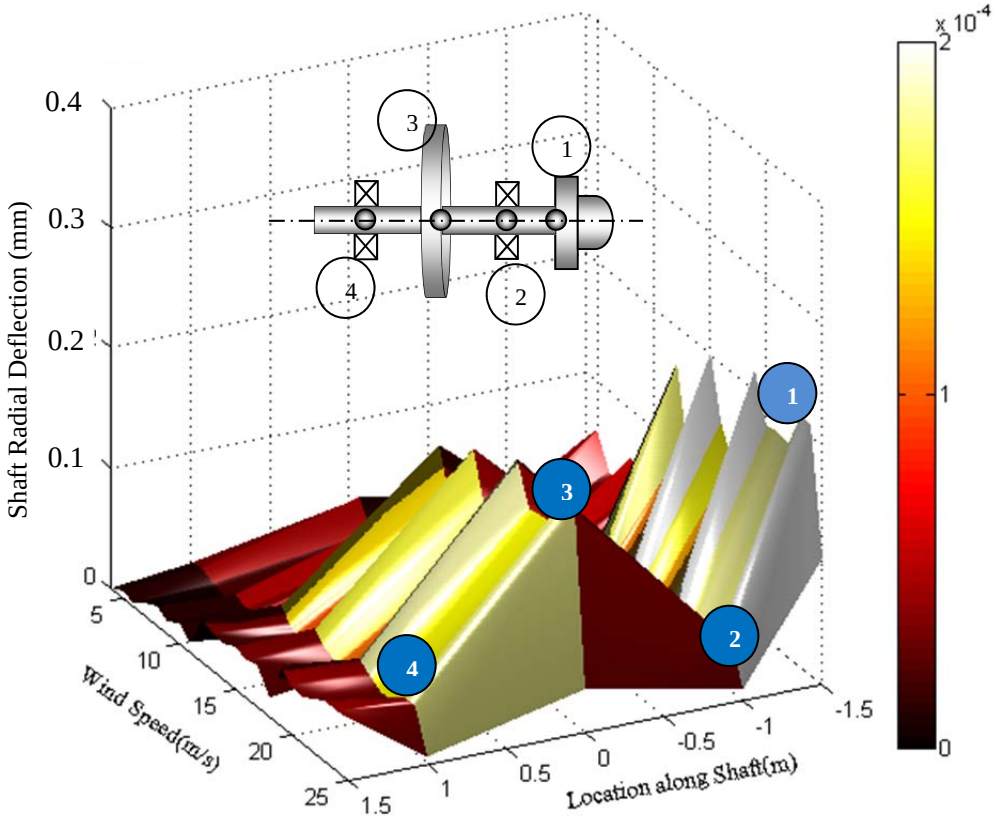

Fig. 7.12 Shaft node deflection profiles at different wind speeds

This also highlights the advantage of the TDI(double row tapered roller bearing) and CRB(cylindrical roller bearing) combinations as recommended by [168] that adds greater rigidity to the system. This exercise was useful to verify that the strength of the shaft (the thickness) was adequate to transmit the specified torque without failure. As the shaft deflections due to bending are within acceptable limits, this helps reduce vibration and ensure reliable operation of the bearings. Thus, these initial results show that the reactions within the drive-train are small enough so that it is reasonable to ignore the feedback effects or spurious pitch trigger action in a direct-drive generator.

7.3 Analysis of FWTDD drive-train system using the 2-step de-coupled approach

As mentioned in section 7.2, the two-step decoupled approach is adopted. This approach is explained in great detail by Xing *et al*.,[51, 52]. Hence only a brief description is provided here. As a first step, fully coupled aero-hydro-servo-elastic simulations for the FWTDD system were carried out in HAWC2. The time histories for global motion response and main shaft loads from HAWC2 simulations were input to a detailed drive-train model in SIMPACK. The internal responses and loading of the drive-train are analysed in SIMPACK.

7.3.1 FWTDD HAWC2 model

The floating version of the direct-drive wind turbine was built in HAWC2 for the specifications described in Chapter 6 (section 6.7). The drive-train model uses the same 1DOF torsional spring-damper system as the land-based turbine (section 7.3). The generator model, mooring line models were implemented as a dynamic link library (DLL). Six degrees of freedom motion sensors provide the instantaneous nacelle position, velocity and accelerations while sensors for the drive-train provide the main shaft moments and forces. These will feed into a stand-alone SIMPACK model.

7.3.2 Design load Case

This study was aimed at preliminary investigations on a fully integrated direct-drive wind turbine model for the purpose of making initial empirical inferences. A complete study must encompass all the design load cases (as defined in IEC-61400-3 [207]) including normal power production, extreme loads, transient events and faults. However, to begin with, the consistency and performance of the drive-train must be verified for normal power production. Therefore, the response analysis and remainder of the discussion is limited to the normal operating condition. For a given average wind speed at hub height, the expected values of significant wave height and peak wave periods were obtained by correlation [179, 180]. Section 6.7 of Chapter 6 provides detailed information on the modelling environment. The typical operating region of the wind turbine covered the wind speeds from 4-25m/s with corresponding

wave heights between 1.96-5.88m. The load cases for these conditions are presented in Table 6.11 of Chapter 6 and are hence not repeated here.

7.3.3 Stand-Alone SIMPACK Model for the FWTDD system

The output from the shaft and nacelle position sensors from HAWC2 simulations feed into a stand-alone model in SIMPACK (Fig. 7.13). The SIMPACK model essentially uses the same drive-train model as described in section 7.2 segregated from the controller, hub and the tower sections (refer to Fig. 7.14). The nacelle is attached to a dummy body steered by a 6DOF joint that accepts the position, velocity and acceleration inputs from HAWC2. The shaft moments, forces and torque input from HAWC2 are applied as time excitation vectors using force element FE-93. The forces due to unbalanced magnetic pull is modelled by using Force element FE-50, that allows implementing the equations (7.4) and (7.5) as mathematical expressions. The two components of the forces(Y and Z) are computed at each instant by kinematic measurements of the shaft displacements in the respective directions and applied between the rotor and stator. These forces act perpendicular to the axis of rotation(X). The generator reaction torque is implemented using force element FE-110 (described using equation 7.17). A proportional integral velocity controller computes the generator torque using the shaft speed from the HAWC2 simulations as the reference input

$$T = K_p(\omega - \omega_{ref}) + K_I \int_0^t (\omega - \omega_{ref})dt \tag{7.19}$$

where, $(\omega - \omega_{ref})$ and $\int_0^t (\omega - \omega_{ref})dt$ are the speed error and the integral speed error respectively. K_P and K_I are the proportional and integral gains for the controller. The proportional gain of the controller was chosen to be the slope of region 2 torque-speed characteristics (i.e. $1x10^7$). The integral gain was chosen to minimise the steady-state speed error to less than 0.5 rad/s.

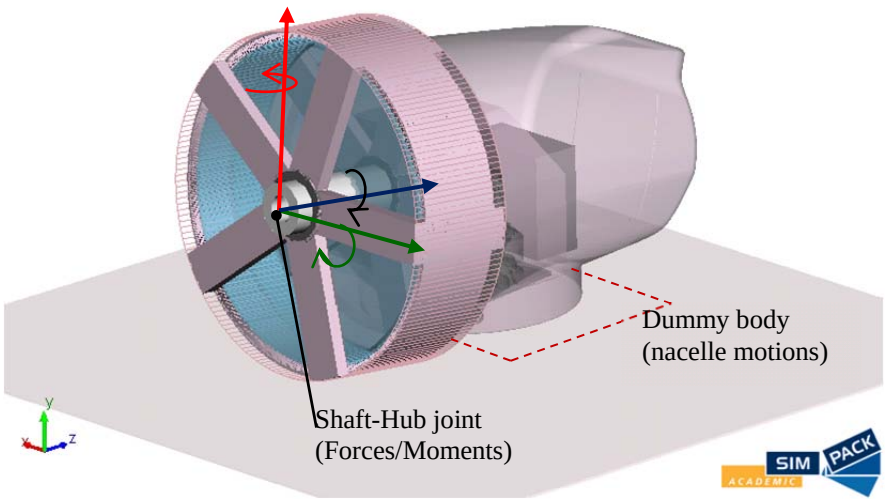

Fig. 7.13 Shaft loads, moments and nacelle motions applied to the stand-alone SIMPACK model

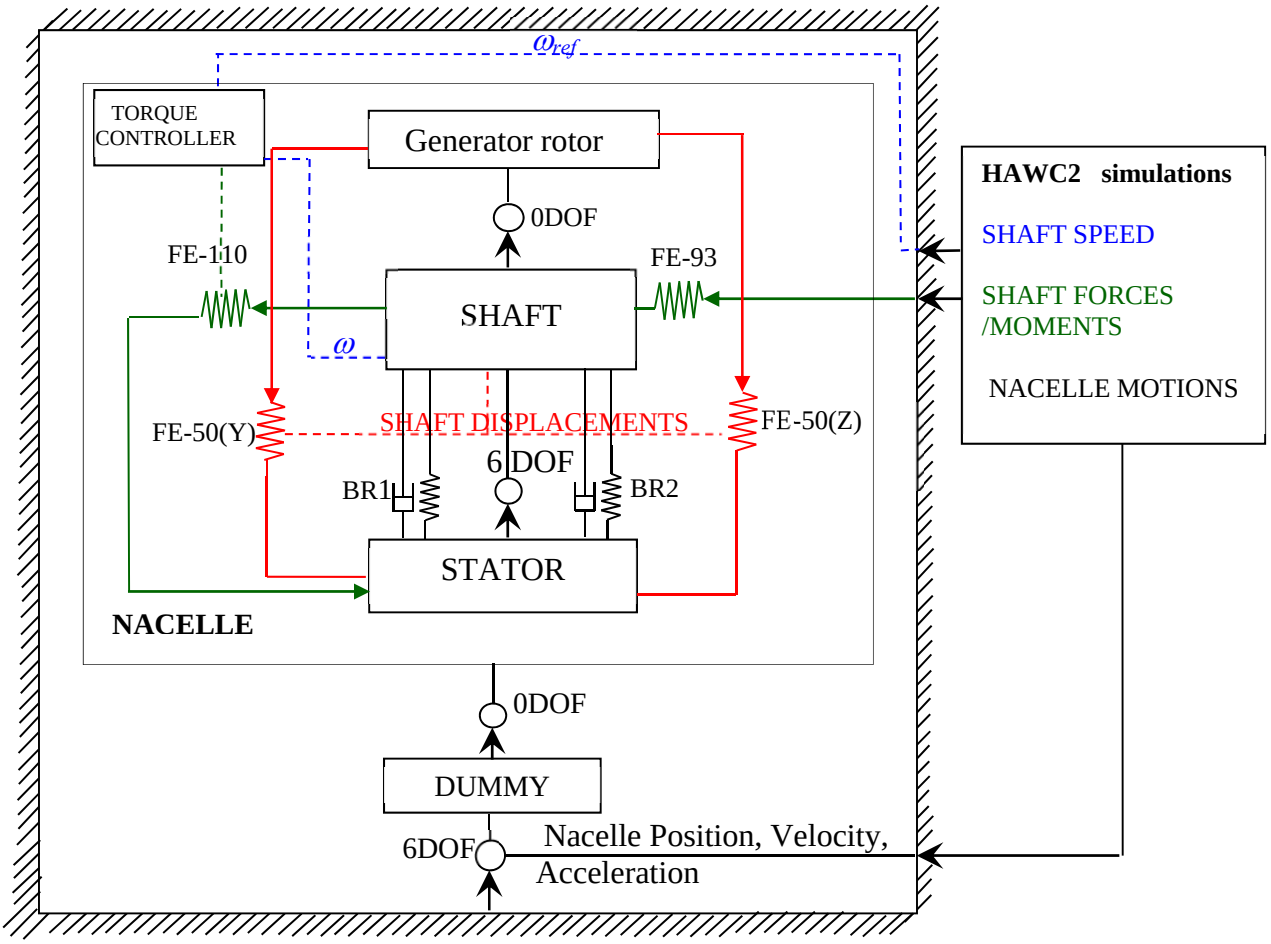

Fig. 7.14 SIMPACK topology diagram for FWTDD analysis

(for definition of symbols, refer to Fig 7.6)

7.4 Analysis and comparison of global drive-train responses

22 one-hour simulations were carried out with the HAWC2 models for the floating and land-based versions of the direct-drive system for the unidirectional wind and wave load cases presented in section 6.7.1 of Chapter 6. The time histories of responses for the main shaft loads were extracted to enable further analysis and comparison.

For a given wind and wave condition, it is reasonable to assume the short-term load response as a stationary random process. The analysis of such processes require statistical treatment of the time histories for the response variables obtained through numerical simulations. The mean, standard deviation and maximum values of measured variables provide some useful information on the loading of drive-train components for determining the adequacy of the design, component strength and predicting their lifetime. A comparison of the main shaft loads (section 7.4.1) predicted by HAWC2 simulations for the WTDD system and FWTDD systems showed only a marginal increase for the FWTDD system which is a favourable attribute.

7.4.1 Comparison of main shaft loads

Figures 7.15(a-c) presents the comparison of the main shaft load statistics for the normal operating range of the wind turbine (i.e. 4-25m/s). The load components compared include the axial force, resultant shear force (the sum contribution of forces in the in-plane direction) and bending moments (the sum contribution of moments in the in-plane direction). These values are expressed as a percentage difference of FWTDD response with the land based counterpart as;

$$\%\ difference = \frac{X_{FWTDD} - X_{WTDD}}{X_{WTDD}} \times 100\,\% \tag{7.20}$$

where, X_{WTDD} is the response variable measured from the land based model and X_{FWTDD} is the corresponding value for the offshore floating model. Figures 7.15(a-c) show that there is only a marginal variation of the mean, standard deviation and maximum values of bending moments and torques for the FWTDD system. The values for bending moments for FWTDD system are lower for wind speeds below rated, yet the difference is negligible with up to 3.5%, 2.5% and 1.79% respectively

for mean, standard deviation and maximum values. Similar trend is noted for torque values below rated wind speeds with the less than 3% difference in standard deviation values. The difference in mean values for the axial forces tends to increase up to 12m/s wind speed and settles close to about 10% for wind speeds above rated(i.e. 12m/s). The mean values for shear forces are lower in the case of FWTDD, with less than 1% difference in the maximum values. Yet, the data points for shear forces for the FWTDD were found to be widely dispersed at wind speeds below rated leading to more than 100% difference in standard deviation. This is also because the absolute values of the standard deviations for shear forces were small. These values range from 2.46-57.8 kN for WTDD and 5.3-61.3 kN for FWTDD system. The same can be inferred for the standard deviations in axial forces that vary from 20-115 kN for the WTDD system and 20-99 kN for the FWTDD system. The maximum values of the main shaft loads for the FWTDD are within 12% as compared to the WTDD system with the exception of axial loads. Maximum axial loads tend to increase at an average of 24% for the FWTDD system.

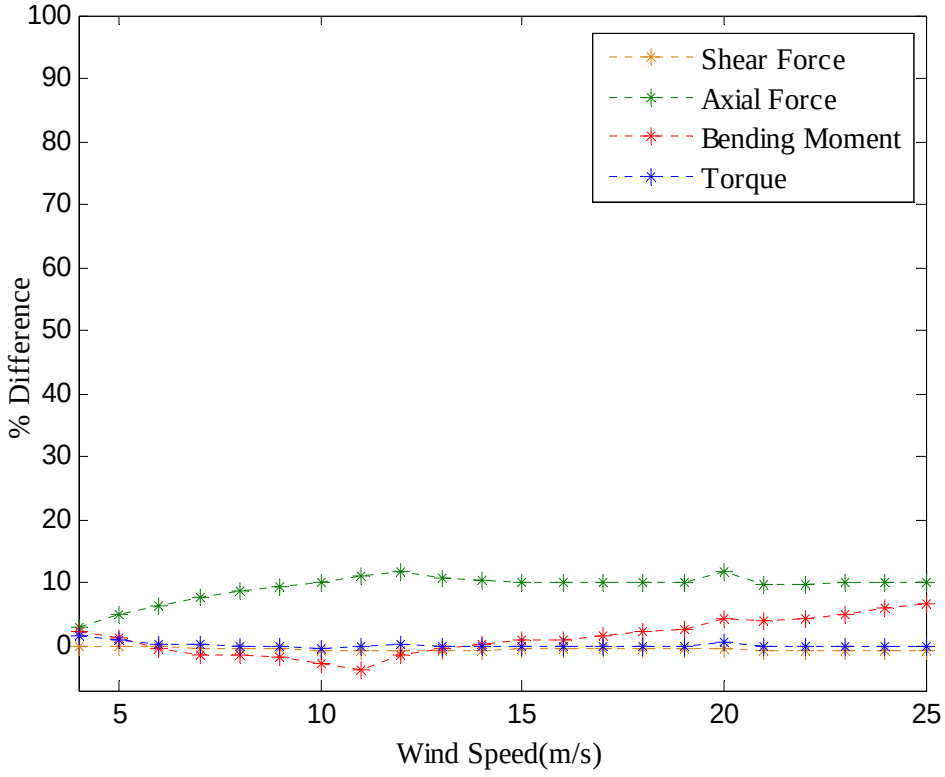

Fig. 7.15 (a)

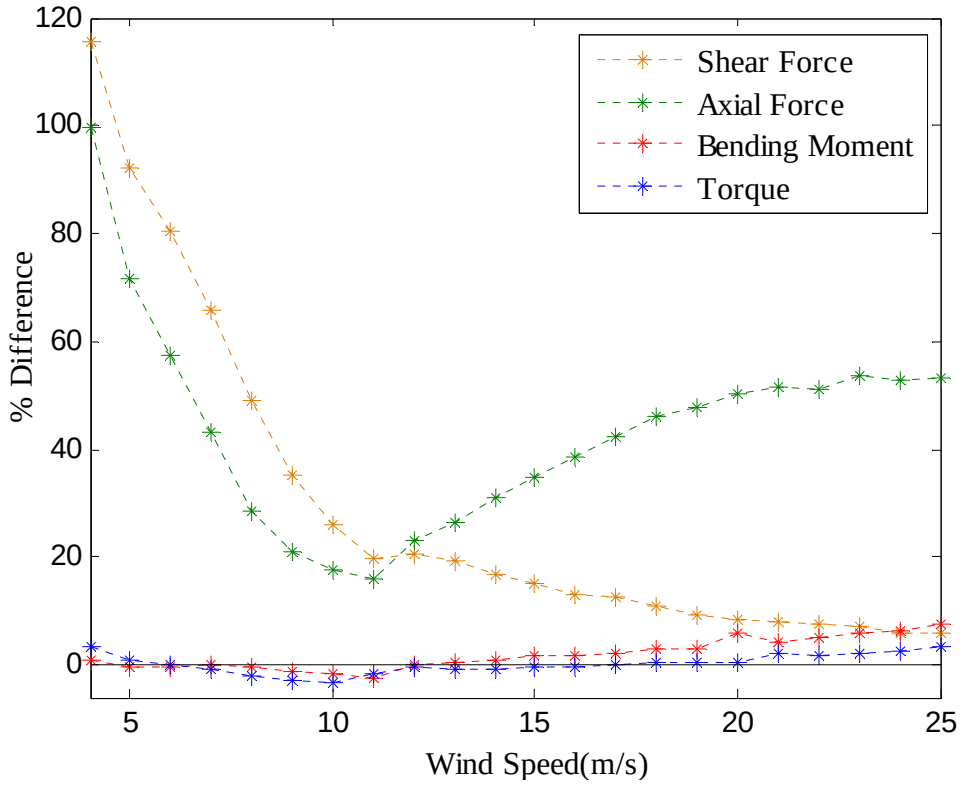

Fig. 7.15 (b)

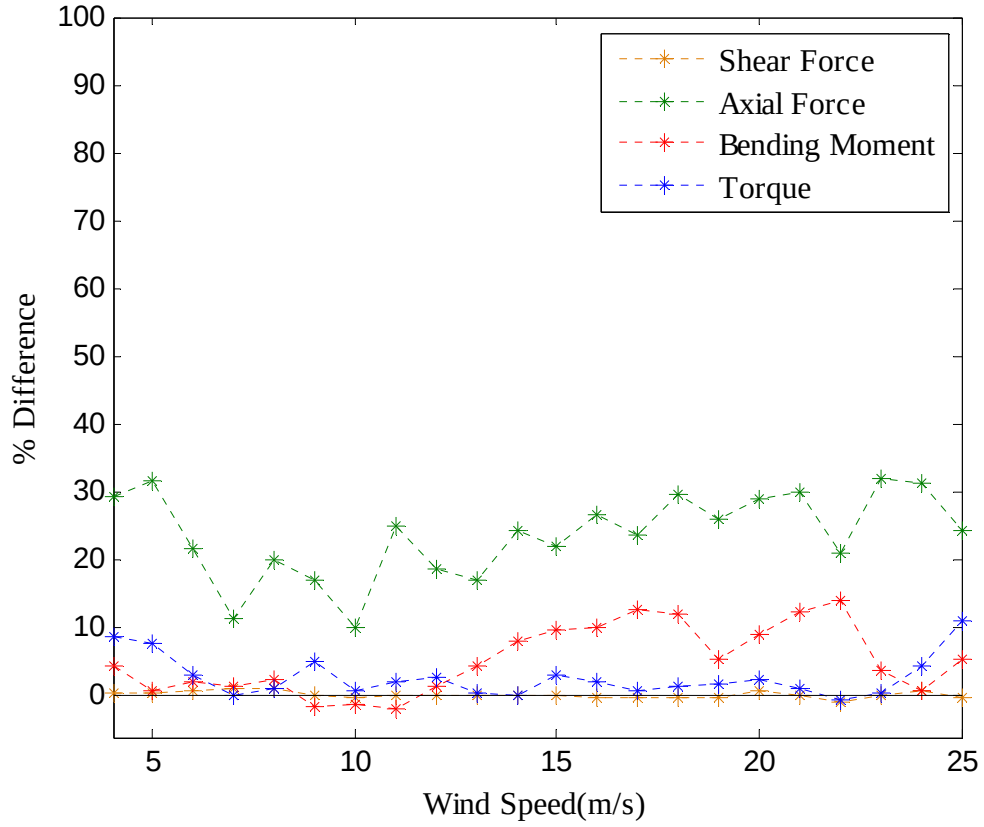

Fig.7.15 (c)

Fig. 7.15 % Difference in Main Shaft loads –WTDD Vs FWTDD (a) Mean Values (b) Standard deviation (c) Maximum Values

The power spectral densities for the main shaft loads at 21m/s wind speed (Figures 7.16-7.19) show the additional sources of excitation for the FWTDD system. Apart from a couple of very low frequency excitations, the load spectra for the main shaft shear force for the FWTDD system show additional response peaks associated with the wave excitation frequency, platform's pitch natural periods and slightly higher excitation due to Rotor 2P frequency. This could explain the reason for the larger standard deviations in shear forces.

Likewise, the main shaft axial load spectra show excitations at wave frequency and the platform's pitch natural frequency. The frequency spectra for the bending moments are very similar for the FWTDD and WTDD system, which accounts for the relatively smaller variation in mean, standard deviation and maximum values. The main shaft torque load spectrum for the FWTDD system resembles that of WTDD system for most part with the exception of wave induced excitation. Thus, these load spectra suggest that the impact of wave excitation and platform's natural frequency can be felt by the load bearing components in the drive-train for the FWTDD system.

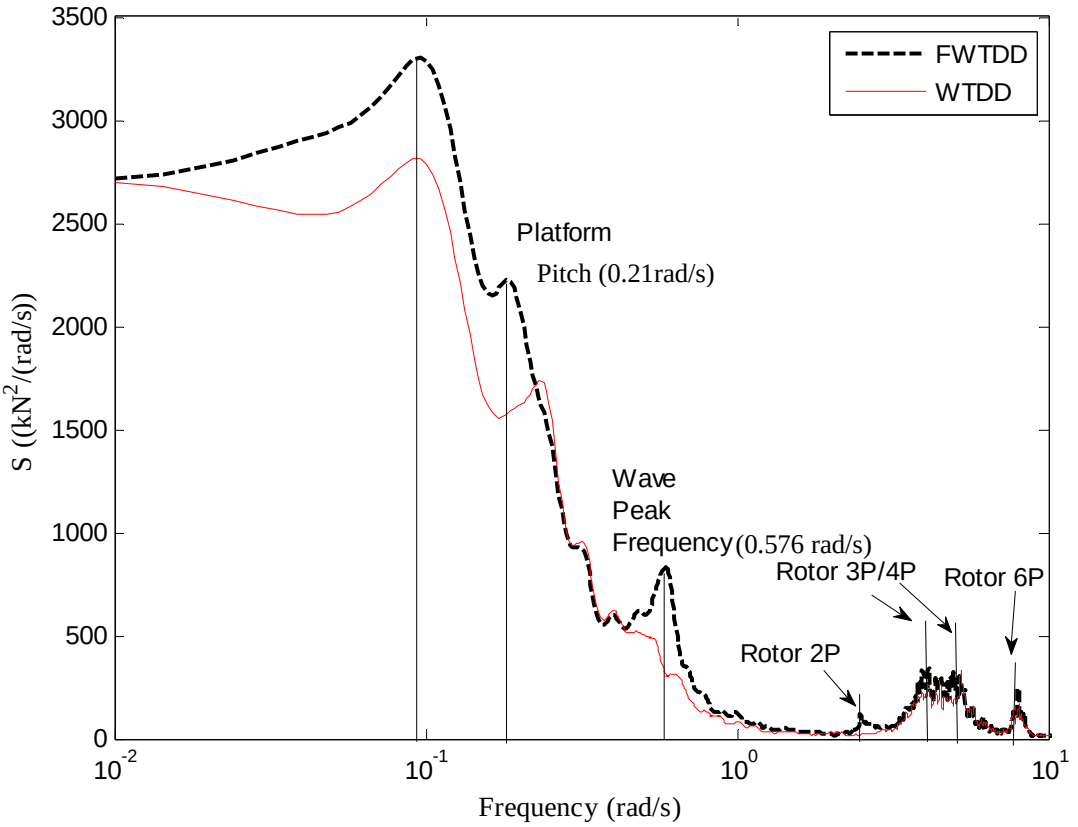

Fig. 7.16 Frequency spectra of main shaft Shear Forces

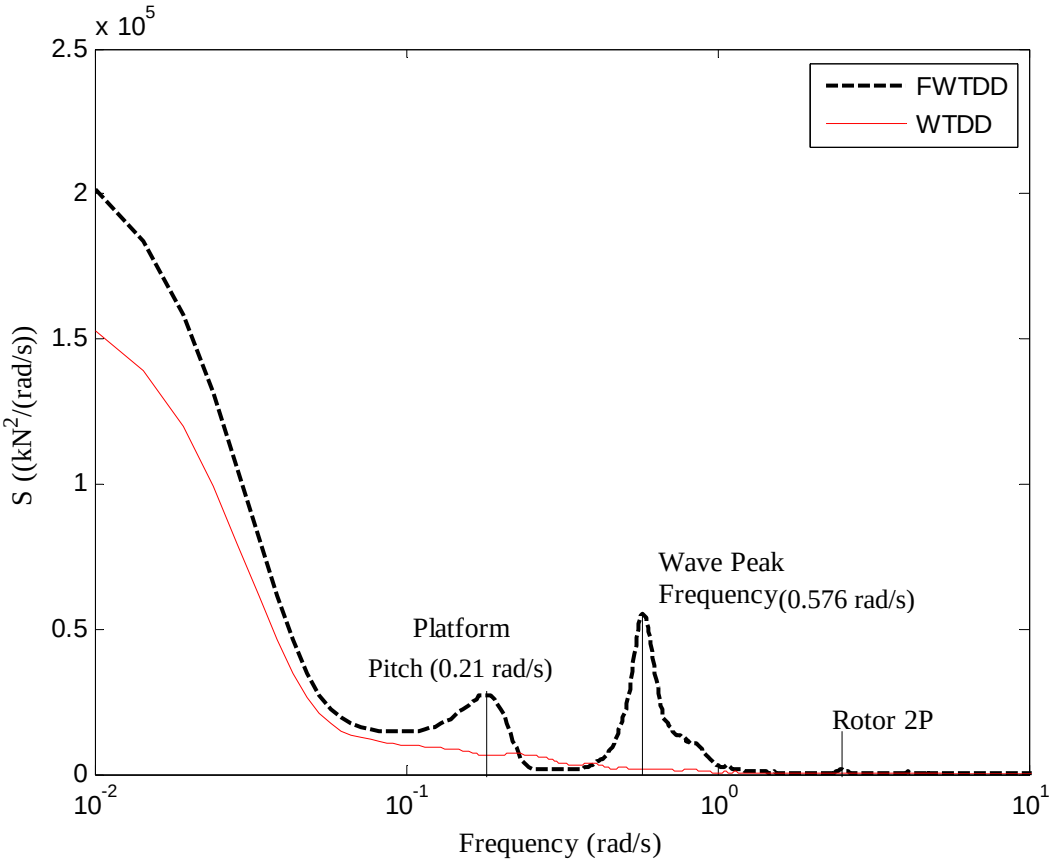

Fig. 7.17 Frequency spectra of main shaft Axial forces

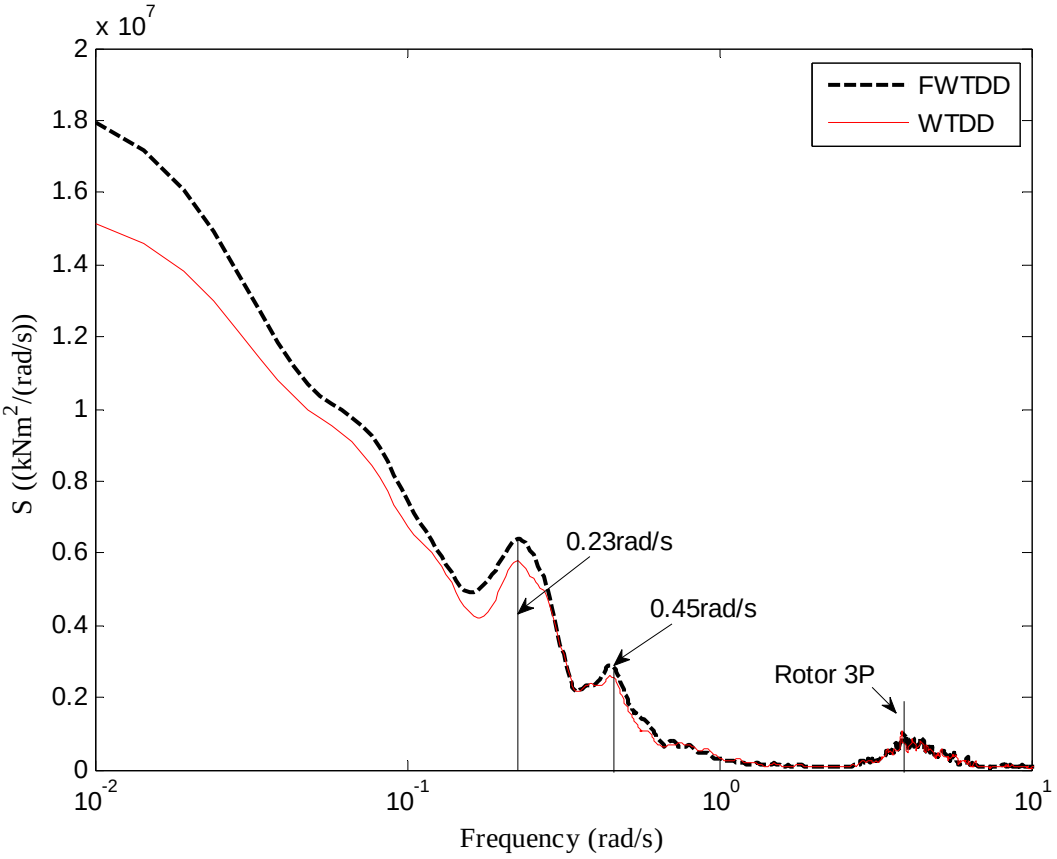

Fig. 7.18 Frequency spectra of main shaft bending moments

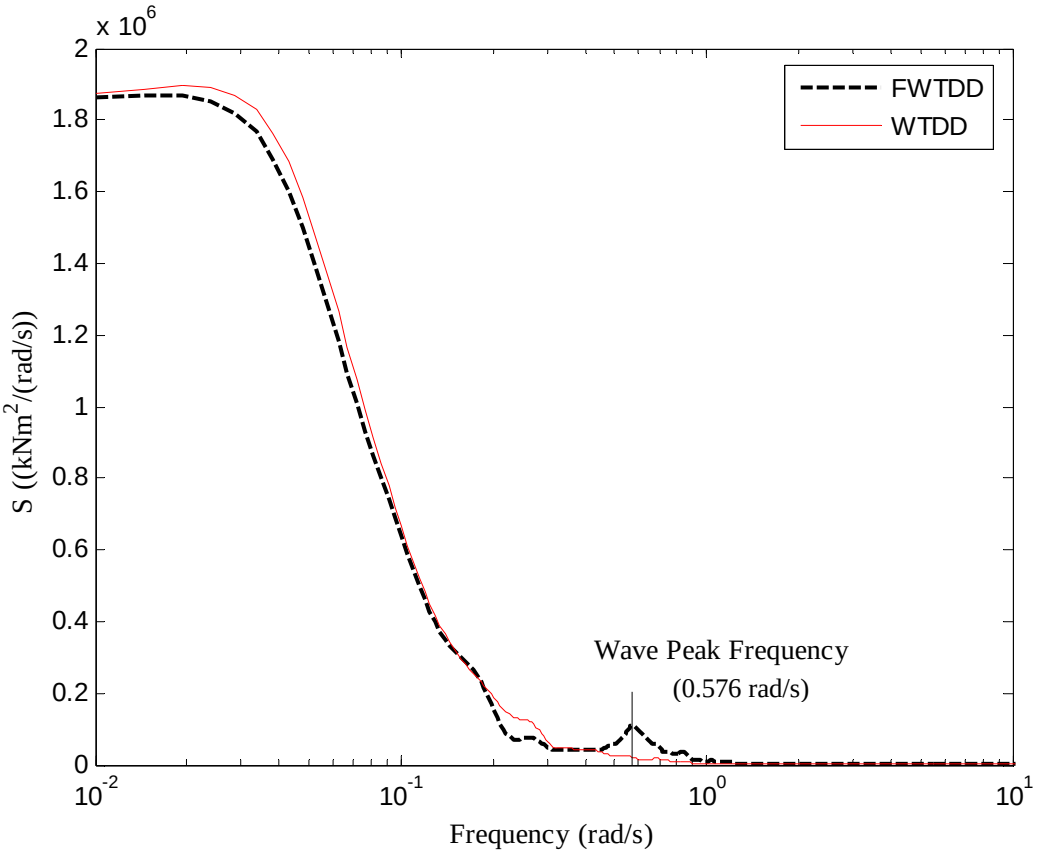

Fig. 7.19 Frequency spectra of main shaft torque

7.5 Internal drive-train response

The drive-train response is assessed by examining the loading on the components and quantifying the possible reaction forces. A set of response variables was used as a measure of the reaction to the combined loading from wind and nacelle accelerations. These include shaft displacements and forces due to unbalanced magnetic pull (as discussed in section 7.2.1) and the load components on the main bearings (axial, radial loads and tilting moments). These were treated as primary response variables. There can be other reaction forces and induced secondary responses that can be expected as a result of the main shaft loads and the primary responses. For example, the shaft can undergo structural deflection or bending and generator structural members can also deflect due to unbalanced magnetic pull. However no effort was made to study these responses or the effect of these on the main response variables. In the following, a comparison of the primary response variables for the FWTDD and WTDD systems is presented. Figures 7.20 to 7.22

show the percentage differences in the mean, standard deviations and maximum values of forces due to UMP, bearing forces and tilting moments of BR1 and BR2, radial and axial shaft displacements of the FWTDD system in comparison with the WTDD system. The results for axial response variables overlap with each other and are hence plotted separately. Figures 7.23 to 7.31 show the plots for the frequency spectra of the response variables (the values shown are for a wind speed of 21m/s). The difference in mean values of the response variables are within 10%. The increase in axial components of bearing forces and shaft displacements generally follow the trend predicted for shaft axial forces by HAWC2 simulations. Thus the axial response of the drive-train can be described as fairly linear. The increase was induced by wave excitation and platform pitch motions. Up to 25 % increase in maximum axial response variables was observed. Air-gap eccentricity (caused by radial shaft displacements) and hence the forces due to UMP were found to increase linearly with increase in wind speeds. The FWTDD system does not bring about any exceptional increases to these values. The frequency spectra for radial loads are very similar for the WTDD and FWTDD systems suggesting no extra excitations. Being the main support element, bearing BR2 saw the greatest loads. The response characteristics are discussed in detail in the following sub-sections.

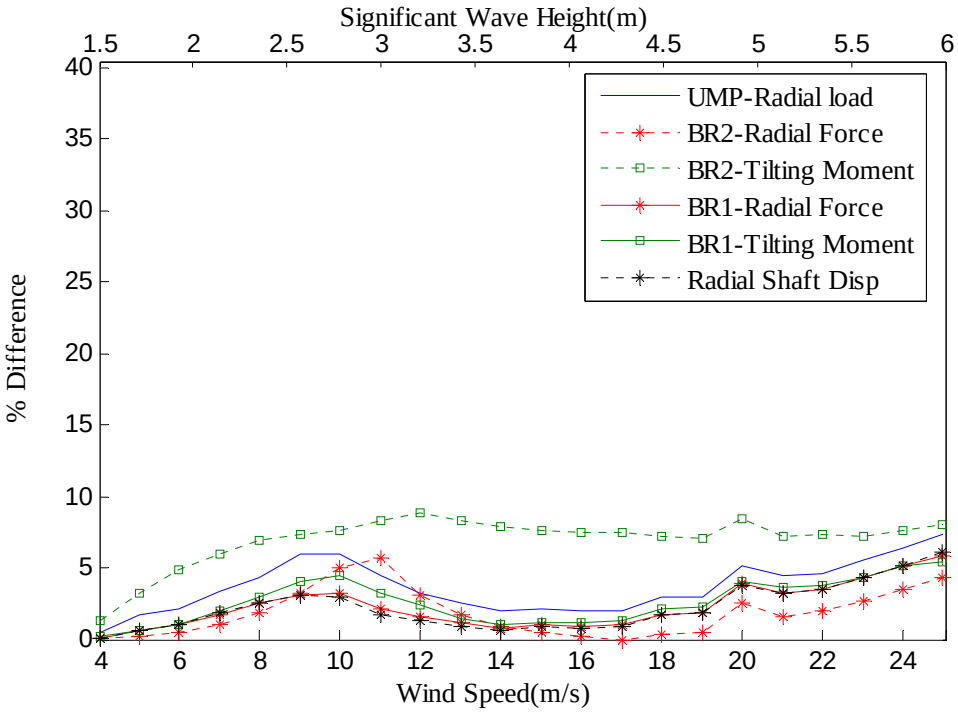

(a)

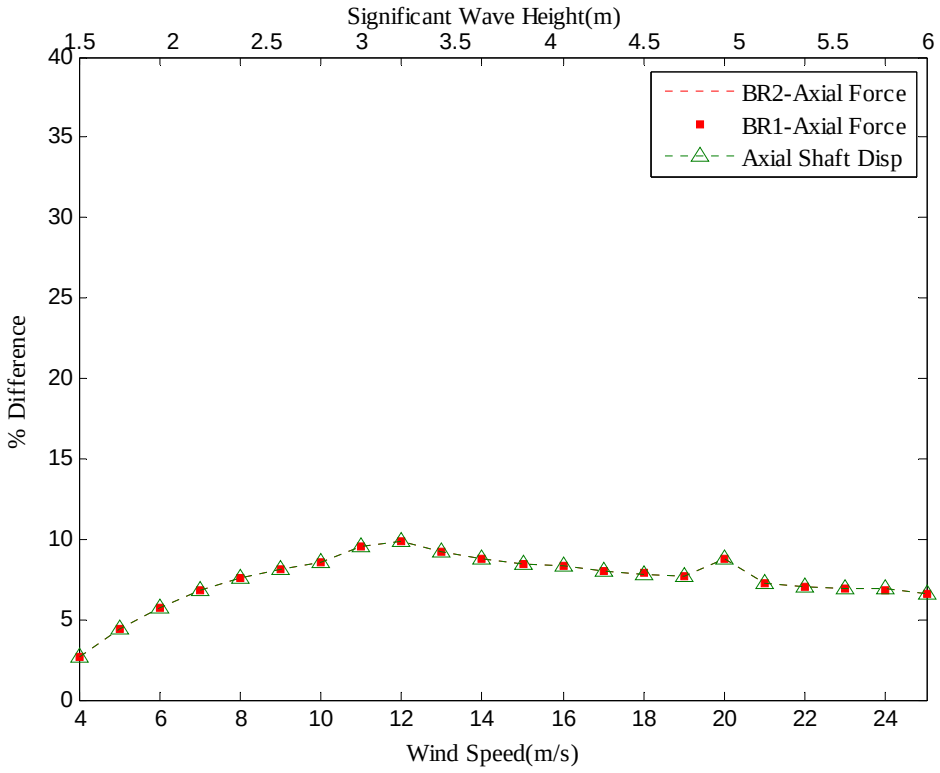

(b)

Fig. 7.20 Internal drive-train responses - % Difference in Mean Values: FWTDD Vs WTDD (a) Radial and tilting responses (b) Axial responses

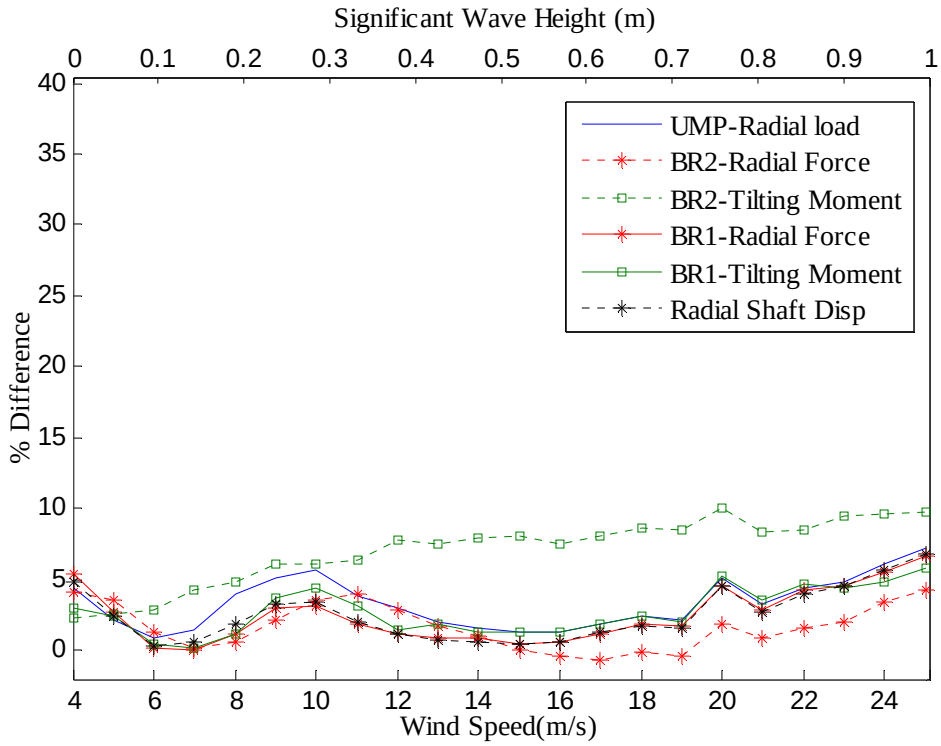

(a)

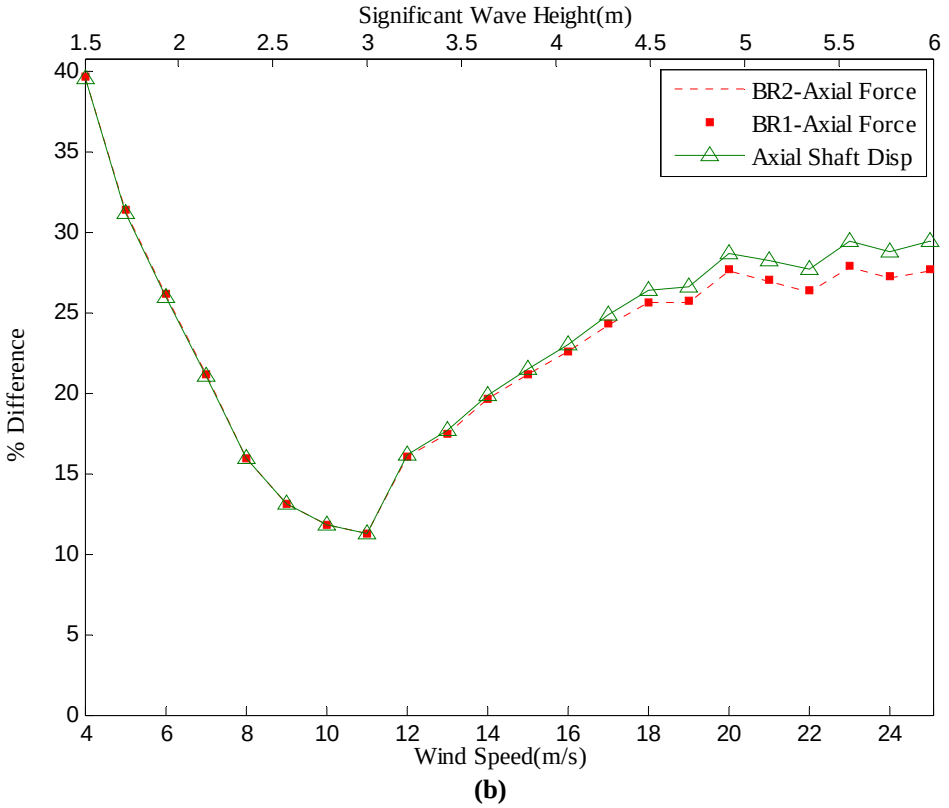

(b)

Fig. 7.21 Internal drive-train response -% Difference in Standard Deviation: FWTDD Vs WTDD (a) Radial and tilting responses (b) Axial responses

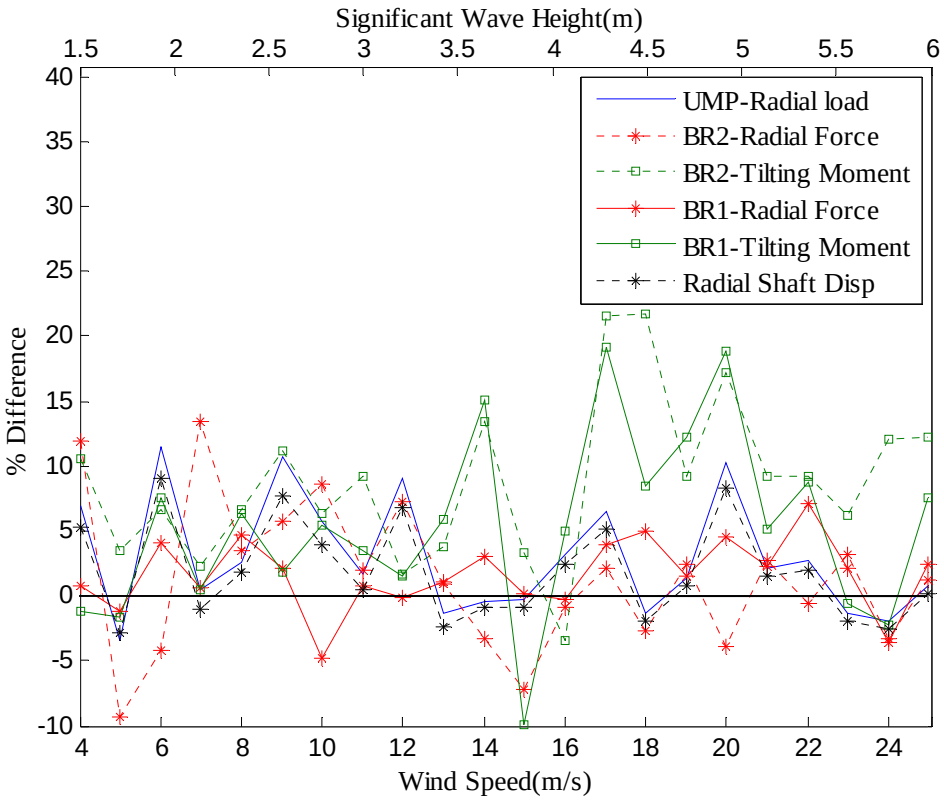

(a)

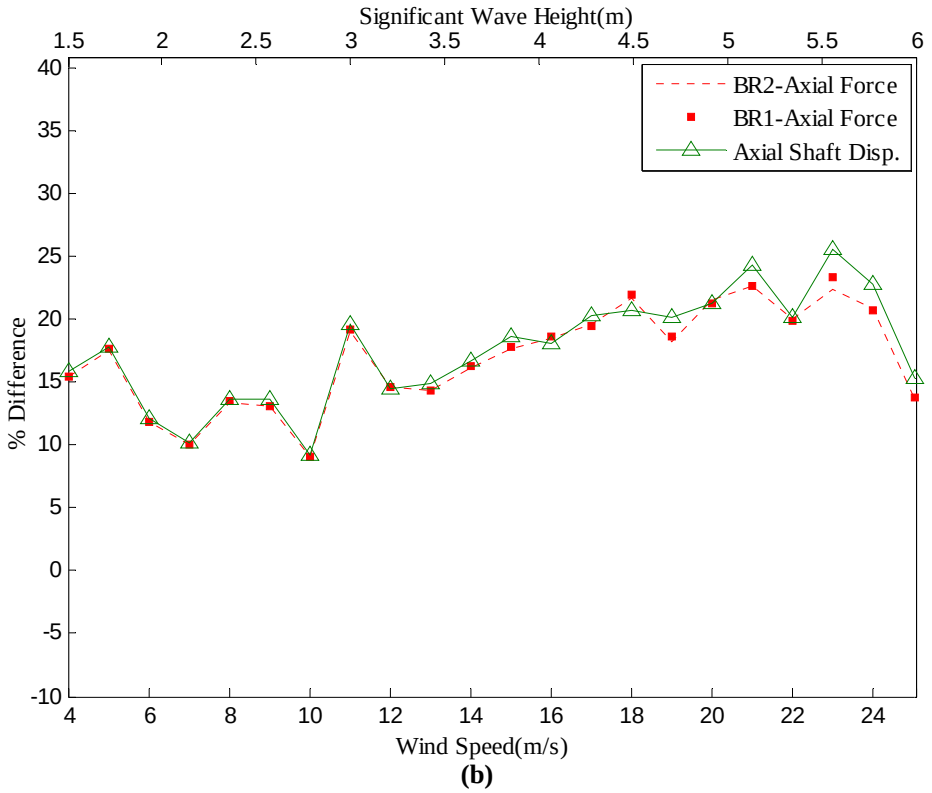

(b)

Fig. 7.22 Internal drive-train response - % Difference in Maximum Values: FWTDD Vs WTDD (a) Radial and tilting responses (b) Axial responses

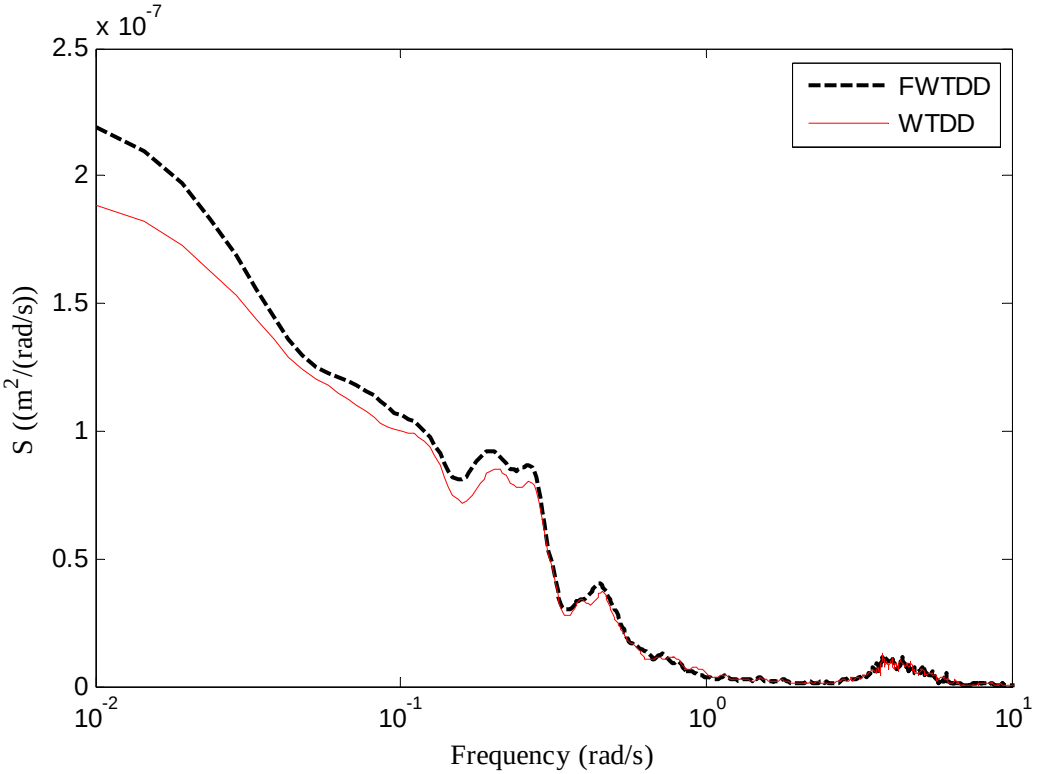

Fig. 7.23 Frequency spectra of Radial Shaft Displacements

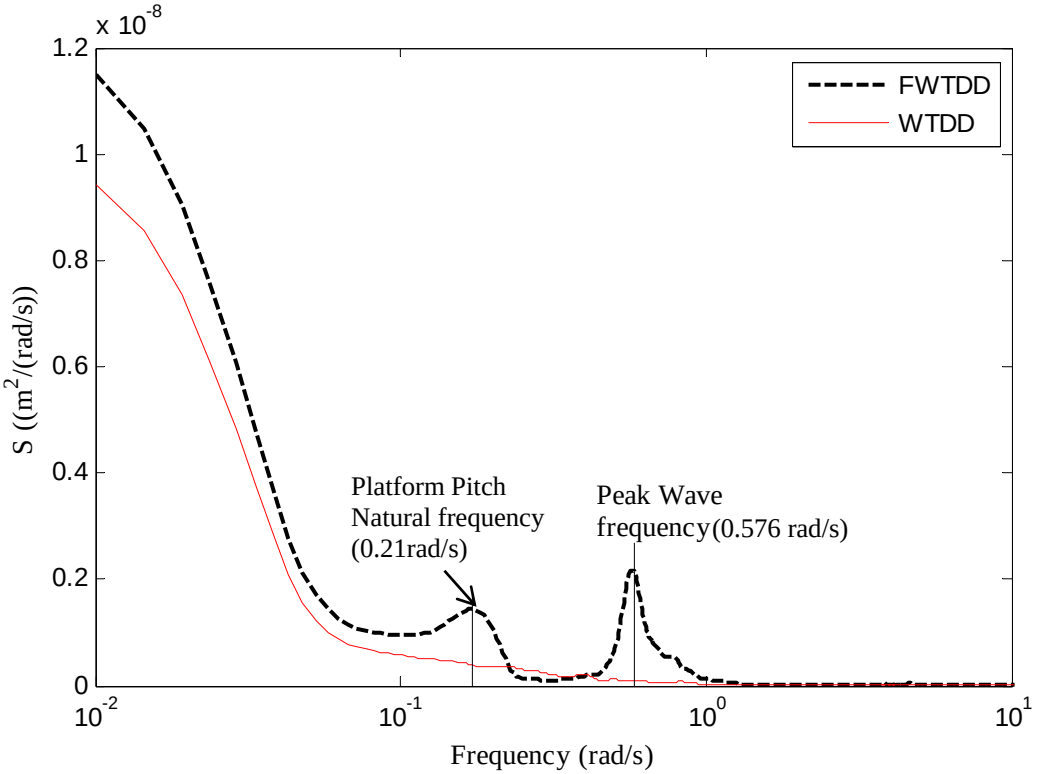

Fig. 7.24 Frequency spectra of Axial Shaft Displacements

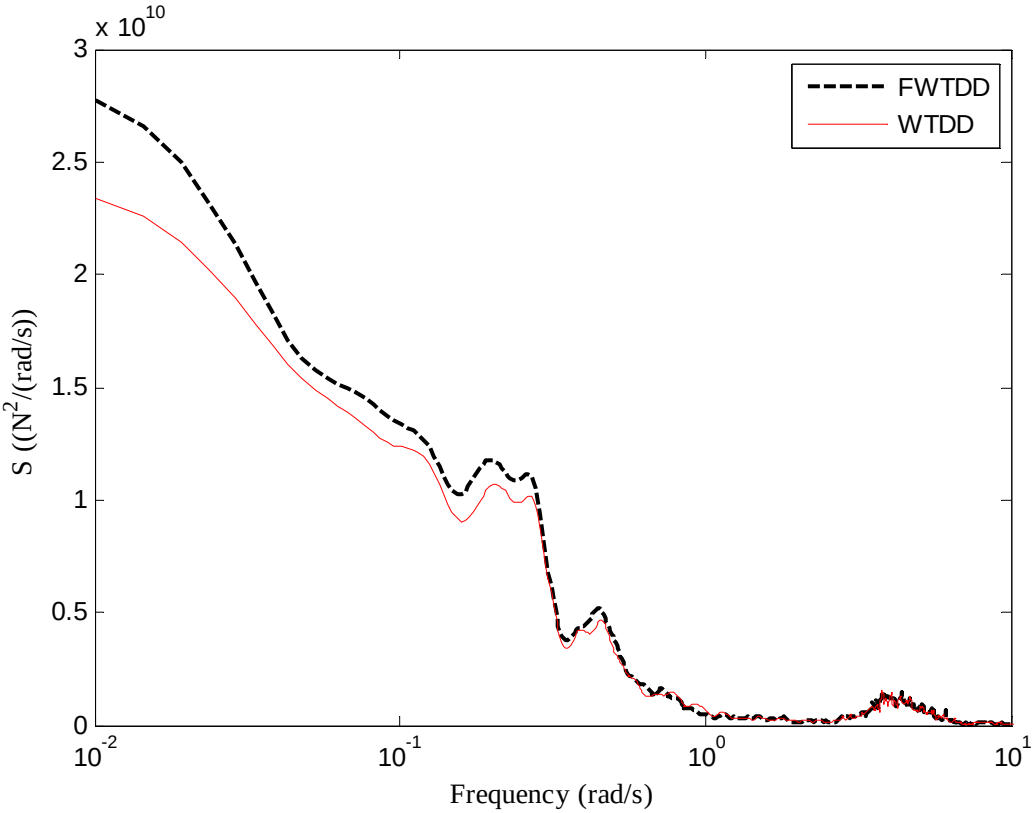

Fig. 7.25 Frequency spectra of UMP forces

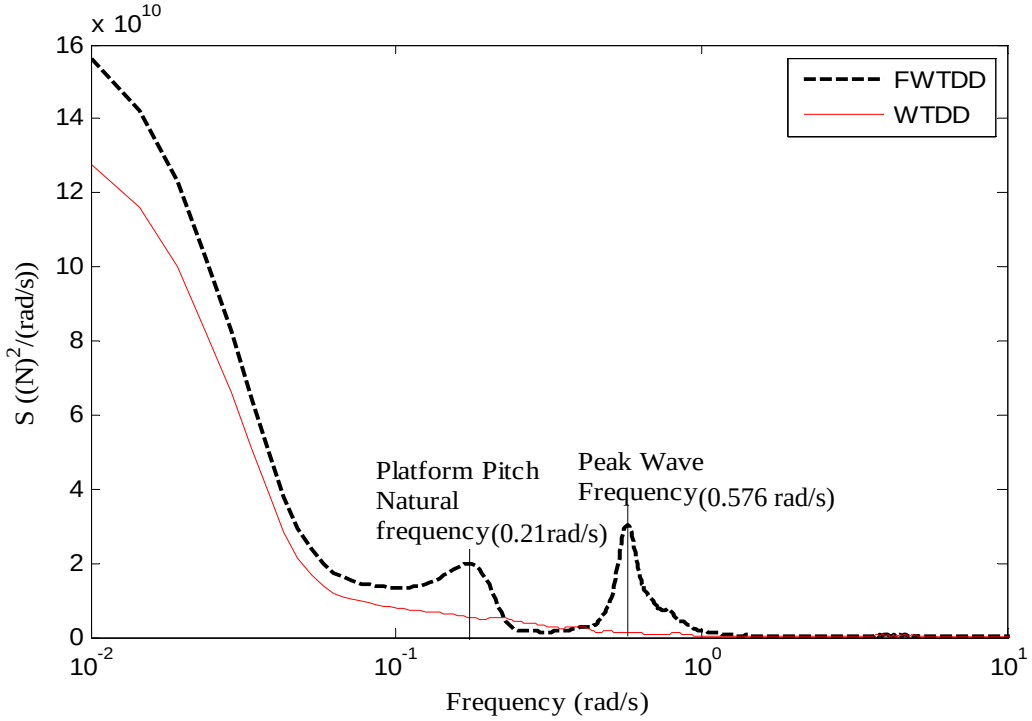

Fig. 7.26 Frequency spectra of BR2 Axial forces

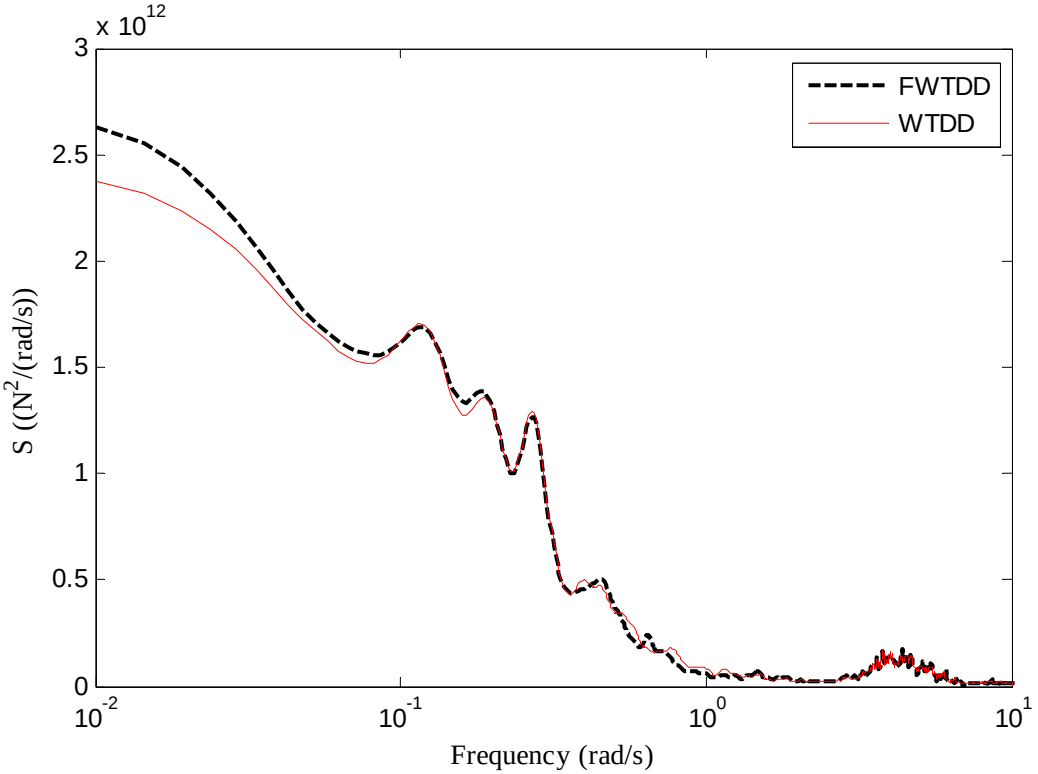

Fig. 7.27 Frequency spectra of BR2 Radial forces

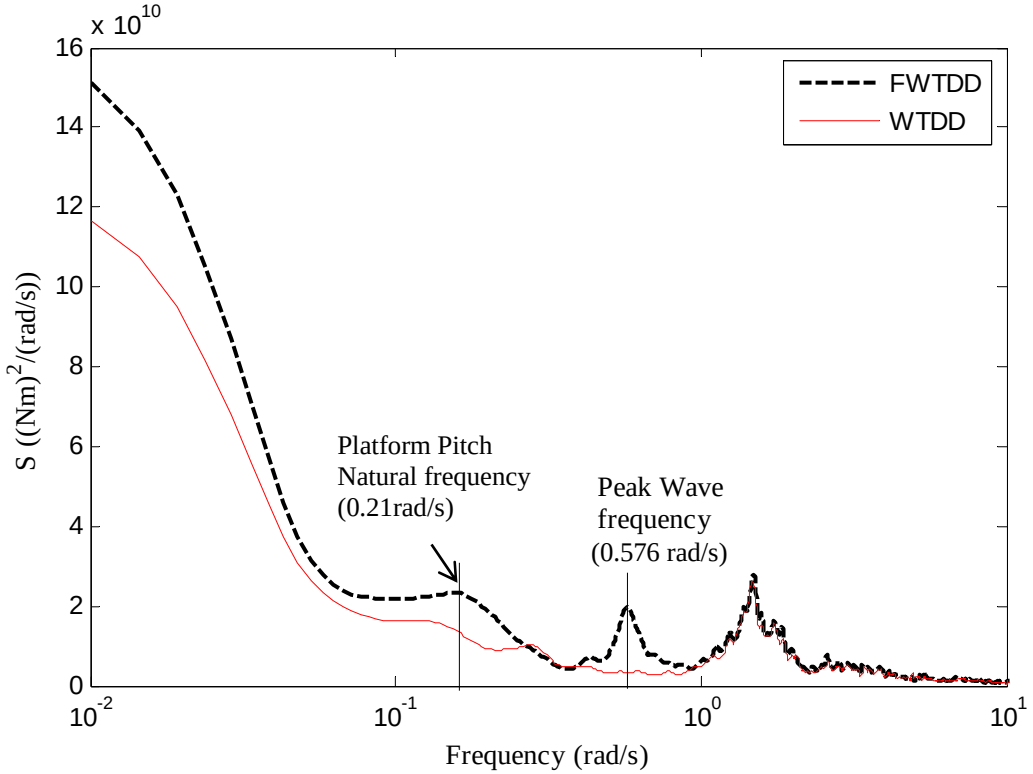

Fig. 7.28 Frequency spectra of BR2 Bending moments

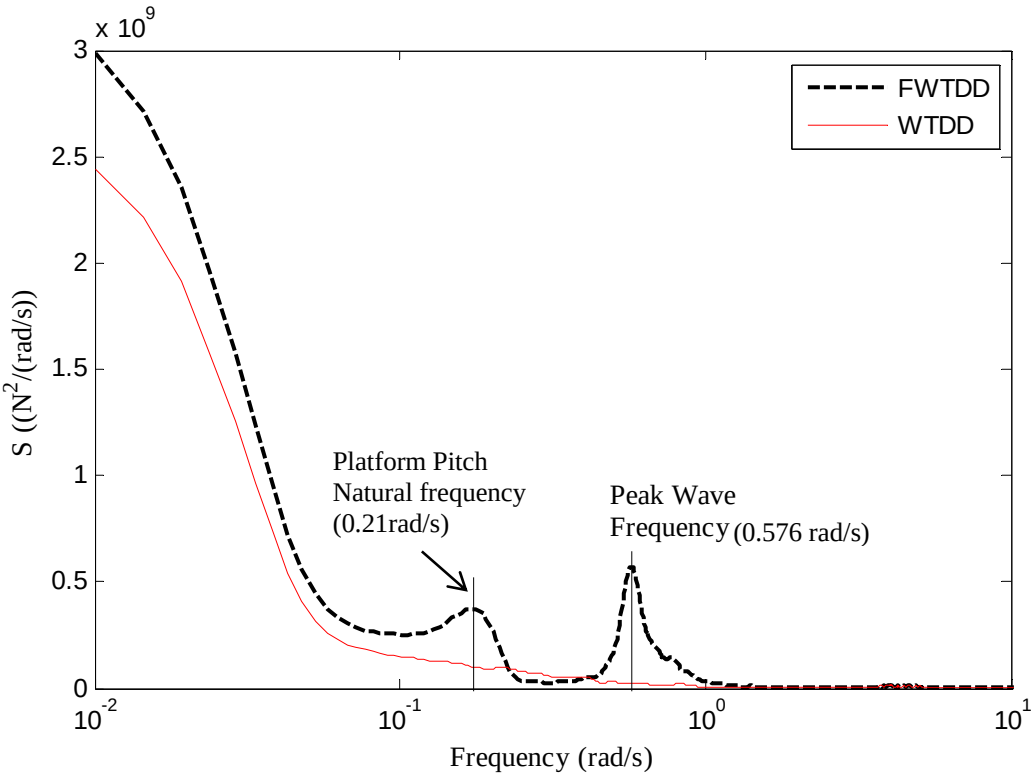

Fig. 7.29 Frequency spectra of BR1 Axial Forces

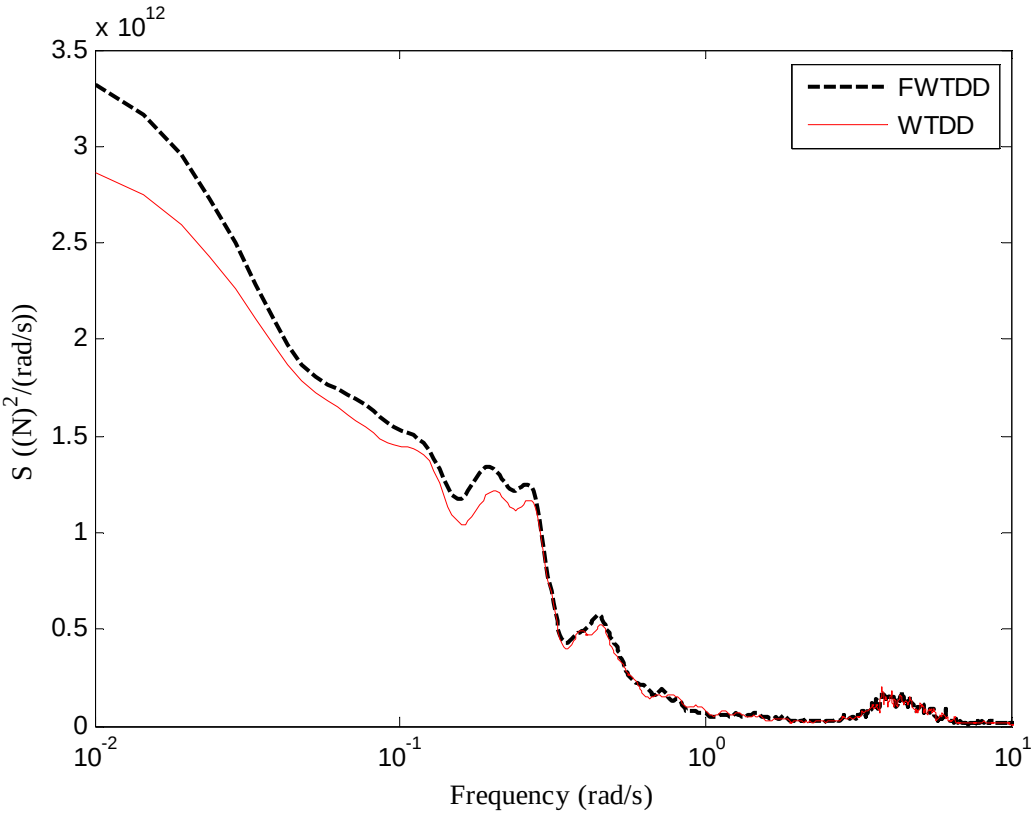

Fig. 7.30 Frequency spectra of BR1 Radial Forces

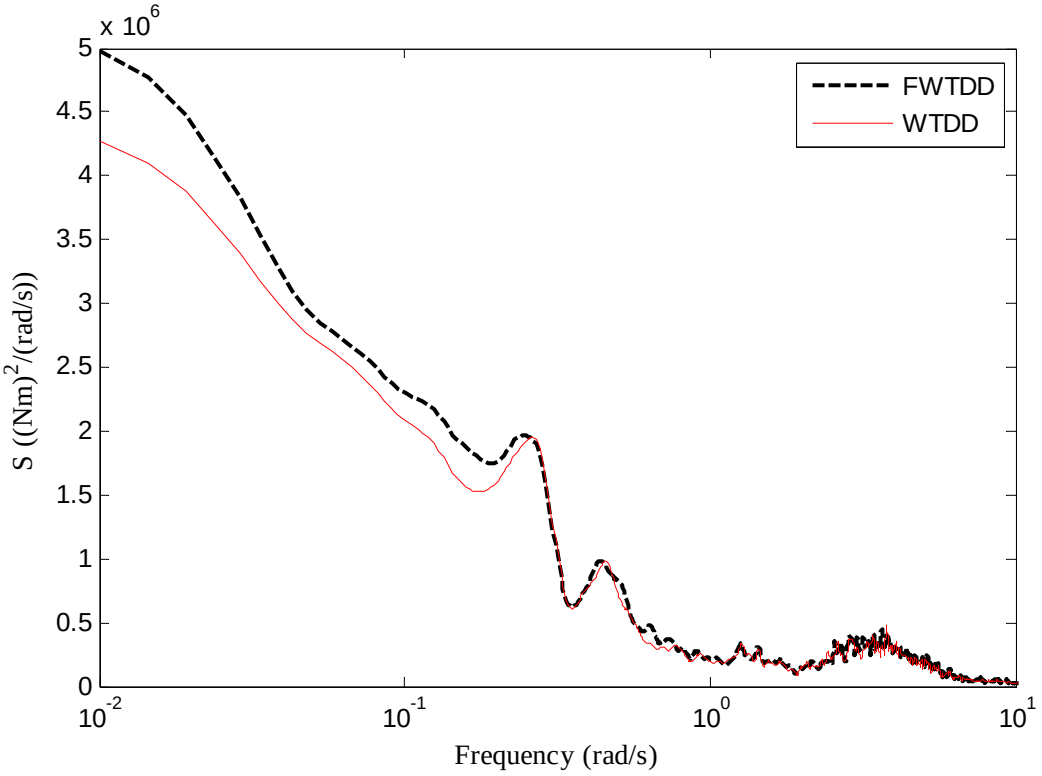

Fig. 7.31 Frequency spectra of BR1 Bending Moments

7.5.1 Shaft Displacements

For a direct-drive generator, proper shaft alignment determines the degree of concentricity of the rotor with the stator (and hence the unbalanced magnetic forces if any). This aspect is greatly influenced by the nature of shaft loading, the durability of bearings that support the shaft rotor assembly and the degree of compliance. For the WTDD system, the stiffness values of the bearings provided by bearing manufacturer (TIMKEN, refer to APPENDIX-B) served as the base case. These values were tested against the expected values of shaft radial displacements and forces due to UMP by a sensitivity study (Chapter 5). The steady state deflection for the chosen level of compliance resulted in 0.3% eccentricity (0.02mm of radial shaft displacement from the centre) and the mean dynamic air-gap eccentricity was about 10%. This resulted in a natural frequency of the shaft transverse vibration in the in-plane(Y and Z) direction to be 100 rad/s and 67 rad/s respectively.

7.5.1.1 Radial Shaft Displacement

Fig. 7.32 shows the plots for the mean and maximum % eccentricity observed for both the systems for the different wind speeds. With increase in wind speeds, the mean values for shaft displacements in the radial direction were observed to linearly increase from 0.19mm at 4m/s to 0.66mm at 25m/s. This resulted in a 10.4% eccentricity (i.e. ratio of radial shaft displacement/nominal air-gap) at 25m/s for the WTDD system. The FWTDD system led to very small increase in these values (2.2% at an average). The maximum difference in mean values of radial displacements for the FWTDD system was still low (6%) and occurs at a wind speed of 25m/s. The

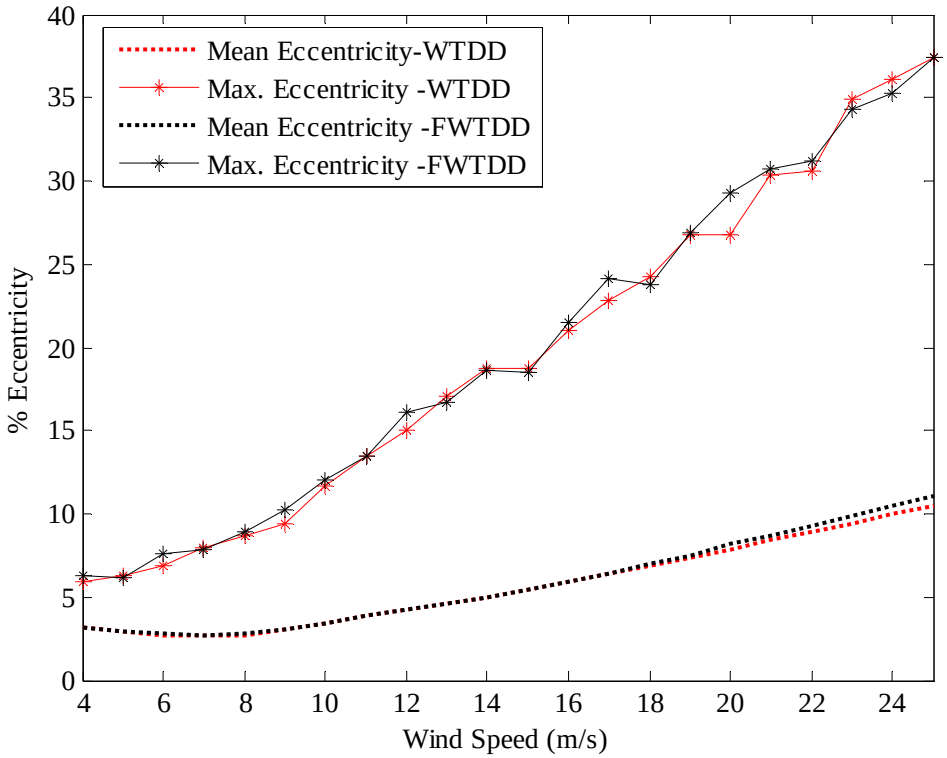

Fig. 7.32 Eccentricity (%) for different wind speeds for WTDD and FWTDD system

percentage difference in standard deviation values for radial displacements between the two systems also followed the same trend as the mean values. The maximum value of shaft displacement can reach upto 2.2mm (i.e. about 36% eccentricity) for the WTDD system at 25m/s wind speed. Since this is a momentary phenomenon, it is expected that this will not introduce secondary deflection. With the FWTDD system, the % change in maximum values lies within $\pm$ 10%, with greatest displacement at 6m/s. The results also suggest that no possible air-gap closure occurs with the

FWTDD system even with a lower bearing compliance for the range of wind speeds studied. The comparison of power spectra (Fig. 7.23) for the two systems show negligible difference in the energy content implying no additional excitations from platform motions or wave frequencies. The energy content of the spectra is small owing to small displacements in the order of a few mm.

7.5.1.2 Axial Shaft displacement

The main bearings supporting the shaft for WTDD system are generally calibrated to accommodate large thrust loads so that the axial shaft displacement is very small. The FWTDD system experiences a noticeable increase in the axial loads and hence greater axial displacements. The trend in the axial displacements shown in Fig. 7.20(b) matches with that of the axial forces in Fig.7.15(a). The maximum difference in mean values (about 10%) appears for a wind speed of 12m/s. The % difference in standard deviations of the main shaft axial displacements (Fig. 7.21(b)) also follow the same trend as the shaft axial forces (Fig. 7.15(b)). With the absolute values of standard deviations being small, a slightly larger percentage difference was observed with the main shaft axial displacements. A maximum difference of 40% was observed at 4m/s with the FWTDD system. This value is lowest at 11m/s. The maximum values for shaft displacements increase by about 17% on an average for the FWTDD system, with the greatest difference (about 25%) observed at 23m/s. As may be noted from the power spectra (Fig.7.24), this difference is partly induced by platform pitch motions and wave excitation. The energy content of the spectra is small owing to small displacements in the order of a few mm.

7.5.1.3 Main Shift Tilt displacement

The bearing tilt stiffness was calibrated to be sufficiently high so that the shaft did not undergo considerable tilting. The tilt displacements observed for a wind speed of 25m/s were negligible as may be noted from the time history in Fig. 7.33. The frequency spectra of shaft tilt displacements in figure 7.34 for both the land based and floating systems showed similar energy content indicating no notable increase or additional excitations for the floating system.

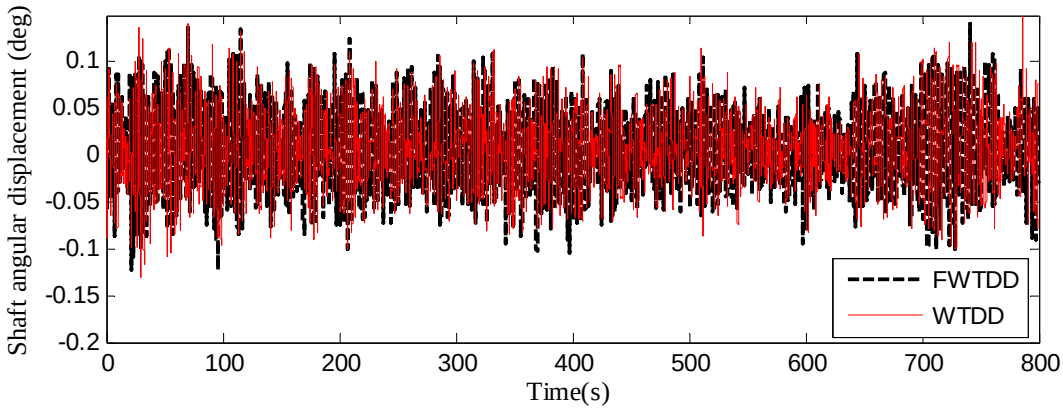

Fig. 7.33 Main Shaft Tilt displacement history for a wind speed of 25m/s.

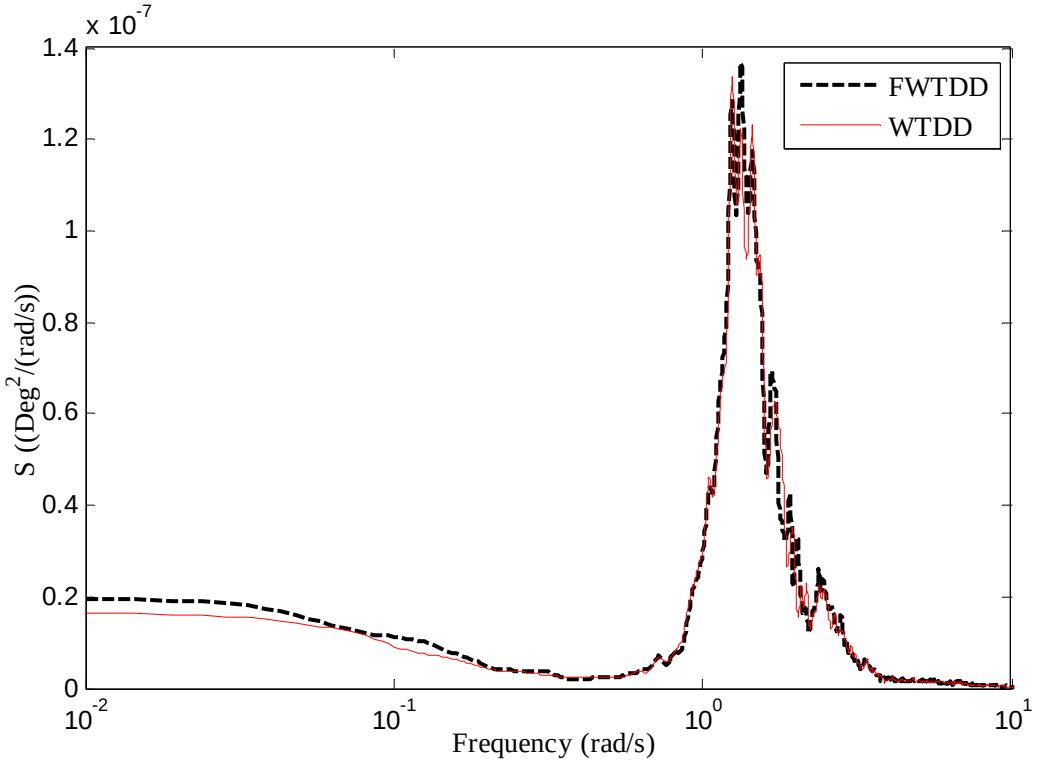

Fig. 7.34 Shaft Tilt displacement spectra for WTDD and FWTDD systems

7.5.2 Net radial Forces due to unbalanced magnetic pull (UMP)

The forces due to unbalanced magnetic pull were obtained by accessing the UMP force element components in SIMPACK. These were modelled to compute the forces from the kinematic measurements of radial shaft displacement using the linear eccentricity model (Section 7.2.1.1) during the solver run. The net radial forces were computed as absolute values obtained by resolving the force components in the Y and Z directions. The mean values of forces due to UMP were found to linearly

increase with increase in wind speeds from 38.7 kN to 200 kN for the WTDD system and 38.8 kN to 222 kN for the FWTDD system. This was generally consistent with the linear increase in the mean values for the shaft displacements observed with increasing wind speeds. Fig. 7.35 presents the plots for the mean and maximum UMP forces at different wind speeds. As may be noted, the percentage increases in mean values also follow the same trend as the radial displacements (eccentricity, Figure 7.32). Referring to Fig. 7.20(a), the FWTDD system introduces less than 10 % increase in mean values of UMP. A maximum of 7.5% difference between the two systems for the mean values occurs for 25m/s wind speed. The percentage difference in standard deviations and maximum values for UMP loads follow the same trend as

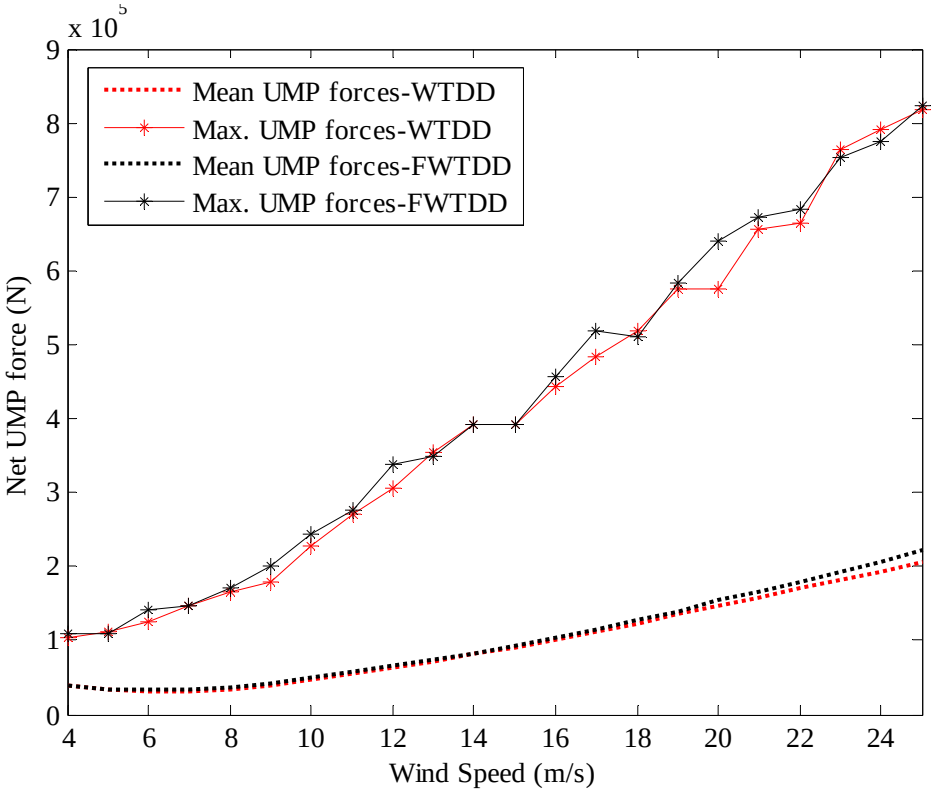

Fig. 7.35 Net forces due to UMP at different wind speeds for WTDD and FWTDD systems

the mean values. As may be observed from the frequency spectra for the UMP loads in Fig.7.25, the FWTDD system is not subjected to additional sporadic excitations that are either wave/motion induced. The shape of the power spectra is very similar to the shape of power spectra for radial shaft displacements (Fig. 7.23).

7.5.3 Bearing Loads

In the past some studies have shown that wave induced motions have a dominating effect on the bearing forces [208]. In general, the bearing stiffness characteristics determine the reaction at the bearings. As with the WTDD system, BR2 was tuned to accommodate the majority of thrust loads and hence the axial reactions from bearing BR2 are greater than BR1 by a factor of approximately 7.5. With increasing wind speed the mean values of axial loads increase from 212 kN to 535 kN for BR2 and 30 kN to 60 kN for BR1 respectively. In the comparison presented against the FWTDD system, the results of the bearing axial loads (green dotted lines) tend to overlap exactly with the results for axial shaft displacements (Fig. 7.20(b)). As can be expected, the mean values of the bearing axial loads trace the pattern followed by the main shaft axial forces (Fig. 7.15(a)). The maximum increase in the mean values was still below 10% with the FWTDD system. The increase in standard deviation and maximum values for the bearing axial loads for the FWTDD system are yet again attributed to wave excitation and platform pitch motions (as noted in Figures 7.26 & 7.29). Higher energy content in axial loading is observed for BR2. It may also be noted that the shape of the power spectra for the bearing axial loads and shaft axial displacements (Fig. 7.24) are very similar.

From the simulations for the WTDD system, it was observed that the radial loads in bearing BR2 are greater than BR1 by a factor of at least 2 until a wind speed of 20m/s. At greater wind speeds, the reactions tend to be comparable. Despite acting like a negative spring that abates the restoring from bearings, the forces due to UMP contributes to less than 3% reduction in the overall mechanical stiffness. Therefore the presence of UMP does not necessarily bring about a perceptible increase in bearing reactions. Fig. 7.36 shows the time histories for UMP and radial bearing load (BR2) at 25m/s wind speed. It may be inferred that if the bearing loads were of the order of few MN, the forces due to UMP were of the order of few kN (average values were less than 8% of the total bearing radial load). This was attributed to the large value of the bearing to magnetic stiffness ratio ($k_{bearings}/k_{mag}$) at all the wind speeds. For the WTDD system, with increase in wind speeds, the mean values of radial loads increase from 800 kN to 1.5 MN and 2.6 MN respectively for BR1 and

BR2 at 25m/s. The mechanics on the FWTDD system differ by less than 10% for the mean values and standard deviations of radial forces. The maximum values on the other hand, fall within +15%. As may be noted from the Figures 7.27 & 7.30, the frequency spectra are very similar and no extraneous excitations occur with the FWTDD system.

The mean values of tilting moments for BR2 increase from 200 kNm at 4m/s to 538 kNm at 25m/s for the WTDD system. BR1 undergoes substantially lower tilting with less than 4 kNm at 25m/s wind speed. The FWTDD system introduces an average increase of about 7% in the mean and standard deviations of BR2 tilting moments. The differences in maximum values are as high as 22% (16-17m/s). The

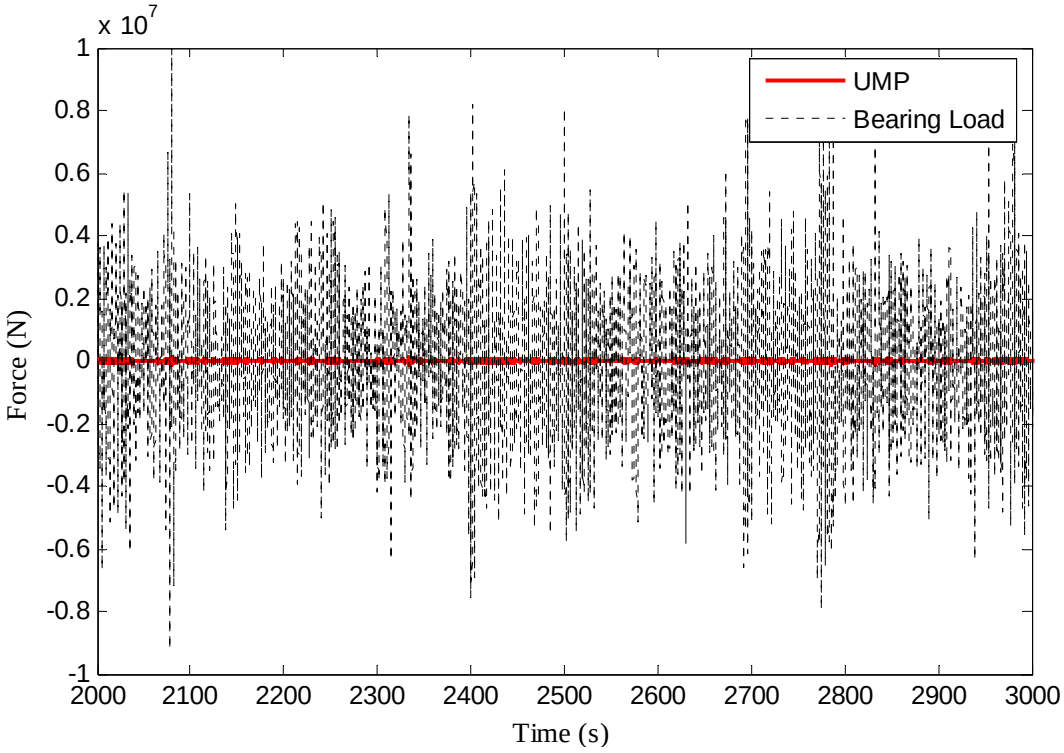

Fig. 7.36 Time histories of bearing radial load (BR2) and forces due to UMP

comparison of frequency spectra for the two systems (Fig. 7.28) shows additional energy content for BR2 around the wave frequency and platform pitch frequencies. Less than 5% increase is noted in the mean values and standard deviations for BR1 tilting moments, suggesting similar load spectra for both systems (Fig. 7.31). The differences in maximum values are limited to $\pm$ 20%.

7.6 Bearing life

The loading response of the bearings suggested up to 25% increase for the FWTDD system. Since higher loads can result in an increase in fatigue damage of the components, it is important to verify the impact of increase in these loads on the bearing life. The IEC standard [207] requires the minimum acceptable calculated lifetime for main shaft bearings for land-based turbines at 90% reliability to be 175000 hours or 20 years. With the design standards not fully defined for the floating wind technology, it would be pre-mature to deduce a hypothesis on bearing survivability. Further, a detailed investigation of bearing life for land and offshore wind turbine systems should be based on all possible design load cases for site-specific conditions as the wind climatic profiles are completely different(especially offshore where internal boundary layer effects and temperature gradients are dominant). However, such an exercise was not within the scope of this research and was hence not pursued. Nevertheless, a preliminary assessment of bearing lifetimes was carried out.

For computing the basic rating life of the bearings, two approaches exist [209]. The standard engineering approach uses a simplified method that considers the mean bearing radial load at each wind speed as an approximation to the time-varying roller contact load. This method neglects the internal distribution of loads, roller misalignments, roller-raceway contact condition, the condition of lubrication, operating temperature etc., which may have an influence on the life. This method therefore deals with the radial load only. A more refined approach considers the internal roller load distribution and determines the life of the raceway separately. The study by Jiang *et al.,*[209] showed that the simplified method can provide a useful estimate as it yields results close to those of the refined method if roller misalignments were not considered. Therefore the simplified method was adopted for this study.

Firstly, the time series of bearing loads were retrieved from SIMPACK simulations for internal drive-train response. The duration of the levels of the mean radial loads were obtained for a given reference time using load duration distribution method.

Statistical analysis methods were then applied to incorporate the wind speed probability density function and obtain the long-term distribution of the bearing internal loads. The bearing fatigue life is estimated from the basic rating life model [210]. Fig. 7.37 shows the fatigue life estimation methodology.

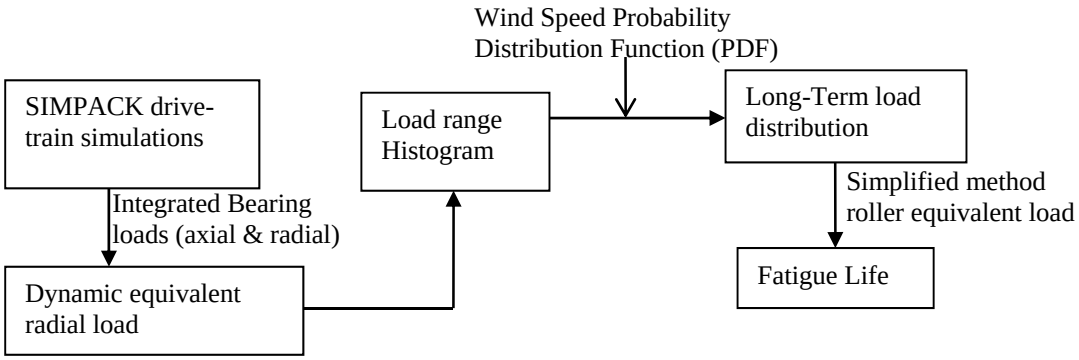

Fig. 7.37 Bearing life estimation methodology

The time-varying integrated bearing loads from SIMPACK simulations were estimated for the operating range of the wind turbine, i.e. between 4-25 m/s. This range covers only the non-stationary operation under turbulent wind conditions, therefore extreme events, non-operational load cases, machine fault, transient events; emergency stops etc., were not considered. As a result, all presented results are expected to differ from loads in practice for diverse reasons. In the absence of site data, IEC wind classes I, II and III corresponding to mean wind speeds of 10, 8.5 and 7.5m/s were considered [211]. The mean wind speeds at hub-height were assumed to be Rayleigh distributed so that the stress range distribution for the entire life time of the structure can be determined. The probability density function used to describe the distribution of wind speed at hub height (V) was given as

$$p(V) = 1 - exp\left[-\left(\frac{\pi V}{2V_{ave}} \right)^2 \right] \tag{7.21}$$

where, V_{ave} is the annual average wind speed at hub height. The turbulence intensities in wind, lateral and horizontal directions were according to IEC specifications [181]. The probability density functions (PDFs) of the three wind turbine classes with average wind speeds of 10, 8.5 and 7.5m/s are shown in Fig. 7.38.

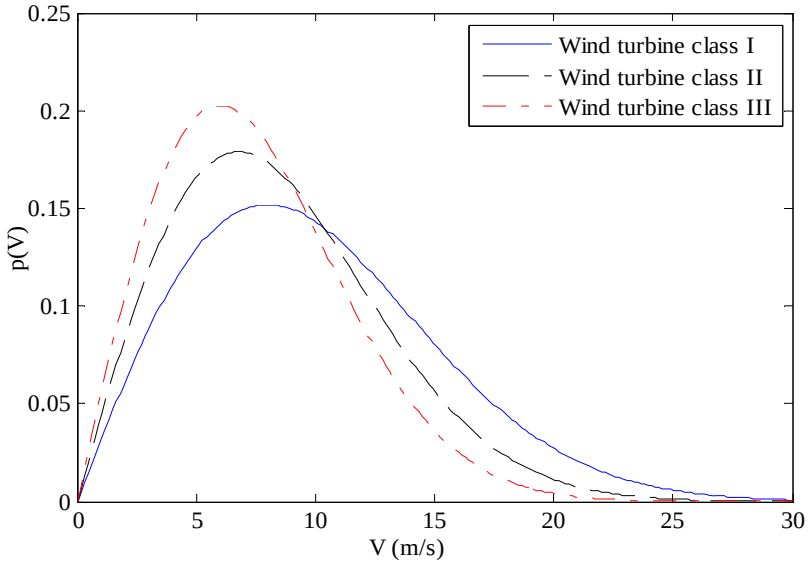

Fig. 7.38 Wind speed PDF for IEC turbine classes I, II and III

A configuration of a double row tapered roller bearing (Inner race construction) for BR2 and single row cylindrical roller bearing (BR1) was selected from the TIMKEN product catalogue[212]. The wind speeds were discretized as short-term wind conditions incremented by 1m/s and twenty-two 10 minute simulations were carried out. Figures 7.39 & 7.40 shows sample time histories of radial and axial loads obtained from SIMPACK for a wind speed of 25m/s for BR2 for FWTDD and WTDD systems.

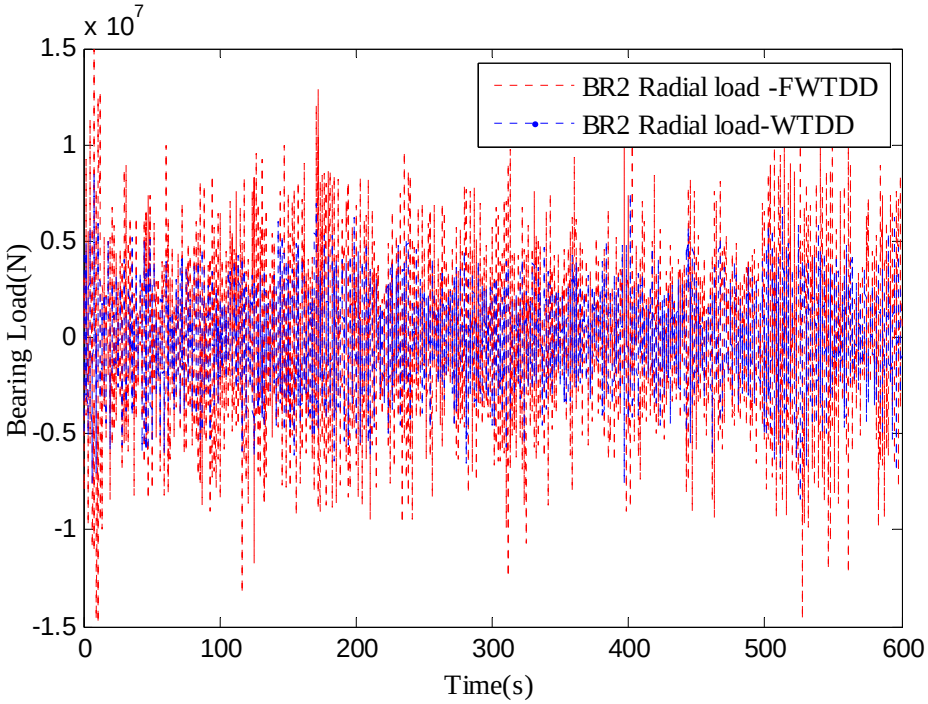

Fig. 7.39 Time history of bearing radial loads

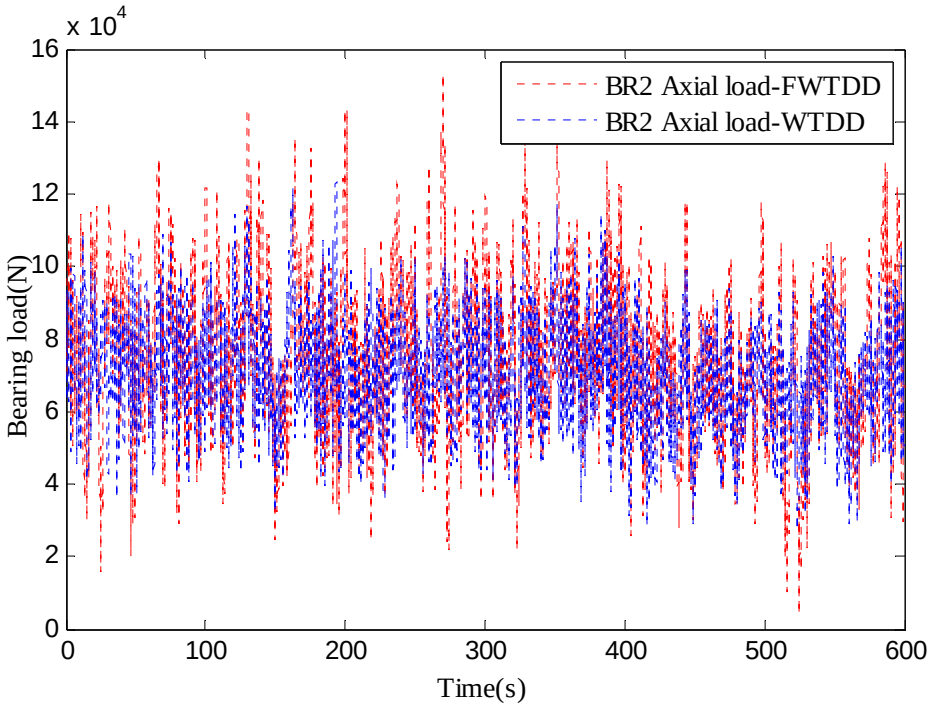

Fig. 7.40 Time history of bearing axial loads

Since the bearings were subjected to a combination of axial as well as radial loads, it was important to determine the dynamic equivalent radial load to be able to use the basic rating life model. This is defined as that hypothetical load, constant in magnitude and direction, acting radially on radial bearings which, if applied, would have the same influence on bearing life as the actual combination of loads to which the bearing is subjected to [213]. Fig. 7.41 illustrates this effect.

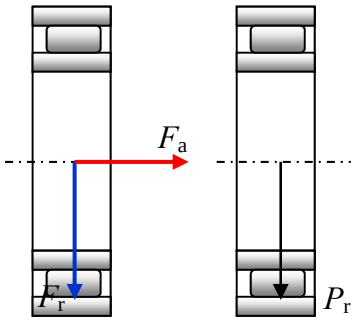

Fig. 7.41 Dynamic equivalent radial load

The dynamic equivalent bearing radial load(P_r) was obtained by adjusting the loads by suitable load factors as per the recommendations of section 7.2 of ISO 281[210] such that

$$P_r = X \cdot F_r + Y \cdot F_a \tag{7.22}$$

where, X is the axial load factor, Y is the radial load factor, F_r is the radial bearing load and F_a is the axial bearing load. The values for the load factors are listed in table 7.1. The load factors for the bearings were taken from relevant product tables in ISO-281 [210] and manufacturer's catalogues [212]. To account for the turbulent wind conditions and variation in load spectrum, the load duration distribution method was adopted [214]. The load histograms for each wind condition were obtained by dividing the time series of equivalent load into equidistant time intervals. 4000 bins were used for the discretisation of the load which had a range between 10kN - 12000kN. At each time interval, the level of load time series was read and counted in each bin. The load range histograms integrating all wind speeds for the bearings BR2 and BR1 for the WTDD system and FWTDD system are shown in Figures 7.42 and 7.43. The subtle shift in load range can be seen by the dotted bars for the FWTDD system. The probability distribution of wind speed was then applied to the load range histogram to get a load range probability density function, m_i for each bin number i.

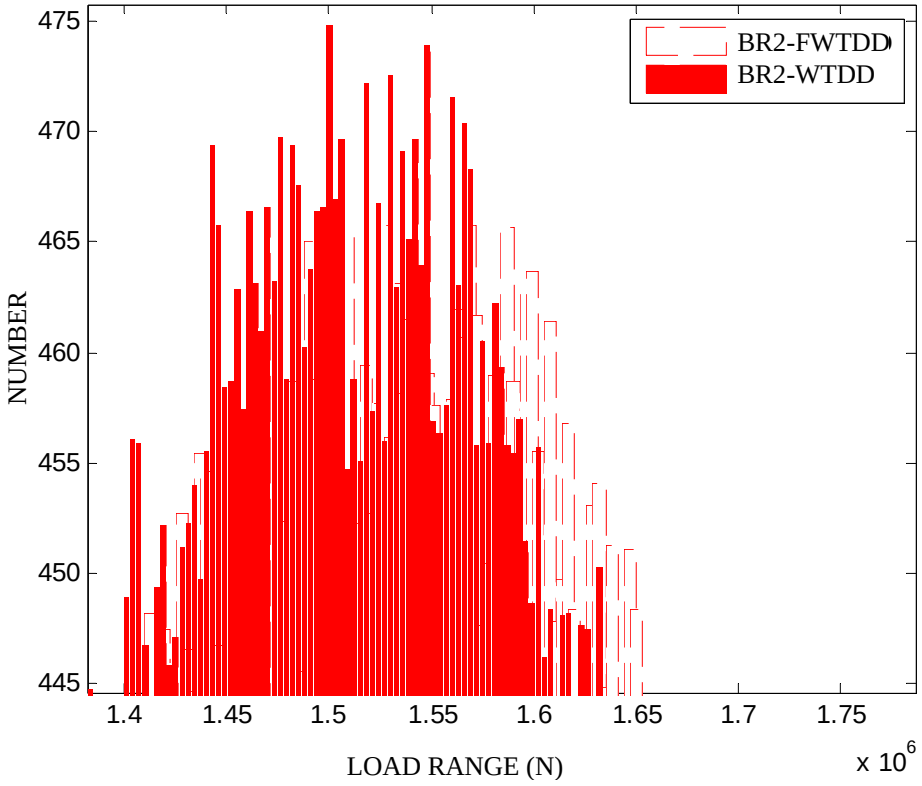

Fig. 7.42 Load range histogram for Bearing BR2

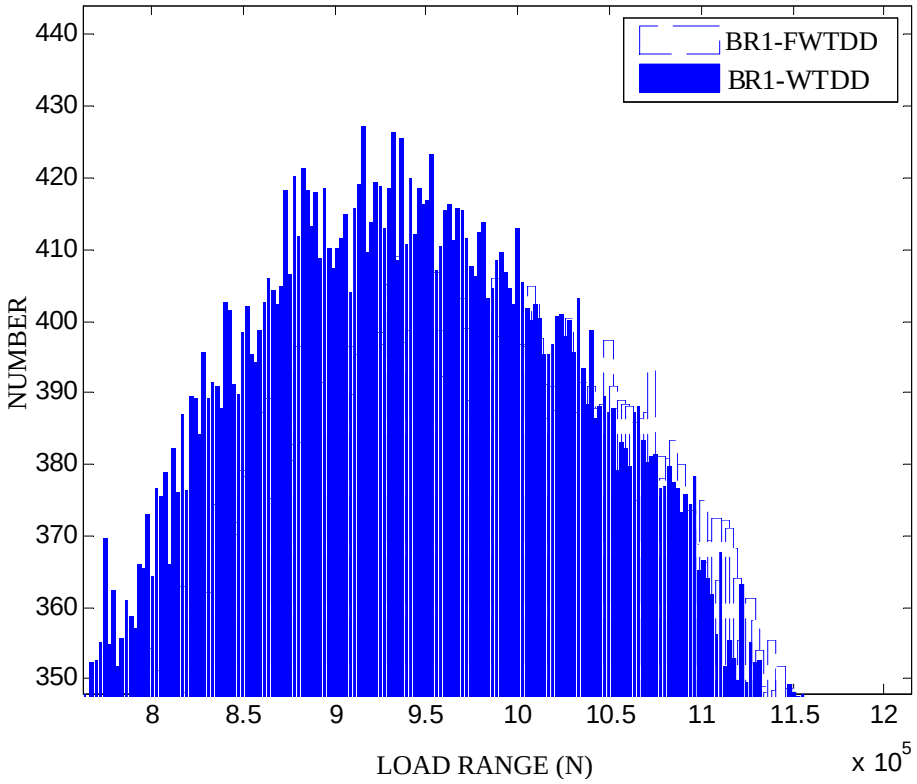

Fig. 7.43 Load range histogram for bearing BR1

The long term equivalent load (P_{eq}) for each wind class was determined as

$$P_{eq} = \sum_{i=1}^{n} (P_i^{\,p} m_i)^{1/p} \tag{7.23}$$

where, P_i the load level of the i^{th} bin, n the number of bins, p the life exponent used for bearing life calculation (=10/3 for roller bearings with line and point contact). The basic rating life associated with 90% reliability of an individual rolling bearing, L_{10} in terms of number of hours was then computed for 10^6 revolutions as [210]:

$$L_{10} = \left(\frac{C_r}{P_{eq}} \right)^p \times \frac{10^6}{60n} \tag{7.24}$$

where, C_r is the basic dynamic load rating of the bearing and P_{eq} the long term equivalent radial load and n, the speed in rpm. Table 7.1 provides the basic dynamic load ratings for the bearings chosen for BR1 and BR2.

Bearing	Basic Dynamic load rating (kN) for 1 million revolutions	Axial load Factor	Radial load factor
BR1(Cylindrical roller bearing)	9030[1]	0.44[3]	0.93[3]
BR2(Tapered roller bearing)	15900[2]	0.94[4]	1.0[4]

[1] TIMKEN catalogue data for CRB (SERIES NU20/900)[212]
[2] TIMKEN catalogue data for TDI (SERIES LM287649D) [212]
[3] TIMKEN handbook[215]
[4] based on Table 8(section 7.2) of ISO-281[210]

Table 7.1 Bearing load factor and ratings

Fig. 7.44 shows that both the bearings are sufficiently durable for the intended wind class with more than 175000 hours. The average percentage reduction in reliability is expected to be 11.5% and 6.2% respectively for bearing BR1 and BR2 in the FWTDD system.

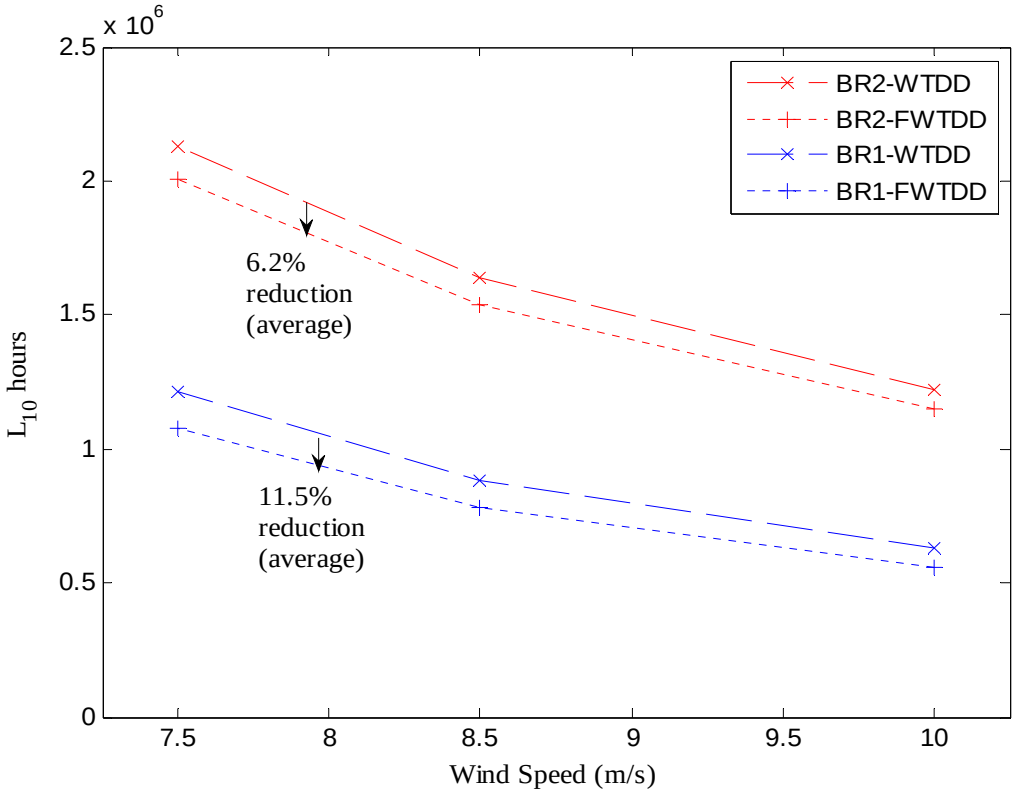

Fig. 7.44 Basic Rating life for bearings for different wind speeds: FWTDD Vs WTDD

It is re-stated that the above predictions do not consider possible machine faults, extreme events and special load cases where the effect of roller misalignment and coupled axial-radial-bending effects become more important. These events can lead to potentially higher loads leading to lower service life than predicted by this study. Therefore, the life models used in this study only provide a rough indication of expected reduction in bearing life when implemented for a FWTDD system. The results must be considered with a good sense of engineering judgment.

7.7 Summary – Part III

The work presented in this chapter extended the investigations on a direct-drive radial flux PMSG model that was custom-built for a spar buoy type wind turbine. The internal dynamics of the drive-train were analysed using a linear combination of a fully coupled aero-hydro-servo-model of the FWTDD system in HAWC2 and a detailed drive-train model in SIMPACK. The global motion response and main shaft loads from HAWC2 simulations were fed to a discrete 6-DOF drive-train model in SIMPACK to examine the component loading and response behaviour. The response variables studied include shaft displacements, forces due to unbalanced magnetic pull and the main bearing loads. A comparison with land-based system was useful in making the following inferences:

- There is only a marginal variation of the mean, standard deviation and maximum values of bending moments and torques for the FWTDD system. This implies a negligible implication on power production.
- Additional shaft axial loads and shear loads were wave and pitch induced in the FWTDD system. Up to 35% increase in maximum axial loads were observed. This implied an increase in bearing loads.
- Shaft Displacements & Eccentricity: Axial increase in shaft displacements for the FWTDD system tends to vary linearly with shaft loads and were mostly wave and pitch induced. Radial displacements (hence eccentricity) tend to increase linearly with wind speeds, yet the FWTDD system does not bring about any significant increases to these values. Also the possibility of air-gap closure did not arise with the FWTDD system.

- Forces due to UMP : Forces due to UMP generally increased with wind speeds and are consisitent with the linear eccentricity model that was assumed. The FWTDD system does not increase these forces considerably.
- Bearing loads: Up to 25% increase in bearing axial loads were observed for the FWTDD system. The forces due to UMP, despite acting as a negative spring do not escalate the bearing radial loads.
- Bearing life : There is a subtle shift in the loading behaviour for bearings for the FWTDD system. Initial results suggest that bearing life expectancies are expected to reduce by an average of 6.2% to 11.5% when operating on the FWTDD system. Yet the bearings are expected to be sufficiently durable for the intended wind class of operation**.**

In summary, the initial model studies and investigations on the dynamics of the direct-drive generator model technically favour the implementation to a floating spar-buoy wind turbine. It is expected that the extra investment on the structural requirements will be outweighed by superior performance and increased reliability with the direct-drive generator.

Chapter 8

Conclusions and Recommendations for further work

8.0 General

Floating wind turbines are being considered a potential technology option in expanding the horizons of offshore wind energy, yet several design challenges still confront their successful development and deployment. Understanding the interactions that exist between the various elements of the FWT calls for a cross-disciplinary research investigation. Published literature revealed some knowledge gaps particularly with regard to hydrodynamic modelling, response prediction and drive-train dynamics. The need for improved mooring line models and lack of public information on the performance of drive-trains for FWTs were the main motivations for this research.

This research work was primarily undertaken to provide a better understanding of the coupled hydrodynamic behaviour through enhanced mooring line model and examine the prospects of direct-drive generators as a possible drive-train candidate for spar buoy type FWT. The research was carried out in three-parts involving experimental testing, numerical modelling and simulations applying the relevant effects of loading due to hydrodynamics, aerodynamics and servo-elastic effects wherever appropriate. Overall, every part of the research accomplished the tasks that were set out and achieved the aims reasonably well within the timeframe. The following sections provide a synoptic outline of each part, including major findings and also suggest on possible directions for further research.

8.1 Part - I

The first phase of the research was initiated by physical model testing of a 1:100 scale model of a stepped-spar buoy wind turbine in the university's curved wave tank for regular and irregular uni-directional sea states. A four-point mooring configuration was chosen to examine possible reductions in responses. Wave

elevation profiles were measured and motion responses of the spar for surge, heave and pitch were recorded at two locations, namely at the centre of gravity and at the nacelle. Response amplitude operator (RAO) was used to quantify the hydrodynamic behaviour in both sea states. The experimentally determined hydrodynamic response was reproduced by numerical simulations for similar wave conditions in OrcaFlex, a FEM-based dynamic time-domain mooring analysis software. Results of a validation exercise (as presented in Chapter 5) have contributed to new knowledge and an improved understanding in the following ways:

- Improved hydrodynamic model: The FEM-based hydrodynamic model of the spar buoy FWT in Orcaflex was superior to quasi-static line representations in better capturing the non-linearities as well as contributions to damping from mooring lines. A close agreement with experimental results gives the confidence to rely on the FEM based approach to carry out further investigations or implement design changes.

- Model feasibility and RAO approach: Motion response of the spar buoy model was presented as RAOs for both regular and irregular sea states. This serves as a more useful design metric since for any given sea state it is easier to interpret the response characteristics from the RAO values presented in this study. Lower dynamic pitch and heave response was observed for wave heights up to 9m confirming the stability of the platform and feasibility of the stepped-spar design.

- Four-point mooring: Significant reduction in surge motions was observed with the four-point mooring suggesting greater damping from the mooring lines. This configuration could be considered as a potential design alternative to the three-point approach.

- A new design parameter and design approach: This study introduced a new approach to evaluation of the hydrodynamic response by examining the coupled response at the centre of mass as well as the nacelle. This led to the formulation of a new design parameter-Nacelle Magnification Factor (NMF) that can help accurately describe the coupled dynamic behaviour of the spar type wind turbine. This could potentially encourage a new design approach to optimising floating wind turbine systems for a given hub height.

8.2 Part - II

Part-II of the research shifted the focus of research to drive-trains for FWTs. Review of past literature showed that drive-train performance in FWTs is a less researched topic. So far, only geared drives have been studied with FWTs, with results showing greater fatigue loading and a high risk of failure. Direct-drive generators were identified as a potential alternative. A radial flux topology of the direct-drive permanent magnet synchronous generator was examined to verify its suitability and any special design considerations for its successful integration with a FWT. The design was qualified based on its ability to maintain a stable air-gap and ensure minimal overall impact. This part of research required more than five separate simulation tools involving finite element methods for structural and electromagnetic analysis, multi-body method for simulating nacelle motions and combined aero-hydro-servo elastic interactions. The major research contributions and findings from Part- II are summarised as follows:

- Generator design: Air-gap management is critical when designing direct-drive generators for a FWT. The structural and mechanical design of a direct-drive generator must be able to cope with two sources of air-gap instability in a FWT. These include instabilities induced by structural deflection or /as well as shaft misalignment (bearing compliance).
- Platform design: For the parked rotor condition, nacelle accelerations $< 0.3g$ do not affect the structural stability of a generator with sufficiently high shaft support stiffness. This confirmed the adequacy of platform design.
- New analytical tools: New analytical tools were developed to compute the magnetic force distributions for eccentric condition caused by external loads. These tools employ a new approach that combines the results of structural and electromagnetic finite element models of the generator.
- Stiffness: Generator structural stiffness must be sufficiently high to overcome the secondary deflection due to eccentricity. A higher bearing stiffness is also necessary to limit the shaft induced eccentricity to acceptable levels. The decision on optimal bearing stiffness must therefore be a compromise with generator support structure stiffness in order to limit the overall eccentricity to

10%. This encourages a potentially new approach to generator structural optimisation.

- Air-gap management: The need to comply with 10% deflection criteria pushes the generator mass significantly, imposing greater structural demand on FWT. Generators with large air-gap can be a potential solution with cost penalty.
- New design philosophy: The biggest challenge of implementing direct-drive-generators would be limiting their weight and also costs at acceptable performance without compromising air-gap tolerances or tower/foundation upgrades. This calls for a new design philosophy that incorporates the knowledge of the drive-train technology in the foundation design and vice-versa.

8.3 Part - III

The final and concluding part of research was aimed at exploring further challenges and opportunities in implementing the direct-drive model for floating wind turbines. This required a good understanding of the drive-train behaviour and the various processes that control it. For this purpose, preliminary specifications were developed for a fully coupled aero-hydro-servo-elastic model of a 5MW FWT supporting a direct-drive generator (termed as FWTDD). This exercise yet again highlighted the weight challenge imposed by direct-drive system, making it difficult to achieve the same draft as that of a geared system. Yet, minimal alterations to tower-foundation design were ensured by making a few practical design adjustments. The control algorithm had to be radically different because of the high torque operation. The behaviour of the developed model was tested using multi-body simulation code, HAWC2. The resonance properties and motion response were consistent with typical response characteristics observed for a spar buoy wind turbine.

As the next step, internal dynamics of the drive-train was analysed using a linear combination of multi-body simulation tools namely HAWC2 and SIMPACK. The global motion response and main drive-shaft loads from HAWC2 simulations were fed to a detailed 6DOF drive-train model in SIMPACK to examine the component loading and reaction. The multi-body model simulated generator reaction using a simplified linear UMP model that was introduced in Part-II. The response variables

studied include eccentricity due to shaft displacements, forces due to unbalanced magnetic pull and the main bearing loads. The results were comparable with land-based system and corroborate the following inferences

- Torque : The torque response statistics were found to resemble closely with the land based system implying a negligible implication to power production
- Shaft loads: Main shaft axial and shear loads are increased by wave excitations and platform motions suggesting greater axial bearing loads.
- Eccentricity and UMP: Shaft axial displacements vary linearly with shaft axial loads while radial displacements(eccentricity) and hence Unbalanced magnetic pull(UMP) increase linearly with wind speeds. The platform motions and shaft loads in a FWTDD system do not necessarily increase eccentricity,UMP or cause the air gap to close.
- Bearing loads: There is a subtle shift in the loading behaviour of bearings for the FWTDD system when compared to land-based wind turbine.The contributions of UMP to bearing radial loads was limited by a large value of stiffness ratio.
- Bearing life : Initial results suggest that bearing life can be reduce by up to 11.5% when operating on the FWTDD system. Despite a marginal increase in loads, the bearings in FWTDD system are expected to be sufficiently durable for the intended wind class of operation.
- Overall, the dynamics of direct-drive generator system demonstrated a linear trend as predicted by HAWC2 model. Thus, it would be logical to consider HAWC2 model to provide an initial impression of the drive-train behaviour.

The initital results of the research established that with only a marginal increase in loads compared to land-based turbine, the direct-drive system is a clear opportunity to demonstrate greater reliability compared to gear-driven FWTs. It is expected that any additional capital investments (on structural requirements) for the FWTDD system will be outweighed by the superior performance with the direct-drive generator. To sum up, the research supports the implementation of direct-drive-generator for the spar–buoy FWTs. Interpretation of results for other configurations must be done with care and good sense of engineering judgment.

8.4 Recommendations for further work

Part-I of this research re-iterated the feasibility of the stepped-spar concept. Yet, there is scope for design optimisation for a given hub height using the NMF approach. Further research must be done with careful consideration of other loads for eg: wind loads, control system action. The FEM based mooring line model is shown to be accurate in representing the coupled hydrodynamic behaviour at reasonable modelling and simulation time. Fully coupled dynamic model including wind and control system action similar to the approach proposed in[64] can be useful in providing greater insight. A detailed investigation on four-point mooring configuration, including line loading characteristics can be useful to ascertain the response improvement reported in this study.

This study adopted the conventional approach for assessing offshore structures assuming the wave fields to be 2-dimensional, long-crested and uni-directional. As the performance, design and control implications of FWTs are highly sensitive to system orientation and directionality of the loads acting on them, further research must include an accurate depiction of the sea state, for eg: short-crested seas providing additional data on the coupled dynamic responses of the system in non-prominent wind-wave directions, which are inherently neglected in long crested wave modelling. The effect of wave directionality can provide new inputs to design optimization and may lead to significant savings in construction costs.

Part-II of this research independently examined the eccentricity effects from structural deflection and shaft displacement. In reality, these effects co-exist, hence the true-air gap behaviour of a direct-drive generator for a FWT may be different from what was predicted by this study. For a more accurate assessment of air-gap behaviour and component durability, further research must attempt to couple the generator structural model to a multi-body model. This will also permit a more comprehensive analysis of generator structural behaviour considering the effect of rotor rotation and control system action on fatigue assessment.

Apart from the deflection criteria, the assessment of structural requirements of a direct-drive generator for a FWT system must account for the overall stability of the

system. The results also showed that bearing stiffness is a key design variable that has to be carefully chosen to limit the overall eccentricity to below 10%. Future studies aimed at generator structural optimisation must factor the effect of bearing compliance to be able to provide a better idea on the generator structural requirements.

Part-III of this research provided a greater understanding of the electromechanical reaction at the generator considering the torsional and translational responses of its mechanical components in response to aero-hydro-servo-elastic loading. At the same time, this has opened up opportunities for carrying out further detailed investigations that are identified as follows:

- The influence from secondary responses(eg: generator structural deflection due to UMP) on air-gap can provide more information on detailed dynamic behaviour.
- In computing the electromechanical reaction at the generator, a simplified linear eccentricity model was used for computing the forces due to UMP. Further research must replace the linear model assumption to include for the non-linearities due to shaft tilting.
- The behaviour of the drive-train was investigated for the normal operating conditions of the wind turbine. Further research must investigate the remaining IEC design load cases, analyse possible generator excitation caused by grid related events.
- Bearing lifetimes predicted in this study are approximate and are based on simplified life models. More accurate estimates on reliability must be based on improved bearing models that take into account the effect roller misalignments, coupled axial-radial-bending effects, lubrication condition, operating temperature, etc.
- Detailed resonance analysis may be performed to assess the possibility of harmful excitations. Further, the implications on power production and economies of building such a system can provide a more accurate picture.

8.5 Summary

This research identified and examined two research problems of a spar-buoy FWT by systematic investigation. First, the hydrodynamic behaviour of a spar buoy model was tested and validated by improved mooring model. The results highlighted the superiority of the presented model over conventional quasi-static approach and encouraged a new approach for response prediction and optimisation. Subsequently, the prospects of a direct-drive generator were examined for the spar-buoy FWT. The results highlighted the structural design challenge and the importance of air-gap management with this type of machine. With a marginal increase in loading and relatively similar dynamics as that of a land-based wind turbine, direct-drive generators can be a potential alternative to gear driven FWTs.

Overall, the aims of the research have been achieved reasonably well; the results presented in this research have contributed to newer knowledge in the understanding of the hydrodynamics and drive-train dynamics of the spar-buoy FWT. It is believed that the solutions and recommendations proposed through this research and can potentially help address the design challenges of FWTs.

Bibliography

[1] BP Energy Outlook 2035,Available from: http://www.bp.com/content/dam/bp/pdf/Energy-economics/Energy-Outlook/Energy_Outlook_2035_booklet.pdf, Accessed:January 2014.

[2] Ren21,RENEWABLES 2012 GLOBAL STATUS REPORT,2012.

[3] European Wind Energy Association,The European offshore wind industry - key trends and statistics 2013,2014.

[4] M. Schwartz, D. Heimiller, S. Haymes, W. Musial, Assessment of Offshore Wind Energy Resources for the United States. National Renewable Laboratory. Technical Report NREL/TP-500-45889,2010.

[5] EEA,Europe's onshore and offshore wind energy potential. An assessment of environmental and economic constraints,Technical report No 6/2009,2009.

[6] The Offshore Valuation Group,A valuation of the UK's offshore renewable energy resource,All-Energy 2010 Conference,Aberdeen,UK,19-20 May 2010.

[7] Global Wind Energy Council, Global Offshore: Current Status and Future Prospects,Available from: http://www.gwec.net/global-offshore-current-status-future-prospects/, Accessed:May 2013.

[8] Offshore Windfarms Map,Available from: http://www.lorc.dk/offshore-wind-farms-map, Accessed:February 2013.

[9] from: http://www.4coffshore.com/offshorewind/, Accessed:January 2014.

[10] from: http://www.oceanweather.com/data/, Accessed:December 2013.

[11] J. Bard,HiPRWind. Large floating wind turbines for intermediate water depths, Wind power R&D Seminar- Deep Sea Offshore wind Trondheim, Norway,20-21 January, 2011.

[12] Hywind – the world's first full-scale floating wind turbine,Available from: http://www.statoil.com/en/TechnologyInnovation/NewEnergy/RenewablePowerProduction/Offshore/Hywind/Pages/HywindPuttingWindPowerToTheTest.aspx, Accessed:May 2013.

[13] from: http://www.bluehgroup.com/, Accessed:January 2013.

[14] from: http://www.principlepowerinc.com/products/windfloat.html, Accessed:May 2013

[15] C. Cermelli, A. Aubault, D. Roddier,Qualification of a Semi-Submersible Floating Foundation for Multi-Megawatt Wind Turbines,OTC-20674-PP,Offshore Technology Conference,2010.

[16] E. Balogh, Deepwater Offshore Wind Power Generation Using Oil and Gas Platform Technology,Available from: http://www.renewableenergyworld.com/rea/news/article/2008/12/deepwater-offshore-wind-power-generation-using-oil-and-gas-platform-technology-54314, Accessed:May 2013.

[17] B.W. Byrne, G.T. Houlsby,Assessing Novel Foundation Options for Offshore Wind Turbines,World Maritime Technology Conference London, UK,March 2006.

[18] B.Andersen, A Comparison of Two and Three Bladed Floating Wind Turbines,M.S Thesis,University of Toledo,2010.

[19] M. Brommundt, L. Krause , K. Merz, M. Muskulus, Mooring System Optimization for Floating Wind Turbines using Frequency Domain Analysis, Energy Procedia, (2012).24, pp.289–296.

[20] A.Cordle, J. Jonkman,State-of-the-art in design tools for floating offshore wind turbines,Proceedings of the Twenty-first (2011) International Offshore and Polar Engineering Conference,Maui, Hawaii,19 – 24 June, 2011.

[21] J.M.Jonkman, Dynamics modeling and loads analysis of an offshore floating wind turbine,PhD Thesis,University of Colorado-Boulder,2007.

[22] Y.H. Bae, M.H. Kim, S.W. Im, I.H. Chang,Aero-Elastic-Control-Floater-Mooring Coupled Dynamic Analysis of Floating Offshore Wind Turbines,Proceedings of the Twenty-first (2011) International Offshore and Polar Engineering Conference,Maui, Hawaii,19 – 24 June, 2011.

[23] Bureau Veritas,Classification and Certification of Floating Offshore Wind Turbines.NI 572 DT R00 E,2010.

[24] ABS, Guide for building and classing Floating Offshore Wind Turbine Installations,Available from: http://www.eagle.org/eagleExternalPortalWEB/ShowProperty/BEA%20Repository/Rules&Guides/Current/195_FOWTI/Guide, Accessed:May 2013.

[25] T. Utsunomiya, S. Yoshida, H. Ookubo, I. Sato, S. Ishida,Dynamic Analysis of a Floating Offshore Wind Turbine Under Extreme Environmental Conditions,31st International Conference on Ocean, Offshore and Arctic Engineering,Rio de janeiro, Brazil,1-6 July 2012.

[26] M. Karimirad, T. Moan, Extreme Dynamic Structural Response Analysis of Catenary Moored Spar Wind Turbine in Harsh Environmental Conditions, Journal of Offsore Mechanics and Arctic Engineering, (2011).133, (4), pp.14 pages.

[27] C. Watanabe, Floating Windmills in Japan Help Wind Down Nuclear Power: Energy,Available from: http://www.bloomberg.com/news/2012-03-29/floating-windmills-in-japan-help-wind-down-nuclear-power-energy.html. , Accessed:May 2013.

[28] T.J. Larsen , T.D. Hanson, A method to avoid negative damped low frequency tower vibrations for a floating pitch controlled wind turbine, Journal of Physics.; Conference Series 75., (2007).

[29] A. Myhr, K.J. Maus, T.A. Nygaard,Experimental and computational comparisons of the OC3-hywind and tension-leg-buoy (TLB) floating wind turbine conceptual designs,Proceedings of the Twenty-first (2011) International Offshore and Polar Engineering Conference,Maui, Hawaii,19-24 June 2011.

[30] L.Wang, B. Sweetman,Conceptual Design of Floating Wind Turbines with Large-Amplitude Motion., In SNAME Annual Meeting,Houston,2011.

[31] K. C. Tong, Technical and economic aspects of a floating offshore wind farm, Wind Engineering and Industrial Aerodynamics :, (1998).(74-76), pp.399-410.

[32] T. Seebai, R. Sundaravadivelu, C.P. Vendhan,Model studies on spar platform with 5MW wind turbine,ASME 2009 28th International Conference on Ocean,Offshore and Arctic Engineering (OMAE2009),Honolulu,Hawaii,31May–5 June 2009.

[33] H. Suzuki, A. Sato,Load on turbine blade induced by motion of floating platform and design requirement for the platform,ASME 2007 26th International Conference on Offshore Mechanics and Arctic Engineering (OMAE2007),San Diego, California, USA,2007.

[34] T. Utsunomiya, T. Sato, H. Matsukuma, K. Yago,Experimental validation for motion of a spar-type floating Offshore wind turbine using 1/22.5 scale model,ASME 2009 28th International Conference on Ocean,Offshore and Arctic Engineering (OMAE2009),Honolulu, Hawaii,31May–5 June 2009.

[35] T. Seebai, R. Sundaravadivelu,Effect of Taut and Catenary Mooring on Spar Platform with 5MW Wind Turbine, In Proceedings of the Eighth (2009) ISOPE Ocean Mining Symposium,Chennai,2009.

[36] T. Utsunomiya, E. Nishida, I. Sato,Wave response experiment on SPAR-type floating bodies for offshore wind turbine,In Proceedings of the Nineteenth International Offshore and Polar Engineering Conference,Osaka,Japan,21-26 June 2009.

[37] A. N. Robertson, J.M. Jonkman,Loads Analysis of Several Offshore Floating Wind Turbine Concepts Proceedings of the Twenty-first (2011) International Offshore and Polar Engineering Conference,Maui, Hawaii,19-24 June 2011.

[38] T. Utsunomiya, H. Matsukuma, S. Minoura, K. Ko, H. Hamamura, O. Kobayashi, I. Sato, Y. Nomoto, K. Yasui,On Sea experiment of a hybrid spar for floating offshore wind turbine using 1/10 scale model,ASME 2010 29th International Conference on Ocean, Offshore and Arctic Engineering (OMAE2010),Shanghai, China,6-11 June 2010.

[39] from: http://www.sway.no/, Accessed:May 2013.

[40] T.Ishihara, Fukushima Floating Offshore Wind Farm Demonstration Project (Fukushima FORWARD),Available from: http://windeng.t.u-tokyo.ac.jp/ishihara/posters/2012_digest.pdf, Accessed:May 2013.

[41] M. J. Muliawan, M. Karimirad, T. Moan, Dynamic response and power performance of a combined Spar-type floating wind turbine and coaxial floating wave energy converter Renewable Energy, (2013).vol. 50, pp.pp. 47-57.

[42] S. Lee, Dynamic response analysis of spar buoy floating wind turbine systems,M.S. Thesis,Massachusetts Institute of Technology,2008.

[43] L.B. Savenije, Modeling the dynamics of a spar-type floating offshore wind turbine,MSc Thesis,Delft University of Technology,2009.

[44] J.R.Browning, J. Jonkman, A. Robertson, A.J. Goupee,Calibration and validation of a spar-type floating offshore wind turbine model using the FAST dynamic simulation tool,The Science of Making Torque from Wind,Oldeburg, Germany,9-11 October,2012.

[45] J.M. Jonkman, M.L. Buhl Jr,Loads Analysis of a Floating Offshore Wind Turbine Using Fully Coupled Simulation,WindPower 2007 Conference & Exhibition Los Angeles, California,3-6June 2007.

[46] M. Karimirad, Stochastic dynamic response analysis of spar-type wind turbines with catenary or taut mooring systems,PhD Thesis,Norwegian University of Science and Technology,2011.

[47] J.M Jonkman,Definition of the Floating System for Phase IV of OC3. NREL Technical Report NREL/TP-500-47535 May 2010.

[48] K.H. Lee, Responses of floating wind turbines to wind and wave excitation,M.S Thesis,Massachussettes Institute of Technology,2005.

[49] Y. Shigeyuki, Power generation assemblies, in: WIPO, IPC: F03D, 2005.

[50] E. Borgen, Floating Wind Power in Deep Water –Competitive with Shallow-water Wind Farms?,Available from: www.sway.no/publish_files/Borgen_2010.pdf, Accessed:May 2013.

[51] Y.Xing, M. Karimirad, T. Moan,Effect of Spar-Type Floating Wind Turbine Nacelle Motion on Drivetrain Dynamics,In Proceedings of EWEA 2012 Annual Event,Copenhagen, Denmark,16-19 April 2012.

[52] Y. Xing, M. Karimirad, T. Moan, Modelling and analysis of floating spar-type wind turbine drivetrain, Wind Energy, (2012).(DOI: 10.1002/we.1590), pp.1-23.

[53] M.I.Kvittem, T. Moan,Effect of Mooring Line Modelling on Motions and Structural Fatigue Damage for a Semisubmersible,Proceedings of the Twenty-second (2012) International Offshore and Polar Engineering Conference (ISOPE),Rhodes, Greece,17-22June 2012.

[54] T. Ishihara, M.B. Waris, K. Kagaya,Dynamic response prediction of floating offshore wind turbine system using fully nonlinear model,EWEA OFFSHORE 2011,Amsterdam, Holland 29 November-1 December 2011.

[55] B. Skaare, T.D. Hanson, F.G. Nielsen, R. Yttervik, A.M. Hansen, K. Thomsen , T.J. Larsen,Integrated Dynamic Analysis of Floating Offshore Wind Turbines,European Wind energy Conference and Exhibition,Milan,7-10 May 2007.

[56] Min-su Kim, Kang-Su Lee, Mann-Eung Lim, H. Shin,Motion Analysis and hydrodynamic force calculation of the 5MW Spar-type floating offshore wind turbine,EWEA Offshore 2011,Amsterdam, The Netherlands,2011.

[57] H.Shin,Model test of the OC3-hywind floating offshore wind turbine,Proceedings of the Twenty-first (2011) International Offshore and Polar Engineering Conference,Maui, Hawaii,19-24 June 2011.

[58] FAST(Fatigue, Aerodynamics, Structures and Turbulence),Available from: http://wind.nrel.gov/designcodes/simulators/fast/, Accessed:February 2013.

[59] S.Gueydon, W. Xu,Floating wind turbine motion assessment,OCEANS'11 MTS/IEEE KONA,Kona, Hawaii,19-22 September 2011.

[60] aNySIM-Time Domain Analysis of Multi Body Dynamics for Offshore Operations,Available from: http://www.marin.nl/web/Facilities-Tools/Software/Offshore-Multibody-Software.htm, Accessed:February 2013.

[61] J.A.Azcona Armendariz, X. Munduate Echarri, D. Merino Hoyos, T.A. Nygaard,Dynamic simulation of mooring lines for floating wind turbines EAWE PhD Seminar on Wind Energy in Europe,TUDelft, Denmark,27-28 October 2011.

[62] B. S. Kallesoe, U.S. Paulsen, A. Kohler, C.H. Hansen,Aero-Hydro- Elastic response of a floating platform supporting several wind turbines,in 49th AIAA Aerospace Sciences Meeting,Orlando, Florida,2011.

[63] M. Hall, B. Buckham, C. Crawford, R.S. Nicoll,The importance of mooring line model fidelity in floating wind turbine simulations,In OCEANS'11 MTS/IEEE KONA,Kona, Hawaii,19-22 September 2011.

[64] M. Masciola, A. Robertson, J.M. Jonkman, F. Driscoll,Investigation of a FAST-OrcaFlex Coupling Module for Integrating Turbine and Mooring Dynamics of Offshore Floating Wind Turbines,2011 International Conference on Offshore Wind Energy and Ocean Energy,Beijing,China,31 October – 2 November 2011.

[65] E. Kreuzer, U. Wilke, Mooring Systems—A Multibody Dynamic Approach, Multibody System Dynamics, (2002).8, (3), pp.279-296.

[66] D. Matha, S. Hauptmann, T. Hecquet, M. Kühn,Methodology and Results of Loads Analysis of Wind Turbines with Advanced Aeroelastic Multi-Body Simulation, DEWEK,Bremen, Germany,2010.

[67] J.M.J. Journée, J.Pinkster,Lecture on Introduction in Ship Hydromechanics.Delft University of Technology,2002.

[68] T.Perez, Ship Motion Control: Course Keeping and Roll Stabilisation Using Rudder and Fins, Springer, 2005.

[69] T.Perez, M. Blanke,Simulation of Ship Motion in Seaway,Technical Report EE02037.Dept. of Electrical and Computer Engineering, The University of Newcastle, NSW,2308, Australia.

[70] The Crown Estate, UK Market Potential and Technology Assessment for floating offshore wind power. An assessment of the commercialization potential of the floating offshore wind industry,Available from: http://www.thecrownestate.co.uk/media/428739/uk-floating-offshore-wind-power-report.pdf, Accessed:February 2013.

[71] E.Hau, Wind turbines: Fundamentals, technologies, Application and Economics, Springer-Verlag Berlin Heidelberg, 2006.

[72] D. McGahn, Drivetrains: Direct Drive Generators, High Temperature Superconductor Based Machines,Available from: http://web.mit.edu/windenergy/windweek/Presentations/P7%20-%20McGahn.pdf, Accessed:February 2013.

[73] from: http://www.goldwindamerica.com/technology-capabilities/pmdd/, Accessed: February 2013.

[74] U.S Department of Energy,Advanced Wind Turbine Drivetrain Concepts: Workshop report,29-30 June 2010.

[75] from: http://www.strompass.de/fileadmin/offshore/documents/Technik/Vestas_V120.pdf, Accessed:April 2013.

[76] from: http://www.areva-wind.com/1/m5000/concept/. Accessed:Feb 2013.

[77] N.Luo,Smart Structural Control Strategies for the Dynamic Load Mitigation in Floating Offshore Wind Turbines,presented at the 6th International Workshop on Advanced Smart Materials and Smart Structures Technology ANCRiSST2011, Dalian, China,25-26 July 2011.

[78] Emerging Opportunities Direct Drive Wind Turbine Market Globally: Breakdown by Technology, Geography, Product and Market Share Analysis.,Available from: http://www.researchandmarkets.com/research/g9r28z/emerging_opportuni, Accessed:July 2013.

[79] Boulder Wind Power,Advanced Gearless drivetrain-Phase I Technical report U.S. DOE Wind and Water Power Program,August 2012.

[80] E. De Vries,Development of two-bladed offshore wind turbine.Windstats Report.Vol. 24, No. 2. Spring 2011 ISSN 0903-5648,2011.

[81] JSW wind turbine system-2MW Permanent magnet synchronous gearless wind turbine generator.,Available from: http://www.jsw.co.jp/en/product/ecology/wind/pdf/JSWJ82_E.pdf. , Accessed:July 2013.

[82] Vannuci(RINA Industry), D., ORECCA.WP3 Technologies state of the Art,Available from: http://www.orecca.eu/c/document_library/get_file?uuid=144f87d6-c41a-4a04-8742-7ebdc88f5a5c&groupId=10129, Accessed:April 2013.

[83] The Hywind O&M Team, Hywind: Two years in operation, what have we learnt and where are we going?,presented at Deep Sea Offshore Wind R&D Seminar,Trondheim, Norway,19th January 2012.

[84] from: http://www.gepower.com/prod_serv/products/wind_turbines/en/downloads/Offshore%20Brochure_GEA18111_wind4.0broch_LR.pdf, Accessed:July 2013.

[85] H. Polinder, F.F.A. Van der Pijl, G.J. de Vilder, P.J. Tavner, Comparison of direct-drive and geared generator concepts for wind turbines, IEEE transactions on energy conversion, 21 (3), pp.pp. 725-733.

[86] H. Li, Z. Chen, Overview of different wind generator systems and their comparisons, IET Renewable power generation, (2007).

[87] Z. Zhang, A. Matveev, S. Ovrebo, R. Nilssen, A. Nysveen,The state of art in Generator Technology for Offshore wind energy conversion systems,IEEE International Electric Machines & Drives Conference(IEMDC),2011.

[88] Y. Amirat, M. Benbouzid, B. Bensaker, R. Wamkeue, State of art of generators for wind energy conversion systems, Electromotion, (2007).14, (4), pp.163-172.

[89] H. Li, Z. Chen, H. Polinder, Research report on numerical evaluation of various variable Speed wind generator systems .Upwind Deliverable No.:D1B2.b.3.,Available from: www.upwind.eu/media/817/Deliverable_1B2.b.3.pdf., Accessed:July 2013.

[90] R.Poore, T. Lettenmaier,Alternative Design Study Report: WindPACT Advanced Wind Turbine Drive-train Designs Study. NREL/SR-500-33196.,August 2003.

[91] P. Jordan, J.C. Wheals,Technology Innovations and Reliability Improvement for Offshore Wind Drive-trains,presented at the 4th China Wind Power Conference and exhibition,Beijing, China,19-21 October 2011.

[92] F. Viadero, A.F. Del Rincon, E. Liaño, M.A. Serna, M.A. Diaz, Dynamic Analysis of an Offshore Wind Turbine Drivetrain on a Floating Support, Condition Monitoring of Machinery in Non-Stationary Operations, (2012).pp.627-634.

[93] Dr.J. Coultate, Wind Turbine Drive technology and cost drivers,Available from: http://www.supergen-wind.org.uk/docs/presentations/4th_Seminar_Presentations/John Coultate_Romax.pdf, Accessed:July 2013.

[94] J.N. Stander, G. Venter, M.J. Kamper, Review of direct drive radial flux permanent magnet generator mechanical design, Wind Energy (April 2012).15, (3), pp.459-472.

[95] S. Eriksson, H. Bernoff, Generator damped torsional vibrations of a vertical axis wind turbine, Wind engineering, (2005).29, (5), pp.449-462.

[96] Z. Zhang, A. Matveev, S. Ovrebo, R. Nilssen, A. Nysveen,State of the Art in Generator Rechnology for Offshore Wind Energy Conversion Systems,2011 IEEE International Electric Machines & Drives Conference(IEMDC),Canada,15-18 May 2011.

[97] J.D. Brostmeyer, J.E. Ryznic Jr, J.W. Wilson, Vertical axis wind turbine with direct-drive generator, in: U.S. Patent 7893556, 22 Feb 2011.

[98] H. Akimoto, J. Tanaka, J. Uzawa, Floating axis wind turbines for offshore power generation- a conceptual study. , Environmental Research letters 6(October-December 2011) 044017, (2011).

[99] D.L. Blonk, Conceptual design and evaluation of economic feasibility of floating vertical axis wind turbines,Msc Thesis,Delft University of technology, Denmark,2010.

[100] K. Leban, E. Ritchie, A. Argeseanu,Design Preliminaries for Direct Drive underWater Wind Turbine Generator,XXth International Conference on Electrical Machines (ICEM),Marseille, 2-5 Sept. 2012.

[101] M. Cahay, E. Luquiau , C. Smadja , F. Silvert,Use of a Vertical Wind Turbine in an Offshore Floating Wind Farm,Offshore Technology Conference,Texas, USA,2–5 May 2011.

[102] U.S. Paulsen, L. Vita, H.A. Madsen, J. Hattel, E. Ritchie, K.M. Leban, P.A. Berthelsen, S. Carstensen, 1st DeepWind 5 MW baseline design, Energy Procedia.Elsevier, 24 pp.27-35.

[103] E. Triantaphyllou, B. Shu, S.N. Sanchez, Multi-Criteria Decision Making: An Operations Research Approach, Ray,T., (J.G. Webster, Ed.), John Wiley & Sons, New York, 1998.

[104] M.R. Dubois, H. Polinder, J.A. Ferreira,Comparison of generator topologies for direct-drive wind turbines,Nordic Countries Power & Industrial Electronics Conference,Aalborg, Denmark,June 2000.

[105] M.Henriksen, B.B. Jensen,Induction generators for direct-drive wind turbines 2011 IEEE International Electric Machines & Drives Conference (IEMDC),Niagara Falls, Ontario,15-18 May 2011.

[106] Direct Drive (Gearless) Wind Turbine Market, By Permanent Magnet (PMSG) & Electrically Excited (EESG) Generator Technology, Turbine Size/Capacity Range – Global Trends & Forecasts to 2017,Available from: http://www.marketsandmarkets.com/Market-Reports/direct-drive-gearless-wind-turbine-market-805.html, Accessed:July 2013.

[107] D. McMillan, G.W. Ault, Techno-economic comparison of operational aspects for direct drive and gearbox-driven wind turbines, IEEE transactions on energy conversion (March 2010).25, (1), pp.191-198.

[108] Wangxiangming, Permanent Magnet Direct Drive technology: A case study of Goldwind's 2.5 MW,Available from: www.all-energy.com.au/userfiles/file/Wang-Xiangming-131011.pdf, Accessed:July 2013.

[109] A. Zavvos, A.S. McDonald, M.A. Mueller, Optimized mechanical structures of direct-drive generators. Upwind Research report (Deliverable No.: D 1B2.b.5),Available from: http://www.upwind.eu/media/823/Deliverable_1B2.b.5.pdf, Accessed:July 2013.

[110] G.Shrestha, H. Polinder, D. Bang, J.A. Ferreira, Structural Flexibility: A Solution for Weight Reduction of Large Direct-Drive Wind-Turbine Generators, IEEE Transactions on Energy Conversion, (2010).25, (3), pp.732-740.

[111] D. Bang, H. Polinder, G. Shrestha, J.A. Ferreira,Review of generator systems for direct drive wind turbines,2008 European Wind Energy Conference,Brussels,April 2008.

[112] A. Aleksashkin, A. Mikkola,Literature review on permanent magnet generators design and dynamic behaviour,2008.

[113] E. Spooner, P. Gordon, C.D. French, Lightweight, ironless-stator, PM generators for direct-drive wind turbines,Second International Conference on Power Electronics Machines and Drives (PEMD 2004),2004.

[114] E. Borgen,Introduction of the Sway Turbine ST10,IQPC 3rd International Conference Drivetrain Concepts for Wind Turbines,Germany,22-24 October 2012.

[115] H.A.Haslum, Umoe Olje og Gass, O.M. Faltinsen, Alternative Shape of Spar Platforms for Use in Hostile Areas,Offshore Technology Conference,Houston, Texas,3-6 May 1999.

[116] D. Rogers, G. Bolton King,Wave generation using Ocean and wave-Manual. Version 3.62.,1997.

[117] G. Payne, Guidance for the experimental tank testing of wave energy converters. University of Edinburgh. Version 01b.,Available from: www.supergen-marine.org.uk/drupal/files/reports/WEC_tank_testing.pdf, Accessed:July 2013.

[118] R. Pascal, J. Lucas, D. Ingram, I. Bryden,Assessing and Improving the Edinburgh Curved Wave Tank,Proceedings of the Nineteenth (2009) International Offshore and Polar Engineering Conference,Osaka, Japan,21-26 June, 2009.

[119] Qualisys Motion Capture, Qualisys product information,Available from: http://www.qualisys.com., Accessed:February 2013.

[120] G.S. Payne, J.R.M. Taylor, T. Bruce, P. Parkin, Assessment of boundaryelement method for modelling a free-floating sloped wave energy device. Part 2: Experimental validation, Ocean Engineering, (2008).35(3-4), pp.342–357.

[121] D. Rogers,WG8 wavegauge manual. Edinburgh Designs Ltd.,July 1997.

[122] LabVIEW System Design Software.,Available from: http://www.ni.com/labview/, Accessed:July 2013.

[123] R.R. Bannerman, A Conductivity Wave Gauge Calibration Device design,Available from: http://calibration-device.webege.com/index.html., Accessed:July 2013.

[124] Solid Edge V20.Solid Edge product information,Available from: http://www.plm.automation.siemens.com/en_us/products/velocity/solidedge/. Accessed:July 2013.

[125] OrcaFlex Manual,Available from: http://www.orcina.com/. Accessed:April 2013.

[126] H. Eriksson, T. Kullander,Assessing feasible mooring technologies for a Demonstrator in the Bornholm Basin as restricted to the modes of operation and limitations for the Demonstrator.,Feb 2013.

[127] M. Murai, R. Nishimura,A study on an experiment of behaviour of a SPAR type offshore wind turbine considering rotation of wind turbine blades,OCEANS'10 IEEE,Sydney,24-27 May 2010.

[128] K.H.Lee, Responses of floating wind turbines to wind and wave excitation,M.S Thesis,Massachusetts Institute of technology,2005

[129] M.J. Tucker, E.G. Pitt, Waves in Ocean engineering, Elsevier, 2001.

[130] O.M. Faltinsen, Sea loads on ships and offshore structures.1st ed. edn,Cambridge: Cambridge, UK: Cambridge University Press., 1990.

[131] S.F. Hoerner, Fluid Dynamic drag, Hoerner Fluid dynamics,NJ 08723, USA , Library of Congress 64-19666, 1965.

[132] J.N. Newman, Marine Hydrodynamics, Wei Cheng Cultural Enterprise Company, 1977.

[133] A.Grauers, Design of Direct-driven Permanent-magnet Generators for Wind Turbines,PhD Thesis,Chalmers University of Technology,1996.

[134] A.S. McDonald, M.A. Mueller, H. Polinder, Structural mass in direct-drive permanent magnet electrical generators, IET Renewable Power Generation. 2007, (2007).

[135] T.J. Larsen, A.M. Hansen,How 2 HAWC2, the user's manual Risø National Laboratory, Technical University of Denmark, Lyngby, Denmark,2012.

[136] SIMPACK.Welcome to SIMPACK,Available from: http://www.simpack.com/, Accessed: March 2013.

[137] D. Meeker, Finite Element Method Magnetics Version 4.2 User's Manual 16 October, 2010.

[138] A.S. McDonald, Structural analysis of low speed, high torque electrical generators for direct-drive renewable energy converters, PhD Thesis,The University of Edinburgh,2008.

[139] A. Zavvos, A.S. McDonald, M.A. Mueller,Electromagnetic and mechanical optimisation of direct-drive generators for Large Wind Turbines,The 5th International Conference on Power Electronics, Machines and drives Conference 2010,Brighton, UK,19-21 April 2010.

[140] D. Bang, Design of Transverse Flux permanent magnet machines for Large Direct-drive Wind Turbines,PhD Thesis,Delft University of Technology,Delft, The Netherlands,2010.

[141] A. Zavvos, A.S. McDonald, M.A. Mueller,Structural Optimisation tools for iron cored permanent magnet generators for large direct-drive wind turbines,Renewable Power Generation Conference (RPG 2011),Edinburgh, UK,6-8 September 2011.

[142] L. Fingersh, M. Hand, A. Laxson,Wind Turbine Design Cost and Scaling Model.NREL Technical Report. NREL/TP-500-40566,December 2006.

[143] Y.K. Chin, P. Kanninen, P. Maki-Ontto, R. Sakki, H. Lendenmann,Phenomenon of Magnetic Force in Permanent Magnet Wind Turbine Generators,International Conference on Electrical Machines and Systems. ICEMS 2009,2009.

[144] T. Wegiel,The model of permanent magnet synchronous machine for diagnostic purpose.Biblioteka Cyfrowa polytechniki Krakowskiej BPJ z.1-E/2008 ISSN 0011-4568,2008.

[145] A. Damaki, M. Mirsalim, M.F. Aghdaei, A simple Analytic method to Model and detect Non-Uniform Air-gaps in Synchronous Generators, Iranian Journal of Electrical & Electronic Engineering, (March 2010).6, (1), pp.29-35.

[146] A. Kallaste, A. Belahcen, A. Kilk, T. Vaimann,Analysis of Eccentricity in a Low-Speed Slotless Permanent-magnet wind generator,Proceedings of 8th International Conference 2012 Electric Power Quality and Supply Reliability,Tartu,11 – 13 June, 2012.

[147] G.R. Slemon, Electric Machines and Drives, Addison-Wesley Publishing Company Inc, 1992.

[148] H.Polinder, Frank F. A. van der Pijl, G.J. de Vilder, P.J. Tavner, Comparison of Direct-Drive and Geared Generator Concepts for Wind Turbines, IEEE Transactions on energy conversion, (2006).21, (3), pp.725-733.

[149] J.Shek, D.G. Dorrell, M. Hsieh, I-Hsien Lin, K. Mostafa, M.A. Mueller, Yu-Han Yeh,Unbalanced forces in electrical generators for wave and tidal devices,10th European wave and tidal energy Conference,Aalborg, Denmark,2-5 September 2013.

[150] SIMPACK Drivetrain Training - Modeling Elements I -Internal Communication,2012

[151] P.J. Tavner, E. Spooner,Light structures for Large Low-speed Machines for Direct-Drive Applications,International Conference on Electrical Machines (ICEM),September 2006.

[152] S. Butterfield, W. Musial, J. Jonkman, P. Sclavounos, Engineering Challenges for Floating Offshore Wind Turbines.NREL/CP-500-38776.,Copenhagen Offshore Wind Conference,Copenhagen, Denmark,26-28 October, 2005.

[153] D. Pavlik, V.K. Garg, J.R. Repp, J. Weiss, A finite element technique for calculating the magnet sizes and inductances of permanent magnet machines, IEEE Transactions on Energy Conversion, (1988).3, (1), pp.116-122.

[154] J.A. Stegmann, M.J. Kamper, Design Aspects of Double-Sided Rotor Radial Flux Air-Cored Permanent- magnet Wind Generator, IEEE Transactions on Industry Applications, (2011).47, (2), pp.767-778.

[155] A. Kallaste, T. Vaimann, O. Pabut,Slow-Speed Ring-shaped permanent magnet generator for wind applications,11th International Symposium on Topical Problems in the Field of Electrical and Power Engineering and Doctoral School of Energy and Geotechnology II,Parnu,2012.

[156] R.S. Longtin, P.L. Jansen, Wind turbine direct -drive air gap control method and system, in: US 7944074 B2, General Electric Company, 2011.

[157] R. Tsouroukdissian, Direct drive wind turbine and method for controlling an air gap,, in: US 20130134712 A1, Alstom Wind S.L.U, 2013.

[158] J.S. Smith, M.B. Jore, M.A. Kvam, D. Samsel, C.P. Butterfield Jr, B.J. Sullivan, J.D. Duford, Air gap control systems and methods, in: US (Ed.) US8362731 B2 Boulder Wind Power, Inc, 2013.

[159] G. Bywaters, P. Mattila, D. Costin, J. Stowell, V. John, S. Hoskins, J. Lynch, T. Cole, A. Cate, C. Badger, B. Freeman,Northern Power NW 1500 Direct-Drive Generator . NREL/SR-500-40177, October 2007.

[160] Germanischer Lloyd, Guideline for the Certification of Wind Turbines Edition 2010 in, Hamburg, Germany, 2010.

[161] T. Zacher, D. Witcher,Analysing drive train dynamics in coupled wind turbine simulations,Proceedings of the European Wind Energy Conference,Copenhagen, Denmark,16-19 April 2012.

[162] R. Rachholz, C. Woernle, J. Zierath,Dynamics of a Controlled Flexible Multibody Model of a 2 MW Wind Turbine,The 2nd Joint International Conference on Multibody System Dynamics,Stuttgart, Germany,29 May –1 June 2012.

[163] E.B.Smith, Nacelle Design for a 10MW reference wind turbine., M.S thesis. Thesis, NTNU,2012.

[164] J.Jonkman, S. Butterfield, W. Musial, G. Scott,Definition of a 5-MW Reference Wind Turbine for Offshore System Development. NREL/TP-500-38060 2009

[165] D.Bang, H. Polinder, Electromagnetic Optimization of Direct-drive generators. Upwind Deliverable No.: D 1B2.b.hp2,Available from: www.upwind.eu/media/832/Deliverable_1B2.b.hp2.pdf., Accessed:April 2013.

[166] from: http://www.mtoi.es/en/productos-y-servicios/index.aspx,

[167] E. Spooner, P. Gordon, C.D. French,Lightweight, ironless-stator, PM generators for direct-drive wind turbines,Second International Conference on Power Electronics, Machines and Drives(PEMD 2004),2004.

[168] M.B. Turi, C.S. Marks, Bearing selection techniques as applied to mainshaft direct and hybrid drives for wind turbines.TIMKEN technical paper,Available from:

http://www.whereyouturn.com/ja-jp/about/NewsRoom/MediaKits/Documents/MainShaftTechPaper.pdf, Accessed:July 2013.

[169] R. Melício, V.M.F. Mendes, J.P.S. Catalão, Wind Turbines with Permanent Magnet Synchronous Generator and Full-Power Converters: Modelling, Control and Simulation,Available from: www.intechopen.com/download/pdf/14814, Accessed:April 2013.

[170] L.Fingersh, M. Hand, A. Laxson,Wind Turbine Design Cost and Scaling Model. NREL/TP-500-40566.,2006.

[171] D.J. Malcolm , A.C. Hansen,WindPACT Turbine Rotor Design Study June 2000 — June 2002.NREL/SR-500-32495 Revised April 2006.

[172] H.J.T. Kooijman, C. Lindenburg, D. Winkelaa, E.L. Van der Hooft, DOWEC 6 MW Pre-Design: Aero-elastic modeling of the DOWEC 6 MW pre-design in PHATAS. DOWEC-F1W2-HJK-01-046/9,Available from: https://www.ecn.nl/fileadmin/ecn/units/wind/docs/dowec/10046_009.pdf, Accessed:February 2013.

[173] SolidWorks 2013,Available from: http://www.solidworks.com/launch/solidworks-2013-overview.htm, Accessed:February 2013.

[174] E. Hau, Vibration Characteristics . Wind Turbines, Springer Berlin Heidelberg., 2013.

[175] P. Ferdinand, E. Beer, R. Johnston Jr, J.T. DeWolf, Mechanics of Materials, The McGraw-Hill Companies, 2002.

[176] from: https://wind.nrel.gov/forum/wind/viewtopic.php?f=4&t=743, Accessed:August 2013.

[177] C.J.A. Versteegh Kivi, N. Voordracht, Direct driven generators in wind turbines Experience with the 5 MW prototype. XEMC Darwind Available from: https://afdelingen.kiviniria.net/media-afdelingen/DOM100000223/Verslagen_presentaties/2011/20111107_XEMC-Darwind_symposium/KeesV-Presentatie_Kivi_TUE_7112011.pdf, Accessed:February 2013.

[178] from: http://www.goldwindamerica.com/technology-capabilities/2-5-mw-pmdd/, Accessed:August 2013.

[179] M. Karimirad, T. Moan, Wave and wind induced dynamic response of a spar-type offshore wind turbine, Journal of Waterway, Port, Coastal and Ocean Engineering (2012).138, (1), pp.9-20.

[180] K. Johannessen, T.S. Meling, S. Haver,Joint distribution for wind and waves in the northern North Sea.,International Offshore and Polar Engineering Conference, International Society of Offshore and Polar Engineers (ISOPE),Cupertino, CA,2001.

[181] IEC 61400 -1. Wind Turbines. Part-1: Design requirements. 3rd edn,2005

[182] D.Matha,Model Development and Loads Analysis of an Offshore Wind Turbine on a Tension Leg Platform, with a Comparison to Other Floating Turbine Concepts. NREL/ SR-500-45891,2009.

[183] A. Zavvos, D. Bang, A.S. McDonald, H. Polinder, M.A. Mueller, Structural analysis and optimisation of transverse flux permanent magnet machines for 5 and 10 MW direct drive wind turbines, Wind Energy, (2012).15, pp.19-43.

[184] A.S. McDonald, M.A. Mueller, A lightweight low speed permanent magnet electrical generatorfor direct-drive wind turbines, Wind Energy, (2009).12, (8), pp.768-780.

[185] B. Maples, M. Hand, W. Musial,Comparative Assessment of Direct Drive High Temperature Superconducting Generators in Multi-Megawatt Class Wind Turbines. Technical Report NREL/TP-5000-49086,October 2010.

[186] H. Polinder, D. Bang, R.P.J.O.M. Van Rooij, A.S. McDonald, M.A. Mueller,10 MW Wind Turbine Direct-Drive Generator Design with Pitch or Active Speed Stall Control,IEEE International Electric Machines & Drives Conference,IEMDC '07,Antalya.,3-5 May 2007.

[187] K. Johnson, L. Fingersh, M. Balas, L. Pao,Methods for Increasing Region 2 Power Capture on a Variable Speed HAWT,Proceedings of the 23rd ASME Wind Energy Symposium,Reno,2004.

[188] A.D. Wright , L.J. Fingersh, Advanced Control Design for Wind Turbines . Part I: Control Design, Implementation, and Initial Tests.NREL/TP-500-42437, (March 2008).

[189] T.J. Larsen, A practical guide to tuning of acontroller for a floating pitch regulated turbine.Risø National Laboratory, Technical University of Denmark (September 2007).

[190] J. Mann,Models in micrometeorology.Technical Report, Risoe National Laboratory 1994.

[191] G.H. Keulegan, L.H. Carpenter, Forces on cylinders and plates in an oscillating fluid., Journal of Research of the National Bureau of Standards, (1958).60, (5), pp.423-440.

[192] M. Karimirad, Q. Meissonnier, Z. Gao, T. Moan, Hydroelastic code-to-code comparison for a tension leg spar-type floating wind turbineq, Marine Structures, (2011).24, pp.412-435.

[193] B. Schlecht, T. Schulze, T. Hähnel, T. Rosenloecher,Multibody System Simulation of Offshore Wind Turbines,EWEA Copenhagen,Denmark,2005.

[194] J.L.M. Peeters, D. Vandepitte, P. Sas, Analysis of Internal Drive Train Dynamics in a Wind Turbine, Wind Energy, 9 (1), pp.141-161.

[195] A.R. Nejad, Y. Xing, T. Moan,Gear Train Internal Dynamics in Large Offshore Wind Turbines,ASME 2012 11th Biennial Conference on Engineering Systems Design and Analysis,Nantes, France,2-4July,2012.

[196] W. Shi, Chang-Wan Kim, Chin-Wha Chung, H.-C. Park, Dynamic modeling and analysis of a wind turbine drivetrain using the torsional dynamic model, International Journal of Precision Engineering and Manufacturing, (January 2013).14, (1), pp.153-159.

[197] J. Helsen, F. Vanhollebeke, F. De Coninck, D. Vandepitte, W. Desmet, Insights in wind turbine drive train dynamics gathered by validating advanced models on a newly developed 13.2 MW dynamically controlled test-rig, Mechantronics, (2011).21, (4), pp.737-752.

[198] G. Bywaters, V. John, J. Lynch, P. Mattila, G. Norton, J. Stowell, M. Salata, O. Labath, A. Chertok, D. Hablanian,Northern Power Systems WindPACT Drive Train Alternative Design Study Report April 12, 2001 to January 31, 2005.

[199] J. Heikkinen, J. Sopanen, V. Ruuskanen, J. Nerg,Dynamic analysis of a direct-driven permanent magnet generator drive train including flexible turbine blades,ASME International Design Engineering Technical Conferences Computers and Information in Engineering Conference, IDETC/CIE 2011,Washington, DC, USA,Aug. 2011.

[200] J. Islam , D. Svechkarenko , R. Chin , A. Szucs , J. Mantere , R. Sakki,Cogging torque and vibration analysis of a direct-driven PM wind generator with concentrated and distributed windings,15th International Conference on Electrical Machines and Systems (ICEMS),Sapporo,21-24 Oct. 2012.

[201] J. Sopanen, V. Ruuskanen, J. Nerg, J. Pyrhonen, Dynamic Torque Analysis of a Wind Turbine Drive Train Including a Direct-Driven Permanent-Magnet Generator, IEEE Transactions on Industrial Electronics, (2011).58, (9), pp. 3859-3867.

[202] L. Frøyd, O.G. Dahlhaug,Rotor Design for a 10 MW Offshore Wind Turbine,Proceedings of the Twenty-first (2011) International Offshore and Polar Engineering Conference,Maui, Hawaii, USA,19-24 June 2011.

[203] S.S.Klair, Design of Nacelle and Rotor Hub for NOWITECH 10MW Reference Turbine,MS Thesis,NTNU,2013.

[204] M. Whittle, W. Shin, J. Trevelyan, J. Wu,A Parametric Study of the Effect of Generator Misalignment on Bearing Fatigue Life in Wind Turbines,EWEA 2011,Brussels,2011

[205] S. Dunkerley, On the Whirling and Vibration of Shaft, Philosophical Transactions of the Royal Society of London. A, (1894).185, pp.279-360.

[206] N. Kelly, B. Jonkman, NWTC Design Codes (TurbSim),Available from: http://wind.nrel.gov/designcodes/preprocessors/turbsim/, Accessed:February 2013.

[207] IEC 61400-3 :Design Requirements for Offshore Wind Turbines,1st edn,2009.

[208] from: http://www.sintef.no/project/Nowitech/Wind_presentations/Fylling,%20I.,%20MARINTEK.pdf, Accessed:July 2013.

[209] Z. Jiang, Y. Xing, W. Dong, T. Moan, Z. Gao,Long-term probability distribution of wind turbine planetary bearing loads,Proceedings of the AWEA WINDPOWER 2013 Conference & Exhibition,Chicago, USA, 5-8 May 2013.

[210] ISO 281: Rolling bearings -dynamic load ratings and rating life. 2nd edn,2007.

[211] Germanischer Lloyd,Guideline for the Certification of Offshore Wind Turbines,2010.

[212] Timken Product Catalogue,Available from: http://www.timken.co.uk/EN-US/PRODUCTS/Pages/Catalogs.aspx, Accessed:August 2013.

[213] from: http://www.skf.com/group/products/bearings-units-housings/ball-bearings/principles/selection-of-bearing-size/dynamic-bearing-loads/equivalent-dynamic-bearing-load/index.html, Accessed:January 2014.

[214] B. Niederstucke, A. Anders, P. Dalhoff, R. Grzybowski,Load data analysis for wind turbine gearboxes .Germanischer Lloyd WindEnergie GmbH, Hamburg,2003.

[215] Timken Spherical and Cylindrical Roller Bearings:Product and Technical Handbook,Available from: http://aldobenito.com.ar/x_control/biblioteca/Rodamientos%20%20de%20 rodillo%20esfericos%20y%20cil%C3%ADndricos.pdf, Accessed:August 2013.

APPENDIX-A

Matlab Function to compute the RAO in irregular waves

```
-------------------------------------------------------
This function analyses the responses and plots RAO
-------------------------------------------------------

%Reference: http://www.mathworks.com/support/tech-
notes/1700/1702.html

close all;
path(path,'G:\fft\NEWMODEL\irregular\ORCAFLEX\New Folder')

A1={'Fp=0.7Hz.xls';'Fp=0.8Hz.xls';'Fp=0.9Hz.xls';'Fp=1.0Hz.xls';'Fp=
1.1Hz.xls';'Fp=1.2Hz.xls';'Fp=1.3Hz.xls';'Fp=1.4Hz.xls';'Fp=1.5Hz.xl
s'};

for m=1:9
X1 = xlsread(char(A1(m)));
time(1:4096,m) = X1(:,17);
wave(1:4096,m) =  X1(:,18);
surge(1:4096,m) = X1(:,1);
heave(1:4096,m) = X1(:,3);
pitch(1:4096,m) = X1(:,5);

wave(1:4096,m) = wave(1:4096,m)-mean(wave(1:4096,m));
surge(1:4096,m) = surge(1:4096,m)-mean(surge(1:4096,m));
heave(1:4096,m) = heave(1:4096,m)-mean(heave(1:4096,m));
pitch(1:4096,m) = pitch(1:4096,m)-mean(pitch(1:4096,m));

delt = time2(2)-time2(1);
sample = 1/delt;
samplerand = sample;
window = length(wave);
noverlap = [];
nfft = [];
fs = sample;
frand = samplerand;
nf = 256;
wave_amp(:,m),f] = pwelch(wave(1:4096,m),[],noverlap,nfft,fs);

figure(1)
plot(f,wave_amp,'bo-'), hold on
xlabel('Frequency (Hz)')
ylabel('Wave spectral density (m^2-s)'), hold on
grid on
xlim([0.02 3]),
tx1 = [time(1:4096,m) wave(1:4096,m)];
S_1 = spec(tx1,256,[],0,[],'cov');
Smeas1 = S_1;
plot(Smeas.f,Smeas.S,'ro-')%spectrum given in m^2*s
hold off

figure(2)
window = length(surge);
```

```
surge_amp(:,m),f] = pwelch(surge(1:4096,m),[],noverlap,nfft,fs);
subplot(2,1,1)
plot(f,surge_amp,'bo-'), hold on
xlabel('Frequency (Hz)')
ylabel('Surge Spectral density (m^2-s)'), hold on
grid on
xlim([0.02 1.6]), hold on
ts1 = [time(1:4096,m) surge(1:4096,m)];
Sts1=spec(ts1,256,[],0,[],'cov');
Smeas_ts1 = Sts1;
plot(Smeas_ts.f,Smeas_ts.S,'ro-')
% hold off

subplot(2,1,2)
surge_rao1(:,m) = sqrt(surge_amp(:,m)./wave_amp(:,m));
surge_rao1_ts(:,m) = sqrt(Smeas_ts1.S./Smeas1.S);
plot(f,surge_rao1,'bo-'); hold on
plot(Smeas.f,surge_rao1_ts,'ro-'); hold on
xlabel('Frequency (Hz)')
ylabel('Surge RAO (m/m)'), hold on
grid on
xlim([0.02 1.6]), hold off

omega = 2*pi*f;
xax = omega.^2*(0.0508)/(2*9.81);
omega_s = 2*pi*Smeas1.f;
xax_s = omega_s.^2*(0.0508)/(2*9.81);

subplot(2,1,3)
plot(xax,surge_rao1,'bo-'); hold on
plot(xax_s,surge_rao1_ts,'ro-'); hold on
xlabel('\omega^2D/(2g)');
ylabel('Surge RAO (m/m)');
xlim([0.04 0.35]);
grid on
hold off

figure(3)
window = length(heave);
fsrand = samplerand;
heave_amp(:,m),f] = pwelch(heave(1:4096,m),[],noverlap,nfft,fs);

subplot(3,1,1)
plot(f,heave_amp,'bo-'), hold on
xlabel('Frequency (Hz)')
ylabel('heave Spectral density (m^2-s)'), hold on
grid on
xlim([0.02 1.6])
th1 = [time(1:4096,m) heave(1:4096,m)];
Sth1=spec(th1,256,[],0,[],'cov');
Smeas_th1 = Sth1;
plot(Smeas_th.f,Smeas_th.S,'ro-')
hold off

subplot(3,1,2)
heave_rao1(:,m) = sqrt(heave_amp(:,m)./wave_amp(:,m));
heave_rao1_th(:,m) = sqrt(Smeas_th1.S./Smeas1.S);
```

```
plot(f,heave_rao1,'bo-'); hold on
plot(Smeas.f,heave_rao1_th,'ro-'); hold on
xlabel('Frequency (Hz)')
ylabel('Heave RAO(m/m)'), hold on
grid on
xlim([0.02 1.6])

subplot(3,1,3)
omega_h = 2*pi*Smeas1.f;
xax_h = omega_h.^2*(0.0508)/(2*9.81);
plot(xax,heave_rao1,'bo-'); hold on
plot(xax_h,heave_rao1_th,'ro-'); hold on
xlabel('\omega^2D/(2g)');
ylabel('Heave RAO (m/m)');
xlim([0.04 0.35]);
grid on
hold off

figure(4)
window = length(pitch);
fsrand = samplerand;
[pitch_amp(:,m),f] = pwelch(pitch(1:4096,m),[],noverlap,nfft,fs);
subplot(4,1,1)
plot(f,pitch_amp,'bo-'), hold on
xlabel('Frequency (Hz)')
ylabel('pitch Spectral density (m^2-s)'), hold on
grid on
xlim([0.02 1.6])
tp1 = [time(1:4096,m) pitch(1:4096,m)];
Stp1=spec(tp1,256,[],0,[],'cov');
Smeas_tp1 = Stp1;
plot(Smeas_tp.f,Smeas_tp.S,'ro-')
hold off

subplot(4,1,2)
pitch_rao1(:,m) = sqrt(pitch_amp(:,m)./wave_amp(:,m));
pitch_rao1_tp(:,m) = sqrt(Smeas_tp1.S./Smeas1.S);
plot(f,pitch_rao1,'bo-'), hold on
plot(Smeas.f,pitch_rao1_tp,'ro-'); hold on
xlabel('Frequency (Hz)')
ylabel('Pitch RAO (deg/m)'), hold on
grid on
xlim([0.02 1.6])
hold off
subplot(4,1,3)
xax = omega.^2*(0.0508)/(2*9.81);
omega_p = 2*pi*Smeas1.f;
xax_p = omega_p.^2*(0.0508)/(2*9.81);
plot(xax,pitch_rao1,'bo-'); hold on
plot(xax_p,pitch_rao1_tp,'ro-'); hold on
xlabel('\omega^2D/(2g)');
ylabel('Pitch RAO (deg/m)');
grid on
xlim([0.04 0.35]);
hold off

end
```

APPENDIX-B

Bearing Stiffness Calculation Basis and Data provided by TIMKEN

Bearing stiffness is an important input when calculating deflections and vibrations in a Finite Element Analysis. A complete and complex way is to model the bearing with several springs per roller and to model the races. Another approach is to consider the bearing connected to the system with two points only located on the axis of rotation (one for each race) and then to define the stiffness between these two points. The matrix provided to customer is mainly for calculation of the shaft and housing deflections

In that case above, several options are available and will be described, from the pure diagonal matrix (accepting negative terms), to a more complex one respecting the coupling between axial and radial load, or moment and radial load, etc. The simple diagonal matrix can only be used at the same load used for defining the bearing stiffness matrix while the matrix including coupling term can be used at slightly different load zones.

This report describes shortly the models used to estimate the miscellaneous bearing stiffness matrices that can be used directly by the customer in its FEA.

1. Node definition

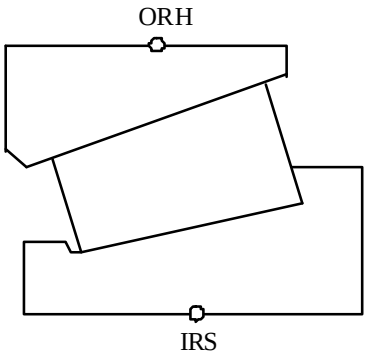

Fig.A.1.1 Bearing Nodal representation

Since the real bearing behavior is non-linear, a linearised bearing stiffness can only be defined for a given loading condition and extrapolated to other conditions close to this value. This linearised bearing stiffness will be defined between the two characteristic nodes IRS and ORH respectively representing the connection to shaft and housing (and located on the axis of rotation at two distinguished axial positions). In order to calculate the

stiffness matrix, the input data are the relative bearing deformations (example $dX = X_{IRS} - X_{ORH}$) and the bearing forces at the load condition. Note that dX includes the relative deformation due to the roller – race Hertzian contact.

2. Linearised bearing stiffness calculation method (Case 1)

2.1 Fully linearised stiffness

The simplest way to do this calculation could be to directly determine the diagonal stiffness matrix by applying the following relations

$$Kx = Fx/dX$$
$$Ky = Fy/dY$$
$$Kz = Fz/dZ$$
$$Kty = My/d\theta y$$
$$Ktz = Mz/d\theta z$$

But as it can be shown on the following graph, this approach is very approximative and cannot be used in another loading condition. Negative axial stiffness value can be obtained for narrow load zone conditions (point A in attached sketch).

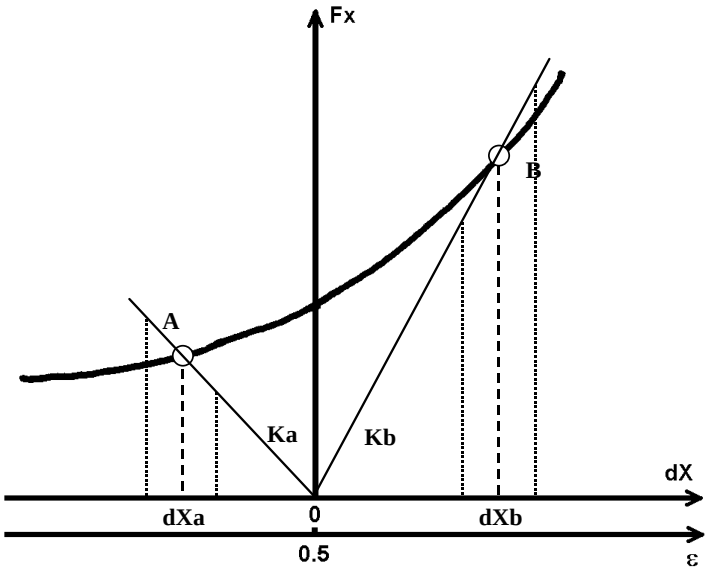

Fig.A.2 Axial force as a function of the relative axial displacement under a given radial load

2.2 Linearised stiffness with induced terms

This second approach is more accurate as it makes use of coupling terms and a reference point corresponding to to a load zone of 180° (no axial displacement) as shown on the graph below. Coupling terms between the axial and radial load, as well as tilting moment (relative to race center) and radial load are included as described in Reference 1, allowing a safer extrapolation to another loading condition (which should nevertheless remain in the vicinity of the one used for defining the stiffness matrix, i.e. the direction of the radial load as well well as the load zone should not change too much).

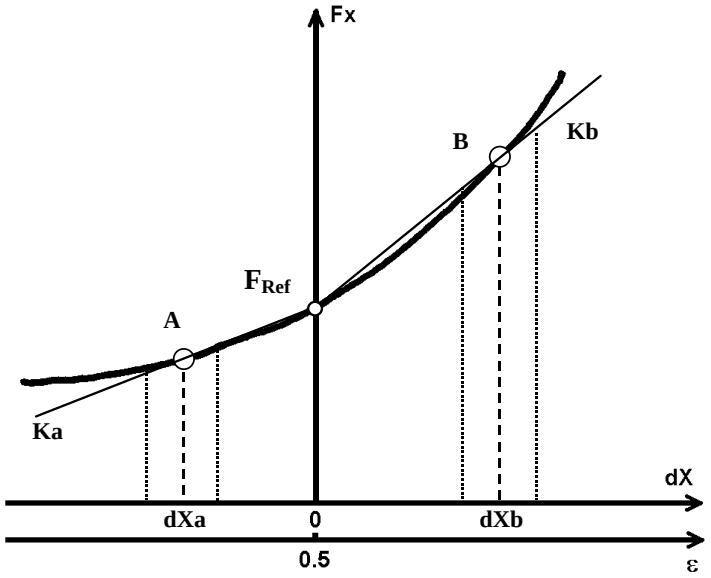

Fig.A.3 Axial force as a function of the relative axial displacement under a given radial load

Using the reference point, the bearing behavior at node IRS is described by:

$$\begin{Bmatrix} Fx \\ Fy \\ Fz \\ My \\ Mz \end{Bmatrix} = \begin{bmatrix} Kxx & 0 & 0 & 0 & 0 \\ 0 & Kyy & 0 & 0 & Ky\theta z \\ 0 & 0 & Kzz & Kz\theta y & 0 \\ 0 & 0 & 0 & K\theta y\theta y & 0 \\ 0 & 0 & 0 & 0 & K\theta z\theta z \end{bmatrix} \cdot \begin{Bmatrix} dX \\ dY \\ dZ \\ d\theta y \\ d\theta z \end{Bmatrix} + \begin{Bmatrix} F_{Ref} \\ 0 \\ 0 \\ -C \cdot Fz \\ C \cdot Fy \end{Bmatrix}$$

By developing the latter relationship, the linearised stiffness matrix including coupling terms can be expressed as:

$$K_{II} = \begin{bmatrix} K'xx & K'xy & K'xz & K'x\theta y & K'x\theta z \\ 0 & K'yy & 0 & 0 & K'y\theta z \\ 0 & 0 & K'zz & K'z\theta y & 0 \\ 0 & 0 & K'\theta yz & K'\theta y\theta y & 0 \\ 0 & K'\theta zy & 0 & 0 & K'\theta z\theta z \end{bmatrix}$$

The final bearing stiffness matrix which takes into account the different axial location of node IRS & ORH, can finally be written:

$$\begin{Bmatrix} F_{IRS} \\ F_{ORH} \end{Bmatrix} = [K_{Brg}] \cdot \begin{Bmatrix} d_{IRS} \\ d_{ORH} \end{Bmatrix} \qquad \text{with} \qquad K_{Brg} = \begin{bmatrix} K_{II} & K_{IO} \\ K_{OI} & K_{OO} \end{bmatrix}$$

The final bearing stiffness matrix K_{Brg} is the most appropriate one for calculating displacements in a linear FEA. An example of these four blocks is given in Appendix 1 point 3.

- Sketch for TDI node positions

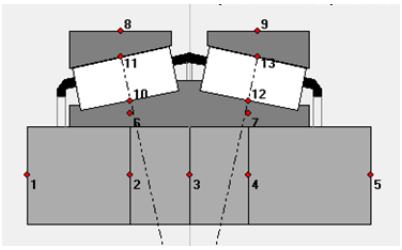

- Sketch for CRB node positions

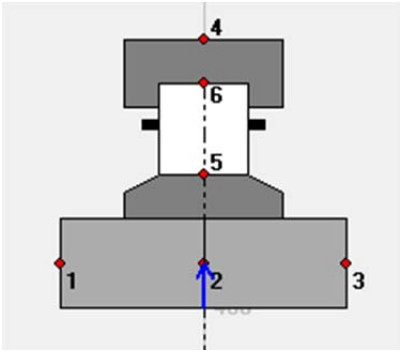

Reference

1. L. Houpert, A Uniform analytical approach for ball and roller bearing, ASME Journal of Tribology, Vol. 119, p. 851 - 857, Oct. 1997.

```
BEARING STIFFNESS FOR TDI
=================================

Row #1
==================


  LINEARIZED STIFFNESS MATRIX FOR LOADS & DISPLACEMENTS CALCULATIONS
  ------------------------------------------------------------------

 Units : N, m, rad

           Node INNER & INNER (2 & 2)
               1.6943575E+08   -2.8935659E+09    2.9267107E+09   -3.5097495E+08   -3.4700018E+08
               0.0000000E+00    1.1186360E+10    0.0000000E+00    0.0000000E+00    1.3414828E+09
               0.0000000E+00    0.0000000E+00    1.1314496E+10   -1.3568490E+09    0.0000000E+00
               0.0000000E+00    0.0000000E+00   -1.3568490E+09    3.6855601E+08    0.0000000E+00
               0.0000000E+00    1.3414828E+09    0.0000000E+00    0.0000000E+00    2.1727134E+08
           Node INNER & OUTER (2 & 8)
              -1.6943575E+08    2.8935659E+09   -2.9267107E+09    3.5097495E+08    3.4700018E+08
               0.0000000E+00   -1.1186360E+10    0.0000000E+00    0.0000000E+00   -1.3414828E+09
               0.0000000E+00    0.0000000E+00   -1.1314496E+10    1.3568490E+09    0.0000000E+00
               0.0000000E+00    0.0000000E+00    1.3568490E+09   -3.6855601E+08    0.0000000E+00
               0.0000000E+00   -1.3414828E+09    0.0000000E+00    0.0000000E+00   -2.1727134E+08
           Node OUTER & INNER (8 & 2)
              -1.6943575E+08    2.8935659E+09   -2.9267107E+09    3.5097495E+08    3.4700018E+08
               0.0000000E+00   -1.1186360E+10    0.0000000E+00    0.0000000E+00   -1.3414828E+09
               0.0000000E+00    0.0000000E+00   -1.1314496E+10    1.3568490E+09    0.0000000E+00
               0.0000000E+00    0.0000000E+00    1.5156948E+09   -3.8760499E+08    0.0000000E+00
               0.0000000E+00   -1.4985296E+09    0.0000000E+00    0.0000000E+00   -2.3610459E+08
           Node OUTER & OUTER (8 & 8)
               1.6943575E+08   -2.8935659E+09    2.9267107E+09   -3.5097495E+08   -3.4700018E+08
               0.0000000E+00    1.1186360E+10    0.0000000E+00    0.0000000E+00    1.3414828E+09
               0.0000000E+00    0.0000000E+00    1.1314496E+10   -1.3568490E+09    0.0000000E+00
               0.0000000E+00    0.0000000E+00   -1.5156948E+09    3.8760499E+08    0.0000000E+00
               0.0000000E+00    1.4985296E+09    0.0000000E+00    0.0000000E+00    2.3610459E+08
```

```
BEARING STIFFNESS FOR TDI
=================================

Row #2
================

  LINEARIZED STIFFNESS MATRIX FOR LOADS & DISPLACEMENTS CALCULATIONS
  ------------------------------------------------------------------

   Units : N, m, rad

           Node INNER & INNER (4 & 4)
               3.4049134E+08    4.4903512E+09   -4.4795293E+09   -5.3719098E+08   -5.3848875E+08
               0.0000000E+00    1.8880203E+10    0.0000000E+00    0.0000000E+00   -2.2641385E+09
               0.0000000E+00    0.0000000E+00    1.8834702E+10    2.2586819E+09    0.0000000E+00
               0.0000000E+00    0.0000000E+00    2.2586819E+09    5.6938735E+08    0.0000000E+00
               0.0000000E+00   -2.2641385E+09    0.0000000E+00    0.0000000E+00    3.3867712E+08
           Node INNER & OUTER (4 & 9)
              -3.4049134E+08   -4.4903512E+09    4.4795293E+09    5.3719098E+08    5.3848875E+08
               0.0000000E+00   -1.8880203E+10    0.0000000E+00    0.0000000E+00    2.2641385E+09
               0.0000000E+00    0.0000000E+00   -1.8834702E+10   -2.2586819E+09    0.0000000E+00
               0.0000000E+00    0.0000000E+00   -2.2586819E+09   -5.6938735E+08    0.0000000E+00
               0.0000000E+00    2.2641385E+09    0.0000000E+00    0.0000000E+00   -3.3867712E+08
           Node OUTER & INNER (9 & 4)
              -3.4049134E+08   -4.4903512E+09    4.4795293E+09    5.3719098E+08    5.3848875E+08
               0.0000000E+00   -1.8880203E+10    0.0000000E+00    0.0000000E+00    2.2641385E+09
               0.0000000E+00    0.0000000E+00   -1.8834702E+10   -2.2586819E+09    0.0000000E+00
               0.0000000E+00    0.0000000E+00   -2.5231048E+09   -6.0109729E+08    0.0000000E+00
               0.0000000E+00    2.5292002E+09    0.0000000E+00    0.0000000E+00   -3.7046366E+08
           Node OUTER & OUTER (9 & 9)
               3.4049134E+08    4.4903512E+09   -4.4795293E+09   -5.3719098E+08   -5.3848875E+08
               0.0000000E+00    1.8880203E+10    0.0000000E+00    0.0000000E+00   -2.2641385E+09
               0.0000000E+00    0.0000000E+00    1.8834702E+10    2.2586819E+09    0.0000000E+00
               0.0000000E+00    0.0000000E+00    2.5231048E+09    6.0109729E+08    0.0000000E+00
               0.0000000E+00   -2.5292002E+09    0.0000000E+00    0.0000000E+00    3.7046366E+08
```

```
BEARING STIFFNESS FOR CRB
===============

  LINEARIZED STIFFNESS MATRIX FOR LOADS & DISPLACEMENTS CALCULATIONS
  ------------------------------------------------------------------

  Units : N, m, rad

          Node INNER & INNER (2 & 2)
              0.0000000E+00    0.0000000E+00    0.0000000E+00    0.0000000E+00    0.0000000E+00
              0.0000000E+00    1.7297122E+09    0.0000000E+00    0.0000000E+00    0.0000000E+00
              0.0000000E+00    0.0000000E+00    1.6505651E+09    0.0000000E+00    0.0000000E+00
              0.0000000E+00    0.0000000E+00    0.0000000E+00    4.6527938E+05    0.0000000E+00
              0.0000000E+00    0.0000000E+00    0.0000000E+00    0.0000000E+00    3.0738568E+06
          Node INNER & OUTER (2 & 4)
              0.0000000E+00    0.0000000E+00    0.0000000E+00    0.0000000E+00    0.0000000E+00
              0.0000000E+00   -1.7297122E+09    0.0000000E+00    0.0000000E+00    0.0000000E+00
              0.0000000E+00    0.0000000E+00   -1.6505651E+09    0.0000000E+00    0.0000000E+00
              0.0000000E+00    0.0000000E+00    0.0000000E+00   -4.6527938E+05    0.0000000E+00
              0.0000000E+00    0.0000000E+00    0.0000000E+00    0.0000000E+00   -3.0738568E+06
          Node OUTER & INNER (4 & 2)
              0.0000000E+00    0.0000000E+00    0.0000000E+00    0.0000000E+00    0.0000000E+00
              0.0000000E+00   -1.7297122E+09    0.0000000E+00    0.0000000E+00    0.0000000E+00
              0.0000000E+00    0.0000000E+00   -1.6505651E+09    0.0000000E+00    0.0000000E+00
              0.0000000E+00    0.0000000E+00    0.0000000E+00   -4.6527938E+05    0.0000000E+00
              0.0000000E+00    0.0000000E+00    0.0000000E+00    0.0000000E+00   -3.0738568E+06
          Node OUTER & OUTER (4 & 4)
              0.0000000E+00    0.0000000E+00    0.0000000E+00    0.0000000E+00    0.0000000E+00
              0.0000000E+00    1.7297122E+09    0.0000000E+00    0.0000000E+00    0.0000000E+00
              0.0000000E+00    0.0000000E+00    1.6505651E+09    0.0000000E+00    0.0000000E+00
              0.0000000E+00    0.0000000E+00    0.0000000E+00    4.6527938E+05    0.0000000E+00
              0.0000000E+00    0.0000000E+00    0.0000000E+00    0.0000000E+00    3.0738568E+06
```